

VOL 1
PART 2

TD 155

1

AD 744630

PROCEEDINGS OF THE

ARRAY

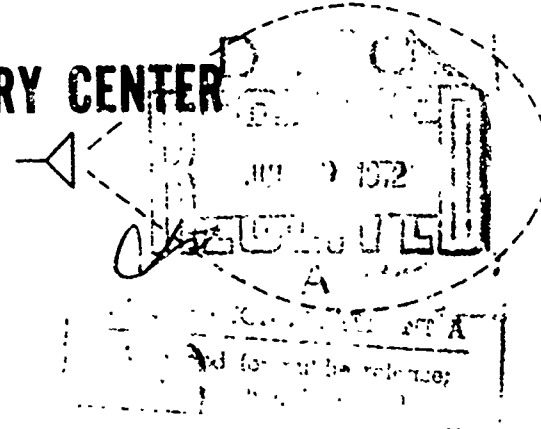
ANTENNA

CONFERENCE

HELD AT

NAVAL ELECTRONICS LABORATORY CENTER
SAN DIEGO, CALIFORNIA 92152

22-24 FEBRUARY 1972



Reproduced by
NATIONAL TECHNICAL
INFORMATION SERVICE
U.S. Department of Commerce
Springfield VA 22151

129

UNCLASSIFIED

Security Classification

DOCUMENT CONTROL DATA - R & D

(Security classification of title, body of abstract and indexing annotation must be entered when the overall report is classified)

1. ORIGINATING ACTIVITY (Corporate author) Naval Electronics Laboratory Center San Diego, California 92152		2a. REPORT SECURITY CLASSIFICATION UNCLASSIFIED	
		2b. GROUP	
3. REPORT TITLE PROCEEDINGS OF THE ARRAY ANTENNA CONFERENCE, 22 - 24 FEBRUARY 1972, Volume I			
4. DESCRIPTIVE NOTES (Type of report and inclusive dates) Conference contributions			
5. AUTHOR(S) (First name, middle initial, last name) Coordinator, J. E. Boyns			
6. REPORT DATE 24 February 1972		7a. TOTAL NO. OF PAGES	7b. NO. OF REFS
8a. CONTRACT OR GRANT NO.		8b. ORIGINATOR'S REPORT NUMBER(S)	
b. PROJECT NO SF11.141.008 (NELC D210)		TD 155, Volume I	
c.		9d. OTHER REPORT NO(S) (Any other numbers that may be assigned this report)	
d.			
10. DISTRIBUTION STATEMENT Approved for public release; distribution unlimited.			
11. SUPPLEMENTARY NOTES		12. SPONSORING MILITARY ACTIVITY Naval Ship Systems Command and Naval Electronics Laboratory Center	
13. ABSTRACT The Array Antenna Conference held at NELC 22 -- 24 February 1972 included 37 papers from government agencies and their contractors in private industry. Topics presented were mainly concerned with array antennas, with emphasis on phased arrays, array techniques, adaptive arrays, conformal arrays, and component techniques. Papers on both theoretical and experimental hardware were presented. The Proceedings are published in two volumes, the first comprising the unclassified papers; the second, the classified papers.			

I

25. ADAPTIVE ARRAYS FOR AIRCRAFT COMMUNICATION SYSTEMS

by

R. T. Compton, Jr.

The Ohio State University ElectroScience Laboratory
Department of Electrical Engineering
Columbus, Ohio 43212
10 January 1972

for

ARRAY ANTENNA CONFERENCE

Naval Electronics Laboratory Center
San Diego, California

22, 23, 24 February 1972

Details of illustrations in
this document may be better
studied on microfiche

25. ADAPTIVE ARRAYS FOR AIRCRAFT COMMUNICATION SYSTEMS*

R. T. Compton, Jr.

The Ohio State University ElectroScience Laboratory
Department of Electrical Engineering
Columbus, Ohio 43212

INTRODUCTION

An adaptive antenna is an antenna that continuously adjusts its own pattern, by means of feedback, while it operates. The pattern of an adaptive antenna at any given time depends on the electromagnetic environment it finds itself in. To date, all adaptive antennas have been arrays, since it is possible to control the pattern of an array easily by varying the gain and phase of the signal from each element.

One important application of adaptive arrays is to the problem of interference rejection in communication systems. An adaptive array can be made to separate a desired signal from interference, by forming a main beam in the direction of the desired signal and forming nulls in the directions of the interference. The array can do this automatically; that is, the antenna designer does not need to know in advance what directions these signals will come from. In addition, adaptive feedback techniques make it possible to use conformal array elements that are irregularly spaced on a curved surface. There is no need for uniform mutual impedances from element to element, or for identical element patterns from each element.

Adaptive arrays have been under study for several years. Widrow, et al.¹, suggested the basic feedback algorithm and did computer simulations of the behavior of such an array. Shor² and Applebaum³ have also studied closely related ideas. An early experimental adaptive array was built at Ohio State and is described in Riegler and Compton⁴.

*The work reported in this paper was supported in part under ONR Contract N00014-67-A-0232-0009 between Office of Naval Research, and The Ohio State University Research Foundation.

Recently, a 4-element adaptive array for the 200-400 MHz band was constructed at Ohio State under navy sponsorship and was used to experiment with a conformal array on an aircraft fuselage mockup. The results of these experiments are discussed in Compton^{5,6} and will form the subject of this paper.

The application of adaptive arrays to interference rejection in coded communication systems is also currently under investigation, both theoretically and experimentally. The behavior of an array with coded signals, based on a bootstrap reference signal generation circuit, has been studied with computer simulations, and the results are discussed by Reinhard⁷. An experimental coded adaptive array has been implemented and is currently under investigation at Ohio State. The results will be documented in a forthcoming report. The problem of establishing initial code timing for the array when interference is present is also currently under study. One approach, the power equalization technique, has been examined in some detail and appears quite promising⁸.

In this paper, we discuss typical pattern characteristics of the 4-element adaptive array described in References 5 and 6. First, we review general adaptive array concepts and then specific experimental results are described.

DESCRIPTION OF THE ADAPTIVE ARRAY

The general configuration of an adaptive array is shown in Fig. 1. The signal from each element, $y_i(t)$, is adjusted in magnitude and phase in the box labeled c_i and then added to produce the array output $s(t)$. The gain and phase adjustment c_i in each channel is under the control of a feedback system. This feedback system adjusts the c_i to minimize the mean-square value of the error signal $e(t)$. The error signal is the difference between a reference signal $R(t)$ and the array output $s(t)$. If the reference $R(t)$ is chosen so it closely approximates the desired signal portion of the array output, then the error signal will consist mainly of the undesired components of the array output, such as interference, jamming, and background radiation. Minimizing the error signal then corresponds to minimizing the antenna response to these undesired signals and results in pattern nulls in the directions from which these signals arrive.

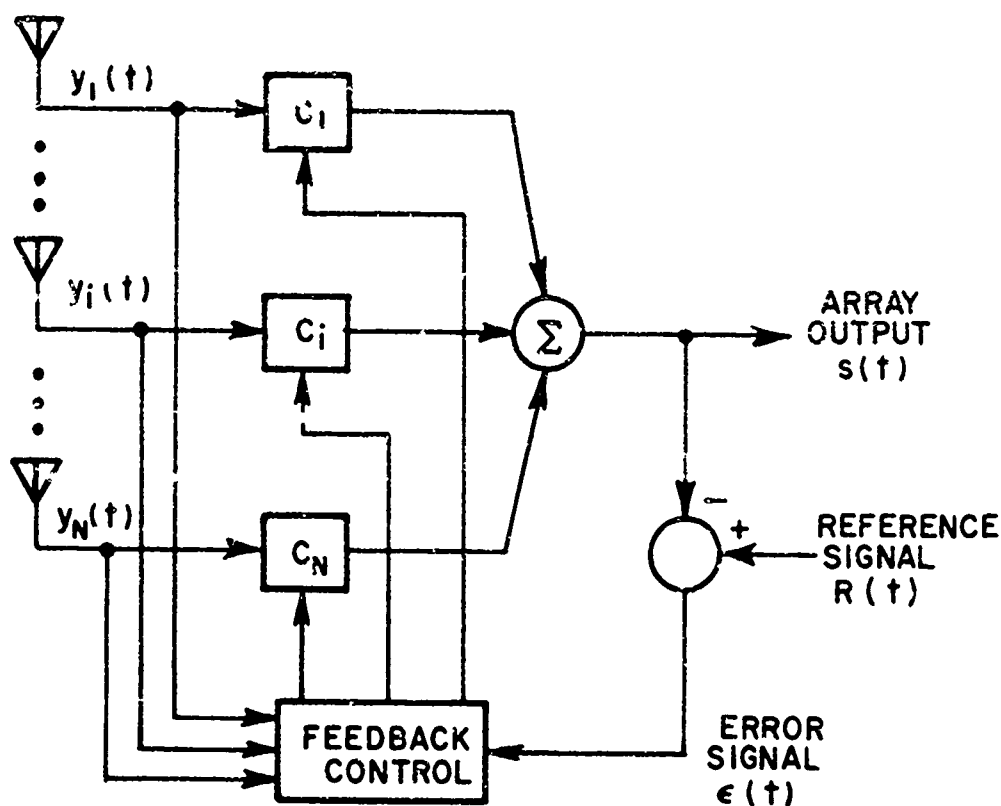


Fig. 1. The adaptive array configuration.

In practice, the gain and phase adjustment of the signal from each element is done by splitting the signal into two quadrature components with a quadrature hybrid, as shown in Fig. 2. The two outputs from the hybrid are separately weighted with real coefficients w_i , whose values are under the control of the feedback loop.

The operation of the feedback loop is based on a steepest-descent gradient technique, as discussed in References 1 and 4. In Fig. 2 $x_1(t)$ and $x_2(t)$ represent the in-phase and quadrature components of the signal from element 1, $x_3(t)$ and $x_4(t)$ represent the in-phase and quadrature components from element 2, and so forth. The total array output is given by

$$(1) \quad s(t) = \sum_{i=1}^{2N} w_i x_i(t).$$

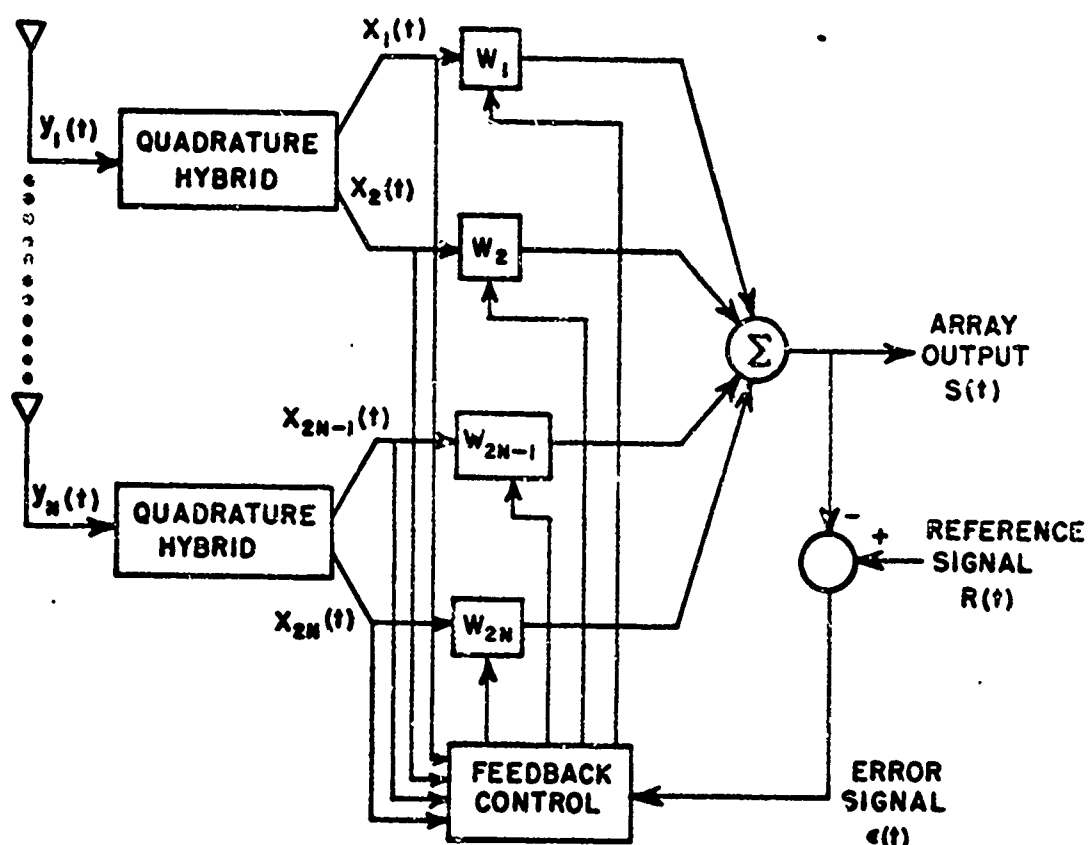


Fig. 2. Quadrature splitting of each element signal.

The error signal is then

$$(2) \quad \epsilon(t) = R(t) - \sum_{i=1}^{2N} w_i x_i(t),$$

and the time-average value of $\epsilon^2(t)$ is

$$(3) \quad \overline{\epsilon^2(t)} = \overline{R^2(t)} - 2 \sum_{i=1}^{2N} w_i \overline{x_i(t) R(t)} + \sum_{i=1}^{2N} \sum_{j=1}^{2N} w_i w_j \overline{x_i(t) x_j(t)}.$$

$\overline{\epsilon^2(t)}$ is a quadratic function of the weights, so there is a unique optimum value for each weight where $\overline{\epsilon^2(t)}$ will be minimum.* To force

*A detailed discussion of the properties of the $\overline{\epsilon^2(t)}$ surface is given in Reference 8.

the weights to the point where $\overline{\epsilon^2(t)}$ is minimal, each w_i is adjusted according to the following feedback rule:

$$(4) \quad \frac{dw_i}{dt} = -k \frac{\partial [\overline{\epsilon^2(t)}]}{\partial w_i},$$

which is known as the LMS Algorithm.^{1,4} Equation (4) is also referred to as a gradient or steepest-descent technique in the adapt control literature⁹.

If Eq. (3) is differentiated with respect to w_i , it is found that

$$(5) \quad \frac{\partial [\overline{\epsilon^2(t)}]}{\partial w_i} = -2 \overline{x_i(t) R(t)} + 2 \sum_{j=1}^{2N} w_j \overline{x_i(t) x_j(t)} = -2 \overline{x_i(t) \epsilon(t)}$$

so the feedback rule in Eq. (4) becomes

$$(6) \quad \frac{dw_i}{dt} = 2k \overline{x_i(t) \epsilon(t)},$$

or, in integral form,

$$(7) \quad w_i = w_{i0} + 2k \int_0^t \overline{x_i(t') \epsilon(t')} dt'.$$

Figure 3 shows the resulting structure of the feedback loop for one of the w_i . The feedback for an entire element involves two such loops, as shown in Fig. 4.

A 4-element adaptive array processor that performs the functions shown in Fig. 4 was constructed and is shown in Fig. 5.

The detailed characteristics of this processor are discussed in Reference 5 and the reader is referred there for details. Figure 6 shows a block diagram of the functions contained in the processor.

This processor was used to take antenna patterns with an array of 4 multiturn loop elements¹⁰ mounted on an aircraft fuselage mockup. Figure 7 shows a photograph of the aircraft mockup, including a wing structure that was added near the elements.

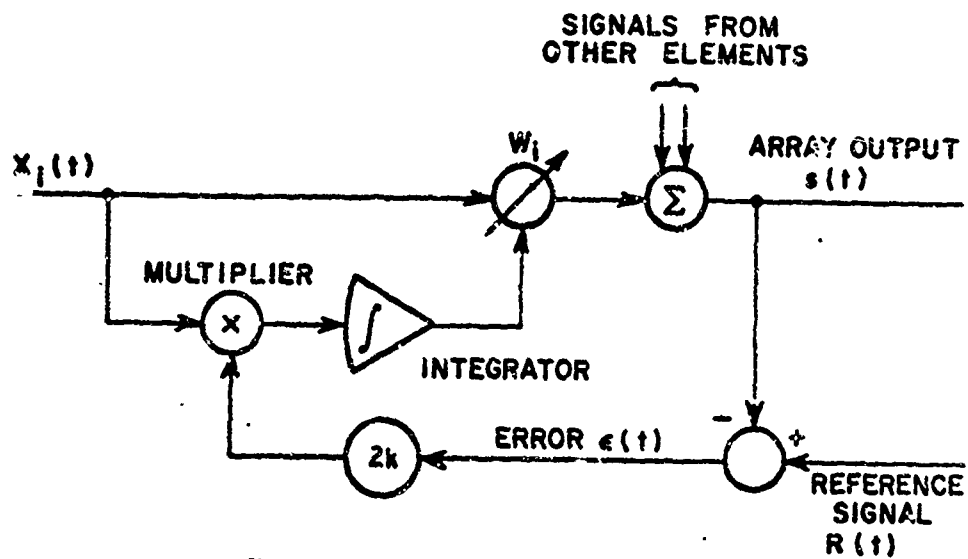


Fig. 3. Basic feedback loop.

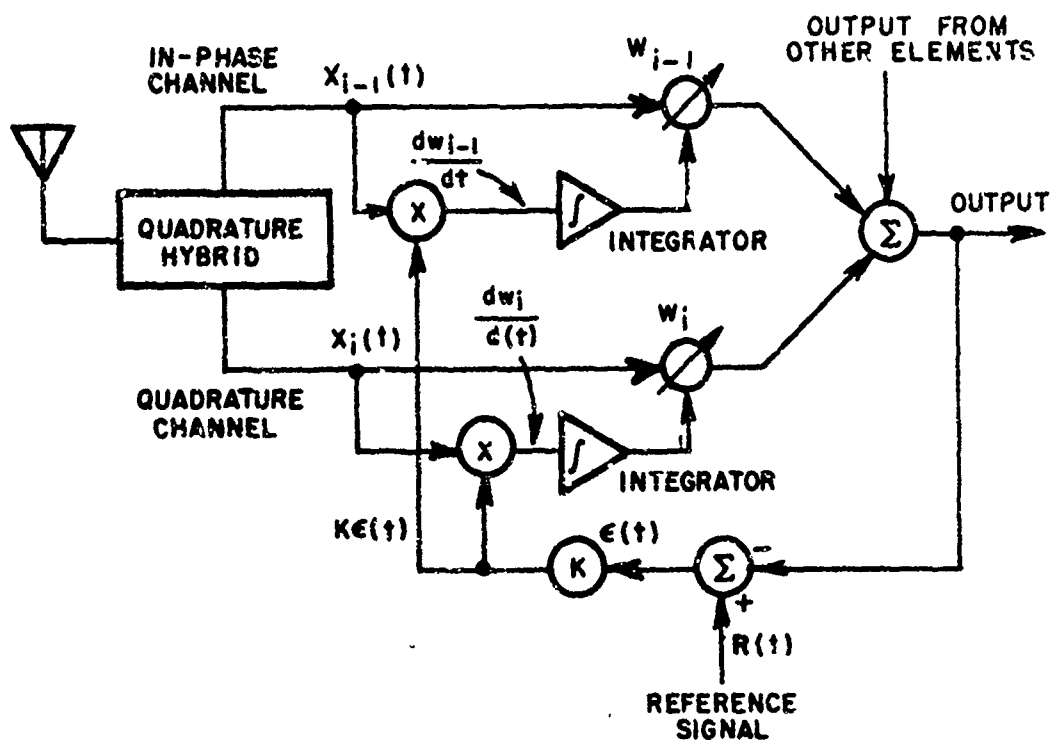


Fig. 4. Feedback loop for each element.



Fig. 5. Adaptive array processor.

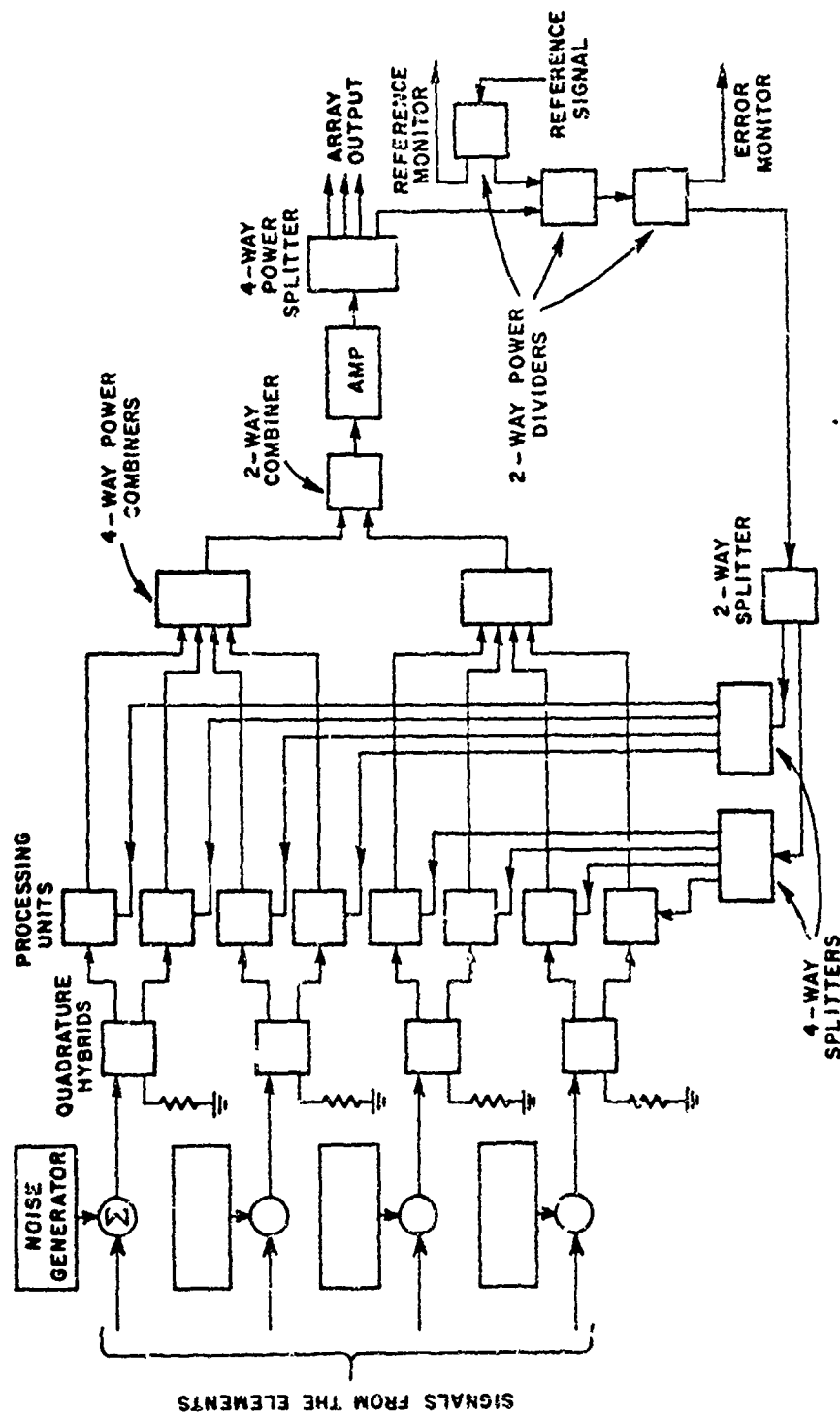


Fig. 6. Complete adaptive array processing system.

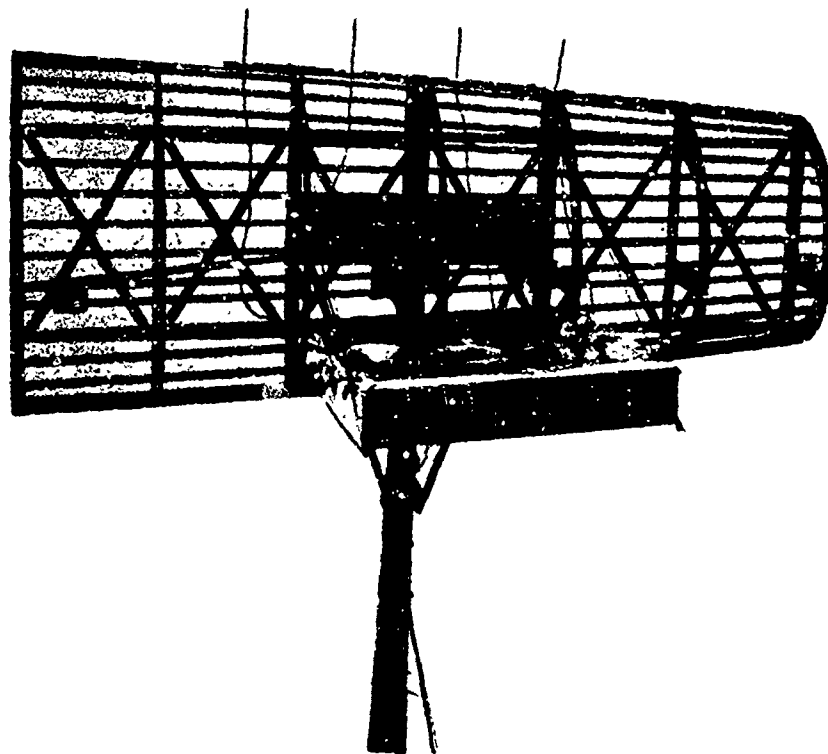


Fig. 7a. Aircraft mockup with wing.

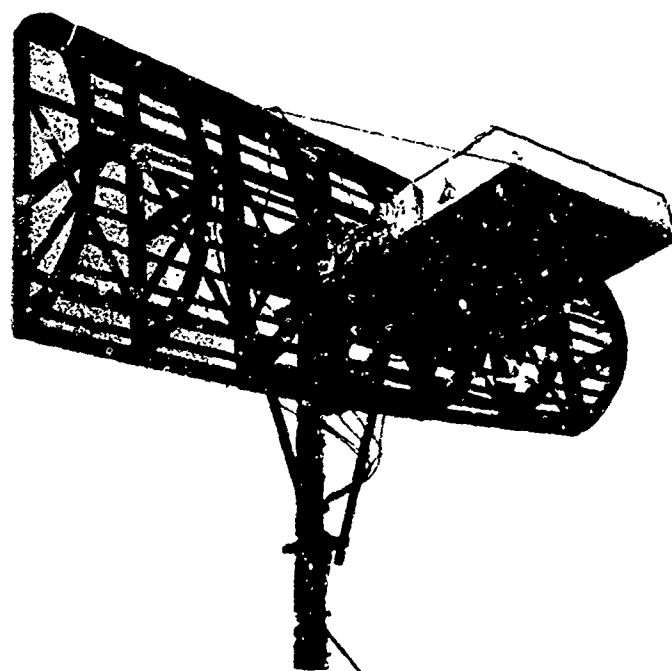


Fig. 7b. Aircraft mockup with wing.

EXPERIMENTAL RESULTS

Patterns were taken at several frequencies in the 200-400 MHz band. The procedure for taking patterns with the array is to illuminate the array from some angle, to allow the weighting coefficients to come to final values, and then to freeze the weights at these values. The pattern is then run with the weights fixed. Figures 8-14 show some typical results obtained at 307 MHz.

In these curves, 0° on the abscissa represents broadside to the array, -90° represents forward endfire (the signal arrives from the front of the aircraft) and $+90^\circ$ represents backward endfire (the signal arrives from the tail). In Fig. 8, the signal arrives from -90° . The weights are allowed to adapt and then are frozen. The pattern is run, and the figure shows the results. In Fig. 9, the signal arrives from -30° , in Fig. 10 it arrives from -30° , and so forth.

These patterns are typical and show two important characteristics of most of the patterns taken with this array:

(1) The main beam tracks the desired signal well in most cases, but the exception occurs at angles where the amplitude response of the elements is changing rapidly. Figures 8 and 14 show beam pointing errors, for example. These errors resulted because the element patterns of all four elements were dropping significantly near $\pm 90^\circ$. When the amplitude response of the elements changed more rapidly with angle than the space phase factors, a beam pointing error resulted.

(2) The patterns often have sidelobes that are not very far down from the main beam. This situation is, however, not necessarily bad. Normally low sidelobes are needed from an antenna to minimize the effect of unwanted radiation from directions outside the main beam. An adaptive array, however, has high sidelobes only in directions from which no signals arrive. When interference is present at some angle, the array will not have a high sidelobe in that direction (as will be clear below). The adaptive array accomplishes the goal of minimizing the effects of unwanted radiation, but in a different way than the conventional antenna.

Next, we show some tests where an interference signal was present as well as the desired signal. In these tests, the array is illuminated with both a desired and an interference signal, the weights are allowed to adapt and then frozen, and the pattern is run. The desired signal is used to generate the reference signal for the array. The interference signal is derived from a separate oscillator and is not coherent with the desired signal or the reference signal.

Figure 15 shows a typical result. The desired signal arrives from $+60^\circ$ and the interference from -60° . One curve shows the pattern that results when no interference is present, and the other shows the pattern with interference. The two curves were taken with no change in gain in the system, and it can be seen how the array holds the desired signal level constant and nulls the interference.

The pattern that results when an interfering signal is present depends not only on the interference angle but also on the interference power. The stronger the interference, the deeper the null. This behavior occurs because the feedback loop gain in the LMS algorithm is proportional to the power of the signals received. Figure 16 shows the same experiment as Fig. 15, except that in this case the power of the interfering signal is varied. One can see that as the interference power is increased, the null originally at about -40° gradually moves over toward the interference and the response in the direction of the interference drops. It is interesting to note that at higher interference powers, a 3 dB increase in interference power produces an improvement in interference rejection greater than 3 dB. For example, when the interference power increases from -3 dB to 0 dB, the pattern response to the interference drops by 5 dB. Hence the stronger interference power (0 dB) results in a weaker interference signal at the array output.

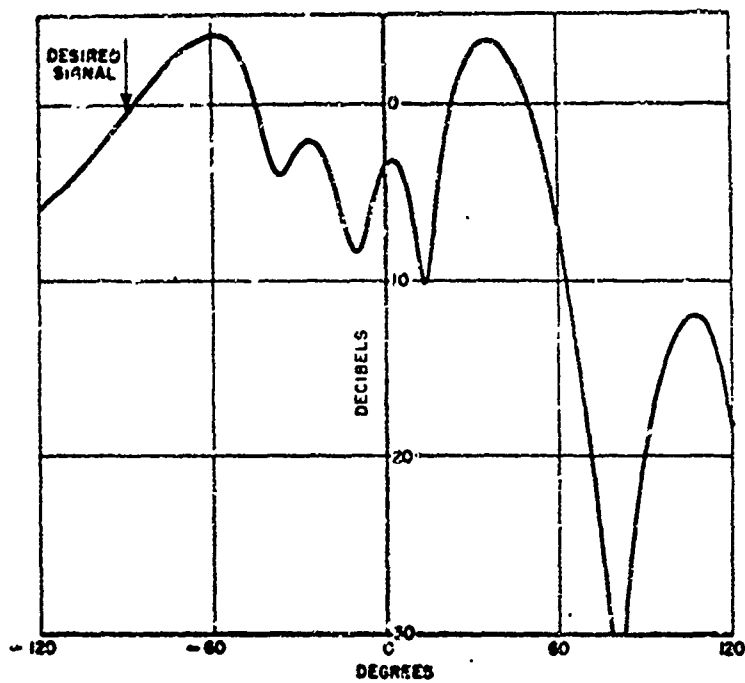


Fig. 8. 307 MHz pattern.

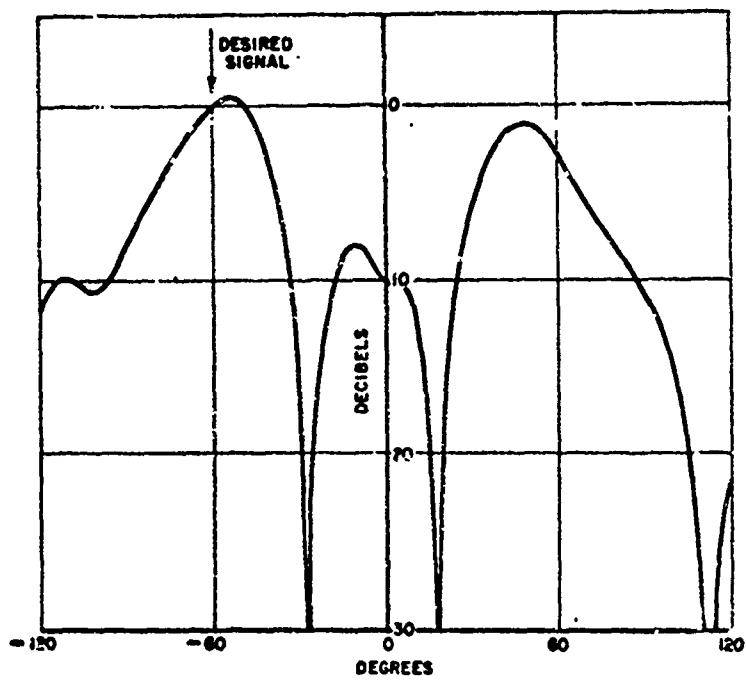


Fig. 9. 307 MHz pattern.

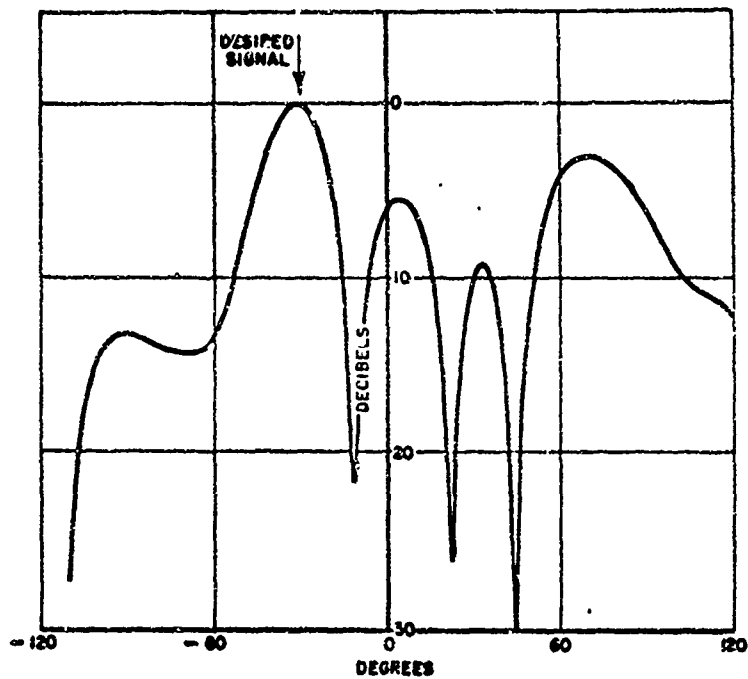


Fig. 10. 307 MHz pattern.

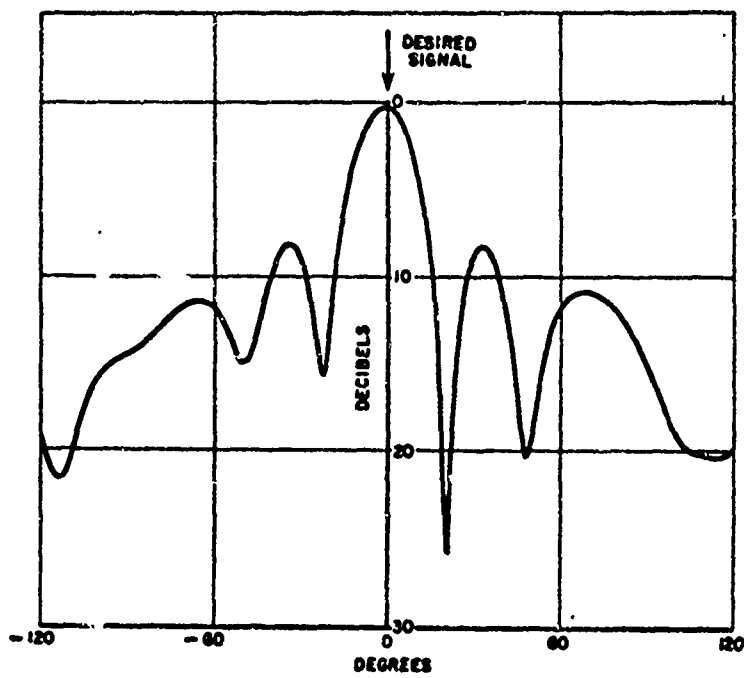


Fig. 11. 307 MHz pattern.

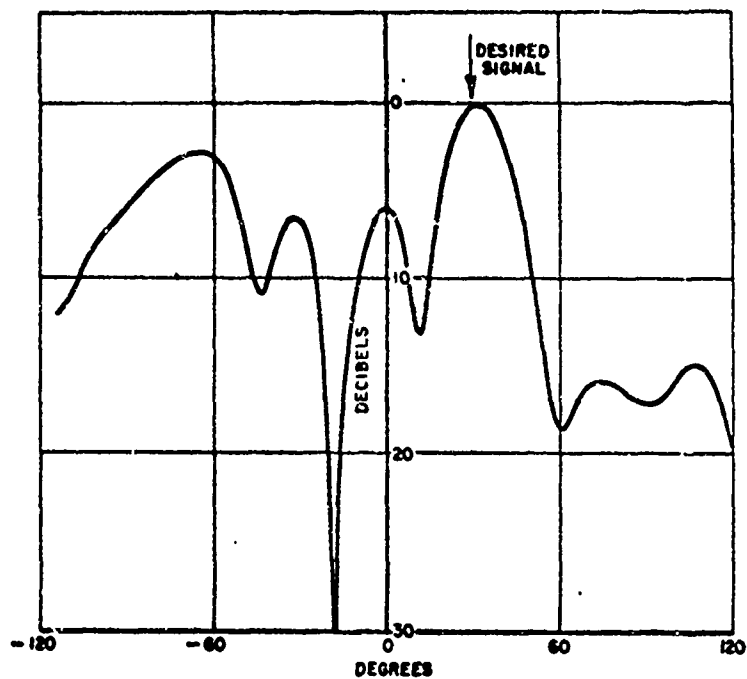


Fig. 12. 307 MHz pattern.

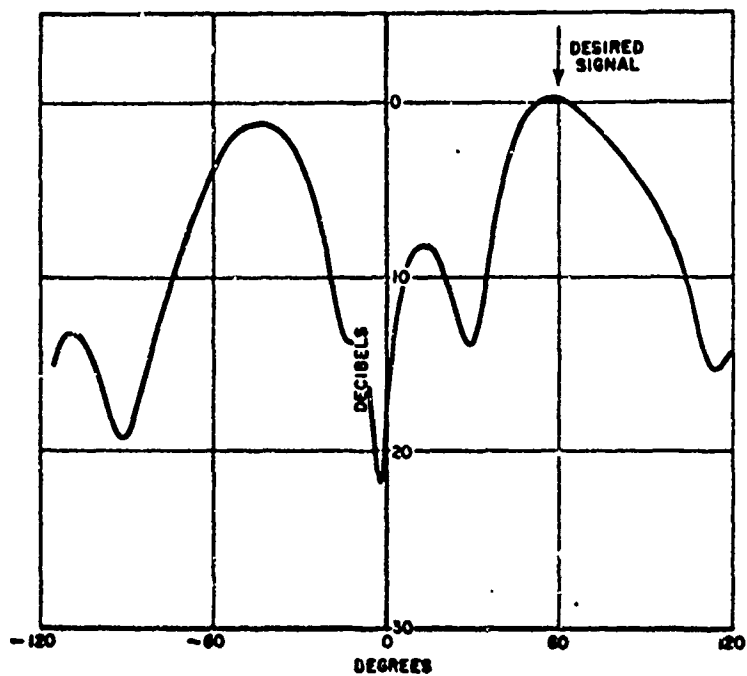


Fig. 13. 307 MHz pattern.

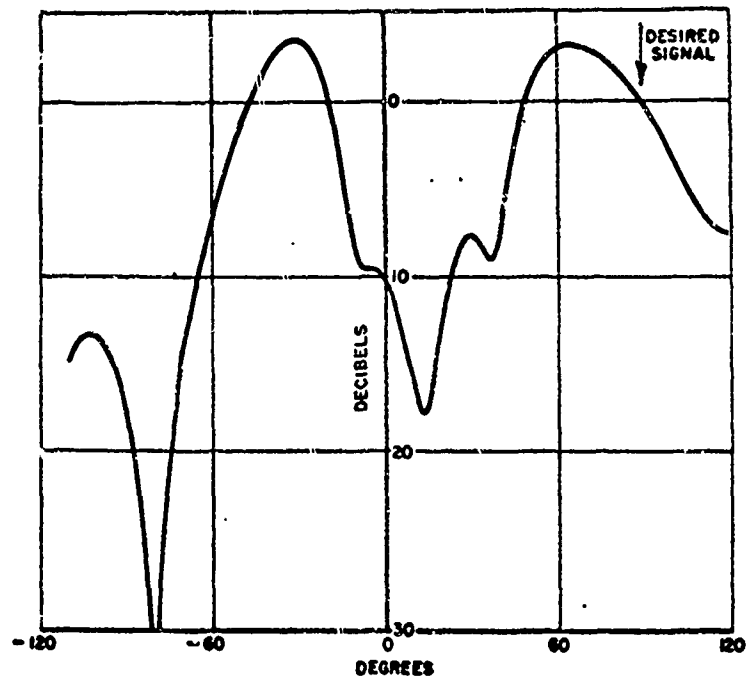


Fig. 14. 307 MHz pattern.

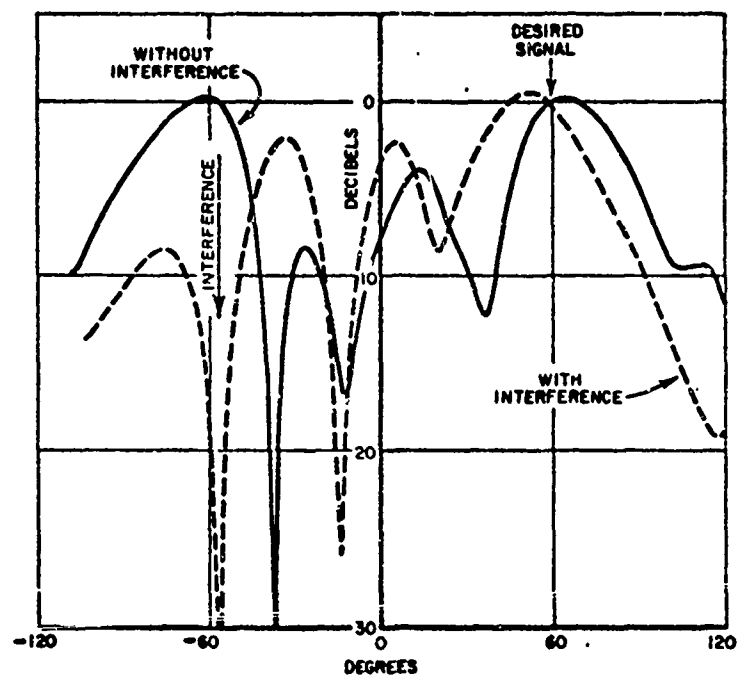


Fig. 15. Patterns with and without interference.

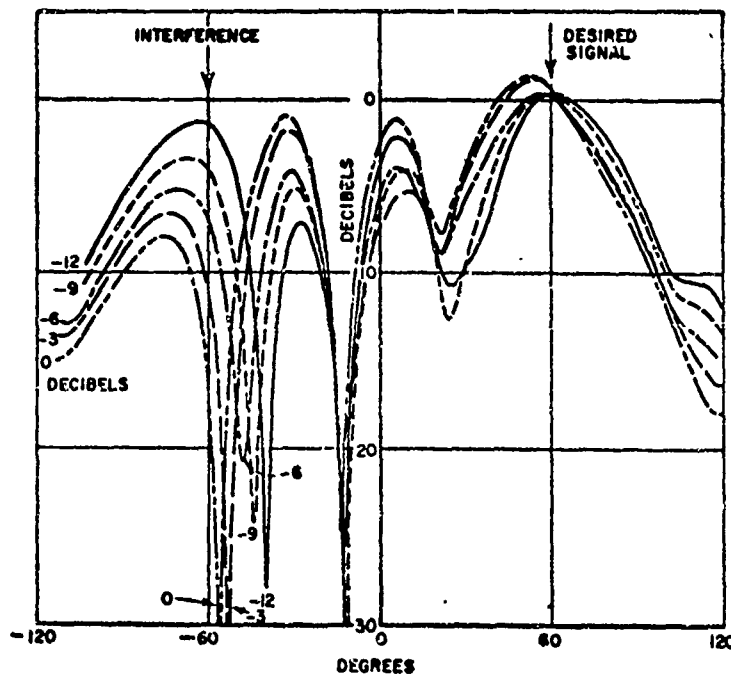


Fig. 16. Effect of interference power.

CONCLUSIONS

The tests performed on this array have demonstrated several things. First, it is clear that the array can adapt properly to desired signals from all angles. It can do this for arbitrary element placement, so that neither the curvature of the surface nor the dependence of mutual impedances on element placement affects the ability of the array to adapt properly. This is a result of considerable practical importance to the antenna designer.

The adaptive processing usually points the beam maximum in the direction of the desired signal. The exception to this occurs when the desired signal falls on the side of a null in the pattern of one of the elements. In that case, the beam maximum may be slightly off.

However, the processors are still combining the element signals in an optimum way for that situation. The largest beam pointing errors in our experiments occurred near endfire, where the sensitivity of all the elements dropped simultaneously. However, this situation would probably not arise in an operational system, because one would place at least some elements to look in every direction.

Secondly, the array is capable of nulling interference signals from arbitrary angles, except for the fundamental limitation that the ability to reject interference falls off when the interference comes too close to the desired signal. The wider the electrical separation between elements, the closer the interference can approach the desired signal in space and still be rejected.

Thirdly, the interference rejection obtained from the adaptive system is a function of the power in the interference. The stronger the interference, the greater is the interference rejection. This feature is both desirable and undesirable. It is desirable because a stronger interfering signal automatically results in more rejection by the array. (In fact, in at least some cases, the array overcompensates - a stronger interference signal results in a weaker interference component at the array output.) However, this feature is undesirable because an amplitude modulated interference signal (e.g., pulse jamming) may cause the weights to fluctuate and thus modulate the desired signal.

REFERENCES

1. Widrow, B., Mantey, P.E., Griffiths, L.J., and Goode, B.B., "Adaptive Antenna Systems," Proc. IEEE, 55, 12 (December 1967), pp. 2143-2159.
2. Shor, S.W.W., "Adaptive Technique to Discriminate Against Coherent Noise in a Narrow-band System," J. Acoust. Soc. Am., 39 (January 1966), pp. 74-78.
3. Applebaum, S.P., "Adaptive Arrays," Special Projects Laboratory Report SPL-TR66-1, August 1966, Syracuse University Research Corporation, Syracuse, N.Y.
4. Riegler, R.L. and Compton, R.T., Jr., "An Adaptive Array for Interference Rejection," Report 2552-4, 16 February 1970, ElectroScience Laboratory, Department of Electrical Engineering, The Ohio State University; prepared under Grant NGR-704-013 for National Aeronautics & Space Administration.
5. Compton, R.T., Jr., "Adaptive Antenna Arrays for Aircraft Communications Systems," Report 3098-1, July 1971, ElectroScience Laboratory, Department of Electrical Engineering, The Ohio State University; prepared under Contract N00014-67-A-0232-0009 for Office of Naval Research, Arlington, Virginia.
6. Compton, R.T., Jr., "Adaptive Antenna Arrays for Aircraft Communication Systems," Report 3098-2, January 1972, ElectroScience Laboratory, Department of Electrical Engineering, The Ohio State University; prepared under Contract N00014-67-A-0232-0009 for Office of Naval Research, Arlington, Va.
7. Reinhard, K.L., "Adaptive Array Techniques for TDMA Network Protection," Section II of R.J. Huff, "Coherent Multiplexing and Array Techniques," Report 2738-3, 9 February 1971, ElectroScience Laboratory, Department of Electrical Engineering, The Ohio State University; prepared under Contract F30602-69-C-0112 for Rome Air Development Center, Griffiss Air Force Base, New York.

8. Compton, R.T., Jr., "Adaptive Arrays - On Power Equalization with Proportional Control," Report 3234-1, December 1971, ElectroScience Laboratory, Department of Electrical Engineering, The Ohio State University; prepared under Contract N00019-71-C-0219 for Naval Air Systems Command.
9. Eveleigh, V.W., Adaptive Control and Optimization Techniques, McGraw-Hill Book Co., New York, 1967, Chapters 5 and 8.
10. Shreve, D.H., "Numerical and Experimental Investigation of Impedance and Matching Techniques Associated with Multiturn Loop Antennas," M.Sc. Thesis, The Ohio State University, July 1970.

26. ADAPTIVE ANTENNA COMPATIBILITY WITH RADAR SIGNAL PROCESSING

by

A. L. McGuffin

General Electric Company, Aircraft Equipment Division, Utica, N. Y.

for

Array Antenna Conference

Naval Electronics Laboratory Center, San Diego, Calif.

22, 23, 24 February 1972

26-1a

26. ADAPTIVE ANTENNA COMPATIBILITY WITH RADAR SIGNAL PROCESSING

A. L. McGuffin

General Electric Company, Aircraft Equipment Division, Utica, N.Y.

INTRODUCTION

One of the advantages of adaptive array antenna processing is improved AMTI motion compensation. The improvement arises from the flexibility in displacing the receive aperture phase center by weighting each element of the array antenna. The use of adaptive processing to exploit this flexibility has been recognized and analyzed.¹ This type of adaptive array processor requires at least two cross correlator control loops and one AMTI delay line for each antenna element. The control loops and the technique of interconnecting loops to achieve adaptive array processing are based on earlier work concerning non-AMTI adaptive array processing.^{2,3} Apparently this technique of interconnecting control loops is an outgrowth of a sidelobe canceller invention.⁴

This paper is concerned with a question of signal processor compatibility which arises when a limit is placed on the number of delay lines and control loops per antenna element. The motivation for imposing a constraint on array circuits arises from practical considerations, including reduction in size, weight, complexity, and cost.

Operating conditions leading to incompatible operation of an adaptive AMTI array processor and a conventional AMTI are described. Also, the type of degradation in overall AMTI performance is discussed. The manifestations of the performance degradation are a loss of signal power, a distorted receive antenna pattern, and a higher adaptive array clutter attenuation ratio that can be accounted for from AMTI considerations.

After a brief discussion of the adaptive processor equations, requirements for avoiding the compatibility problem are outlined. A simple suboptimal alternative in which the adaptive processor performance criterion is based on a number of assumed targets in the main beam is discussed. The objective of this processor modification is to maintain high antenna gain by specifying a mainlobe angular pass band as a region from which the desired signal is expected. This is a variation of a non-AMTI adaptive array technique which has been called mainlobe maintenance.

Performance analysis results are presented to compare this angular interval configuration with the single target performance criterion adaptive processor. Although radar performance is improved, the degree of improvement depends on antenna look angle with respect to ground track.

THE SIGNAL PROCESSOR COMPATIBILITY PROBLEM

In adaptive array antenna processing, a set of complex, multiplicative weights, denoted by w_1, w_2, \dots, w_m in Figure 1, are employed to adjust the amplitude and phase of

1. Brennan, L. E., et al., Space-Time Processing in Airborne Radars, Report No. TSC-PD-061-2, Technology Service Corp. to NASC, 24 February 1971.
2. Applebaum, S. P., Adaptive Arrays, Report No. SPL-709 under contract AF30(603)-3523, Special Projects Laboratory, Syracuse University Research Corp., 1964.
3. Gostin, J. J., Matched Weighting - A Self Optimizing Aperture Illumination Function, Technical Information Series Report R67EMH38, General Electric Company, 1967.
4. Applebaum, S. P., U.S. Patent (classified).

signals received at each antenna element. The delay lines shown in Figure 1 make it possible to control the frequency response as well as the angular response of the antenna processor by manipulating the weights. To perform AMTI filtering, including motion compensation functions comparable to TACCAR and DPCA, each delay line in Figure 1 is chosen to have a one PRI delay. Adaptive AMTI array antenna processing is achieved when an appropriate adaptive filter controls the complex weights.

By controlling the first k weights, w_1, w_2, \dots, w_k in Figure 1, the receive aperture illumination for undelayed signals can be adjusted to displace the antenna phase center as well as control sidelobe characteristics. When each set of weights for delayed signals, $(w_{k+1}, w_{k+2}, \dots, w_{2k}), (w_{2k+1}, w_{2k+2}, \dots, w_{3k}),$ etc. is also appropriately adjusted, AMTI with motion compensation is realized. Within limits, sidelobe interference can be reduced simultaneously by presenting very low sidelobe gain at the direction of arrival of interference.

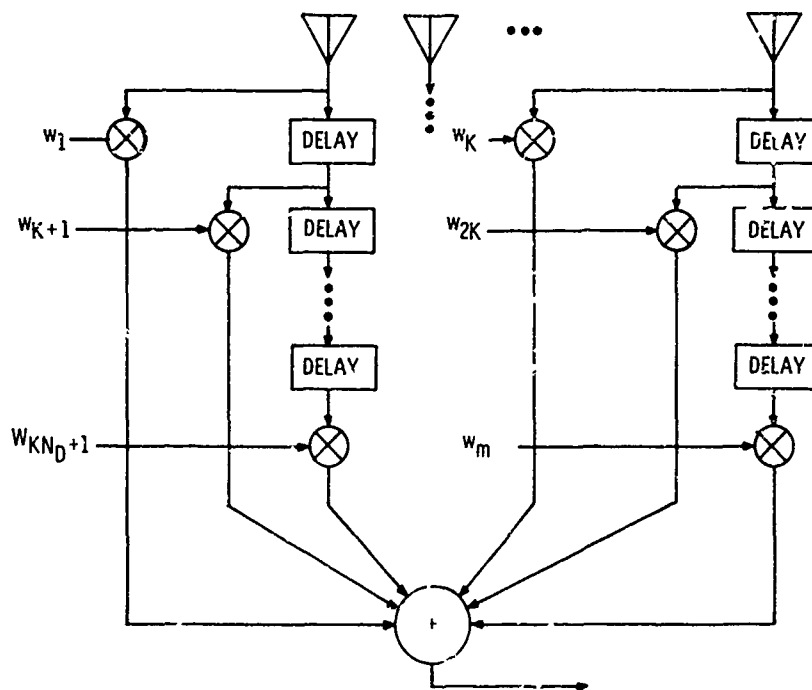


Figure 1. Adaptive Antenna Weighting

The number of delay lines, etc. needed for each antenna element is determined by factors such as clutter internal motion, the stability of local oscillators, and other random signal distortion due to the use of imperfect circuits. As these factors cause a greater reduction in the clutter correlation from PRI to PRI, an AMTI must process more pulses to provide effective clutter attenuation. It is assumed that two to four delay lines per antenna element are required for satisfactory AMTI.

An attractive means of reducing complexity and implementing a smaller, lighter signal processor is to simplify the adaptive AMTI array processor and employ a conventional AMTI downstream from the antenna processor as illustrated in Figure 2. For example, a four-pulse adaptive AMTI array processor (3 delays per element) might be replaced by a two-pulse adaptive AMTI array followed by a three-pulse conventional AMTI.

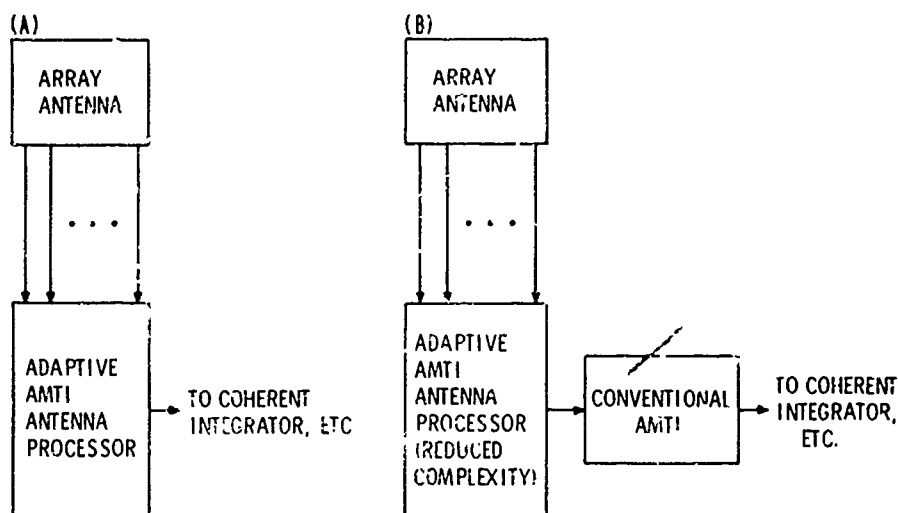


Figure 2. Use of Simplified Adaptive AMTI Processor

Here the term conventional AMTI is only to indicate an AMTI circuit not included in the adaptive antenna processor. The downstream AMTI in Figure 2(b) may have control loops similar to those of the adaptive AMTI array processor.

Clearly, the choice of practical constraints on the adaptive antenna processor complexity should be such that AMTI performance remains satisfactory. Moreover, the criterion of satisfactory performance is the combined performance of the adaptive antenna processor and the conventional AMTI. This overall performance is heavily dependent on the signals at the interface between the two processors.

As a result of reducing the quantity of adaptive array processor AMTI circuits, the purely AMTI cancellation of mainlobe clutter may be diminished, leaving a residue of clutter at its output terminals. For example, two-pulse AMTI clutter attenuation is no better than $1 - \rho$, where ρ is the PRI-to-PRI clutter correlation coefficient. If $\rho = 0.999$, then an input clutter-to-noise ratio of 60 db produces an uncanceled residue clutter-to-noise ratio of 30 db at the AMTI output terminals. When mainlobe clutter of this magnitude appears in the feedback to the adaptive array processor, radar antenna pattern distortion and radar performance degradation are likely to occur.

A loss of antenna gain associated with the pattern distortion causes the degradation of radar performance. It should be emphasized that the adaptive array processor performance as indicated by its input and output $S/(C + N)$ (signal-to-interference) ratios is not degraded. However, at the output terminals of the AMTI following the adaptive array (Figure 2) there is generally a reduction in $S/(C + N)$. This loss is due to the reduced signal power associated with the loss of antenna gain. Under the conditions just described, a "conventional" adaptive AMTI array processor is not fully compatible with downstream AMTI.

The manner in which mainlobe gain is reduced can be visualized by considering the interaction between the adapted receive pattern and the residue of uncanceled mainlobe clutter in the adaptive processor output signals. Since the adaptive processor structure is based on the assumed presence of a single target, the processor always "thinks" there is a target in the center of the main beam. Mainlobe clutter received at any point in the beam other than the antenna look direction can be attenuated relative to a look angle signal by adjusting the aperture illumination for a narrower but lower gain main beam.

Moreover, the consequent reduction of true signal amplitude is not observed by the adaptive processor. Therefore, as "viewed" by the adaptive processor, uncanceled main-lobe clutter due to limited array AMTI performance capability can be legitimately suppressed by means of a narrower, lower gain main lobe. Apparently, this process continues until sidelobe clutter or degraded array AMTI performance offsets the apparent improvement.

High side lobes accompany the changes in the main lobe. The degree to which these higher side lobes affect adaptive array AMTI performance depends on two main factors: (1) the locations of the receive phase centers for delayed and undelayed clutter, and (2) the similarity of the receive patterns for delayed and undelayed clutter. If the phase centers are properly spaced along the ground track and if the two receive patterns maintain high PRI-to-PRI clutter correlation, then good adaptive array AMTI performance is possible in spite of high side lobes.

The compatibility problem just described can be attributed to the built-in performance criterion of the adaptive processor. The feedback which controls the adaptive processor does not account for the existence of additional signal processing. Since the adaptive processor senses only interference, it is not responsive to a true target signal. Moreover, the input vector representing the assumed signal direction ordinarily specifies a single discrete target angle such as the center of the main lobe.

ADAPTIVE PROCESSOR MODEL FOR PERFORMANCE CALCULATIONS

The control loops of the adaptive processor are based on those found in maximum signal-to-noise ratio adaptive arrays. However, the processor structure is such that the adapted weights approach minimum mean square error weights.⁵ The optimal minimum mean square weights, $\underline{w}^T = [w_1, w_2, \dots, w_m]$, are

$$\underline{w} = \underline{R}^{-1} \underline{\Phi}_{rd}^* \quad (1)$$

where \underline{R} is the m by m matrix having elements

$$R_{ij} = E \{ r_i r_j^* \}$$

which are cross correlations of observed signals, r_i, r_j , from different antenna elements or received during different PRI (or both). The column vector $\underline{\Phi}_{rd}^*$ has elements which are the cross correlations, $E \{ r_j d^* \}$, between observed signals, r_j , and the desired signal, d . Each r_j is a sum of the signal, interference, and noise, or $r_j = s_j + z_j + n_j$, where z_j and n_j are interference and receiver noise respectively.

Equation (1) can be written in a form resembling the adaptive processor weight equations by defining the desired signal in terms of a signal vector $\underline{s}^T = [s_1, s_2, \dots, s_m]$ and a beam forming m -vector $\underline{b}^T = [b_1, b_2, \dots, b_K, 0, 0, \dots, 0]$. The integer K is the number of antenna elements, $m = K(N_D + 1)$, and N_D is the number of PRI delay lines per antenna element. Let

$$d = \underline{b}' \underline{s}$$

where $\underline{b}' = \underline{b}^{*T}$ = conjugate transpose of \underline{b} . Then $\underline{\Phi}_{rd}^*$ can be written

$$\underline{\Phi}_{rd}^* = E \{ \underline{r} \underline{s}' \underline{b} \}$$

5. Widrow, B., Mantey, P.E., Griffiths, L.J., and Goods, B.B., "Adaptive Antenna Systems," Proc. IEEE, Vol. 55, No. 12, Dec. 1967

or

$$\underline{\phi}_{rd} = \underline{R}_s \underline{b} \quad (2)$$

where $\underline{R}_s = E\{\underline{s}\underline{s}'\}$ because the signal, interference, and noise vectors, \underline{s} , \underline{z} , and \underline{u} respectively, are assumed to be independent. The presence of clutter or interference in \underline{R} can be indicated explicitly by the use of

$$\underline{R} = \underline{M} + \underline{R}_s \quad (3)$$

where $\underline{M} = E\{(\underline{z} + \underline{n})(\underline{z}' + \underline{n}')\}$ = interference covariance matrix. The substitution of (3) and (2) into (1) yields

$$\underline{w} = [\underline{M} + \underline{R}_s]^{-1} \underline{R}_s \underline{b} \quad (4)$$

which can be conveniently compared with the processor weight equations.

The adaptive processor weight equations for steady state performance can be written from the control loop diagram in Figure 3 and the processor diagram presented in Figure 4. It is assumed that the filter in each loop approximates the expectation of its input signals except for low duty cycle signals such as echoes from point targets. That is, a filter input of

$$v_{in} = r_i r_j^* = (s_i + z_i + n_i)(s_j^* + z_j^* + n_j^*)$$

results in an output of

$$v_{out} = E\{(z_i + n_i)(z_j^* + n_j^*)\} = K(\tau_{ij}) + N\delta_{ij} = M_{ij}$$

where $K(\tau_{ij})$ is the cross covariance $E\{z_i z_j^*\}$, δ_{ij} is the Kronecker delta, and N is the receiver noise power.

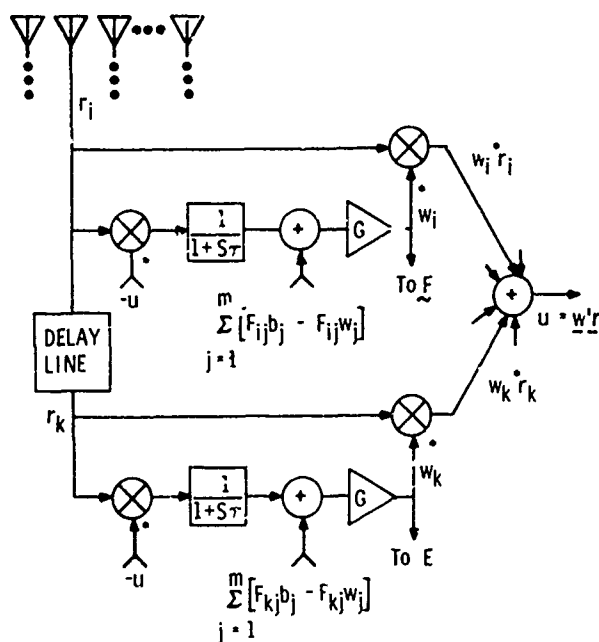


Figure 3. Adaptive Processor Control Loop

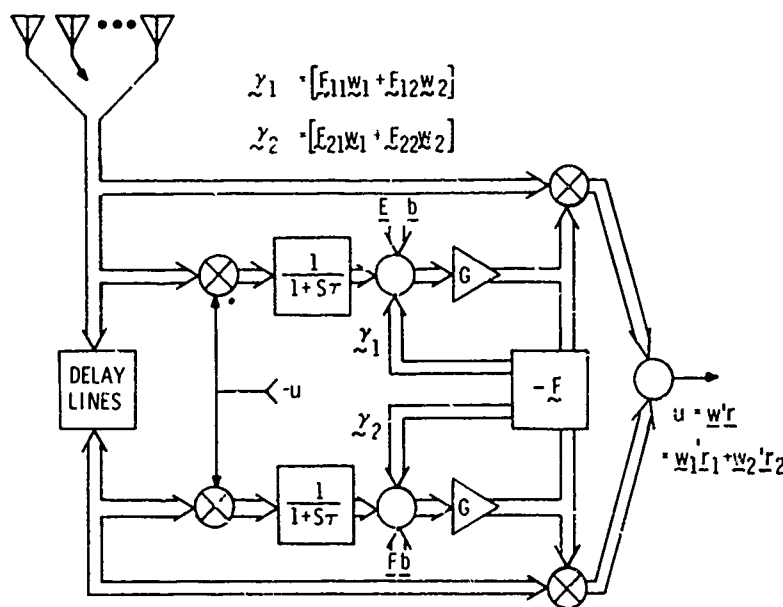


Figure 4. Processor Diagram

From Figure 3 one can write

$$w_i = G \sum_{j=1}^m [F_{ij} b_j - (F_{ij} + M_{ij}) w_j]$$

where $m = (N_D + 1)K$ = the number of elements in \underline{w} . The matrix equation for \underline{w} is

$$\underline{w} = G[\underline{F}\underline{b} - (\underline{F} + \underline{M})\underline{w}]$$

or

$$\underline{w} = \left[\frac{1}{G} \underline{I} + \underline{M} + \underline{F} \right]^{-1} \underline{F}\underline{b} \quad (5)$$

The use of AMTI adaptive array processing can be indicated explicitly by partitioning each m by m matrix into K by K submatrices and each m -vector into K -vectors. For example, the equations for two-pulse AMTI are

$$\begin{bmatrix} \underline{w}_1 \\ \underline{w}_2 \end{bmatrix} = \begin{bmatrix} \frac{1}{G} \underline{I} + \underline{M}_{11} + \underline{F}_{11} & \underline{M}_{12} + \underline{F}_{12} \\ \underline{M}_{21} + \underline{F}_{21} & \frac{1}{G} \underline{I} + \underline{M}_{22} + \underline{F}_{22} \end{bmatrix}^{-1} \begin{bmatrix} \underline{F}_{11} & \underline{F}_{12} \\ \underline{F}_{21} & \underline{F}_{22} \end{bmatrix} \begin{bmatrix} \underline{b} \\ 0 \end{bmatrix} \quad (6)$$

where

$$\underline{w}_1^T = [w_1, w_2, \dots, w_k]$$

$$\underline{w}_2^T = [w_{k+1}, w_{k+2}, \dots, w_{2k}]$$

etc.

The submatrices \underline{M}_{12} and \underline{M}_{21} in (6) have elements which are cross covariances of clutter received during different pulse repetition intervals. Consequently, in matrices \underline{M}_{12} and \underline{M}_{21} the matrix elements include the PRI-to-PRI clutter doppler phase shift as well as the relative phase between antenna element signals due to direction of arrival.

A comparison of (4) and (5) indicates that the matrix \underline{F} represents an estimate of the signal correlation matrix, \underline{R}_s . Any available a priori knowledge of target azimuth can be utilized in selecting the elements of \underline{F} and the beamforming vector, \underline{b} . In the performance calculations that follow, it has been assumed that radar antenna steering is implemented upstream from the adaptive antenna processor, either by means of steering weights or mechanical scanning, as illustrated in Figure 5. Therefore, \underline{b} is a set of constant real weights. Moreover, the matrix \underline{F} can be a set of constant elements dependent on assumed target angle with respect to the look direction.

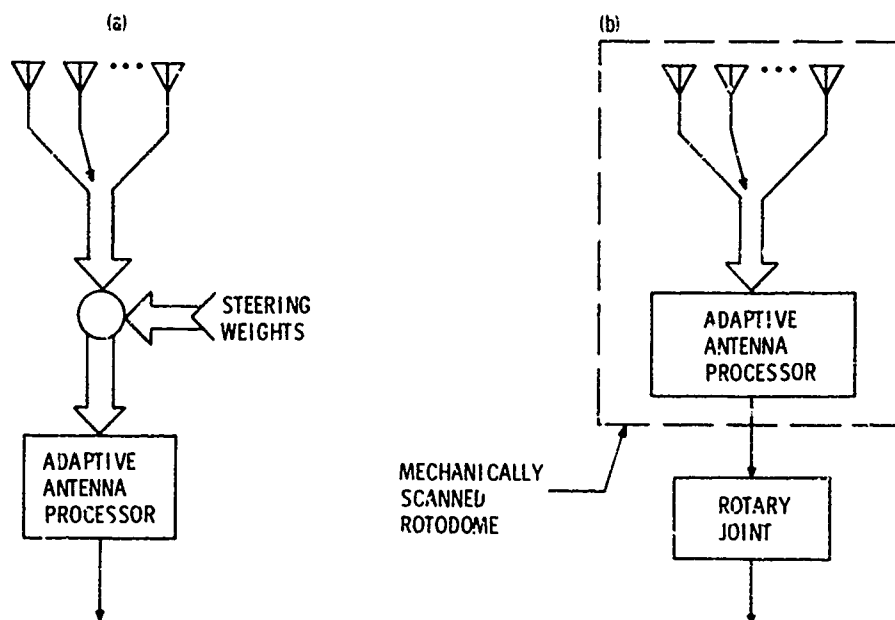


Figure 5. Radar Antenna Steering

When \underline{F} is the matrix of a single target at the look direction, the vector $\underline{V} = \underline{F}\underline{b}$ is equivalent to the signal vector \underline{S} usually appearing in maximum signal-to-noise ratio adaptive array equations. In this case, the performance of the maximum S/N processor is generally equivalent to the performance of the minimum mean square error processor discussed here.

Each element of the covariance matrix \underline{M} is a summation of cross covariance functions due to the independent clutter scatterers. The antenna element patterns and receiver pass bands are assumed to be identical at all elements. Therefore, all element signals are similar except for differences in propagation time arising from element locations and AMTI delay lines. The n -th clutter scatterer echo at the k -th and l -th antenna elements with relative AMTI delay of N_p PRI, for example, contributes the term

$$M_{ij}(n) = P_c G_T G_E E_T^2(\theta_n) E_E^2(\theta_n) \rho[N_p] k[\tau_{ij}(n)] + N \delta_{ij}$$

where $k[\tau_{ij}(n)] = \text{normalized covariance function} = \rho[N_p] [\cos \omega \tau_{ij}(n) - j \sin \omega \tau_{ij}(n)]$

$$\tau_{ij}(n) = \tau_{ko}(\theta_n) - \tau_{lo}(\theta_n) + \frac{2V_n N_p}{c}$$

$\rho[N_p] = \text{PRI-to-PRI clutter correlation as observed in radar receiver}$

θ_n = azimuth of scatterer relative to look angle

G_E = antenna element gain

$c = 3(10^8)$ meters per second

P_c = received clutter power from normalized scatterer with isotropic antenna

σ_n = radar cross section of the n-th scatterer

G_T = transmit antenna gain

$E_T(\theta_n)$ = transmit pattern

$E_E(\theta_n)$ = element pattern

N = receiver noise power

τ_{ko} = delay at element k with respect to signal received at origin

τ_{lo} = delay at element l with respect to signal received at origin

T = PRI

V_n = relative radial velocity of n-th scatterer

After the array antenna weights are computed from (5), the desired performance parameters, $S / (C + N)$ and $(C + N) / N$ at the adaptive array output terminals, are found from the equations

$$\left(\frac{S}{C + N} \right)_{AA} = \frac{\underline{w}' \underline{R} \underline{w}}{\underline{w}' \underline{M} \underline{w}} \quad (7)$$

$$\left(\frac{C + N}{N} \right)_{AA} = \frac{\underline{w}' \underline{M} \underline{w}}{\underline{w}' \underline{w} \underline{N}} \quad (8)$$

The effective input $S / (C + N)$ and $(C + N) / N$ ratios are those of signals received by the unadapted or quiescent receive beam.

$$\left(\frac{S}{C + N} \right)_R = \frac{\underline{b}' \underline{R} \underline{b}}{\underline{b}' \underline{b} \underline{N}} \quad (9)$$

$$\left(\frac{C + N}{N} \right)_R = \frac{\underline{b}' \underline{M} \underline{b}}{\underline{b}' \underline{b} \underline{N}} \quad (10)$$

COMPATIBILITY OF CONSTRAINED SIZE ADAPTIVE PROCESSOR WITH DOWNSTREAM AMTI

The essential characteristics of a constrained size adaptive AMTI array processor which is compatible with additional downstream AMTI can be described by reconsidering the desired signal at the interface between the adaptive processor and the conventional AMTI. As used here, the term "constrained" indicates only that the number of AMTI type circuits per antenna element has been limited due to practical considerations.

A compatible adaptive processor will not attenuate mainlobe clutter on the basis of purely spatial discriminants, at least not to such a degree that the main beam gain is reduced to an unacceptable level. If the desired (interface) signal is defined to include received signals from a main beam angular interval rather than a single point, then a narrower, lower gain mainlobe adaptation tends to attenuate desired signals. Therefore, a mainlobe angular pass band performance criterion tends to preserve mainlobe gains. Although more mainlobe clutter can then appear in the adaptive antenna processor output signals, the use of conventional AMTI in cascade with the antenna processor indicates that a certain fraction of mainlobe clutter is acceptable at that point.

One approach to determining the processor structure for compatible operation is to write new weight equations based on the redefined desired signal. If \underline{c} is a suitable vector of the summation of returns from the mainlobe angular interval and \underline{s}_{Σ} is a summation of signal vectors of targets within the same interval, the new desired signal is

$$\underline{d}_c = \underline{b}'(\underline{s}_{\Sigma} + \underline{c}) \quad (11)$$

The resultant cross correlation vector, $\underline{\phi}_{rd}$, is

$$\underline{\phi}_{rd} = (\underline{R}_{\Sigma} + \underline{K}_c) \underline{b}$$

where $\underline{K}_c = E\{\underline{c}\underline{c}'\}$ and $\underline{R}_{\Sigma} = E\{\underline{s}_{\Sigma}\underline{s}_{\Sigma}'\}$

Since the clutter which determines \underline{K}_c is a subset of the clutter which determines \underline{M} , the new weight equation is

$$\underline{w} = [\underline{M} + \underline{R}_{\Sigma}]^{-1} [\underline{R}_{\Sigma} + \underline{K}_c] \underline{b} \quad (12)$$

A comparison of (12) with (4) and (5) indicates that the modified adaptive processor equation can be written

$$\underline{w} = \left[\frac{1}{G} \underline{I} + \underline{M} + \underline{F}_{\Sigma} \right]^{-1} [\underline{F}_{\Sigma} + \underline{K}_c] \underline{b} \quad (13)$$

However, equation (13) implies that the mainlobe clutter is estimated precisely by the processor. Unfortunately, there are problems associated with determining such an estimate. A discussion of the additional processing needed to estimate \underline{K}_c is beyond the scope of this paper. However, it is apparent that the task of obtaining a precise estimate of \underline{K}_c may offset the simplicity attained by reducing the quantity of AMTI circuits per antenna element. A simple alternative is to modify only the assumed target characteristics.

A mainlobe angular pass band can be approximated without estimating mainlobe clutter if additional changes in \underline{F}_{Σ} , including changes based on the assumption of high desired signal amplitudes and arbitrary target locations, are implemented. When \underline{F}_{Σ} represents a set of sufficiently strong signals uniformly spaced over a mainlobe angular interval, the adaptive processor tends to be inhibited from reducing antenna gain in this interval.

A simple change in \underline{F} converts the adaptive processor from a single-target angle processor to an angular interval processor. If \underline{F} represents a single target, then

$$\underline{F} = E\{\underline{g}\underline{g}'\} \sim \underline{g}\underline{g}'$$

where \underline{g} is a vector whose components have the same element-to-element phase as a signal from the assumed target angle. A cluster of mainlobe targets is represented by requiring that

$$\underline{F}_{\Sigma} = E\{[\underline{g}(\theta_1) + \underline{g}(\theta_2) + \dots \underline{g}(\theta_1)][\underline{g}'(\theta_1) + \dots \underline{g}'(\theta_1)]\}$$

where each θ_i is a target angle and each vector $\underline{g}(\theta_i)$ has element-to-element phases corresponding to that angle. If the different targets are assumed to be statistically independent, then

$$\underline{F}_{\Sigma} = \sum_{i=1}^1 E\{\underline{g}(\theta_i)\underline{g}'(\theta_i)\}$$

The simplest configuration is obtained by selecting an \underline{F}_{Σ} matrix with constant elements.

CALCULATED PERFORMANCE

The main objectives of these performance calculations are to illustrate the radar performance degradation described and to compare the two adaptive array processors, a single target and an angular interval processor, in several examples. As described earlier, the difference between the processors depends on the matrix \underline{F} .

The signal processing units accounted for in the calculated performance examples presented are shown in Figure 6. The radar transmit antenna pattern is the same as the unadapted (quiescent) receive pattern in all performance calculations discussed here. Also, except as noted, the correlation coefficient of clutter from PRI to PRI is $\rho = 0.99965$ for all computations, which limits the performance of a two-pulse AMTI to no better than 34.6 db of clutter attenuation.

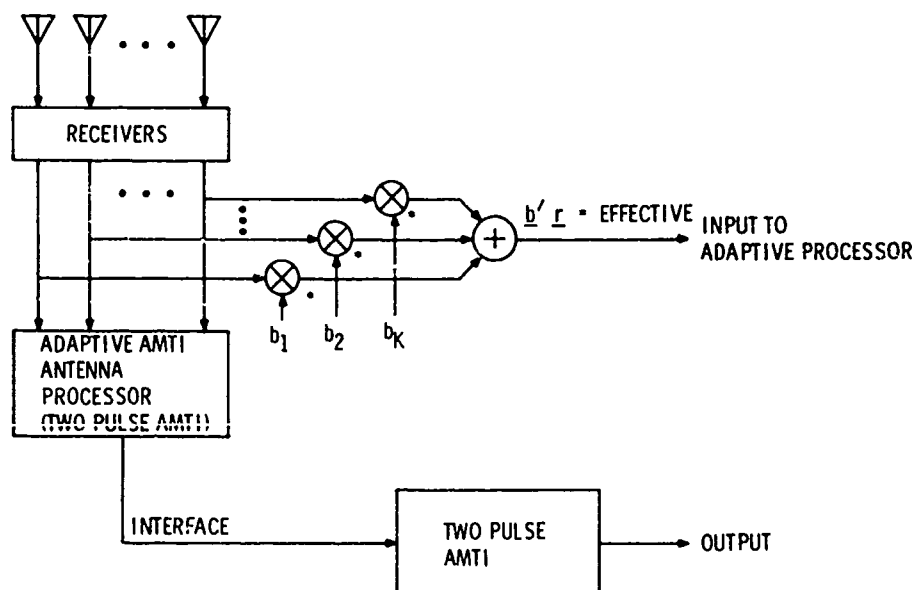


Figure 6. Signal Processing for Performance Calculations

Figure 7 presents the unadapted receive pattern of the 12-element array antenna model for the first example. This antenna, which has 0.85λ element spacing and directional (40-degree beamwidth) element patterns, is comparable to a mechanically scanned AEW rotodome antenna. However, the uniform element weighting assumed here is not typical for such antennas. The angular relationships of the target, antenna look angle, and clutter with respect to aircraft (platform) ground track are summarized in Figure 8. Altitude of the radar platform is not accounted for in these calculations.

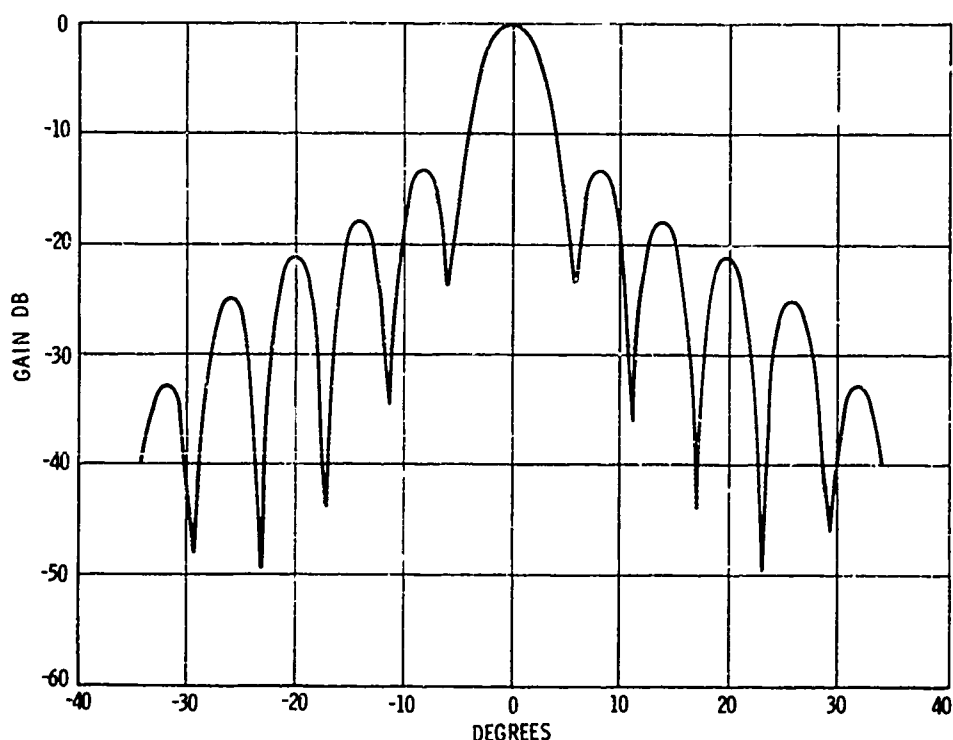
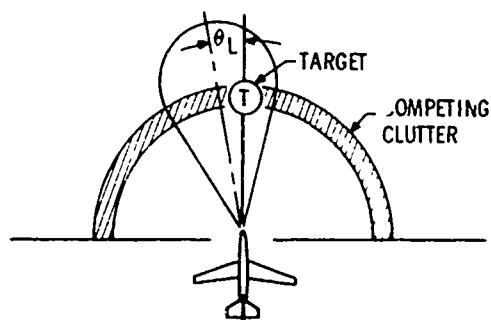


Figure 7. Unadapted Receive Pattern, 0.85λ Element Spacing



GROUND TRACK
ANTENNA LOOK DIRECTION
TARGET ANGLE
ANGULAR CLUTTER INTERVAL
BEAMWIDTH (3 DB)
AIRCRAFT VELOCITY
(FRACTION OF APERTURE TRAVELED
DURING EACH PRI)

0°
 -1°
 0°
 -90° TO 90°
 6°
 6.5%

Figure 8. Angular Relationships, First Example

First, the performance of a two-pulse AMTI adaptive array processor with a single target-angle structure is computed. Figure 9 presents the receive pattern determined by the adapted weights. This receive pattern, which has high side lobes and no distinct main lobe, results in a two-way radar pattern whose highest side lobes are shown on the right-hand side of the receive main lobe in Figure 9.

Table 1 presents the signal and clutter levels at three points: (1) as received with the unadapted beam, (2), at the interface between the adaptive processor and the conventional AMTI and (3) at the AMTI output terminals. The signal and clutter received via the unadapted pattern determine the effective input to the adaptive antenna processor in terms of the ratios $S/(C + N)$ and $(C + N)/N$.

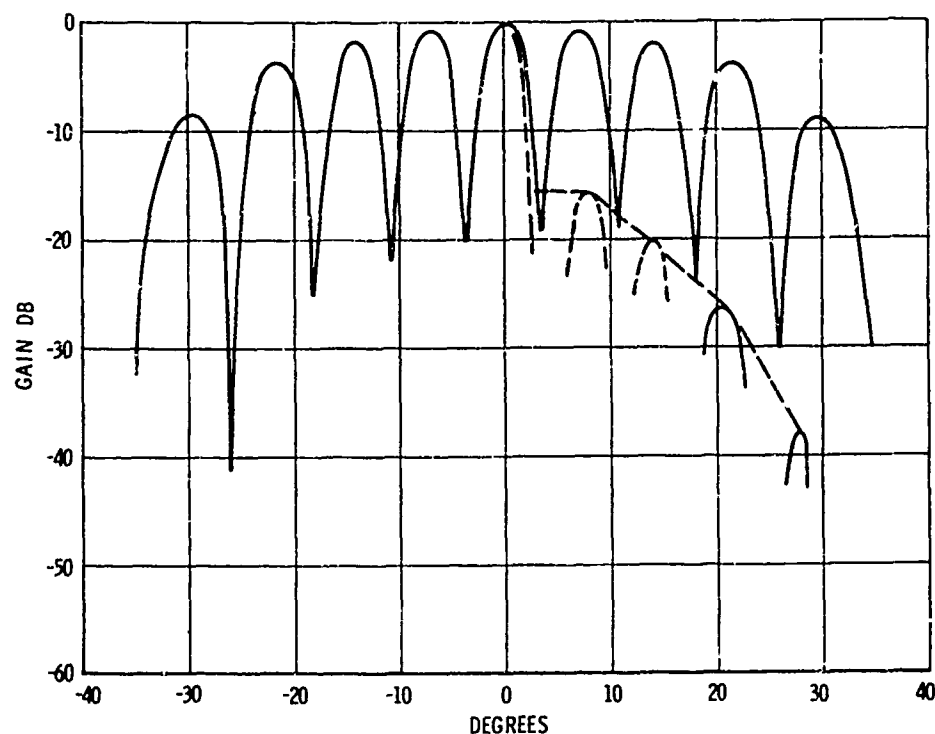


Figure 9. Adapted Receive Pattern, Single Target Angle Processor, 0.85λ Element Spacing

Considering the receive pattern distortion illustrated in Figure 9, one would expect that a loss of mainlobe gain has been caused by the use of an adaptive processor. The magnitude of this loss can be determined from Table 1. The S/N ratio of the single target, which has been assumed to have the most favorable doppler frequency, would increase by 3 db in passing through a lossless two-pulse AMTI rather than the adaptive processor. However, the S/N at the adaptive processor output, or the interface between the adaptive antenna processor and the conventional downstream AMTI, is only 16.3 db. This S/N can be compared with the 23.3 db attainable with a lossless processor to show the adaptive array loss of gain is about 7 db.

It is interesting to observe that in Table 1 the adaptive array clutter attenuation, i.e., the ratio of $(C + N)/N$ as received to $(C + N)/N$ at the interface in Table 1, is 42 db. This is significantly higher than the 34.6 clutter attenuation attainable with a conventional AMTI in place of the adaptive array processor. Apparently, the distorted pattern has provided the additional clutter attenuation. The remaining data in Table 1, particularly the output of the downstream AMTI, is discussed later by comparing these results with the computed performance of a "target interval" adaptive array processor.

When the F matrix is changed to represent five assumed target angles, these angles being spaced at one-degree intervals from -2 degrees to +2 degrees with respect to the antenna look angle, the adapted receive pattern becomes as shown in Figure 10. Again, the highest side lobes of the two-way radar pattern are shown on the right-hand side of the main lobe (Figure 10). The results of preserving a distinct receive main lobe can be seen from Table 2.

First, it is apparent that if only the adaptive array were employed, so that the interface signals would be the final output signals, then performance in terms of signal-to-

TABLE 1

	<u>Received</u>	<u>Interface</u>	<u>Output</u>
$\frac{C+N}{N}$	60.3 db	18.3 db	0.6 db
$\frac{S}{C+N}$	-39.9 db	-2.3 db	17.0 db
S/N	20.3 db	16.3 db	17.5 db

Maximum S/N possible at interface = 23.3 db

S/N loss at interface = 7 db (= adaptive array loss)

TABLE 2

	<u>Received</u>	<u>Interface</u>	<u>Output</u>
$\frac{C+N}{N}$	60.3 db	24.7 db	0.9 db
$\frac{S}{C+N}$	-39.9 db	-2.4 db	22.8 db
$\frac{C+N}{N}$ Change*	0 db	+6.4 db	+0.3 db
$\frac{S}{C+N}$ Improvement*	0 db	-0.1 db	5.8 db
S/N Improvement*	0 db	6.1 db	6.2 db

S/N loss at interface = 0.9 db

* With respect to Table 1

interference ratio is no better than before. This is indicated by the practically equal interface $S/(C+N)$ ratios in Tables 1 and 2. At the output terminals of the conventional AMTI, on the other hand, the $S/(C+N)$ is increased from 17 db in Table 1 to 22.8 db in Table 2, an improvement of 5.8 db. This is comparable to the increase in S/N and $(C+N)/N$ at the interface between the adaptive array and the downstream AMTI. As before, the adaptive array S/N loss, which is 0.9 db, is determined by comparing the computed interface S/N with the ideal S/N at that point. The higher adapted mainlobe gain in Table 2 is accompanied by additional mainlobe clutter in the adaptive array output, but the signal can be extracted from the clutter.

A slightly different 12-element array antenna whose unadapted pattern is presented in Figure 11 was employed in the remaining performance calculations. Here the element spacing is 0.5λ , and the element pattern is $\cos \theta$, where θ is the signal direction of arrival relative to the look direction. The beamwidth is about 9 degrees, which is wider than the beam of most practical radar antennas.

Figure 12 presents the adapted receive pattern for a single-target angle adaptive array processor and the array antenna just described. The angular relationships between ground track, look direction, and target are shown in Figure 13. From Figure 12 and Table 3, one can see that the reduction in mainlobe gain is about 7 db.

Changing to a five-target angle F matrix with assumed target locations spaced uniformly from -2 degrees to +2 degrees with respect to antenna look direction restores a

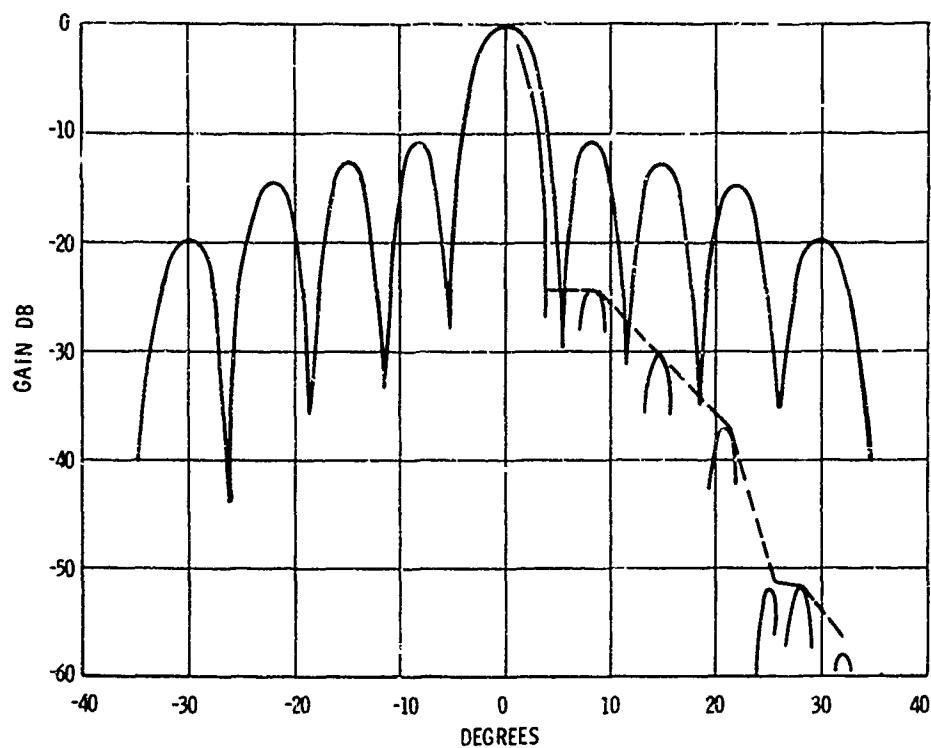


Figure 10. Adapted Receive Pattern with Angular Interval Processor, 0.85λ Element Spacing

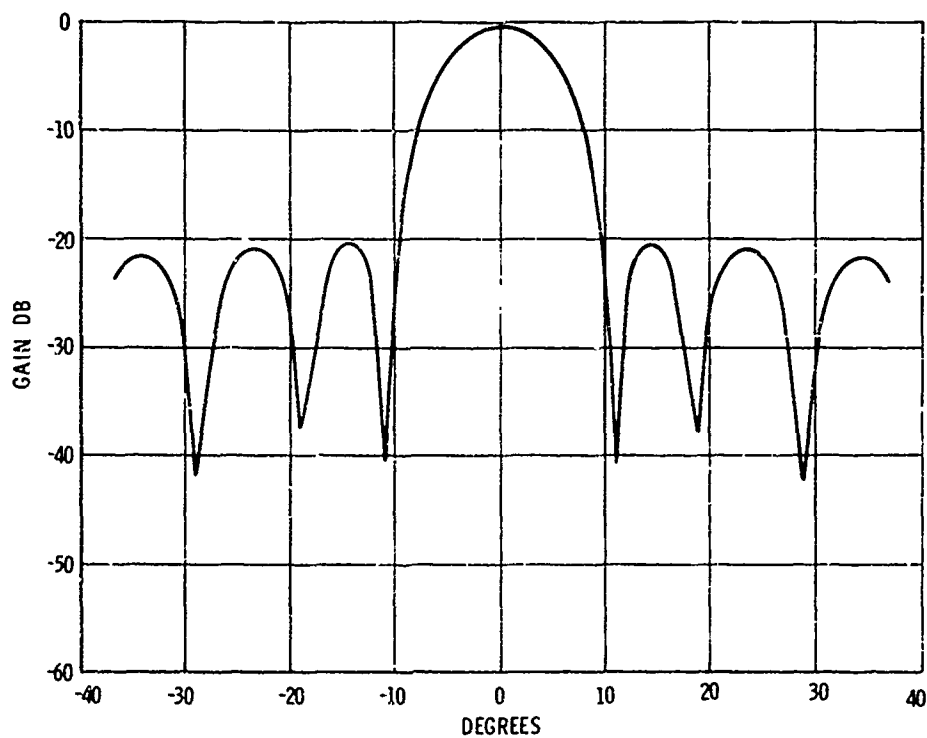


Figure 11. Unadapted Receive Pattern, 0.5λ Element Spacing

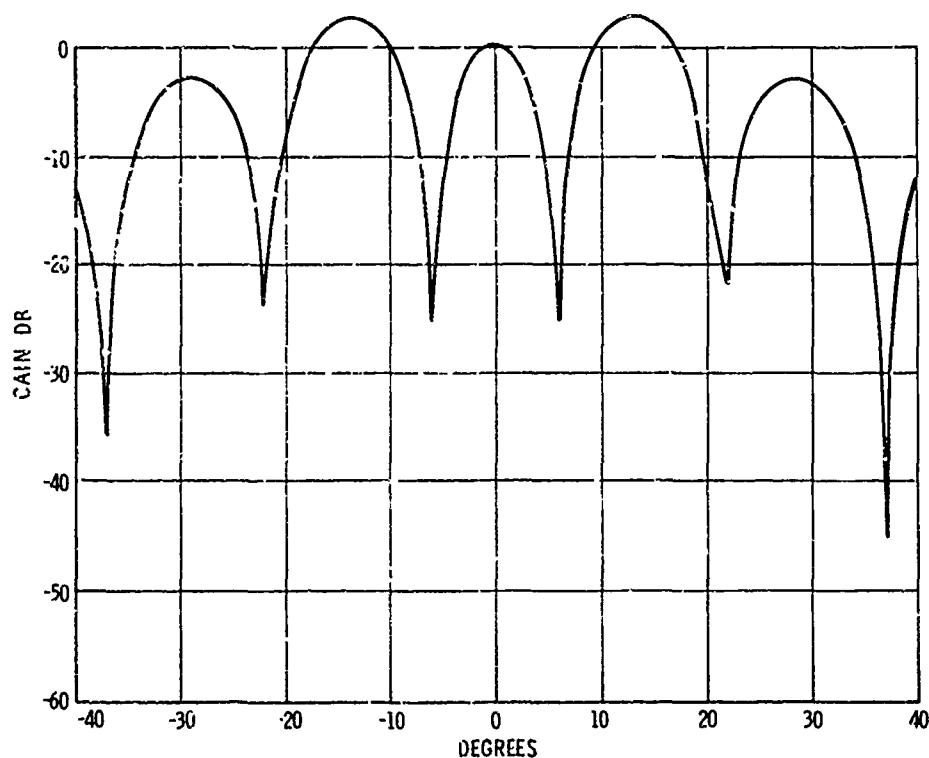


Figure 12. Adapted Receive Pattern, Single Target Angle Processor, 0.5λ Element Spacing

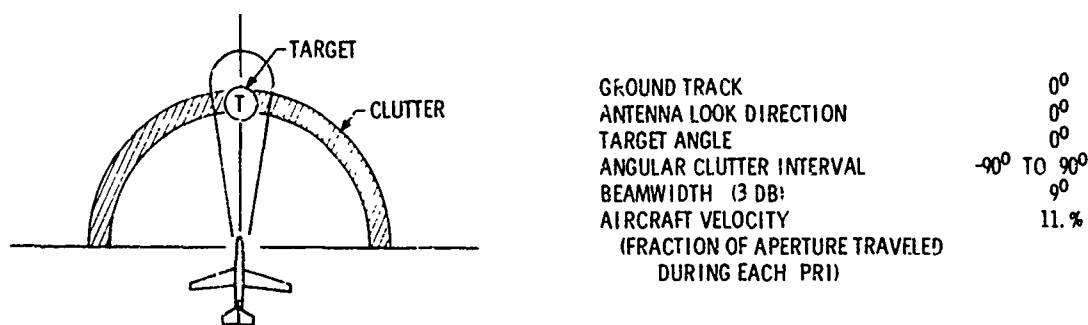


Figure 13. Angular Relationships, Second Example

modest main lobe as illustrated by Figure 14. Table 4 provides a comparison with the computed performance for the single target model. Although the receive pattern side lobes (Figure 14) are rather high, the performance data is comparable to that of the six-degree beam array of the first example (Table 2).

If the F matrix is modified by "adding" assumed target angles at -3 degrees and $+3$ degrees from the look direction, the adapted pattern has a slightly better main lobe as can be seen in Figure 15. As shown by Table 5, this change does not provide an additional improvement in output $S/(C+N)$. It can be seen that a small (and perhaps insignificant) reduction in the output $S/(C+N)$ has occurred.

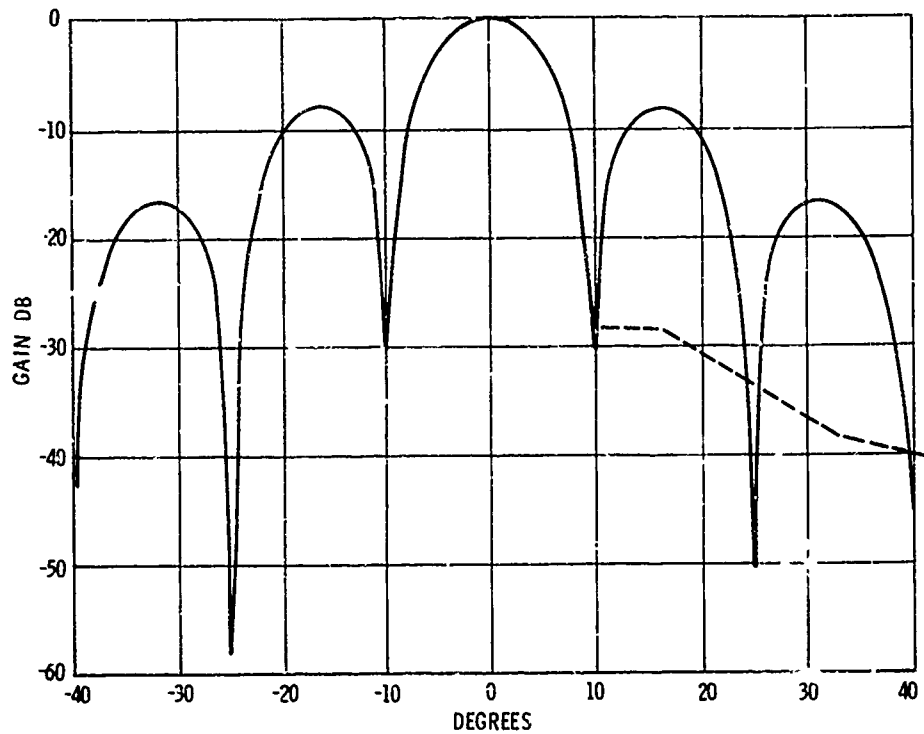


Figure 14. Adapted Receive Pattern, with Angular Interval Processor, 0.5λ Element Spacing

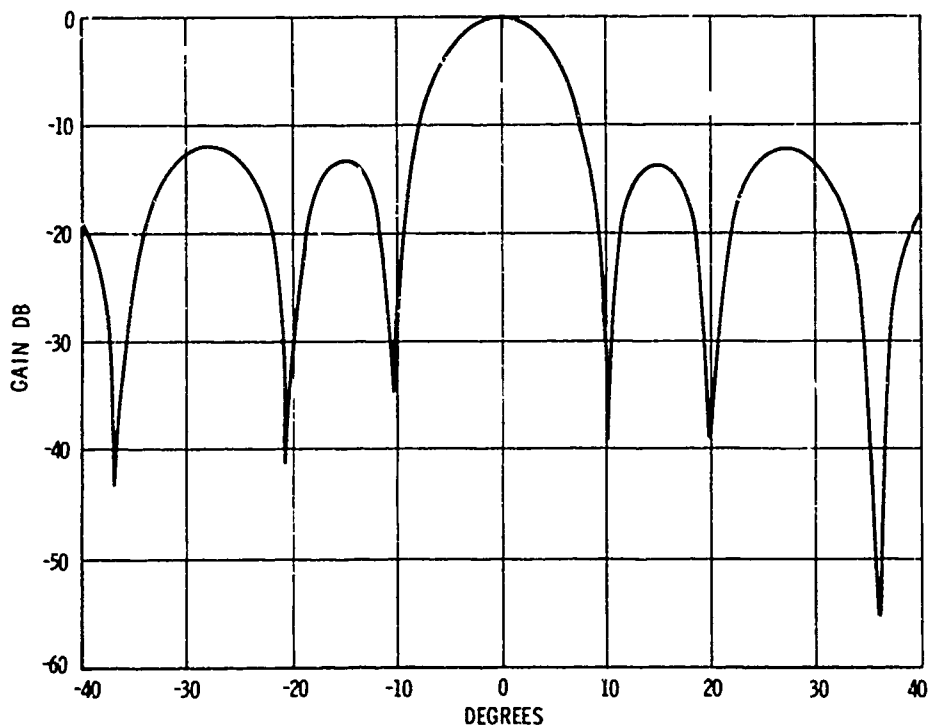


Figure 15. Adapted Receive Pattern with 6-degree Angular Interval

TABLE 3

	<u>Received</u>	<u>Interface</u>	<u>Output</u>
$\frac{C+N}{N}$	59.6 db	16.8 db	1.7 db
$\frac{S}{C+N}$	-39 db	-0.5 db	16.5 db

S/N loss at interface = 7.3 db

TABLE 4

	<u>Received</u>	<u>Interface</u>	<u>Output</u>
$\frac{C+N}{N}$	59.6 db	24 db	1 db
$\frac{S}{C+N}$	-39 db	-1.3 db	23 db
Change in $\frac{C+N}{N}$ *	0 db	7.2 db	-0.7 db
$\frac{S}{C+N}$ Improvement*	0 db	-0.8 db	6.5 db

S/N loss at interface = 0.9 db

* Relative to Table 3

TABLE 5

	<u>Received</u>	<u>Interface</u>	<u>Output</u>
$\frac{C+N}{N}$	59.6 db	24 db	1.7 db
$\frac{S}{C+N}$	-39 db	-1.4 db	22.6 db
$\frac{C+N}{N}$ Change*	0 db	7.2 db	0 db
$\frac{S}{C+N}$ Improvement*	0 db	-0.9 db	6.1 db

S/N loss at interface = 0.9 db

* With respect to Table 3, the single target angle model with the same antenna

Finally, performance is calculated with the antenna look direction and the true target both 90 degrees off the ground track as illustrated in Figure 16. The single-target angle adaptive array receive pattern is presented in Figure 17. The related performance data in Table 6 indicates that the AMTI output performance is degraded compared with the performance when looking along the ground track (Tables 1, 3). This degradation, which appears to be the result of clutter spectral spreading, is the combined performance of adaptive array and downstream AMTI, not in the adaptive array itself.

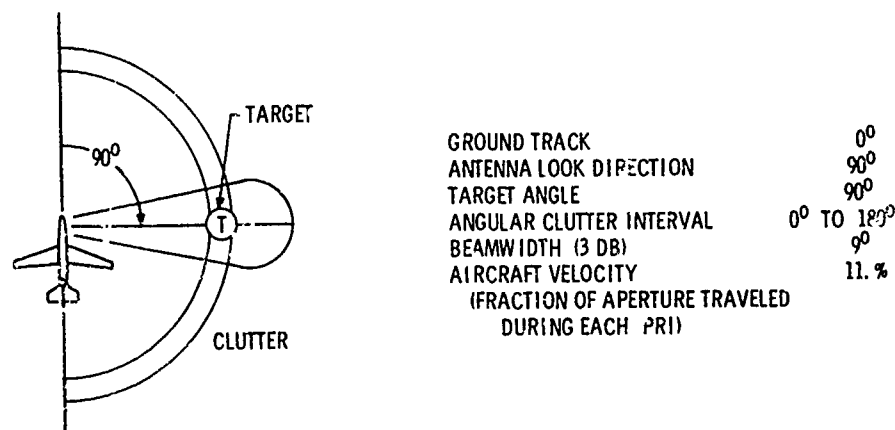


Figure 16. Angular Relationships, Third Example

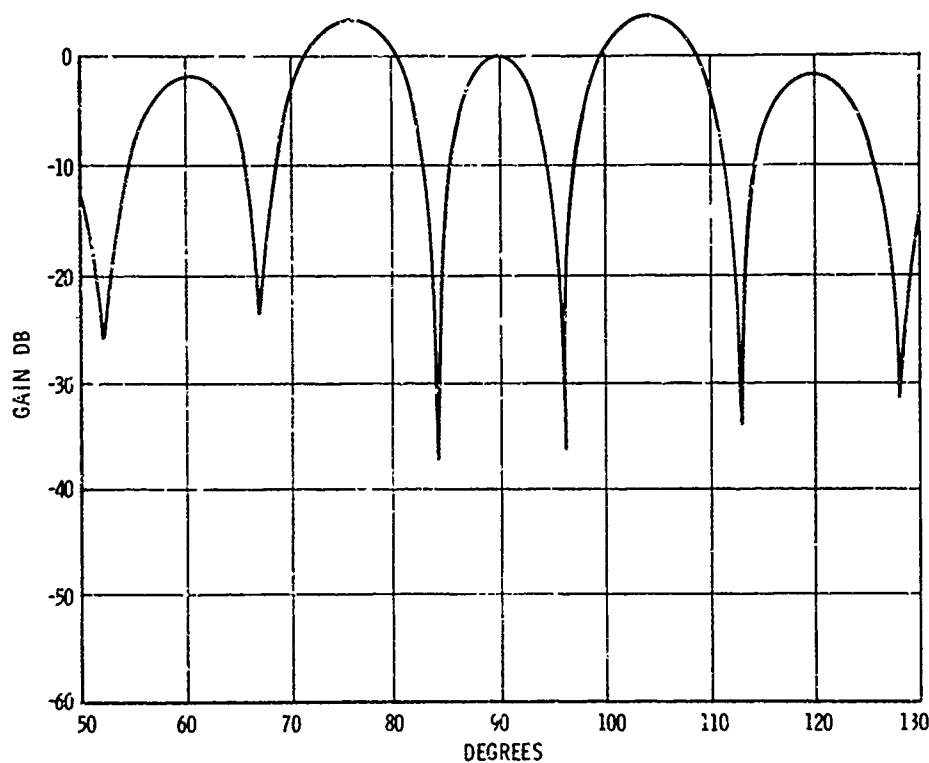


Figure 17. Adapted Receive Pattern, Single Target Angle Processor, 0.5λ Element Spacing

The use of a five-target angular pass band is not as effective here as in the performance calculations where the target was near the ground track. Figure 18 and Table 7 present the adapted pattern and performance data, respectively, for this case. The S/N loss is reduced from 7.9 db to about 1 db, but the S/(C + N) improvement is only 1.3 db rather than the 6 db to 7 db improvement attained in the earlier examples. Again, the mainlobe clutter spectral spreading arising from the off ground track look angle appears to have reduced the effectiveness of the downstream AMTI.

TABLE 6

	<u>Received</u>	<u>Interface</u>	<u>Output</u>
$\frac{C + N}{N}$	59.6 db	16.3 db	6.8 db
$\frac{S}{C + N}$	-39 db	-0.6 db	12.1 db

S/N loss at interface = 7.9 db

TABLE 7

	<u>Received</u>	<u>Interface</u>	<u>Output</u>
$\frac{C + N}{N}$	59.6 db	24 db	11.1 db
$\frac{S}{C + N}$	-39 db	-1.5 db	13.4 db
$\frac{C + N}{N}$ Change*	0 db	7.7 db	4.3 db
$\frac{S}{C + N}$ Improvement*	0 db	-0.9 db	1.3 db

S/N loss at interface = 1 db

* With respect to Table 6

CONCLUSIONS

A type of compatibility problem which may occur when conventional AMTI follows an adaptive AMTI antenna processor is identified. The receive antenna pattern distortion related to this problem is significant only when the two-way pattern becomes unacceptable. However, the loss of mainlobe gain degrades radar performance.

Performance analysis results were presented to indicate the magnitude of the loss in system gain.

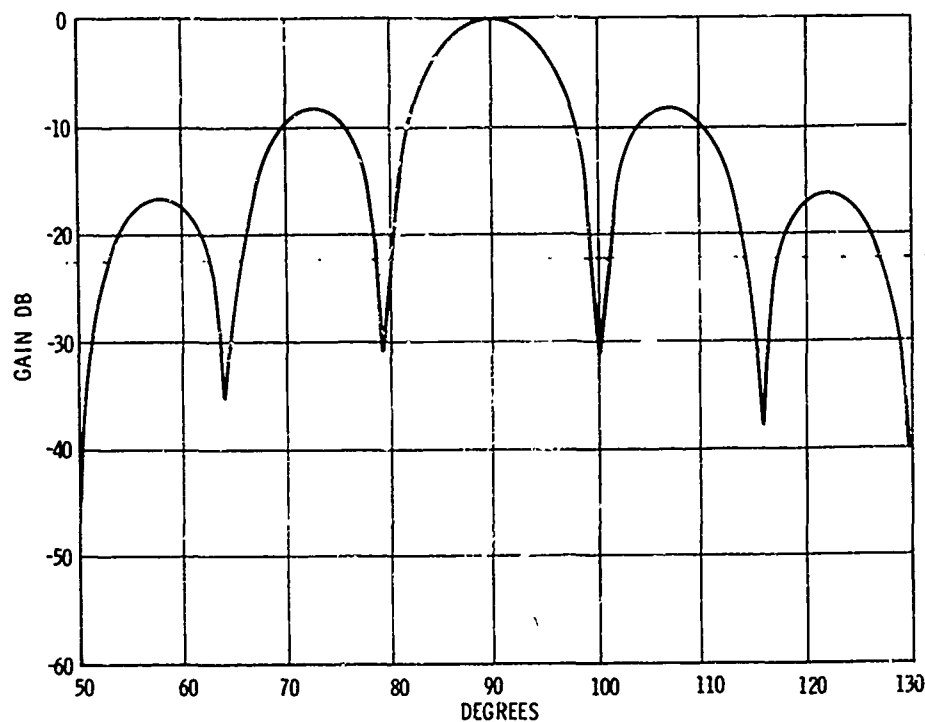


Figure 18. Adapted Receive Pattern, with Angular Interval Processor, 0.5λ Element Spacing

Gross level characteristics for an adaptive processor which reduces the S/N loss were discussed. However, it appears to be necessary to include circuits which can estimate mainlobe clutter if fully compatible performance is required.

A simple suboptimal adaptive processor can be implemented by modifying the minimum mean square error processor. The modification consists of altering the linear transformation, \bar{F} , to indicate an angular mainlobe interval rather than a discrete angle as the region for desired signals. Performance calculations which were conducted indicate that radar performance is improved by this modification. Additional work is required to fully evaluate this approach and other alternatives.

28. ADAPTIVE NULL STEERING for RF ANTENNA ARRAYS

by

WADE E. BUTCHER

RADIATION SYSTEMS DIVISION
A Subsidiary of
Harris-Intertype Corporation
Melbourne, Florida 32901

R. J. SIMS
SATCOM Agency
Ft. Monmouth, N.J.

for

ARRAY ANTENNA CONFERENCE

Naval Electronics Laboratory Center
San Diego, California

22, 23, 24 February 1972

28-1a

INTRODUCTION

Radiation Systems Division has investigated various techniques of utilizing the null-steering capabilities of phased arrays to provide rejection of interfering signals. Several innovations that evolved during one study appear to provide performance under realistic assumptions that is superior to that reported in the open literature. This paper is intended to provide an indication of the study effort and to present numerical results indicating the potential value of the adaptation methods used.

To better define the meaning of adaptive null steering, consider the simple illustration in Figure 1.

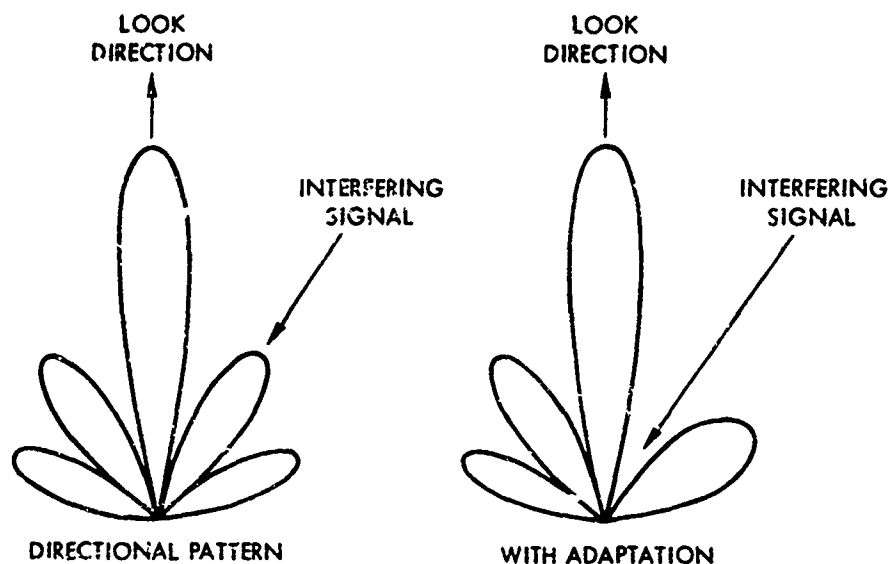


Figure 1. Simple Illustration of Null Steering

When the direction to a desired signal is known, several techniques are available to steer a main beam in the desired look direction. This steering, however, is generally done without consideration of the resultant sidelobe and null directions. Thus, one or more interfering signals may be incident directly upon a sidelobe of the array pattern with an ensuing degradation in system performance. The purpose of an adaptive system, as discussed in this paper, is to sense the environment and automatically steer nulls in the interference directions while maintaining a beam in the desired look direction. There are many applications where such rejection of directional interference is useful.

Although adaptive techniques for improved signal reception have been used for low-frequency applications, such as seismic array data, practical digital implementation for an RF system has not been done. In seismic array, the data rate is

sufficiently slow to allow digital processing and filtering of the signals - obviously, no digital computer exists that allows processing at RF rates. The alternate approach is analog filtering and adaptation. This technique is feasible for RF applications, but appears to be more limited than a digital implementation. The method discussed here employs a hybrid approach: the information path is analog, but the adaptation is performed digitally. The use of a digital processor to perform the adaptation offers a great deal of flexibility that cannot be achieved with the analog system. In addition, theoretical advances could be easily incorporated into a digital system at minimum cost.

Problem Formulation

The basic model considered is that shown in Figure 2. Each array element is followed by a transversal filter whose weights, W_i , are adjustable. The sum of all these transversal filter outputs then produces the total array output signal, y . Obviously, for the model shown, no restriction is placed on the number of antenna elements, array geometry, or upon the number of tap points contained in each transversal filter.

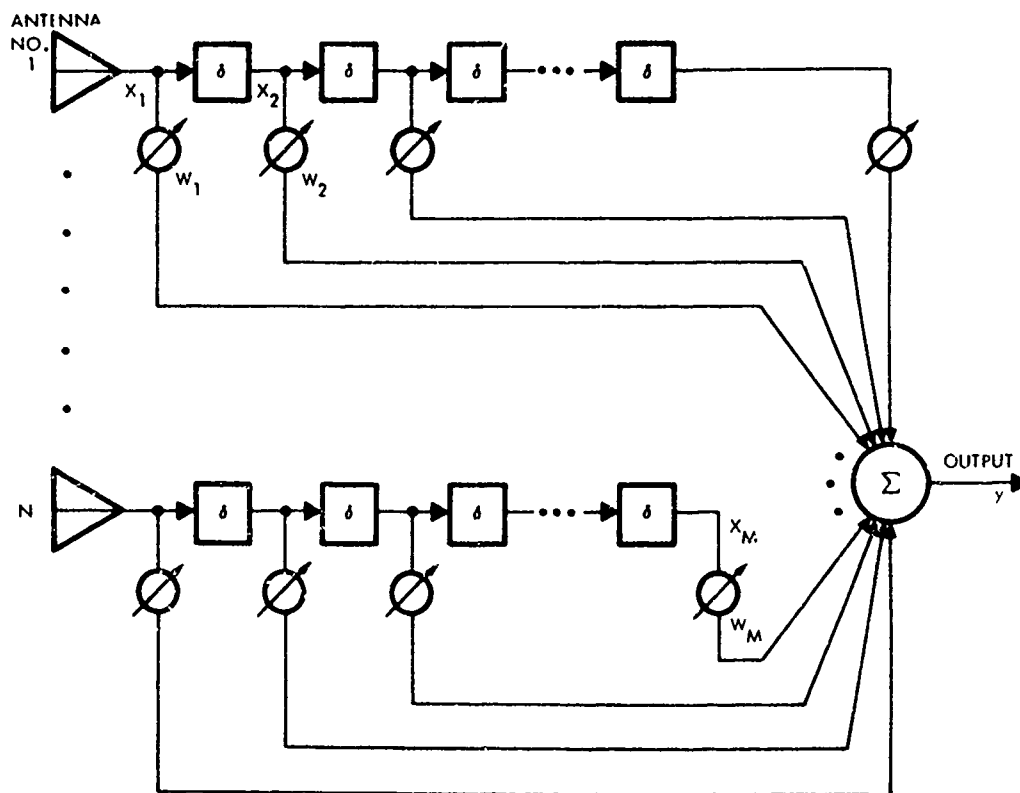


Figure 2. General Array Configuration

Consider discrete instants of time given by kT where T is a sampling period and k is an integer. Defining the signals at tap point i as X_i , a vector of all tap point signals at a specific sample time, k , can be expressed as

$$\underline{X}(k) \triangleq [X_1(kT) \ X_2(kT) \ \dots \ X_M(kT)]$$

where M is the total number of tap points and weights in the system. The weight vector may be defined in similar fashion as

$$\underline{W}(k) \triangleq [W_1(kT) \ W_2(kT) \ \dots \ W_M(kT)]$$

Using these definitions, the array output signal at instant k is

$$y(k) = \underline{W}(k) \underline{X}(k)'$$

where prime denotes transpose. It must be made clear that this discussion does not imply that the signals are processed through the transversal filters and summed digitally. The signals involved are continuous time functions, but they will be examined at discrete intervals to achieve the desired interference rejection.

The tap point signals will contain components due to interfering signals and noise in addition to the target signal. Ideally, the weights W_i could be adjusted such that the array output signal would equal the target signal. Practically speaking, we would like to adjust the weights so the array output represents the target signal as closely as possible. This, then, is the goal of the techniques discussed in this paper.

Optimal Solution

In order to discuss an optimal solution, we must first define the criteria upon which the optimization is based. Assume for the moment that the desired response of the system is precisely known and given by $y_d(k)$. Therefore, at sampling instant k the system error is

$$e(k) = y_d(k) - y(k) \tag{1}$$

Optimum weights can be defined as those weights that minimize some function of this error signal.

One common criterion for optimization is minimization of the mean square error, one pleasing factor being that a least mean square error formulation generally leads to a workable solution. Therefore, let us consider the tap point signals as stationary stochastic variables, and define the optimum weights as those that minimize the expected value of the squared error. The figure of merit thus becomes

$$\overline{e^2} = E [e^2(k)] \quad (2)$$

where E denotes expected value.

The set of weights that minimize $\overline{e^2}$ can be derived in a straightforward manner and are given by

$$\underline{W}_{\text{opt}} = \Phi(x, x)^{-1} \Phi(x, d) \quad (3)$$

where

$$\Phi(x, x) \triangleq E [\underline{X}' \underline{X}]$$

and

$$\Phi(x, d) \triangleq E [\underline{X}' y_d]$$

This is a well-known result: specifically, the Wiener-Hopf equation. It has been used in a variety of applications, one of these being the processing of digital seismic array data. [1]

At this point the logical question is why the subject should be further pursued. The answer lies in the computational difficulties presented by Equation (3). First, the correlation functions required must be estimated, since an exact determination is not possible from a finite amount of data. Second, and more restrictive, is the requirement for inversion of a matrix of order M . When M is large - a probable condition for realistic situations - this matrix inversion may be prohibitive. In addition, there is the dilemma posed by the requirement for precise knowledge of y_d . Thus the search for alternate methods for achieving an equivalent result.

Iterative Solution

One technique for obtaining an optimal solution under certain conditions is an iterative method based upon gradient search techniques. This method requires iterations where the weights at each step are adjusted according to the gradient of the error previously defined. That is

$$\underline{W}(k+1)' = \underline{W}(k)' + \mu \nabla(k) \quad (4)$$

where

$\underline{W}(k) \triangleq$ weight vector before adaptation

$\underline{W}(k+1) \triangleq$ weight vector after adaptation

$\mu \triangleq$ Scalar constant controlling convergence rate and stability

$\nabla(k) \triangleq$ gradient vector of $e^2(k)$ with respect to \underline{W}

The exact form assumed by Equation (4) depends on the technique for estimating the gradient vector $\nabla(k)$. A summary of the more common variations and the inherent disadvantages of each is given by Griffiths. [2]

One expansion of Equation (4) uses the estimated value of the instantaneous error gradient. This estimated gradient is obtained from a single time sample of the squared error as

$$\nabla(k) \cong \nabla[e^2(k)] = -2e(k)\underline{X}(k)' \quad (5)$$

Using this result, the adaptation algorithm becomes

$$\underline{W}(k+1)' = \underline{W}(k)' - 2\mu [\gamma_d(k) - y(k)] \underline{X}(k)' \quad (6)$$

One advantage of Equation (6) is that it requires only the present weights and instantaneous values of the signals at each iteration. The major disadvantage is the necessity of γ_d at each iteration.

The algorithm given by Equation (6) converges to the same result as that given by Equation (3) if γ_d is the same function in both methods. This may be impossible since a statistical description is required in one case and a time series in the other. In any case, convergence of the iterative procedure requires [3] that

$$0 > \mu > -1/\text{total signal power} \quad (7)$$

where

$$\text{total signal power} = \sum_{i=1}^M E[X_i^2] \quad (8)$$

A MODIFIED HYBRID APPROACH

The approach to the problem of adaptive null steering as considered in this paper is a slight perturbation upon the algorithm given by Equation (6). The present method has resulted from an evolutionary process of theoretical considerations and computer simulations demonstrating feasibility. It has been found desirable to consider two cases as separate entities, since the identical algorithm implementation does not seem suitable for both. These cases are: (1) no frequency uncertainty in knowledge of the target signal carrier, and (2) frequency uncertainty, or the absence of an appreciable magnitude carrier altogether.

Subfrequency Sampling

Before any functional description of a hybrid system with intended application to RF signals can be made, the question of possible sampling rates must be addressed. Obviously, no existing digital processor allows an appreciable number of computations at RF signal rates. Therefore, let us examine the possibility of slower sampling rates and the corresponding slower adaptation in conjunction with RF signals. There is nothing inherent in Equation (4) that in any way restricts the time interval between instants k and $k+1$. The only requirement for validity of the weight adjustment in this manner is that the error gradient $\underline{\nabla}(k)$ be accurately estimated at instant k . If this condition is satisfied, then the adjustment of the weight vector specified is valid whether instants k and $k+1$ are separated by a fraction of a signal frequency cycle or by several hundred cycles, assuming, of course, that the environment is stationary.

Actually, the convergence proofs normally associated with the adaptation algorithms assume that successive samples of the signals are statistically independent. This constraint, even though it appears overly restrictive, is better met by subfrequency sampling (a sampling rate slower than the target signal frequency) than by a rapid sampling rate. In reality, a probable restriction is that no frequency components of the interfering environment are exactly equal to the target signal carrier frequency in the folded frequency spectrum, where the folding frequency is equal to the sampling frequency divided by two. In order to achieve this condition, a random sampling rate might be required rather than a truly periodic sampling rate. The hardship thus imposed would be in the case of a pilot signal that is actually injected into the array. However, it is felt that this problem could be overcome if a random sampling rate is, in fact, required.

Adaptation Algorithm

The heart of this or any comparable system is the adaptation algorithm employed. The basic technique presented here is to use the algorithm previously discussed which is given by

$$\underline{W}(k+1)' = \underline{W}(k)' - 2\mu e(k) \underline{X}(k)' \quad (9)$$

with perturbations in the formation of the error signal $e(k)$, in the values used for $X(k)$, and in the values used for the initial weights. Exact implementation depends on the accuracy of the *a priori* information about the target signal.

Under ideal conditions - where the pilot signal is an exact representation of the target signal - the initial weight values are immaterial. Since in all realistic situations this condition is not fulfilled, the final solution is dependent upon the initial weight vector. Therefore, it seems logical to use a set of weights that produce a beam in the desired look direction for the initial weight vector. This selection has been made in most of the numerical results to be discussed. However, if directional information is unknown, we must start with an isotropic pattern.

Type I Adaptation

For Type I adaptation a precise estimate of the target signal carrier frequency, or of some spectral component of the target, is required. In practice, this condition might be achieved by a narrow band phase-locked loop, especially in the case of a cooperative target that might transmit a suitable pilot signal. This pilot signal might be a pure tone, or it could be coded to aid in the adaptation procedure. If a precise frequency pilot signal is available, the error signal at each iteration is

$$e(k) = p(k) - y(k) \quad (10)$$

where $p(k)$ and $y(k)$ are samples of the pilot and system output, respectively. The weights are then adjusted according to Equation (9).

Type II Adaptation

In Type II adaptation the target signal carrier is assumed to be unknown or absent, but the direction to the target is assumed to be known. This situation is appropriate for fixed stations or for a search operation. Type II requires the pilot signal to be artificially inserted into the system, or system model, in order to train the array in the desired direction. This insertion is easily accomplished in the software, but would be difficult to implement with hardware, and would perturb the array output.

To clarify the meaning of software insertion of a pilot signal consider the following. Knowing the array geometry and the pilot frequency and direction of arrival, the relative phase of the pilot at each antenna element may be computed as though the pilot were actually a signal incident on the array. Then at each sampling instant these relative phase angles can be used to compute pilot samples that would appear at each tap point in the system if the pilot signal were part of the environment. These pilot samples are linearly added to the actual tap point signals in the software to accomplish artificial insertion. This insertion constrains the array to have a main beam in the pilot direction and frequency, since the pilot is considered the desired signal when an error signal is formed. Any signals present in the environment which differ substantially from the pilot in frequency and/or

direction will be "nulled" by the adaptive system. The amount of difference allowable depends on the physical configuration of the array. The computations at each sampling instant can be minimized by using a table to obtain the required pilot samples. Precomputed address differences for the various tap points are used to obtain the appropriate pilot sample for each point.

Thus, in Type II adaptation the computation at each iteration is performed with Equation (9), but the $X(k)$ vector consists of two components: the actual environment and the artificial pilot signal. The error signal is computed as

$$e(k) = y_d(k) - y(k)$$

where $y_d(k)$ is the system output due to the pilot signal using the original weight vector, and $y(k)$ is the system output due to the pilot and environment using the present weight vector. This formation of the error signal maintains the system gain in the desired look direction at that produced by the original weight vector, which is the maximum achievable. Of course, variations on the Type II adaptation are possible.

COMPUTER SIMULATION AND RESULTS

In order to illustrate the feasibility of the hybrid approach, a FORTRAN computer program was prepared to simulate a phased array with the associated adaptive processor. It was not intended to perform an exhaustive study of all aspects of the technique, but merely to investigate various error signal and adaptive algorithm formulations, and to show that the hybrid approach gives promising results for several example cases of CW and modulated signals, frequency uncertainties, and interference amplitudes.

Because it is assumed that interfering signals may arrive from any azimuth angle, an array having circular symmetry in the azimuth plane was chosen for the simulation. Since we had previously performed studies of circular arrays, a program was readily available to compute the azimuth pattern of such an array with arbitrary complex feeding coefficients and arbitrary element pattern. Because the goal of the study was to establish the feasibility of the adaptive processor and not to investigate array configurations, a simple circular array of eight isotropic sources was used for most of the simulations. This choice could represent an array of vertical monopoles above a ground plane. Several different arc length element spacings were used in the study. In addition, a limited study of the effects of various numbers of elements was performed.

The transversal filter elements were assumed to be simple time delays, with an equivalent phase shift of 90° between taps at 30 MHz. Typically, four tap points per filter were used. The 30-MHz operating frequency might represent the RF band of interest of the system, or it could be an intermediate frequency resulting from down- or up-conversion of the desired RF.

The numerical investigation was generally restricted to simulating a small number of examples for each of the specific cases of interest. These cases fell into the two broad categories of a known target frequency (Type I), and a degree of uncertainty in the estimate of the target frequency (Type II). For all the examples, the signal center frequency was taken as 30 MHz, and the center frequencies of the interfering signals, f_1 , f_2 , and f_3 , were 29.0, 31.0, and 30.5, respectively. In all cases the target and interference signal phases, relative to the array reference point (the center), were arbitrarily chosen constants. All of the simulations reported in this paper were made at a processor sampling rate of 10.113 kHz.

Type I Adaptation

For this example, all four signals were CW. Table 1 presents the signal to interference ratios, in decibels, for each of the three interfering signals. The column headed "isotropic" represents the relative strength of the target and each particular interference in the environment. The column headed "initial" gives the ratios after the initial weights have been set (forming a beam in the target direction), but before the adaptation has been begun. The third column, labeled "final," gives the ratios after the total number of iterations has been completed. For this example, the total number of iterations was 2000, and the convergence factor, μ , was -0.0025.

Table 1. Signal-to-Interference Ratios (Type I with CW Signals)

Signal	Isotropic	Initial	Final
f_1	6.0	42.8	81.6
f_2	6.0	32.8	78.6
f_3	6.0	14.1	79.8

Figure 3 illustrates the array azimuth response for this example. The solid curve is the array pattern, at 30 MHz, after the initial weights were set to form a beam in the zero direction. The element spacing, S , was one-third wavelength. (The initial pattern at the interfering frequencies was very near that shown for 30 MHz; i.e., the initial response was broadband.) The arrows at the top of the figure are located at the azimuth angle of each of the signals. The dotted curves show the array response after adaptation, in the azimuth vicinity and at the center frequency of each particular signal. The Δ values given, in decibels, are the differences between the initial and final array responses, again at the frequencies indicated.

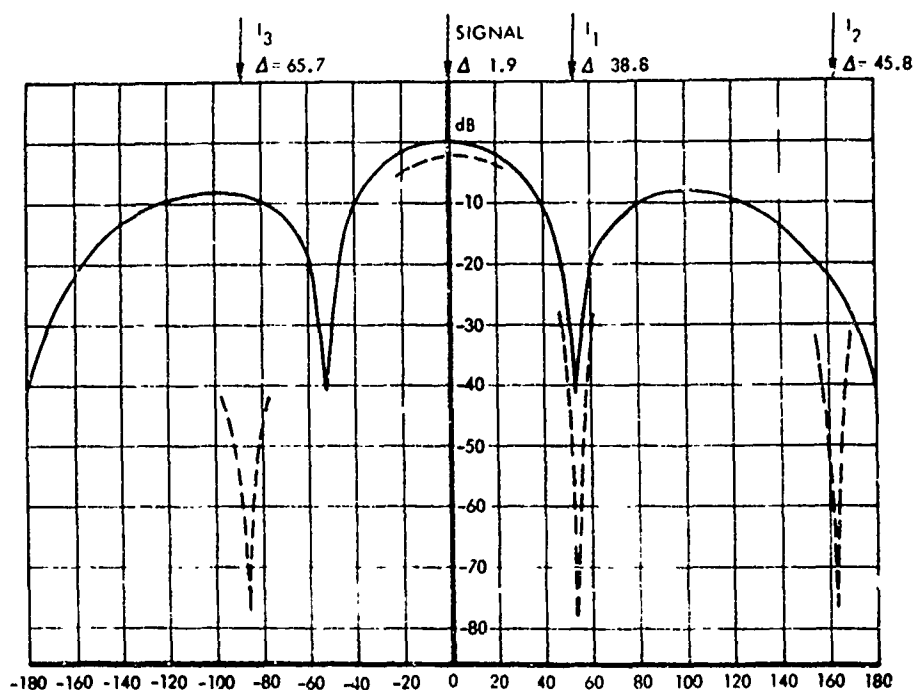


Figure 3. CW Target and Interference, Estimated Target Amplitude

Type II Adaptation

As previously mentioned, the case in which the target carrier frequency is known precisely is possibly an unrealistic one. Accordingly, a great deal of effort was expended in developing a software approach in which appropriate pilot samples are "inserted" to make the processor insensitive to the frequency difference between the pilot and target signals. This approach also leaves the processor performance relatively unchanged for various target modulations. All of the remaining examples were implemented using this technique. The target center frequency estimate was assumed to be 3 kHz in error; i.e., equal to 30.003 MHz.

The first case to be examined here is the one for all CW signals. An estimate of the target amplitude is not critical for this approach. The results for 5000 iterations and a -0.0001 convergence factor are shown in Figure 4. Although the results are not nearly as impressive as those for Type I, it must be remembered that the techniques used in the previous example will not work at all for the 3-kHz uncertainty present here.

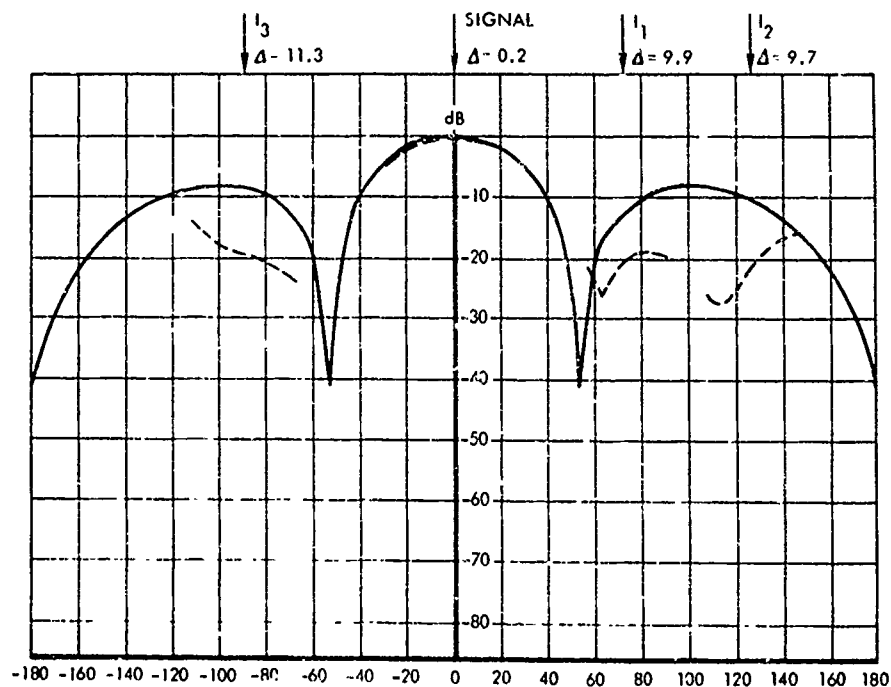


Figure 4. CW Target and Interference - Type II

A perturbation on the previous example is one in which one of the three interfering signals and the target signal are 100 percent amplitude modulated, with the target modulation being at 750 kHz, and the modulation on signal I_3 at 500 kHz. The results are shown in Table 2. The adaptation was continued for 5000 iterations, and the convergence factor was again -0.0001.

Table 2. Target and One Interference Signal Modulated

Signal	Isotropic	Initial	Final
I_1	5.0	16.9	29.6
I_2	6.0	17.9	27.6
I_3	6.0	14.0	29.0

If the adaptive array is to operate in an environment where the interference is intentional (jamming), the relative magnitude of the interference would be expected to be much larger. To investigate this case, the amplitude of I_1 was

increased such that the signal-to-interference ratio in the environment was -16.9 dB. Figure 5 shows the results for 4000 iterations under this condition. All signals were CW. It is interesting to note that the processor apparently "overreacted" in its attempt to suppress the large interference, because the final signal-to-interference ratios for I_2 and I_3 are slightly less than in Figure 4, while the ratio for I_1 is much improved.

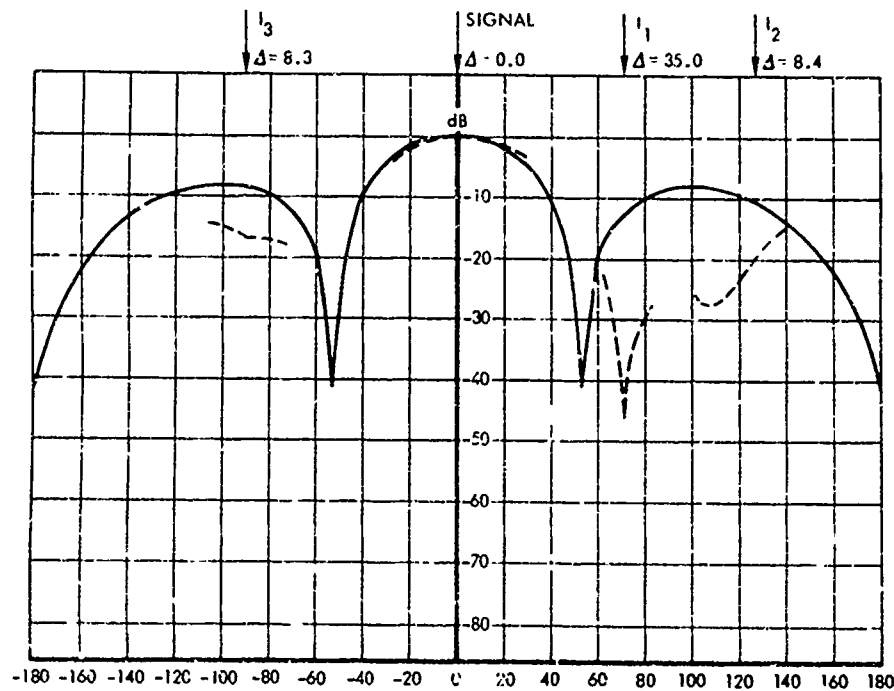


Figure 5. One Large Interfering Signal Environment

The effect of changing the number of elements in the array was investigated for the signal condition of Table 2. Both the initial and adapted signal-to-interference ratios are presented in Table 3 for three values of N , the number of elements. The arc length spacing of the elements was one-third wavelength at 30 MHz in each case. As expected, the system is capable of better interference rejection when more elements are contained in the array. In each case 5,000 iterations with a convergence factor of -0.0001 were used. The results for $N=8$ differ from those in Table 2 due to the independence of the two simulations and a different pilot amplitude.

Table 3. Effect of the Number of Elements

Signal	Isotropic	N=4		N=8		N=16	
		Initial	Final	Initial	Final	Initial	Final
l_1	6.0	12.7	17.1	16.9	27.1	20.3	44.2
l_2	6.0	31.5	21.4	17.9	26.9	19.3	37.3
l_3	6.0	18.9	30.0	14.0	29.4	18.0	41.0

Next, consider the effect of adaptation in the presence of a broadband target and interfering signal. One concern was that the system would be capable of rejecting (in the frequency domain) the signal modulation components while still maintaining a main beam in the desired look direction. The adaptation here was Type II with a CW pilot at 30.003 MHz. The array consisted of 8 elements; 5000 iterations were performed. The target was frequency modulated at 600 kHz with a modulation index ($\Delta f/f_m$) of 5. The center frequency was 30 MHz and azimuth direction 0° . Modulation on the single interference was identical to that of the target, but the center frequency was 29 MHz and the azimuth direction 72° .

Figure 6 shows the array frequency response after adaptation in the target signal direction (0°) for two cases: 2 and 4 weights in each transverse filter, respectively. Also shown is the target signal spectrum.

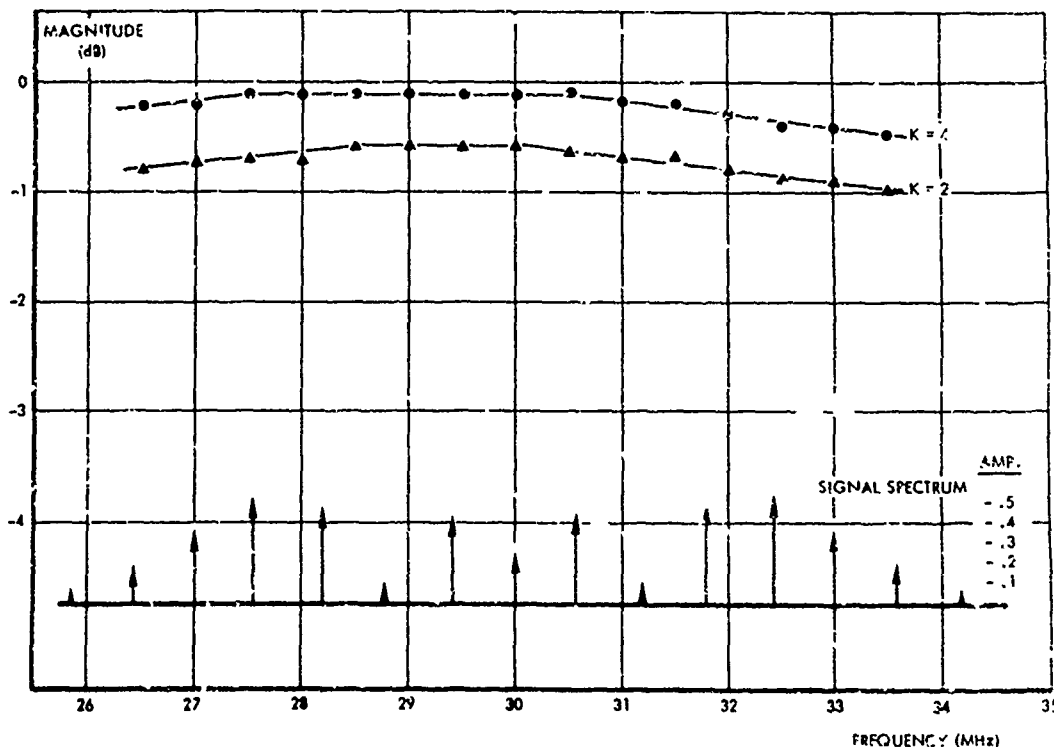


Figure 6. Main Beam Response for Wideband Target

Figure 7 depicts plots of the array frequency response in the direction of the interfering signal for the initial pattern, adapted with 2 weights per filter, and adapted with 4 weights per filter. Also given are the adapted array response to a CW interference at 29 MHz and the broadband interference spectrum. These results show that the system is capable of broadband interference rejection.

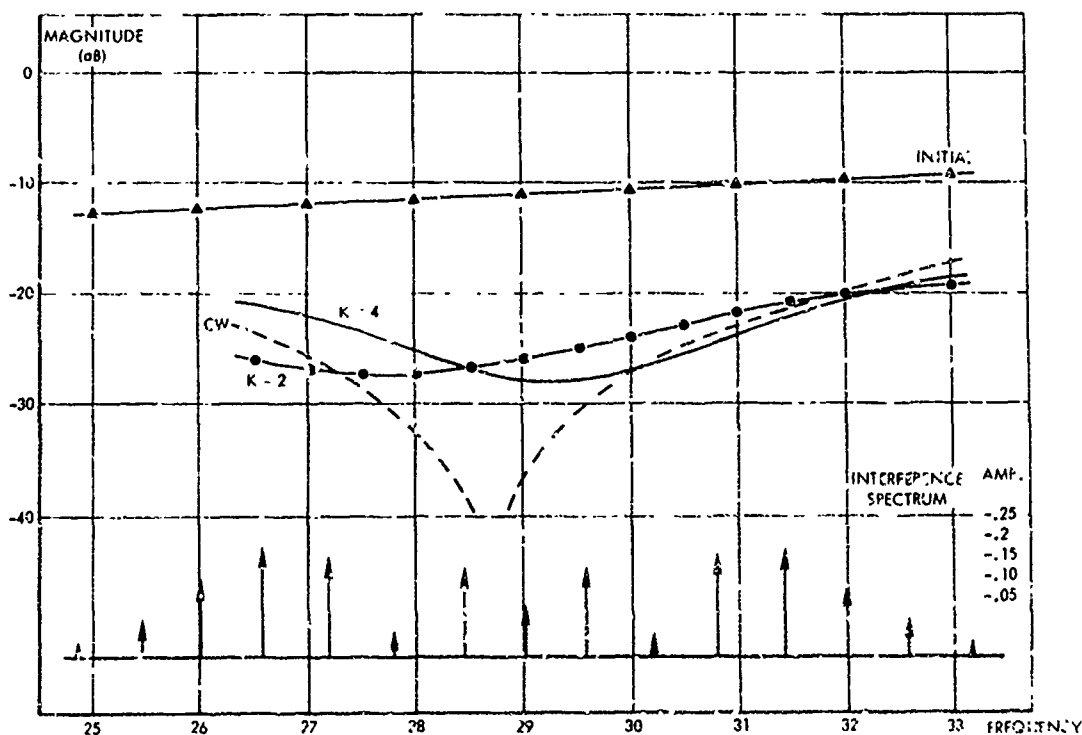


Figure 7. Array Response to Interference at 72 Azimuth Centered at 29 MHz

Summary

A technique that allows utilization of digital processing for RF adaptive arrays has been described, and simulated results presented to demonstrate the basic feasibility of the concept. Subfrequency sampling makes digital processing possible for RF arrays and using a pilot signal inserted in the software provides the most realistic performance for the algorithms considered. Present study efforts are leading to improved algorithms.

REFERENCES

- [1] Burg, J. P. "Three-Dimensional Filtering With an Array of Seismometers," Geophysics, October 1964, pp. 693-713.
- [2] Griffiths, L. J. "A Simple Adaptive Algorithm for Real-Time Processing in Adaptive Arrays," Proceedings of the IEEE, October 1969, pp. 1696-1704.
- [3] Widrow, et al. "Adaptive Antenna Systems," Proceedings of the IEEE, December 1967, pp. 2143-2159.

29. A TECHNIQUE FOR GENERATION OF PHASE
SHIFTS REQUIRED FOR CIRCULARLY POLARIZED
AND ADAPTIVE ARRAY ANTENNAS

by

P. M. Hansen

Code 2100

Naval Electronics Laboratory Center
San Diego, California 92152

for

ARRAY ANTENNA CONFERENCE

22, 23, 24 February 1972

Naval Electronics Laboratory Center
San Diego, California

29-1a

INTRODUCTION

One method of generating a circularly polarized wave is to use two crossed dipoles in phase quadrature. The antenna itself is conceptually simple. The problem arises when one tries to generate a 90° phase shift over a wide frequency range. One solution to this problem lies in the techniques used for quadrature detectors. A typical quadrature detector is illustrated in figure 29-1.

The total phase shift through the networks varies with frequency. However, the difference in phase at the input to the two product detectors is exactly 90° over a wide frequency range. Analog circuits are readily available that will provide the 90° phase shift over four octaves or more.

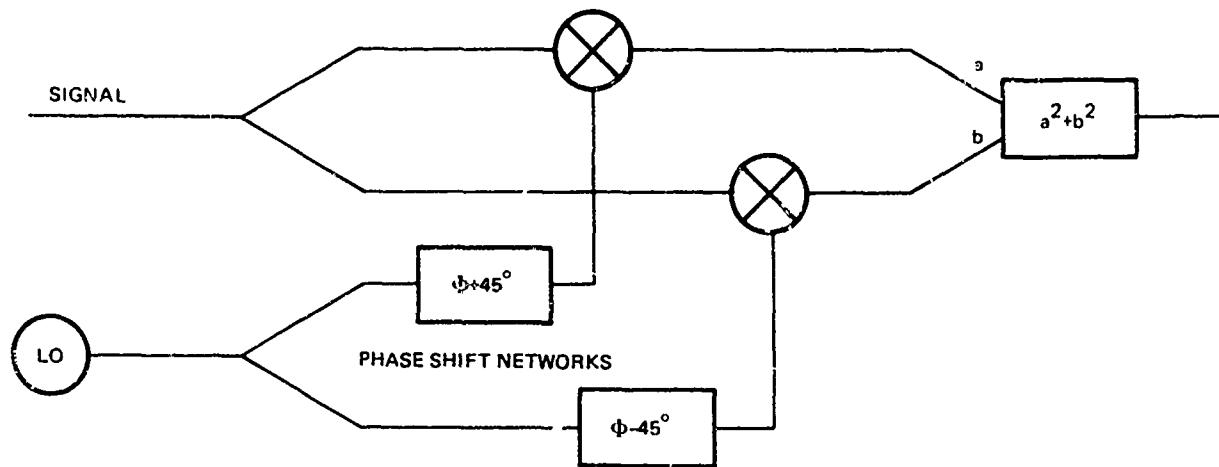


Figure 29-1. Typical quadrature detector.

CIRCULARLY POLARIZED TRANSMIT ANTENNA

The same technique can be applied to generate a circularly polarized antenna. The technique is illustrated in figure 29-2.

If the signal is a modulated carrier represented by

$$S = a(t) \cos \omega_1 t$$

then the signal arriving at antenna 1 will be

$$S_1 = a(t) \cos (\omega_c t + \Phi + 45^\circ)^*$$

$$\text{where } \omega_c = \omega_1 + \omega_0$$

the signal at antenna 2 will be

$$S_2 = a(t) \cos (\omega_c t + \Phi - 45^\circ)$$

These two signals may be rewritten as

$$S_1 = a(t) \cos(\omega_c t + \Phi')$$

$$S_2 = a(t) \sin(\omega_c t + \Phi')$$

(Note Φ is a function of frequency)

$$\text{where } \Phi' = \Phi + 45^\circ$$

The currents on antenna 1 and antenna 2 are in phase quadrature if the antennas have small mutual coupling and the effect is a circularly polarized transmitting antenna.

A circularly polarized receive antenna is illustrated in figure 29-3.

The same local oscillator and phase shift network could be used for transmitting and receiving functions. The phase quadrature of the two channel is maintained over a broad range of frequencies. The only problem is antenna impedance matching over this frequency range. For receiving, this problem can be solved by active impedance matching.

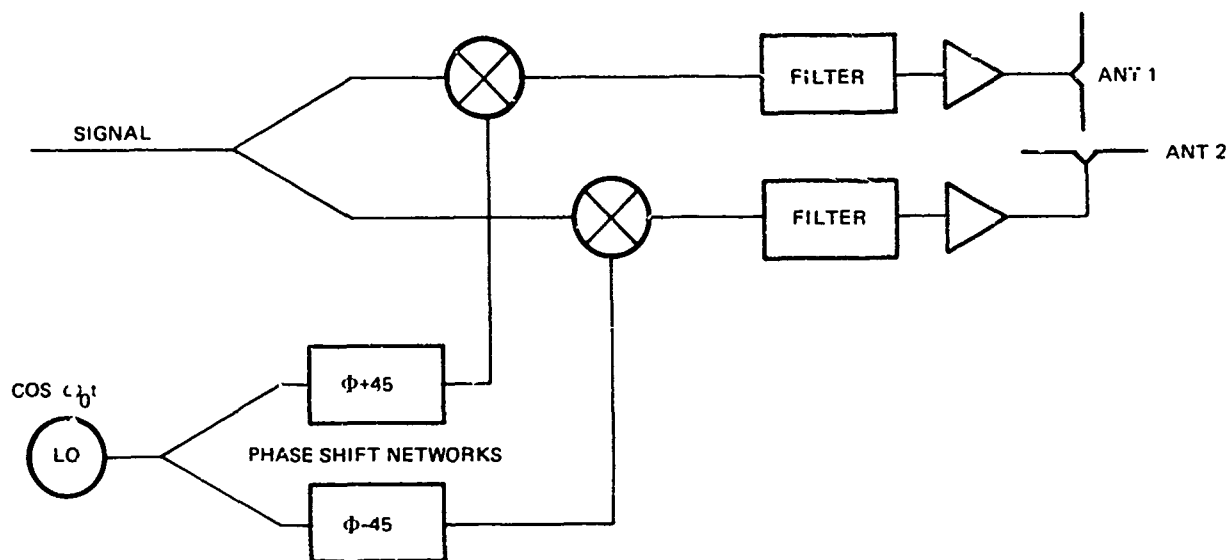


Figure 29-2. Broadband circularly polarized antenna.

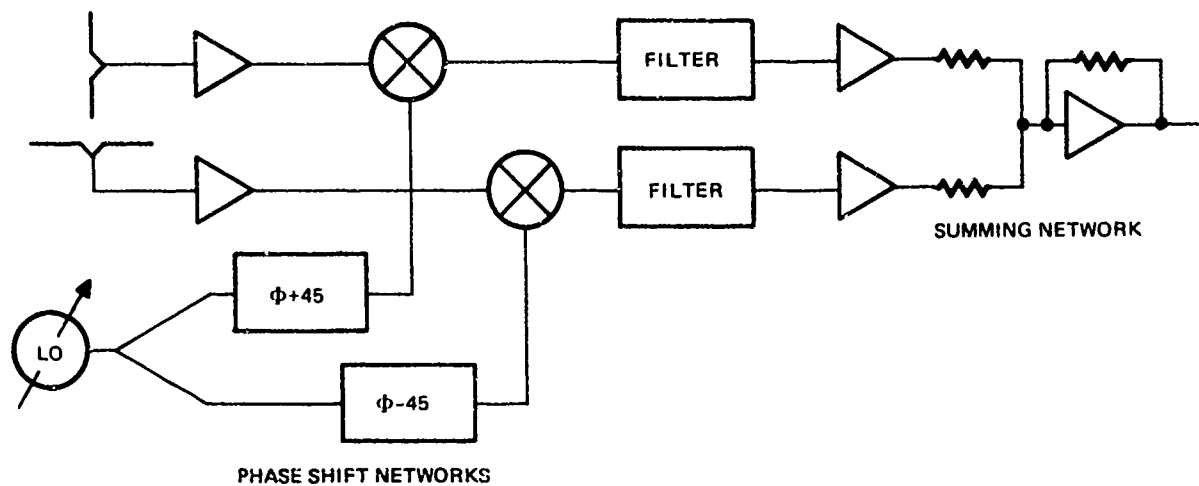


Figure 29-3. Circularly polarized receiving antenna.

PHASED ARRAY APPLICATIONS

A general phased-array antenna has both the phase and amplitude of each element fixed. The technique of phase shifting at an intermediate frequency can be used to develop the phase shifts required for a general phased array. A typical receiving application is illustrated in figure 29-4.

The a_i 's are the magnitude coefficients for each element while the δ_i 's are the phase shifts for each element. The same techniques could be applied to a transmitting antenna.

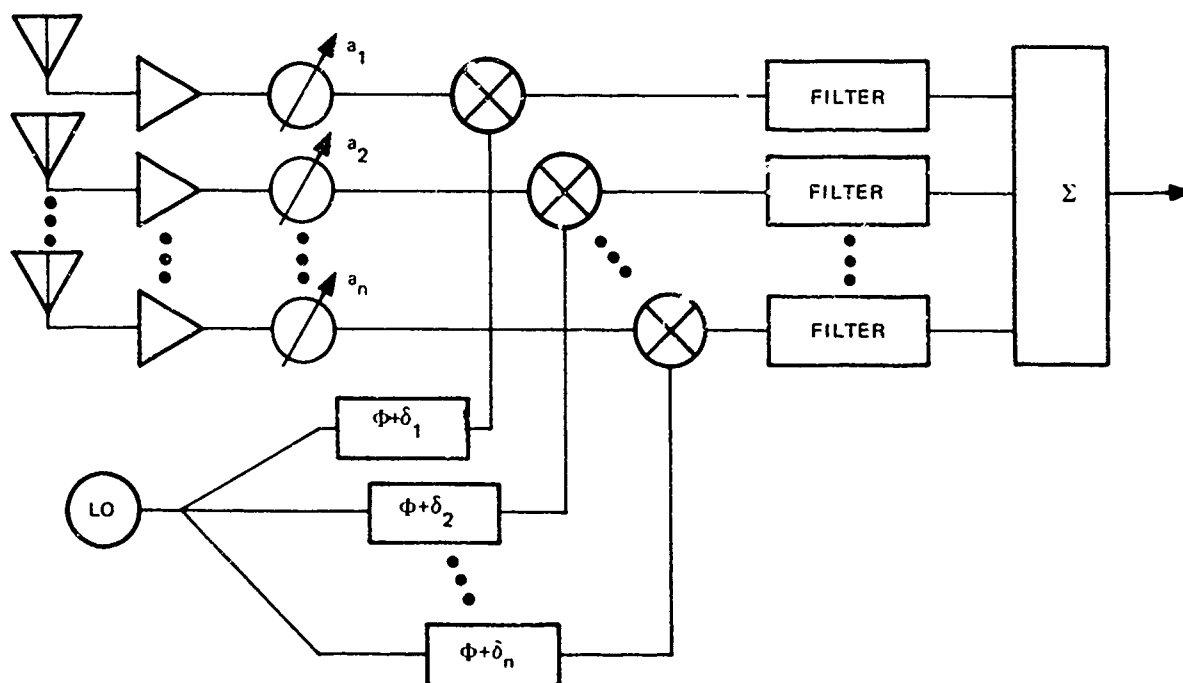


Figure 29-4. Generalized phased array.

DIGITAL TECHNIQUES

Present-day digital technology can be used to generate the phase-shifted local oscillator signals. One simple technique is illustrated in figure 29-5.

The shift register has only one stage set. The multiplexers are used to determine which stage of the shift register drives a phase-locked loop oscillator. If there are n bits in the shift register, the phase shift corresponding to a shift of one bit is given by

$$\Delta\Phi = \frac{360^\circ}{n}$$

Consequently, a 360-stage shift register will yield a phase resolution of 1° .

The digital technique outlined in figure 29-5 is equivalent to generating the phase shift at a fixed frequency and then up-converting. The advantage of the digital method lies in the fact that the phase shifts are programmable, and could be set by computer control. This would provide the means for realizing an adaptive array.

An adaptive receiving system composed of a minicomputer, and a receiver with programmable phase shifters could be attached to an arbitrary set of antennas to optimize reception. Applications would be at a NAVCOMMSTA receive site or on shipboard. In addition, each channel could have a programmable gain control in order to truly optimize SNR.

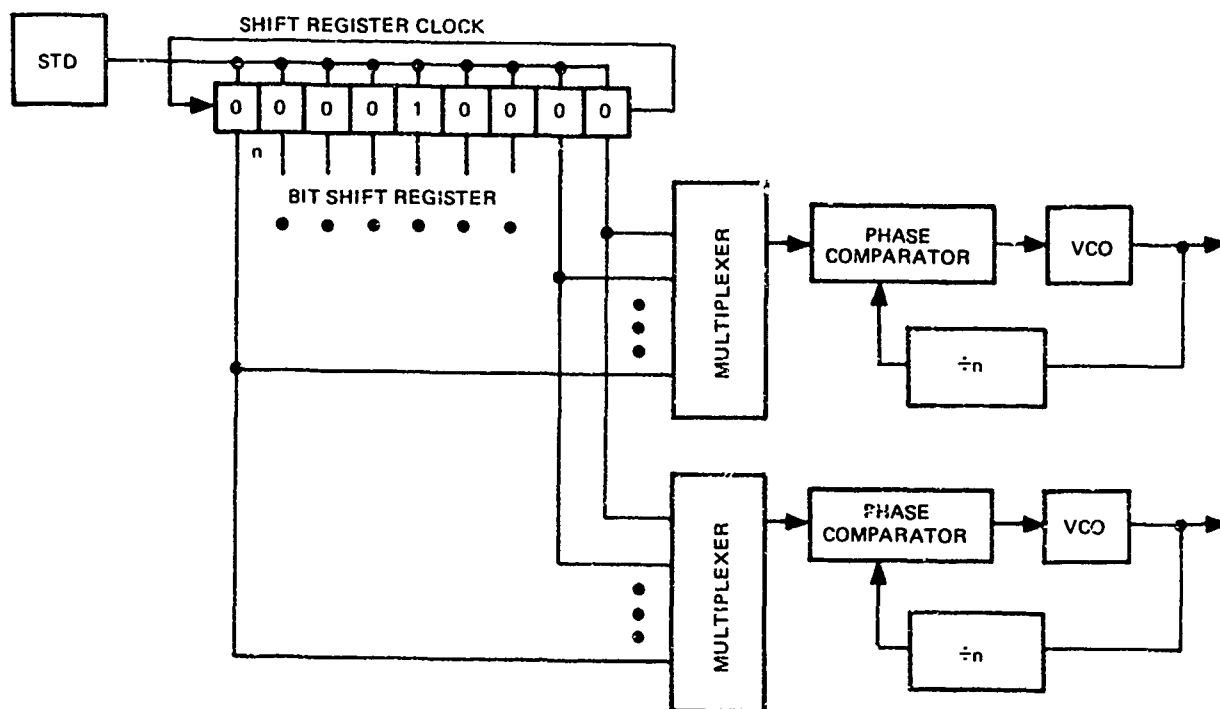


Figure 29-5. Phase and frequency-programmable local oscillator.

CONCLUSION

Quadrature detection techniques suggest a method of obtaining the phase quadrature necessary for a circularly polarized antenna over a broad bandwidth. The method is to phase-shift a local oscillator used in frequency conversion. This method could be applied to realize a general phased array. Simple digital techniques are suggested for realizing an adaptive receiving system controlled by a minicomputer.

30. DESIGN AND ADAPTIVE CONTROL OF CONFORMAL ARRAYS

by

L. E. Brennan

Technology Service Corporation
Santa Monica, California 90401

for

ARRAY ANTENNA CONFERENCE

Naval Electronics Laboratory Center
San Diego, California

22, 23, 24 February 1972

30-1a

1. INTRODUCTION

While conformal array antennas offer many advantages over conventional planar arrays or reflector antennas, they are more difficult to design. A theory of conformal arrays which specifies optimum array excitation functions, similar to the Dolph-Chebychev theory of linear and planar arrays, has not been developed. The problem is further complicated by variations in element patterns; the elements of an array flush-mounted on a curved surface are oriented in different directions. Section 2 of this paper describes a method of computing optimum excitation functions for conformal array antennas. This theory is based on the earlier work on adaptive array antennas [1,2,3]. Examples in Section 2 show that very low sidelobe levels can be achieved for conformal array configurations employing the sets of array weights computed with this theory.

Conformal array receiving antennas can also be implemented adaptively, employing an array of adaptive control loops which generate the element weights. Earlier studies [4] have shown that an adaptive receiving array reduces sidelobes selectively in the directions of greatest interference, compensates for the effect of scatterers (e.g., aircraft structure) in the antenna near-field, and that the adaptive system converges rapidly to a near-optimum solution. Application of this technique for sidelobe reduction to conformal array antennas is discussed in Section 3.

One important advantage of adaptive array antennas is the ability of these systems to compensate for gain and phase errors in the individual array element channels. In the extreme case of a missing element, e.g., due to an open circuit in one of the element channels, the weights applied to the remaining elements of the array are readjusted adaptively to optimize the antenna pattern. This subject is discussed in Section 4. An example illustrates the substantial reduction in sidelobes which can be achieved by readjustment of element weights after one element is removed from an array.

2. DESIGN OF CONFORMAL ARRAYS

This section outlines a method of computing optimum illumination functions, i.e., optimum element weights, for conformal array antennas mounted on arbitrary curved surfaces. The optimization criterion is minimum average sidelobe level for a given antenna gain and beamwidth. The shape of the array surface, element locations, element patterns, and element orientations are considered in the optimization. The technique for computing optimum element weights is outlined in this section and examples are given to show that, in many cases, low sidelobe levels can be obtained with conformal arrays.

Let x_n and y_n denote the location of the n th array element in cartesian coordinates, as defined in Figure 1, and ψ_n the orientation of the n th element relative to the y axis. Only curved arrays lying in the x - y plane will be considered in this section. However, the

techniques outlined here can be generalized to curved surface arrays in three dimensions with arbitrary element patterns. Let $E_n(\phi)$ denote the element pattern of the n th array element relative to the element orientation. In the θ coordinate of Figure 1, this element pattern is $E_n(\theta - \psi_n)$. For a given set of complex element weights, $\{w_n\}$, the E-field pattern of the antenna is

$$E_T(\theta) = \sum_{n=1}^N w_n E_n(\theta - \psi_n) e^{-\frac{2\pi i}{\lambda} [y_n \cos \theta - x_n \sin \theta]} \quad (1)$$

where

$E_T(\theta)$ = E-field pattern of array

λ = wavelength

The antenna gain $G(\theta)$ is proportional to $|E_T(\theta)|^2$.

Let θ_s denote the desired scan angle. When a plane wave is incident on the array from the angle θ_s , the outputs of the array elements are

$$s_n = E_n(\theta_s - \psi_n) e^{-\frac{2\pi i}{\lambda} [y_n \cos \theta_s - x_n \sin \theta_s]} \quad (2)$$

and the array output is

$$\sum_{n=1}^N w_n s_n$$

When the system performance is limited by receiver noise rather than external interference (e.g., clutter or jamming) received through the sidelobes, the optimum set of element weights is given by

$$w_n = K s_n^* \quad (3)$$

where

K = arbitrary constant

s_n^* = complex conjugate of s_n

Note that the w_n , s_n , and possibly E_n , are complex quantities, i.e., both phase and amplitude information are retained.

Next a design beamwidth for the array, θ_B , is selected. This beamwidth should be greater than the diffraction-limited beamwidth of the array. For example, at zero degree scan angle, $\theta_B > (x_n - x_1)/\lambda$. As in linear arrays, as the beamwidth is allowed to increase, lower sidelobe levels can be achieved. The next step in the design procedure is selection of a hypothetical noise field in the sidelobe region. To minimize the average or integrated sidelobe gain, a uniform noise field is selected. To reduce sidelobes selectively in any given angular region, a stronger external noise field is selected for this region. A covariance matrix is computed for this hypothetical external

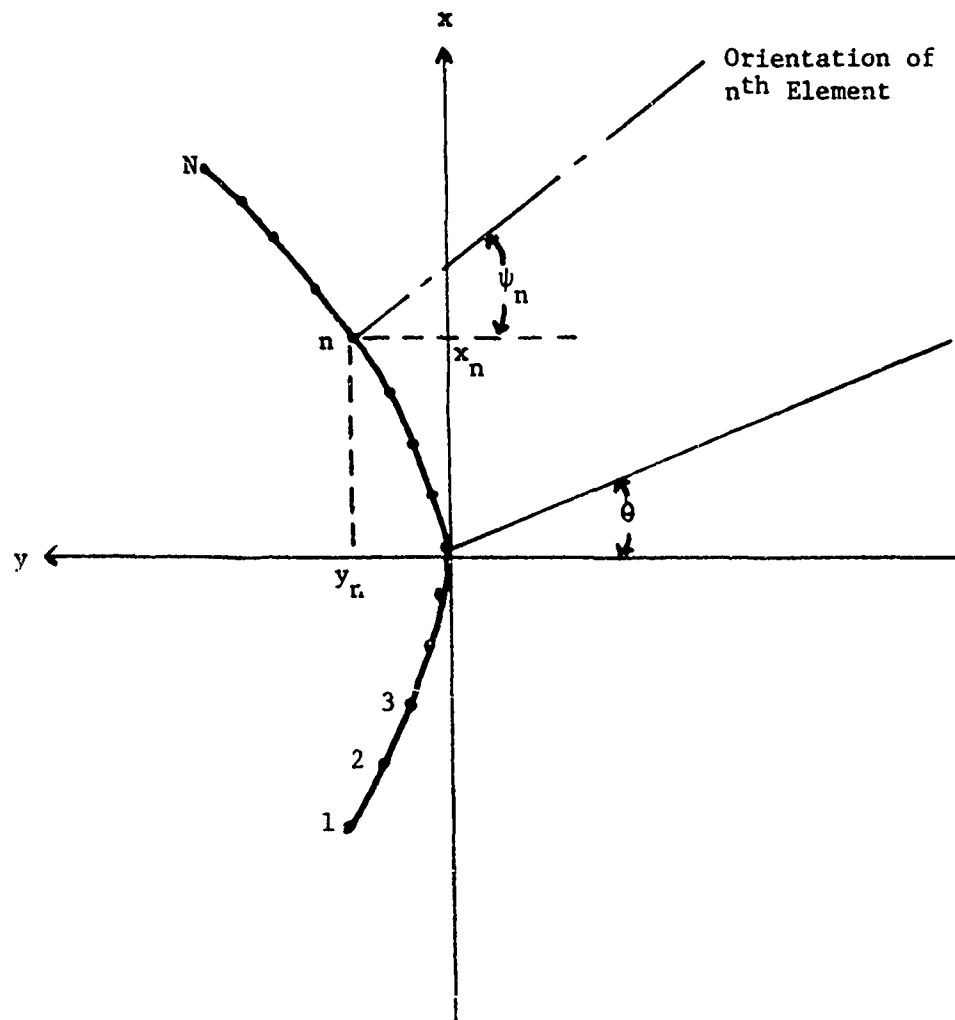


Figure 1. Coordinates of Conformal Array

noise field. If v_n denotes the noise voltage in the n th element channel from this external noise field, the elements of the covariance matrix, M , are

$$M_{mn} = \overline{v_m^* v_n} \quad (4)$$

To minimize the average sidelobe level, i.e., for a uniform hypothetical noise field:

$$M_{mn} = \int_{|\theta - \theta_s| > \theta_B/2} E_m^*(\theta - \psi_m) E_n(\theta - \psi_n) e^{\frac{2\pi i}{\lambda} [(y_m - y_n) \cos \theta - (x_m - x_n) \sin \theta]} d\theta \quad (5)$$

Let W denote a column vector of array weights w_n and S^* a column vector of steering signals s_n^* , where s_n is defined in Eq. (2). The optimum set of element weights is then given by

$$W = M^{-1} S^* \quad (6)$$

where M^{-1} is the inverse of the covariance matrix M . This set of array weights maximizes the ratio of main-beam gain, $G(\theta_s)$, to the average sidelobe level outside the angular region $(\theta_s - \theta_B/2, \theta_s + \theta_B/2)$.

In some cases it is desirable to reduce the sidelobes selectively in certain directions. For example, in high-PRF airborne radars, it is usually important to reduce the sidelobes at low elevation angles where ground clutter returns are received from short range. To reduce the sidelobes selectively, the integrand of Eq. (5) is multiplied by a variable density function $\rho(\theta)$. Lower sidelobe levels in the angular region $\theta_1 < \theta < \theta_2$ are obtained by setting $\rho(\theta) = 1$ outside this region and $\rho(\theta) > 1$ within this region. An example is given later to illustrate this case.

To reiterate, the steps in selecting a set of optimum array weights $\{w_n\}$ are:

- a. Definition of the problem. The element locations (x_n, y_n) , element orientations ψ_n , and element patterns E_n are defined.
- b. A desired scan angle θ_s and beamwidth θ_B , greater than the diffraction-limited beamwidth, are selected.
- c. Steering signals s_n^* are computed using Eq. (2).
- d. The covariance matrix for a hypothetical external noise field in the sidelobe region is computed using Eq. (5).
- e. The optimum array weights are computed by solving the system of linear equations, Eq. (6).

Using this technique for conformal array optimization, the optimum element weights and resulting antenna patterns were computed for a variety of cases. In all cases presented here the array elements are oriented normal to the surface of the array and cosine element patterns are assumed.

$$E_n(\theta) = \cos(\theta - \psi_n) \quad (7)$$

The array contains 40 elements spaced $\lambda/2$ apart along the parabola $y = 0.1x^2$. The hypothetical noise field assumed in computing the covariance matrix, M , is uniformly distributed between $-\pi/2 + \psi_1$ and $\pi/2 + \psi_N$, the entire θ interval visible to any array element, with $|\theta - \theta_s| < \theta_B/2$ excluded.

Three examples of conformal array patterns are shown in Figures 2 through 4 for scan angles of 0° , 20° , and 40° , respectively, from the axis of the parabola. The shape of the array surface is shown in Figure 2. The allowed beamwidth, θ_B , is shown on each curve. The scan angle (θ_s), number of elements (N), and element spacing in wavelengths are also indicated on the curves. The average sidelobe gain in the region $|\theta - \theta_s| > \theta_B/2$ is shown, normalized to the peak gain at $\theta = \theta_s$. These results show that, using this design technique, very low sidelobe levels can be achieved with conformal arrays on surfaces with significant curvature.

Some broadening of the main beam must be allowed to achieve the necessary weight tapering for low sidelobes. A comparison of Figures 3 and 5 illustrates the effect of main beamwidth on sidelobe level. The parameters are the same in these two cases except for allowed beamwidth, which is 18° in Figure 3 and 15° in Figure 5. Reducing the beamwidth from 18° to 15° results in a 7.3 dB increase in average sidelobe level.

In the preceding examples the hypothetical interference assumed in computing the covariance matrix was uniformly distributed in the sidelobe region. The sidelobes can be reduced more in selected angular regions by increasing the interference assumed in these regions. Since the array weights computed with this program maximize the ratio of main-beam gain to total interference (for the hypothetical interference distribution) in the output, lower sidelobes are obtained in directions of greater interference. This is illustrated in Figure 6. The parameters for this case are those of Figure 5. Note in Figure 5 that a large sidelobe occurs in the region from -135° to -100° . The lighter curve in Figure 6 is a replica of the pattern of Figure 5. The heavier curve was obtained by assuming an interference field 40 dB greater in the region of $\theta < -90^\circ$, as indicated in Figure 6. Note that this reduced the sidelobe level in this region to a level below -60 dB. The sidelobes increased at other angles when the weights were changed to selectively reduce sidelobes in this region.

The effects of mutual coupling between array elements was not considered in any of the preceding examples. To include the mutual coupling effect, the element patterns $E_n(\theta - \psi_n)$ would be replaced by measured element patterns when all elements are present and terminated

MAIN BEAMWIDTH(DEG)= 14.0

SCAN ANGLE(DEG)= 0.0

NUMBER OF ELEMENTS= 40

COSINE ELEMENT PATTERNS

ELEMENTS NORMAL TO SURFACE

ELEMENT SPACING= .50

AVE S/L(DB)= -53.7

SURFACE- Y= 0.00 X+ .10 X**2

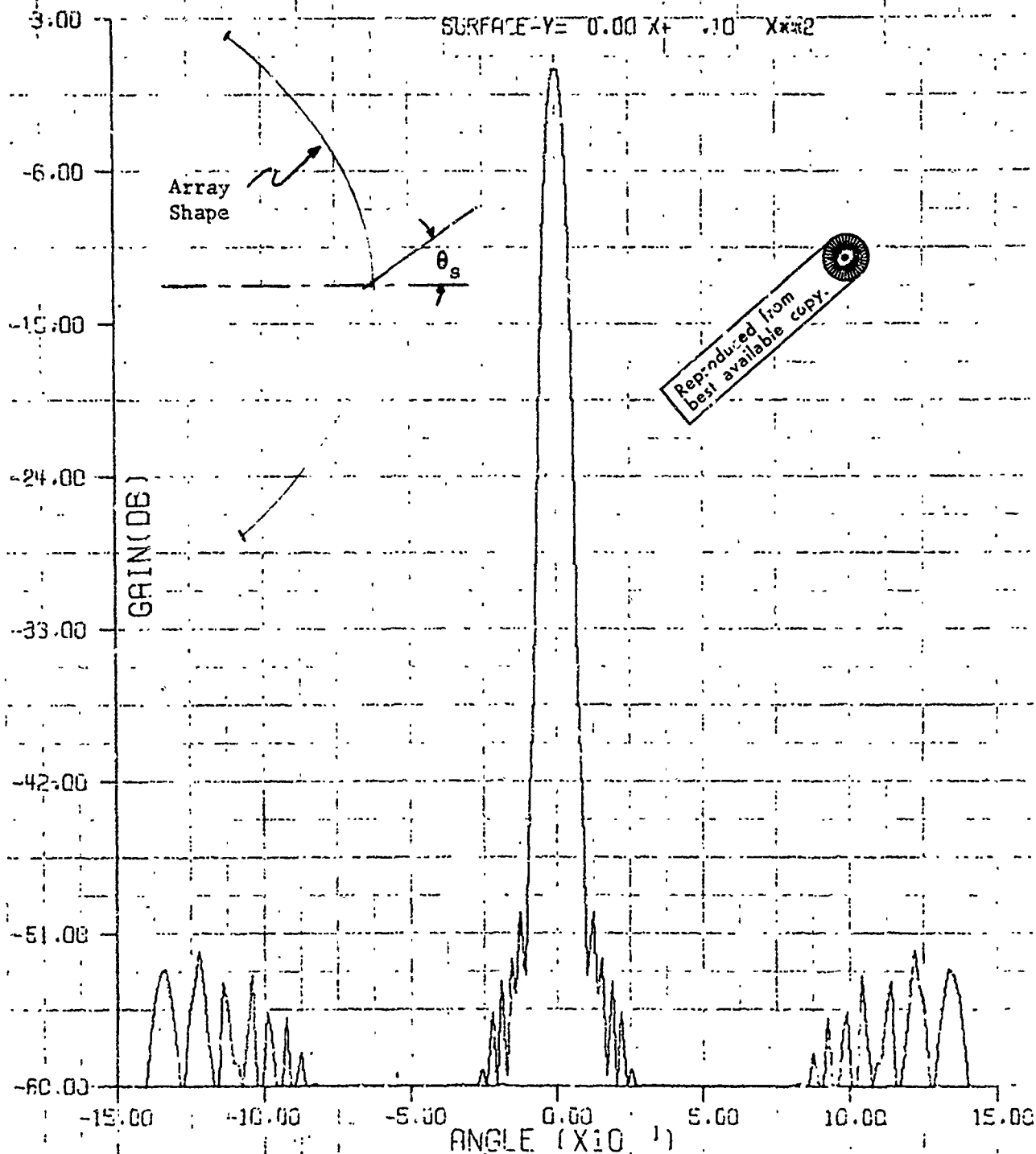


Figure 2. Conformal Array Gain

MAIN BEAMWIDTH(DEG)= 18.0

SCAN ANGLE(DEG)= 20.0

NUMBER OF ELEMENTS= 40

COSINE ELEMENT PATTERNS

ELEMENTS NORMAL TO SURFACE

ELEMENT SPACING= .50

AVE S/L(DB)= -58.0

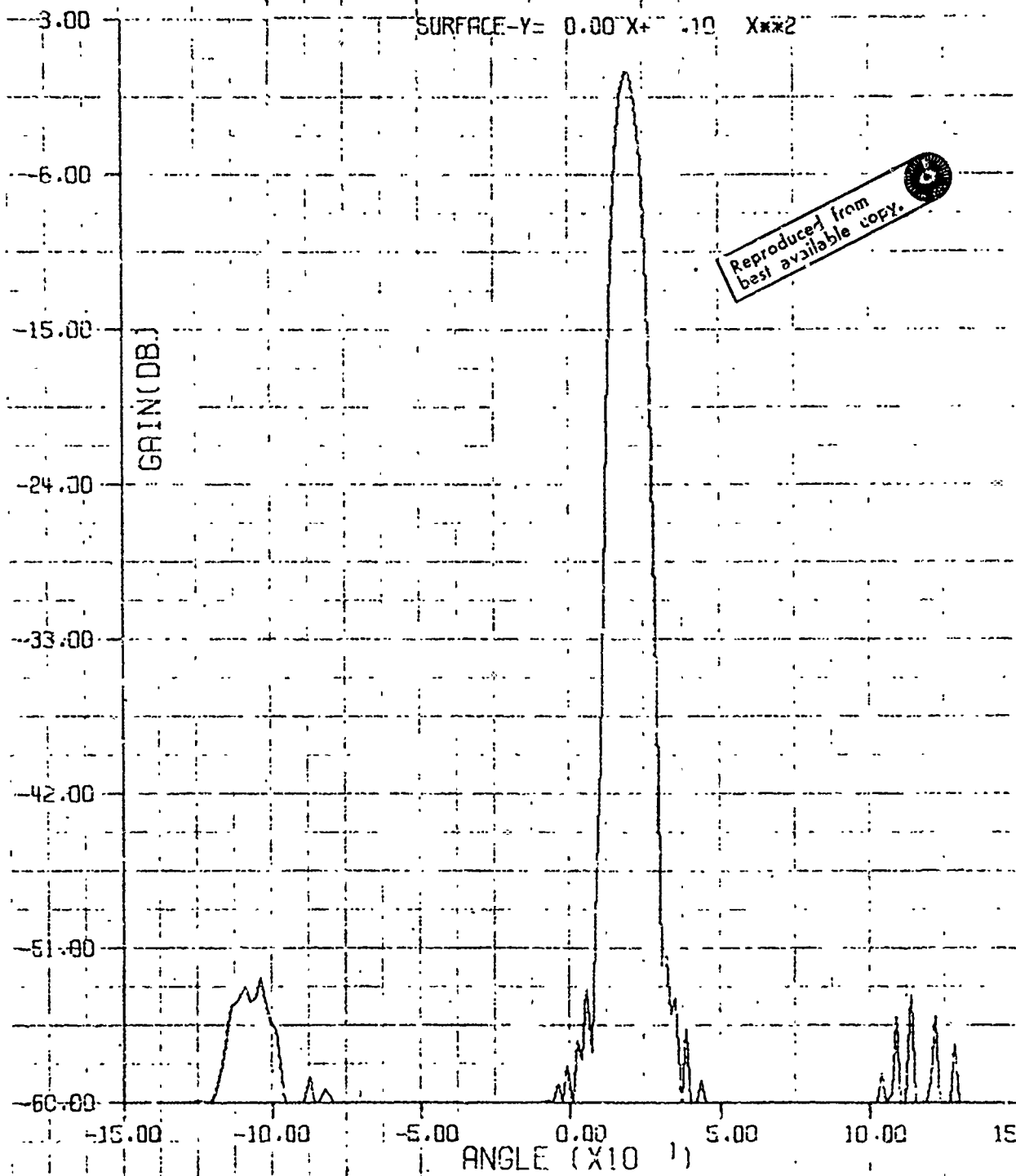


Figure 3. Conformal Array Gain

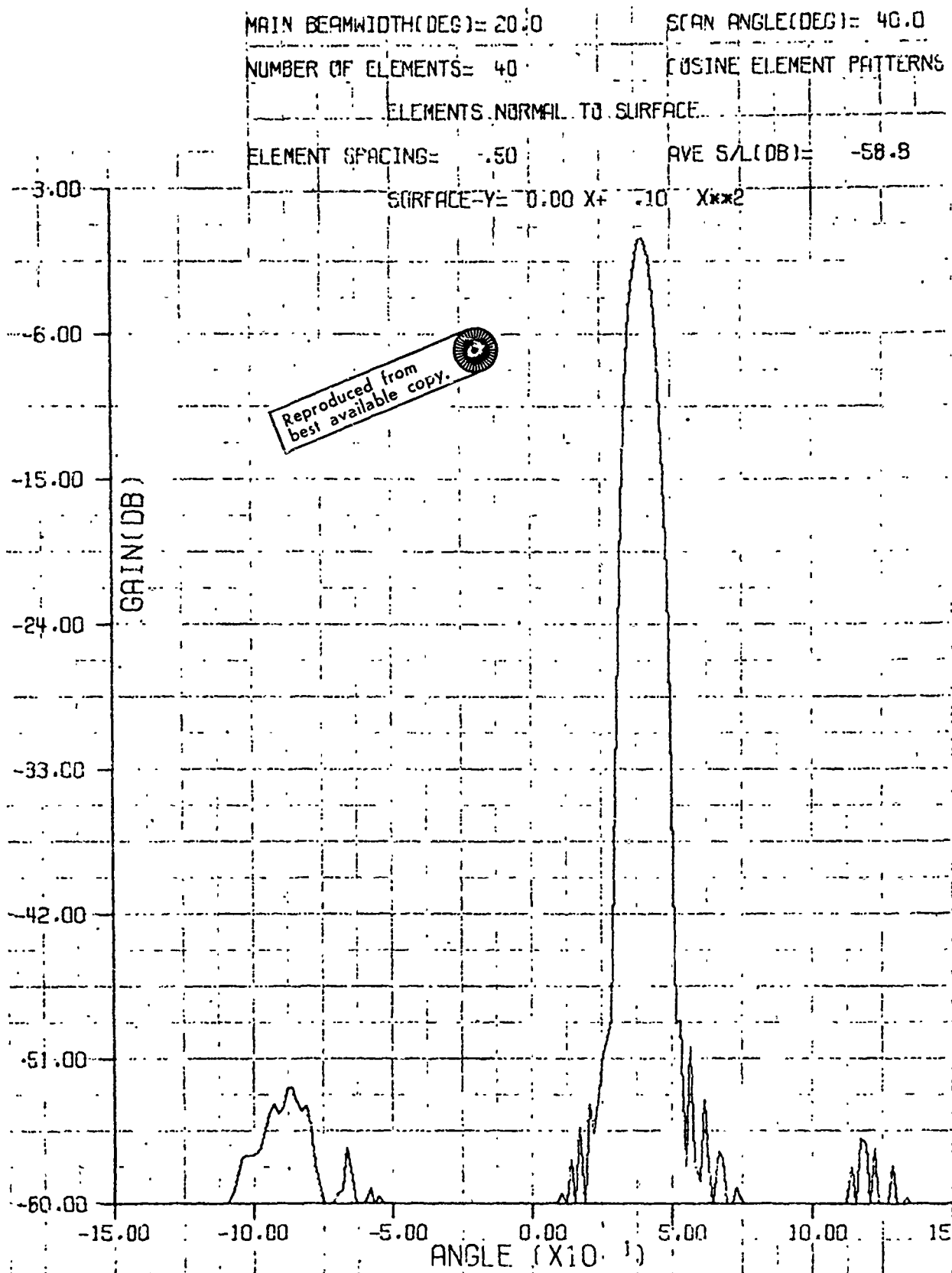


Figure 4. Conformal Array Gain

MAIN BEAMWIDTH(DEG)= 15.0

SCAN ANGLE(DEG)= 20.0

NUMBER OF ELEMENTS= 40

COSINE ELEMENT PATTERNS

ELEMENTS NORMAL TO SURFACE

ELEMENT SPACING= .50

AVE S/L(DB)= -50.7

SURFACE-Y= 0.00 X+ .10 X**2

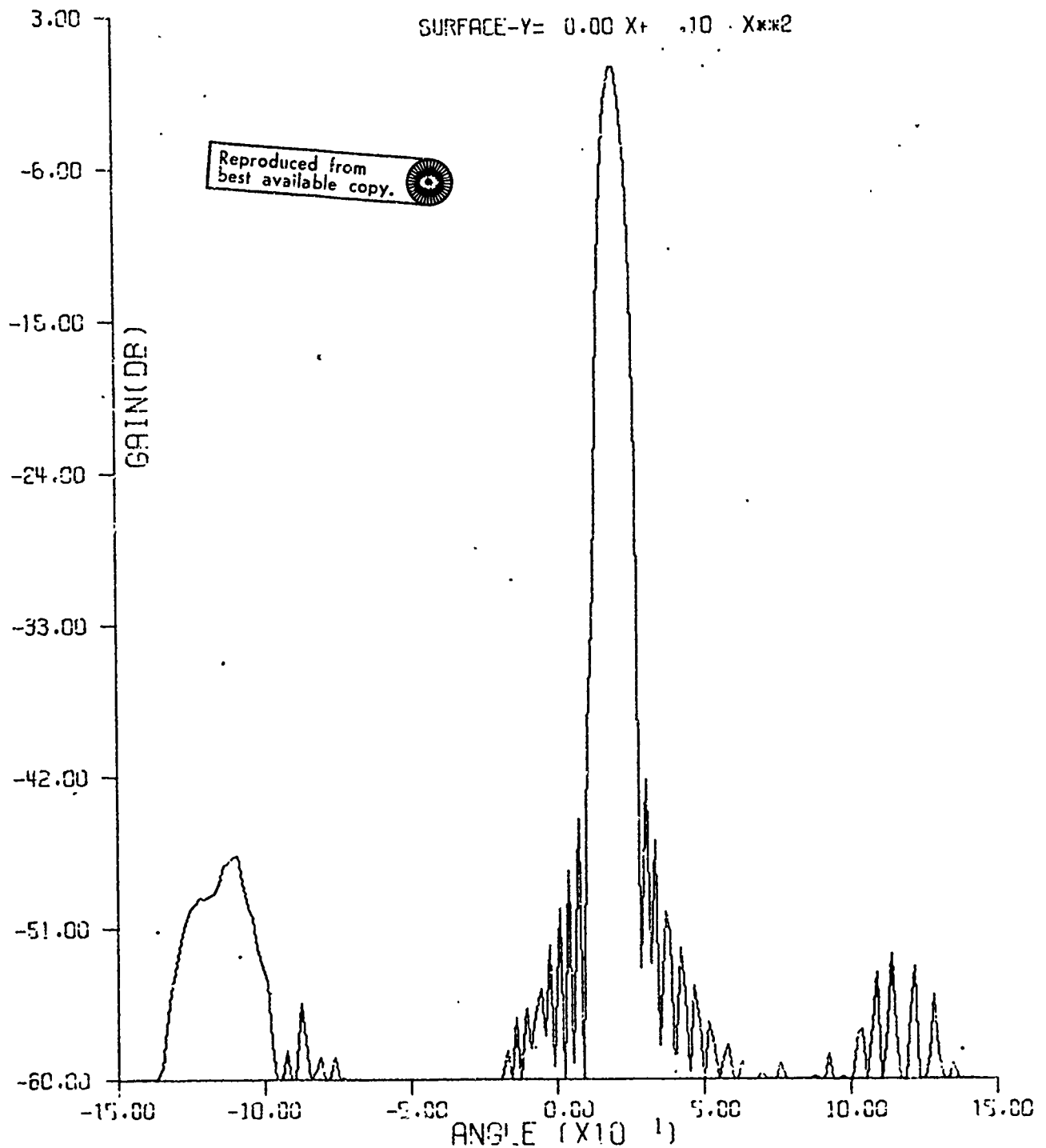


Figure 5. Conformal Array Gain

MAIN BEAMWIDTH(DEG)= 15.0

SCAN ANGLE(DEG)= 20.0

NUMBER OF ELEMENTS= 40

COSINE ELEMENT PATTERNS

ELEMENTS NORMAL TO SURFACE

ELEMENT SPACING= .50

AVE S/L(OB)= -41.2

SURFACE-Y= 0.00 X+ .10 X**2

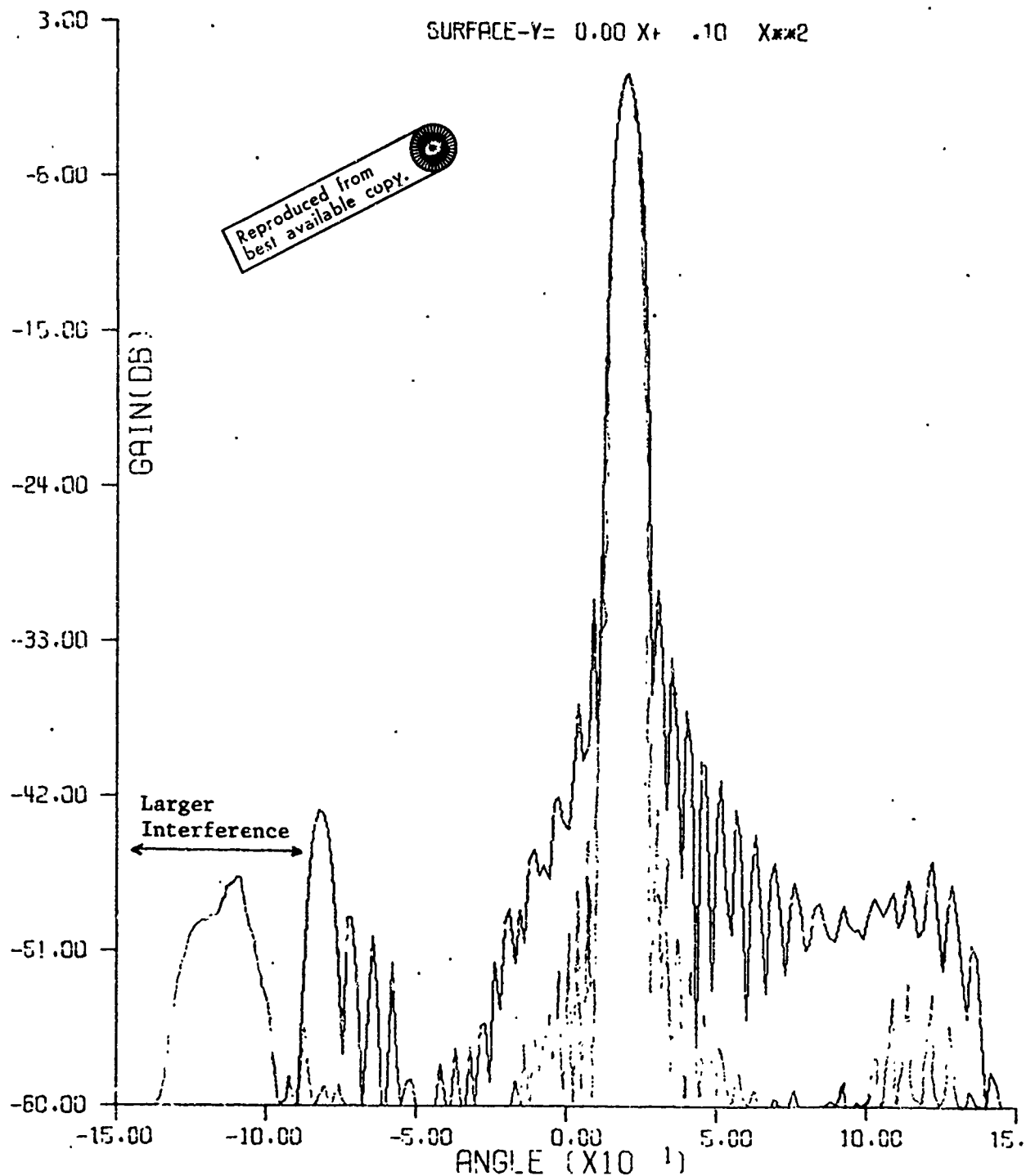


Figure 6. Conformal Array Gain

in their respective impedances. With this one modification, the theory outlined here can be used to design conformal array antennas optimized with mutual coupling effects included.

3. ADAPTIVE CONFORMAL ARRAYS

A method of adaptively reducing the antenna sidelobe level in a coherent airborne radar was described in [4]. This technique, ADAPTAR (Adaptive AMTI Radar), can also be applied to conformal array antennas. Earlier studies [4,5] have shown that this technique can provide a significant reduction in sidelobe level in airborne radars employing a linear array antenna. The adaptive receiving array senses and compensates for such important effects as nonuniform distributions of clutter, discrete interference sources or jammers in the sidelobe region, and aircraft structure in the near-field of the antenna.

A functional block diagram of ADAPTAR, applicable to either linear or conformal array antennas, is shown in Figure 7. The solid lines in the figure represent column vectors of complex quantities, e.g., V is $(v_1, v_2, v_3, \dots, v_N)^T$, where v_n is the complex voltage received in the n th array element channel and T denotes the transpose. Each v_n is multiplied by a complex weight, w_n . Both phase and amplitude information are retained in these variables. The array output is $W^T V$ or

$$\sum_{n=1}^N w_n v_n$$

where N is the number of elements in the array. Each of the weights, w_n , is controlled adaptively by a separate control loop similar to a sidelobe cancellation circuit.

Each element output is passed through a main-beam reject filter, labeled F_1 in Figure 7. These filters process several consecutive pulses from each range cell to remove the main-beam clutter return. The remaining input consists primarily of sidelobe clutter return and jamming or other interference. The signal returns from moving targets will also be passed by the filters F_1 , but do not contribute significantly to the adaptive loop inputs since these signals are typically of very short duration. In effect, the control loops cross-correlate the v_n in each channel with the output $W^T V$ to obtain the output U of Figure 7, which then controls the array weights. Steering signals, S^* , are also introduced in the loops to control the main-beam scan direction. Except for these steering signals, the adaptive loops are the same for conformal arrays as for linear arrays.

A duplexer is required in each element channel between filters F_1 and the array elements when the same antenna array is used for transmitting and receiving. A separate transmitter (e.g., solid-state module) could be used for each element or a corporate feed to divide the power from a single transmitter between the N array elements.

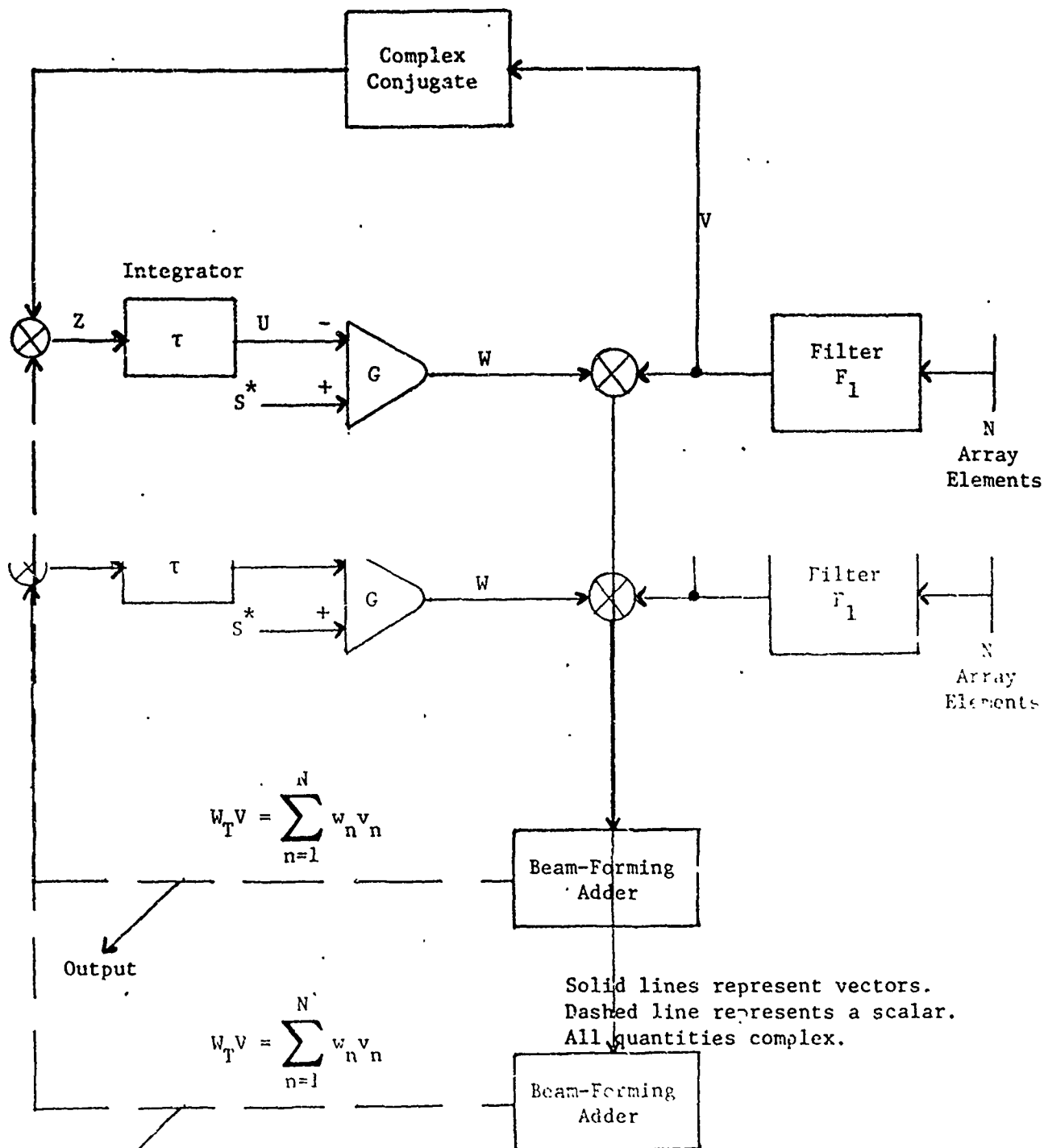


Figure 7. Vector Representation of Adaptive Receiving Array

Solid lines represent vectors.
Dashed line represents a scalar.
All quantities complex.

The average array weights in an adaptive receiving array satisfy the equation*

$$\tau \dot{W} + (GM + I)W = GS^* \quad (8)$$

where

τ = time constant of the integrator

W = column vector of array weights

G = gain of amplifiers in control loops

M = covariance matrix of noise at loop inputs

$M_{mn} = E\{v_m^* v_n\}$ = elements of M

I = identity matrix

S^* = column vector of steering signals

For large gain, G , the array weights approach the steady-state solution

$$W = M^{-1} S^* \quad (9)$$

This is the optimum set of weights for detecting a signal from the direction matched to S^* in a noise field represented by the covariance matrix M .

Since the covariance matrix, M , is Hermitian (i.e., $M_{mn} = M_{nm}^*$), there exists a unitary transformation which diagonalizes M and transforms Eq. (8) to a set of N independent first-order linear differential equations. This system of equations has the form

$$\tau \dot{\omega} + (G\Lambda + I)\omega = G\mathcal{S}^* \quad (10)$$

where Λ is a diagonal matrix with elements equal to the eigenvalues, λ_n , of M . The solution to this system of equations is

$$\omega_n = \frac{\mathcal{S}_n^*}{\left(\lambda_n + \frac{1}{G}\right)} + \left(\omega_{n0} - \frac{\mathcal{S}_n^*}{\left(\lambda_n + \frac{1}{G}\right)} \right) e^{-\frac{G\lambda_n + 1}{\tau} t} \quad (11)$$

where

ω_n = weights in transformed space

\mathcal{S}_n^* = steering signals in transformed space

*The reader is referred to [3] for a derivation of this equation and a detailed theory of adaptive arrays. A more complete discussion of ADAPTAR and simulation results obtained for this technique with linear array antennas are contained in [4].

ω_{n0} = initial value of ω_n

This analytic solution to the system of equations was used to obtain the transient results presented later in this section.

As noted above, the major difference between linear adaptive arrays and conformal adaptive arrays is the difference in steering signals. In both cases, the steering signals s_n^* are matched to an incident plane wave from the desired scan direction. In an equally spaced linear array the steering signals have equal magnitudes and a constant phase shift between elements. In a conformal array, the optimum set of steering signals is given by Eq. (2). The amplitudes of the steering signals in this case are proportional to the element patterns in the scan direction. The phasor terms in Eq. (2) align the different received signals such that the signals from the different elements add in-phase when $W = S^*$. This is the optimum set of array weights when there is no external interference and the system is limited by receiver noise of equal power in all the element channels.

As reported in [4], simulations were performed for a large number of linear adaptive array cases. These simulation results were compared with the transient solutions given by Eq. (11) and found to correspond very closely provided control loop noise in the adaptive loops is small. It has also been shown [3] that the total noise in the array output is increased due to control loop noise (i.e., random fluctuations in the array weights, w_n) by the factor

$$f = 1 + \frac{G}{2\pi} \sum_{n=1}^N \lambda_n \quad (12)$$

When this factor is near unity, e.g., $f < 1.4$, the simulation and analytic solutions (Eq. (11)) show close correspondence. The sidelobe levels in the simulations were slightly higher than the computed sidelobes due to this noise contribution. In the transient results presented here, the loop noise factor, f , was set equal to 1.3.

The steady-state and transient performance of ADAPTAR in conformal array antennas, based on the above equations, was analyzed for a variety of cases. Steps in the computation are as follows.

- a. Definition of the problem. The element locations (x_n, y_n), orientations (ψ_n), and element patterns (E_n) are selected. Cosine element patterns with the elements oriented normal to the array surface were assumed in all cases.
- b. Selection of a scan angle (θ_s) and clutter-free main beamwidth (θ_B). It is assumed that the main-beam clutter at angles $|\theta - \theta_s| < \theta_B/2$ is removed completely by the filters F_1 .*

* Examples are given in [4] of physically realizable filters F_1 and the effect of imperfect main-beam clutter rejection on array performance.

- c. Using Eq. (2), steering signals for the adaptive array, s_n^* , are computed.
- d. The transmit antenna pattern is computed, assuming weights s_n^* are used on transmit.
- e. Assuming a uniform clutter distribution in θ , illuminated by the transmit pattern, the covariance matrix M is computed. Zero clutter is assumed for $|\theta - \theta_s| < \theta_B/2$.
- f. The initial array weights on receive are set equal to s_n^* .
- g. The problem is transformed to normal coordinates, transforming the covariance matrix to a diagonal matrix of ordered eigenvalues. The unitary transformation, containing the ordered set of eigenvectors, is applied to the steering signals and initial array weights to obtain $\{\omega_{n0}\}$ and $\{\omega_n^*\}$.
- h. The eigenvalues are summed and G/T selected so that $f = 1.3$ in Eq. (12).
- i. A number of loop iterations is selected (corresponding to the processing of returns from this number of contiguous range cells after filtering by F_1) and the transient weights are computed from Eq. (11).
- j. The steady-state weights are computed, both in normal coordinates by setting $t = \infty$ in Eq. (11) and by inversion of the original covariance matrix using Eq. (9). These results, after transformation of the ω_n back to array coordinates, are printed for comparison as a check on the computation.
- k. The antenna patterns corresponding to the original weights ($\omega_n = s_n^*$), the transient weights (again transformed back to ω_n coordinates), and the steady-state weights are computed and plotted.

Results obtained in three cases are shown in Figures 8 through 10. In each example, the array contains 20 elements spaced $\lambda/2$ along the surface. The scan angle and equation of the array surface are indicated on each curve. In these examples, main beamwidth is the angle from which F_1 removes all clutter. Three curves of antenna gain are shown in each figure. The curve marked with circles is the transmit antenna gain and the initial pattern of the receiving array. The curve marked with squares is the pattern obtained with optimum receiving array weights. The third curve, marked with triangles, represents the transient response of the adaptive array after a specified number of independent samples of the input noise process have been processed. This number of loop iterations, corresponding to a number of contiguous range resolution cells in a pulsed radar, is indicated in parentheses after "transient." The average sidelobe level for $|\theta - \theta_s| > \theta_B/2$ is shown for the

MAIN BEAMWIDTH(DEG)= 25.0

SCAN ANGLE(DEG)= 0.0

NUMBER OF ELEMENTS= 20

COSINE ELEMENT PATTERNS

ELEMENTS NORMAL TO SURFACE

ELEMENT SPACING= .50

AVE S/L(DB)= -30.6 INITIAL

SURFACE-Y= 0.00 X+ .10 X**2

-49.3 TRANSIENT (5000)

-55.3 STEADY STATE

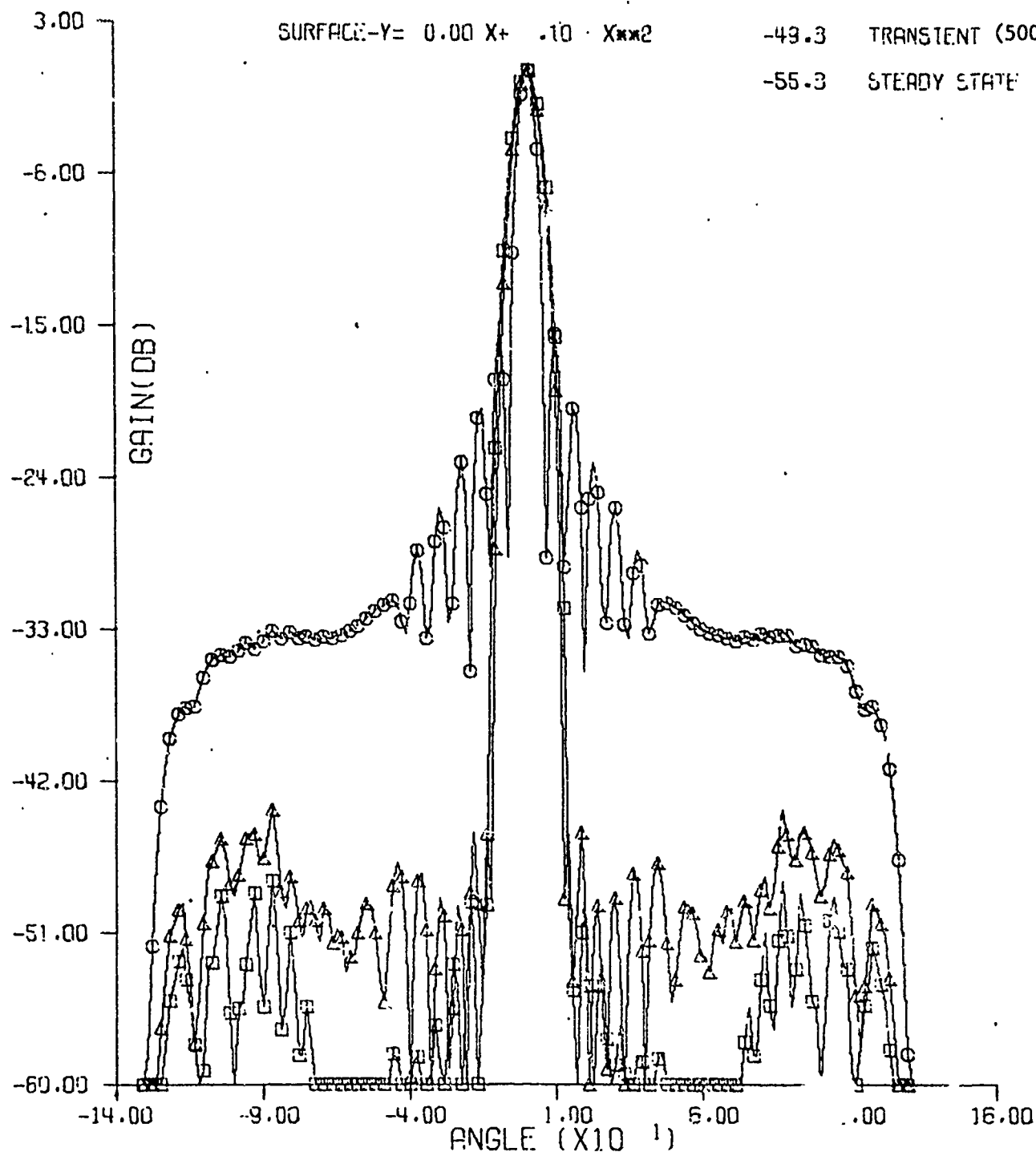


Figure 8. Conformal Adaptive Array Gain

MAIN BEAMWIDTH(DEG)= 30.0

SCAN ANGLE(DEG)= 20.0

NUMBER OF ELEMENTS= 20

COSINE ELEMENT PATTERNS

ELEMENTS NORMAL TO SURFACE

ELEMENT SPACING= .50

AVE S/L(DB)= -30.4

INITIAL

SURFACE-Y= 0.00 X+ .10 X**2

-47.5

TRANSIENT (5000)

-52.7

STEADY STATE

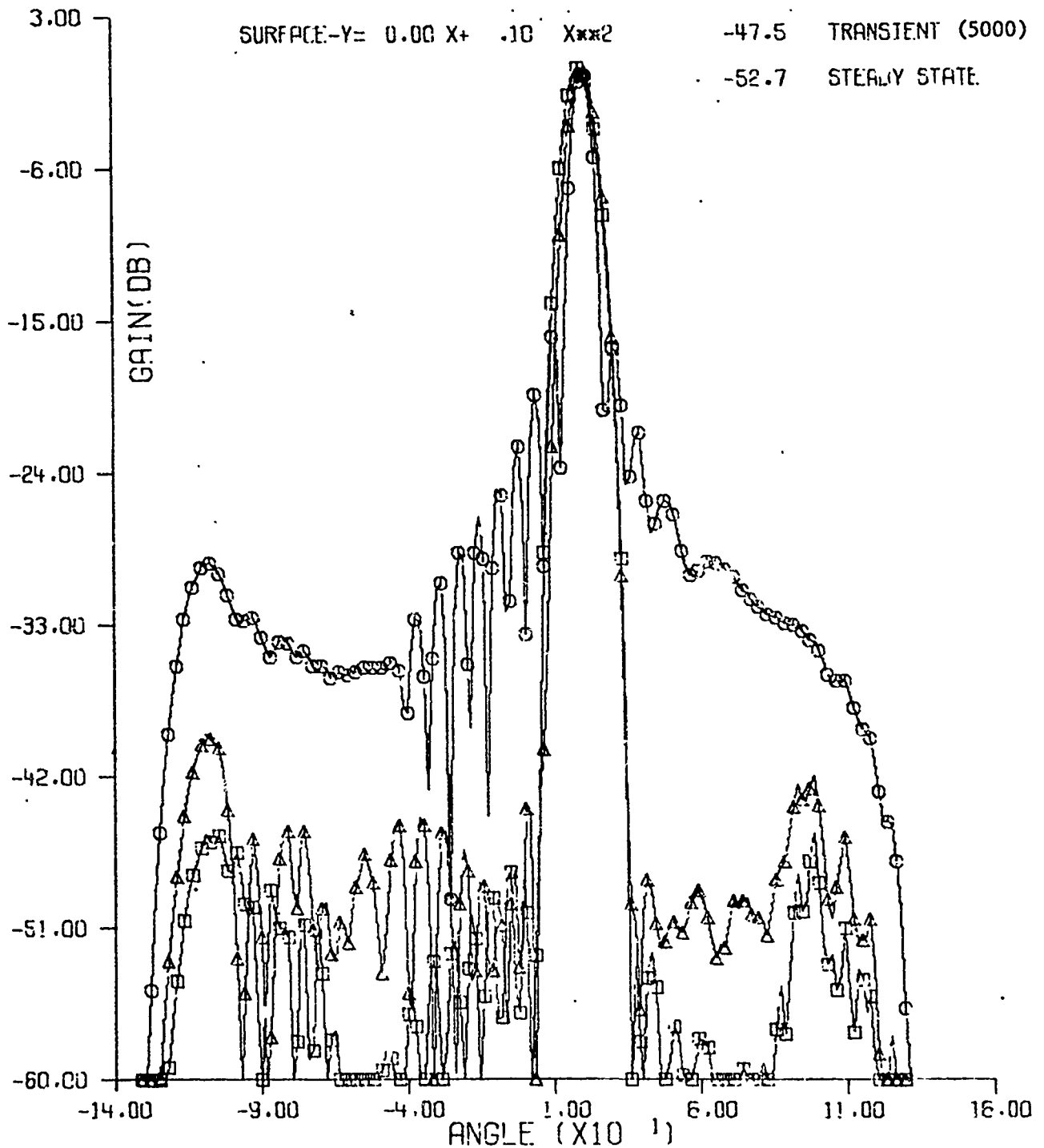


Figure 9. Conformal Adaptive Array Gain

MAIN BEAM ANGLE(DEC)= 40.0

SCAN ANGLE(DEC)= 40.0

NUMBER OF ELEMENTS= 20

COSINE ELEMENT PATTERNS

ELEMENTS NORMAL TO SURFACE

ELEMENT SPACING= .50

AVE S/L(1B)= -29.6 INITIAL

SURFACE-Y= 0.00 X= .10 Xx2

-43.8 TRANSIENT (5000)

-49.6 STEADY STATE

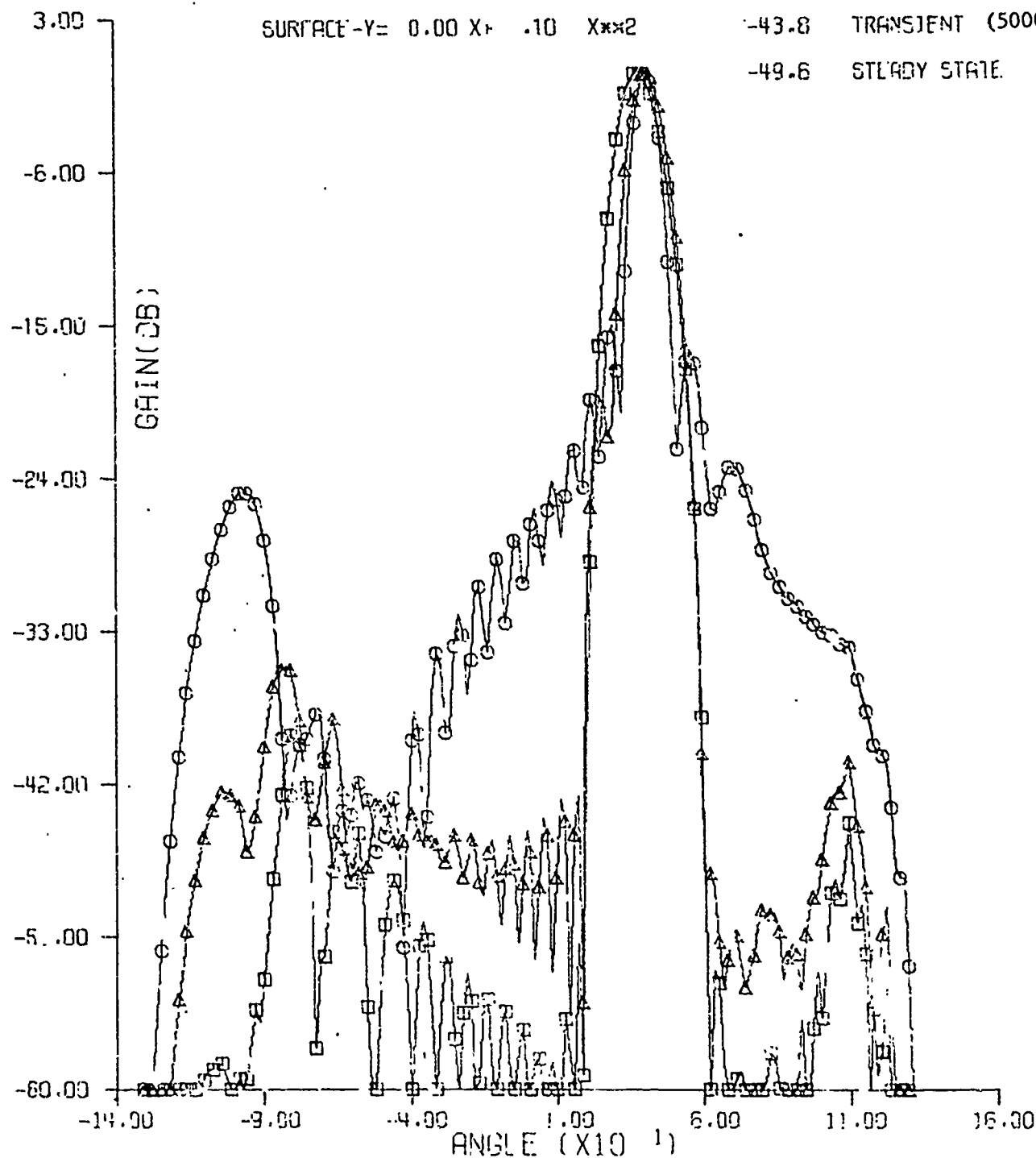


Figure 10. Conformal Adaptive Array Gain

initial, transient, and steady-state antenna patterns. In these examples the average sidelobe levels refer to the one-way receiving patterns.

The scan angle relative to the axis of the parabola is 0° in Figure 8, 20° in Figure 9, and 40° in Figure 10. In each of these examples, the transient response curve was obtained after 5000 samples of data were processed by the adaptive array. A substantial reduction in sidelobe level was obtained in each case. Additional examples of adaptive conformal array performance are presented in [6]. The effect on the interference-free beamwidth, θ_B , on transient response is also discussed in this reference.

4. ADAPTIVE COMPENSATION FOR MISSING ARRAY ELEMENTS

One major advantage of adaptive receiving array antennas is the ability of these systems to sense the failure of array elements and compensate for the missing elements. The array weights are controlled, as shown in Figure 7, by adaptive loops which cross-correlate the array output with the signals in the individual element channels. When the array weights are near-optimum values, the noise residue in the output is generally small. If one element fails, the output noise increases. Each adaptive control loop senses this increase and changes its w_n by an amount proportional to the cross-correlation between the signal in its channel and the noise residue. The array weights readjust to values which minimize the noise output for the remaining array elements.

This capability of adaptive arrays is illustrated in Figures 11 through 13. The pattern obtained with a parabolic array of 40 elements, with optimum weights applied to all elements is shown in Figure 11 as a reference case. The pattern for the same array and element weights, except that the weight on element 11 is zero, is shown in Figure 12. This pattern would result from the outage of the 11th array element. Figure 13 shows the pattern for the same array with element 11 missing and the remaining weights reoptimized. Note that an adaptive system would reduce the average sidelobe significantly in this case, particularly in the angular region from 0° to -100° . Other examples of missing element compensation in adaptive arrays are presented in [6].

5. SUMMARY AND CONCLUSIONS

A method of selecting optimum element weights for a conformal array antenna on an arbitrarily shaped surface was described in Section 2. Antenna patterns obtained using this design technique were presented for a variety of cases and show that, for moderately curved surfaces, low sidelobe levels can be achieved in conformal arrays.

In coherent airborne radars, ADAPTAR can be used with conformal array antennas to adaptively reduce sidelobes and maximize the ratio of main-beam gain to sidelobe clutter. An example is presented in Section 3 which shows that, with a moderately curved array antenna, good steady-state and transient performance can be obtained with this technique.

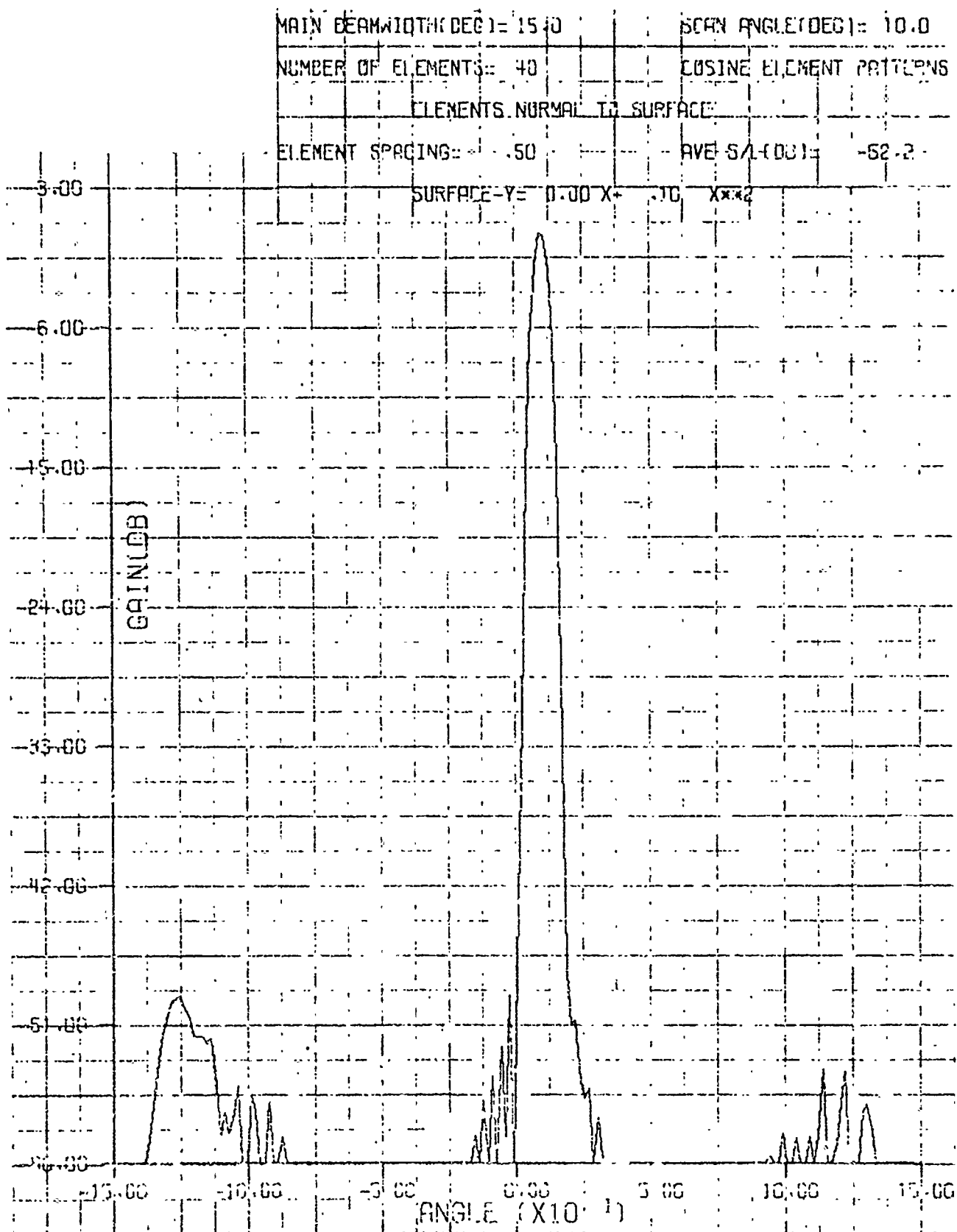


Figure 11. Conformal Array Gain - Reference Case

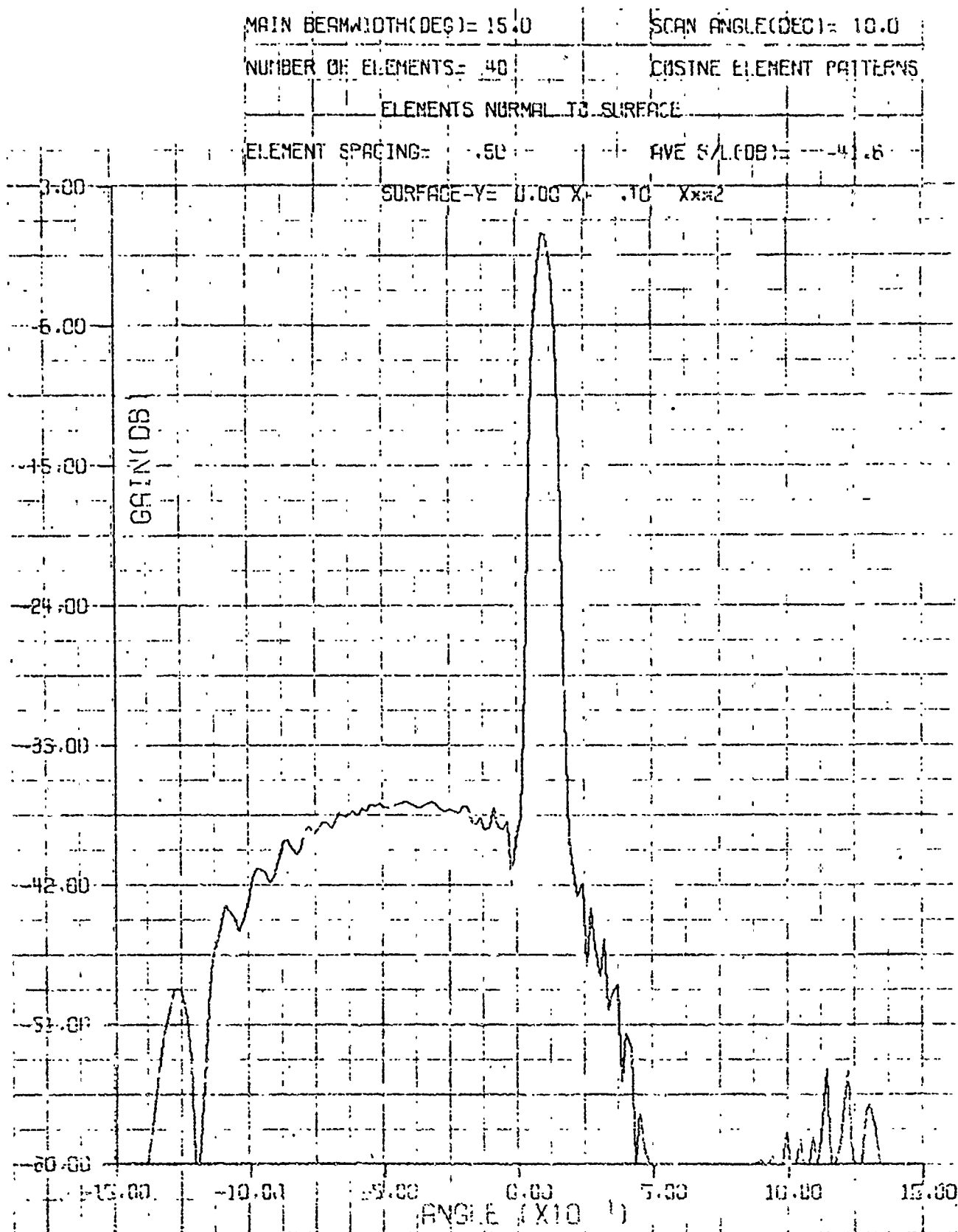


Figure 12. Conformal Array Gain - $w_{11} = 0$

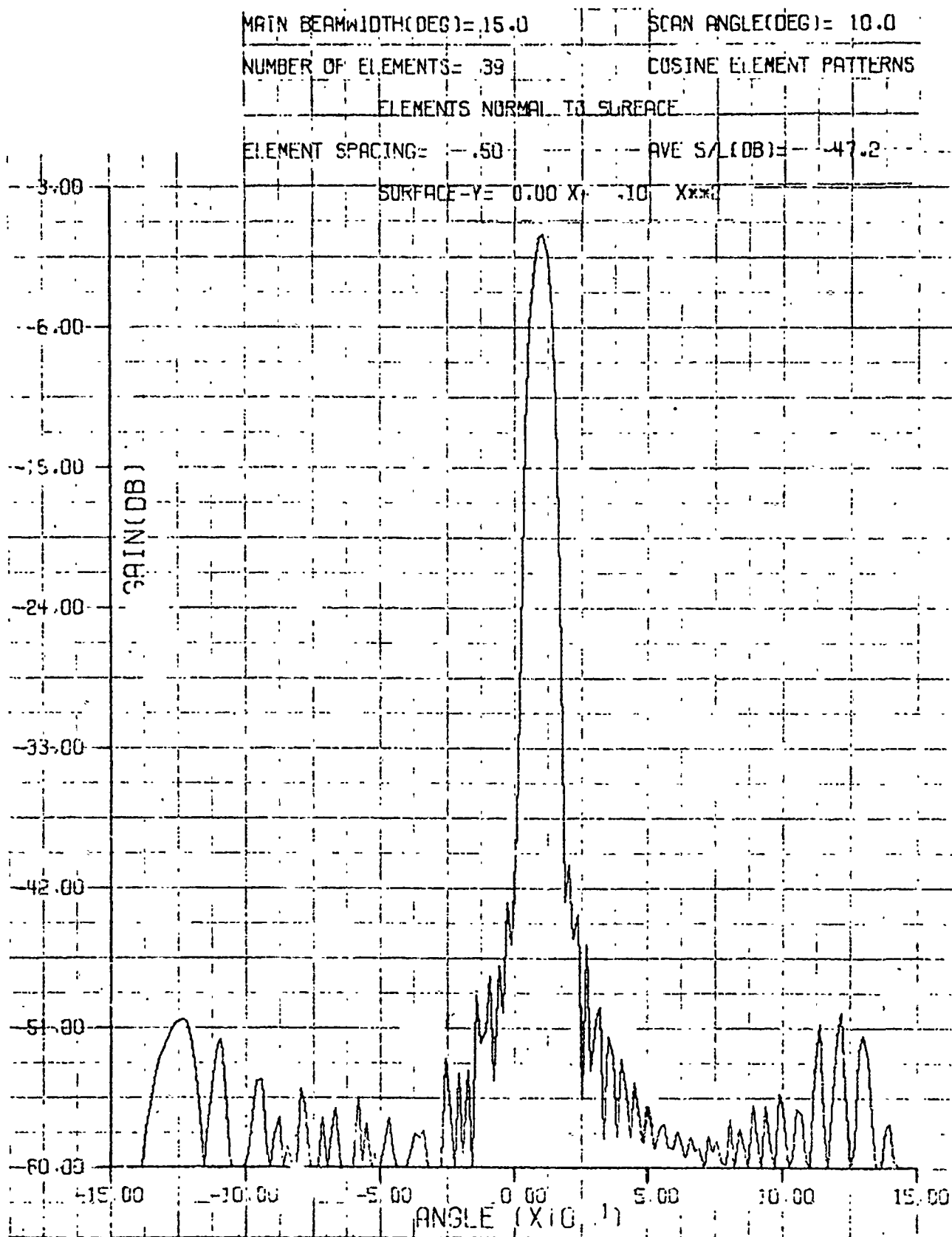


Figure 13. Conformal Array Gain - Element 11 Missing

One important advantage of adaptive array antennas is the ability of these systems to compensate for element failures. The example of Section 4 illustrates the significant reduction in sidelobe levels that can be achieved by reoptimization of the remaining element weights.

REFERENCES

1. S. P. Applebaum, "Adaptive Arrays," Syracuse Univ. Research Corp. Report SPL-769, June 1964.
2. B. Widrow, et al., "Adaptive Antenna Systems," Proc. IEEE, December 1967, pp. 2143-2158.
3. L. E. Brennan, I. S. Reed, and E. L. Pugh, "Control Loop Noise in Adaptive Array Antennas," IEEE Trans. AES, March 1971.
4. "Adaptive Array Techniques for Coherent Airborne Radars (U)," Technology Service Corp. Report TSC-PD-030-1, Final Report on Contract N00019-69-C-0662, 26 February 1970. Confidential
5. "ADAPTAR Space-Time Processing in Airborne Radars," Technology Service Corp. Report TSC-PD-061-2, Final Report on Contract N00019-70-C-0387, 24 February 1971.
6. L. E. Brennan, "Conformal Array Antennas," Technology Service Corp. Report TSC-PD-072-1, Final Report on Contract N00019-71-C-0163, October 1971.

32. A TECHNIQUE FOR CONTROL OF CONFORMAL ARRAYS

by

G. V. VAUGHN

Code 2330

Naval Electronics Laboratory Center
San Diego, California 92152

for

ARRAY ANTENNA CONFERENCE

22, 23, 24 February 1972

Naval Electronics Laboratory Center
San Diego, California 92152

32-1a

INTRODUCTION

Conventional, mechanically scanned antennas are not adequate for future high-speed aircraft and missile systems, because of their poor beam agility and insufficient multiple-beam capability. The physical adaptation of conventional-array antennas to the airframe may also cause problems. One possible solution to these problems is a phased-array antenna that conforms to the surface of the aircraft.

One of the most important problems to be overcome in the implementation of conformal arrays is the control of the steering of the beams. It may be possible to theoretically compute the phase and amplitude distributions for the elements to give desirable beam radiation patterns, but if the hardware and/or software have not been constructed, then these distributions and the theory have no significance. The "conformal" arrays that have been investigated in the past have usually had simple shapes such as the cylindrical and conical arrays. The techniques developed to control these arrays depend on the properties of that particular shape. In this report a technique for controlling the phase of the elements will be described that may be used on general conformal surfaces.

PHASE CONTROL OF CONFORMAL ARRAYS ON SPECIAL SURFACES

The complexity of the hardware necessary to scan the beams of conformal phased arrays increases greatly as the geometry of the surface becomes more complex. Some examples in two dimensions are used to illustrate the point.

In the simplest case, a linear array with equally spaced elements, the phase needed at element n (fig. 32-1) is given by

$$\psi_n = (n - 1)d_r \cos(\phi)$$

where

n = element number

d_r = spacing between elements in radians

ϕ = angle scanned from endfire

This excitation may be implemented with a single adder at each element. The first element is the reference element; the second has phase equal to $d_r \cos(\phi)$. This value is either computed in real time or stored. The phase of each succeeding element is achieved by adding $d_r \cos(\phi)$ to the preceding element phase. Thus, to properly phase these elements, an adder at each element and a generator for $d_r \cos(\phi)$ are required.

The next level of complexity is the circular array in which the elements are spaced at equal angular increments (fig. 32-2). The phasing required is given by

$$\psi_n = \rho_r \cos[\phi - (n - 1)\delta]$$

where

ρ_r = radius of circle in radians

n = element number

δ = angular spacing of elements

ϕ = beam pointing direction

In this case the phasing required is calculated by evaluating $\cos[\phi - (n - 1)\delta]$ for each element. Thus, there are n times as many calculations as in the linear array case.

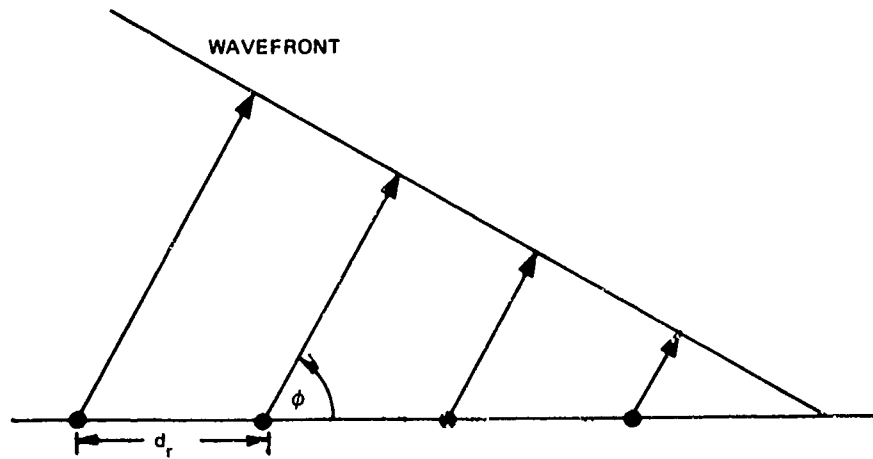


Figure 32-1. Geometry of linear array scanned ϕ degrees from endfire.

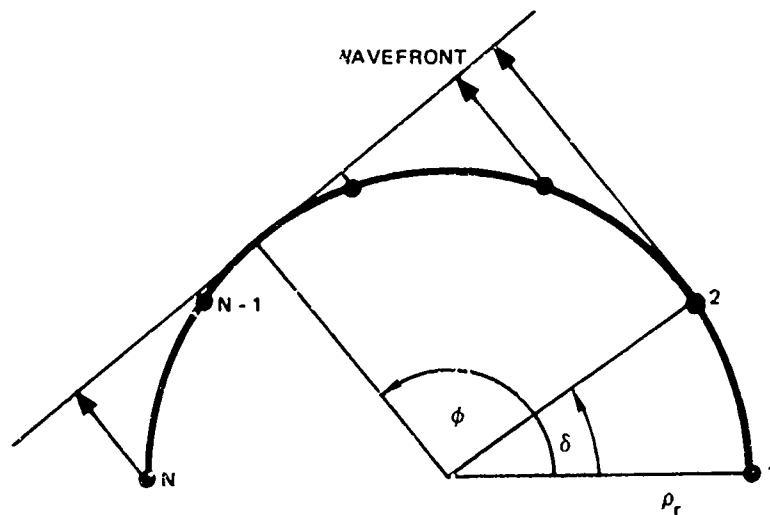


Figure 32-2. Geometry of circular array scanned to ϕ degrees. Elements are spaced δ degrees apart.

CONFORMAL ARRAYS ON GENERAL SURFACES

Now consider an array on a general surface (fig. 32-3). The position of the element is given by the components in some convenient coordinate system. The phasing necessary to scan the beam in the chosen direction, ϕ , is given by

$$\psi_n = \pm \sqrt{(X_n - XX)^2 + (Y_n - YY)^2} \cdot 2\pi/\lambda$$

where

$$XX = [(X_1 \tan^2 \phi + X_n) + (Y_n - Y_1) \tan \phi] / (1 + \tan^2 \phi)$$

$$YY = Y_1 + (XX - X_1) \tan \phi$$

ϕ = beam scanning direction

X_1, Y_1 = coordinates of reference element

X_n, Y_n = coordinates of n^{th} element

These equations are discussed in the Appendix.

After this expression has been evaluated, a test must be performed to determine the sign of the square-root term, that is, whether the phase is advanced or retarded with respect to the reference element.

Thus, it is seen that a complicated expression must be calculated for each element for each beam pointing direction. The cost of hardware and software required to implement this configuration could make the system impractical.

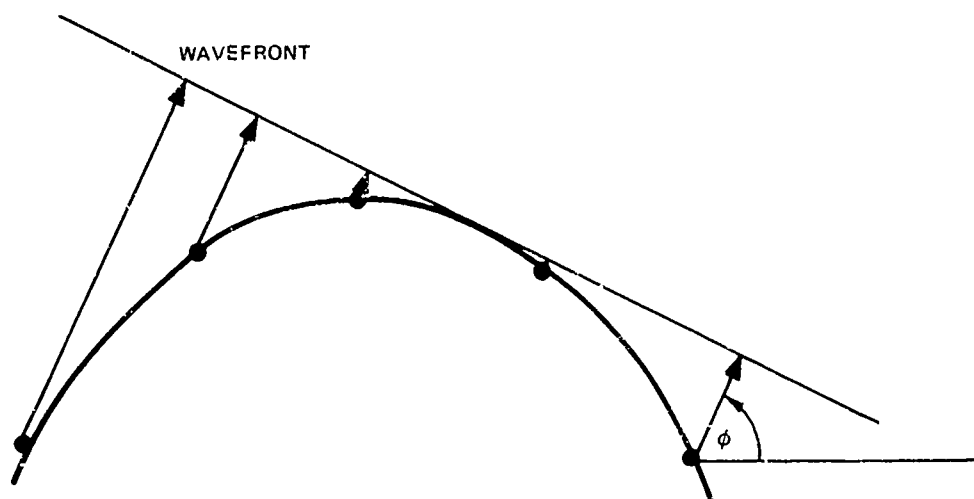


Figure 32-3. Geometry of conformal array scanned to ϕ .

A TECHNIQUE TO SIMPLIFY CONTROL OF ARRAYS ON GENERAL SURFACES

A simplification of the hardware necessary to control a conformal array can be achieved by using the technique to be described.

Consider elements of a general conformal array which are phased in such a way that the wave emanating from the array is a plane wave traveling in a given direction. This can be thought of as a projection of the elements on some plane surface as in figure 32-4. In the two-dimensional case under consideration, we now have the equivalent of a linear array. By judiciously placing the elements on the surface, the projected linear array will have equally spaced elements.

Now, the beam may be scanned by using the simpler well-known techniques of the linear array. Thus, by using this method, a reduction in the hardware and software necessary to control the phase of a conformal array can be achieved.

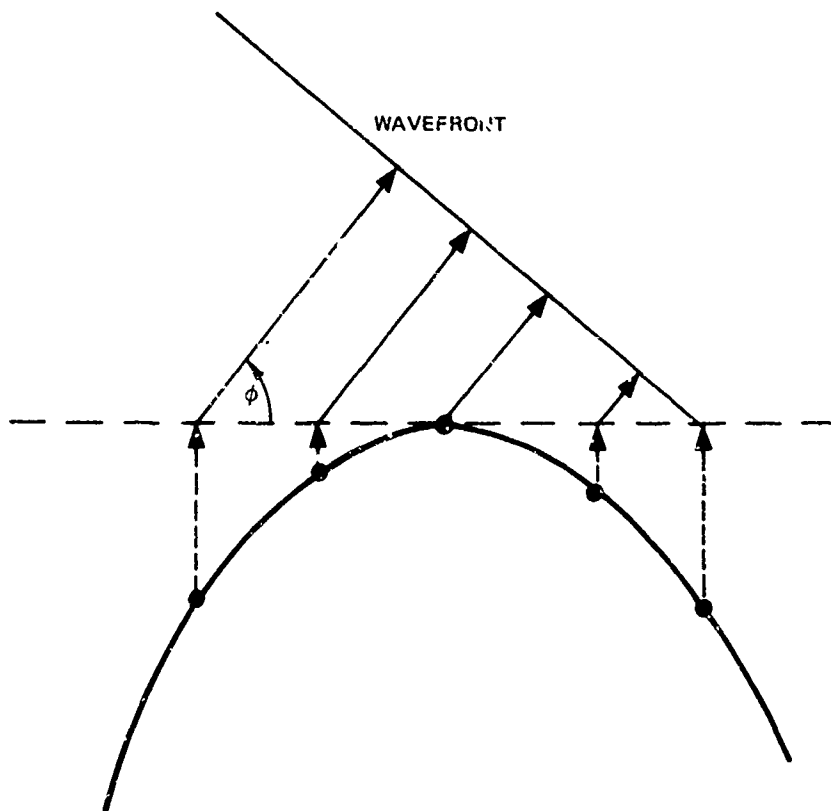


Figure 32-4 Geometry of conformal array whose elements are projected onto a plane surface.

SYNTHESIS OF THE CONFORMAL ARRAY

A conformal array using this technique was synthesized using a digital computer. Array patterns were plotted for many different cases. The antenna was assumed to be on a parabolic surface; however, the technique used to achieve the phasing was general and could be used on any surface. The equation for a parabola is $X^2 = 4pY$ where $Y = -p$ is the directrix of the parabola. Figure 32-5 shows the parabolas used in this study.

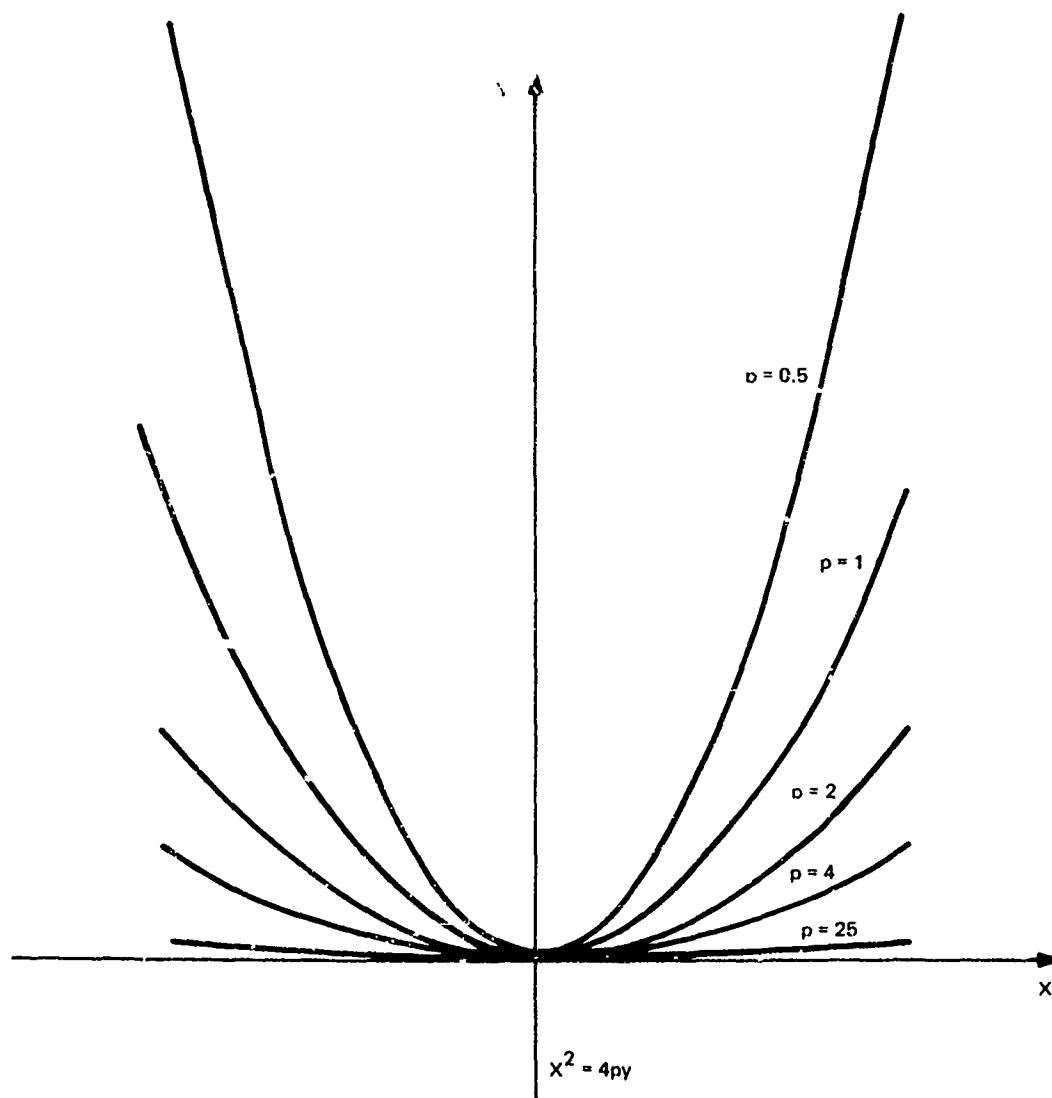


Figure 32-5. Plot of the different parabolas used in this study.

RESULTS

The resulting array patterns are shown in figures 32-6A-J through 32-10A-D. The element patterns are assumed to be evenly weighted cosine patterns. The line plots are the array patterns resulting from using the approximation technique described. The X's in the figure constitute the pattern that would result if the approximation technique were not used. It can be seen from the figures that as the beam is steered off broadside, the approximation is not valid. This is also true as the surface curvature increases. The reasons for this can be seen from examination of figure 32-11. The phase on element N necessary to point the beam in the ϕ direction is proportional to the length AB. Since the phase required to steer the beam in the ϕ direction is proportional to the distance ACD, the approximated results degrade as the beam is steered to angles off broadside and as the surface curvature is increased.

The results of the plots are summarized in figure 32-12 which gives the desired beam pointing angle versus the resultant scan angle for the different parabolas.

The results could be improved by a projection of the elements on a circular surface in lieu of the plane. The difference between AB and ACD would then be decreased, and the phasing would be a better approximation; however, the improved results would be achieved by using more complex control mechanisms required to scan circular arrays.

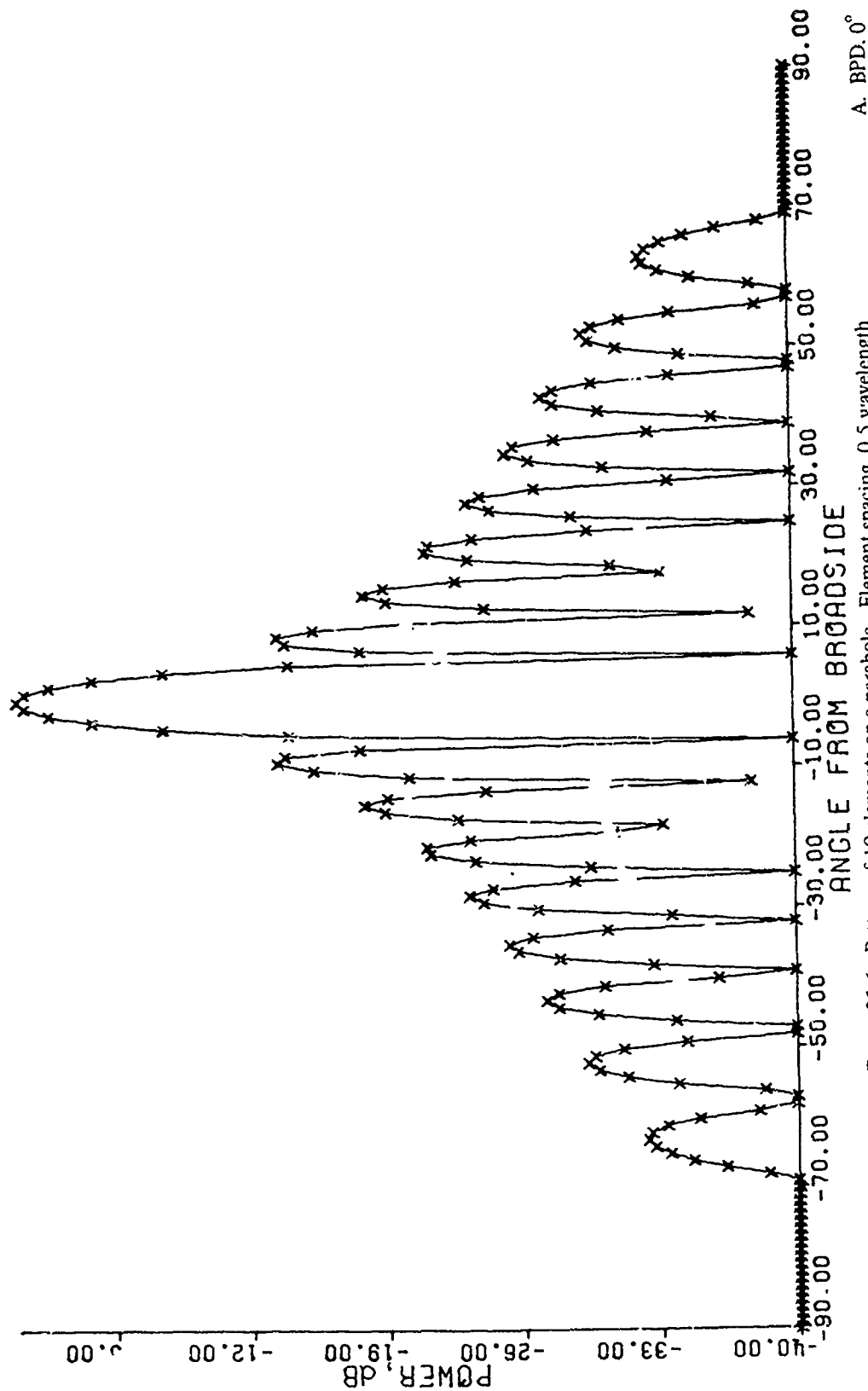
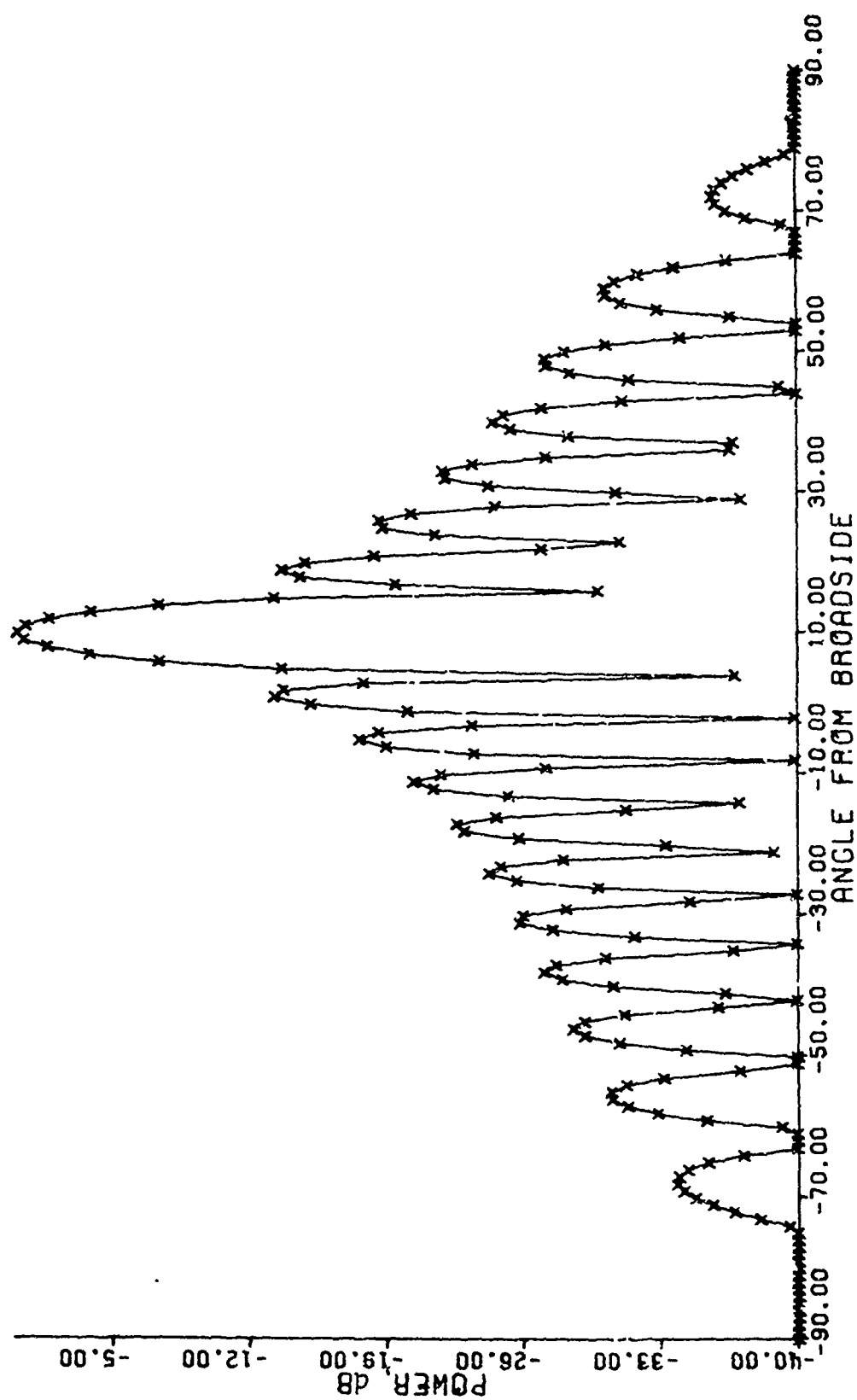
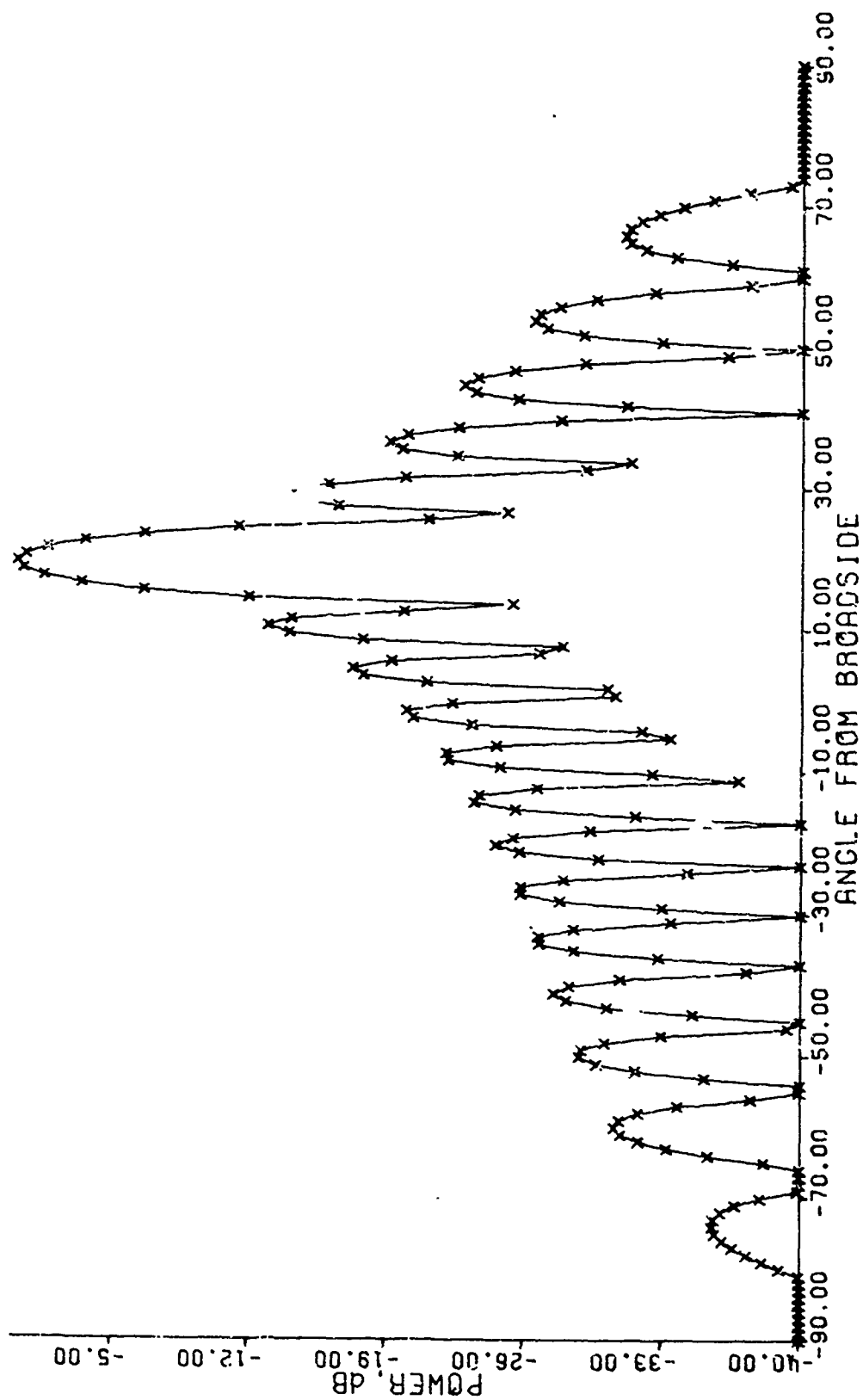


Figure 32-6. Pattern of 19 elements on a parabola. Element spacing, 0.5 wavelength projected on the X-axis. Element patterns are evenly weighted cos patterns. $P = 25.0$. Various beam pointing directions.



B. BPD, 10°

Figure 32-6 (Continued).



C. BPD, 20°

Figure 32-6 (Continued).

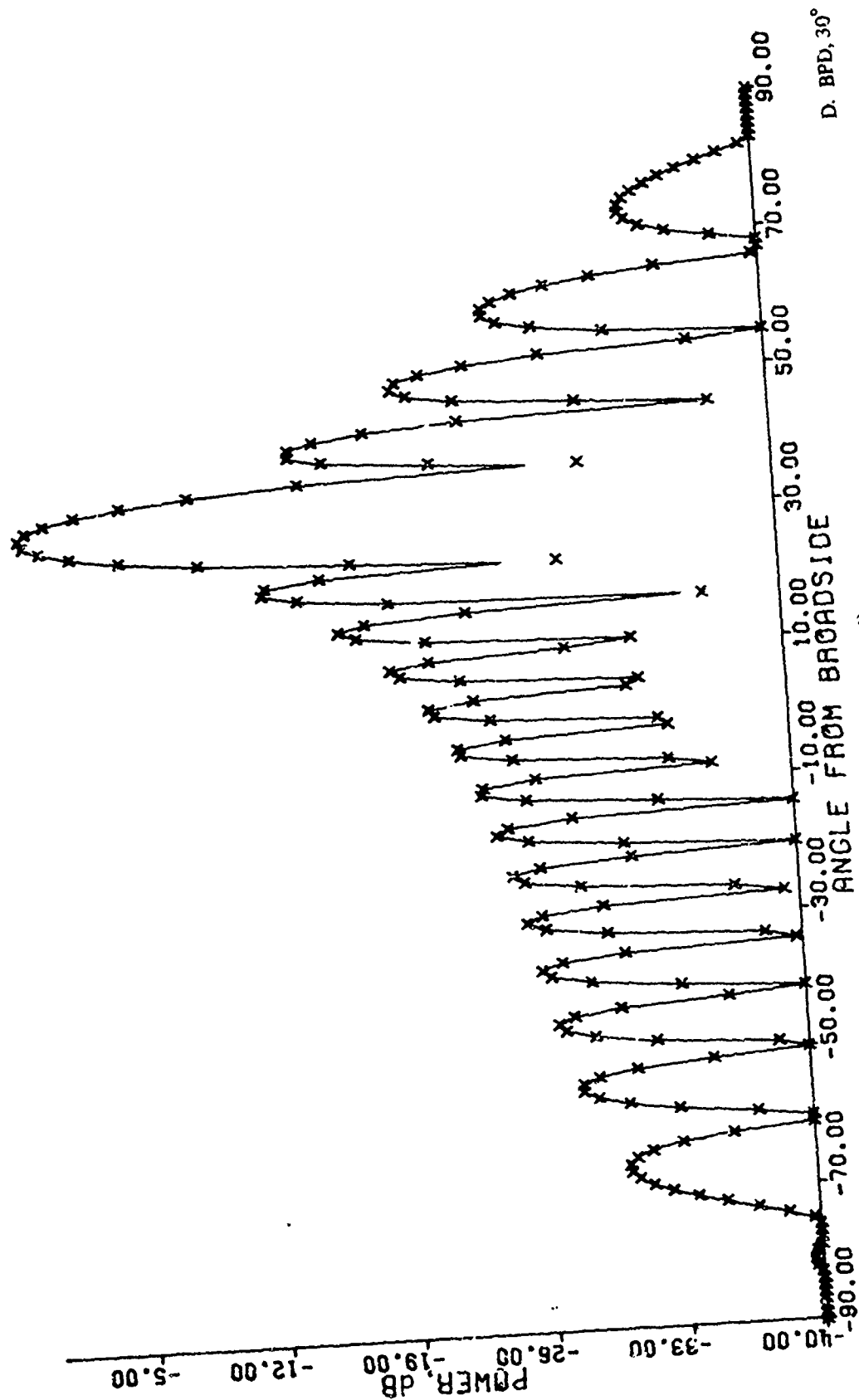
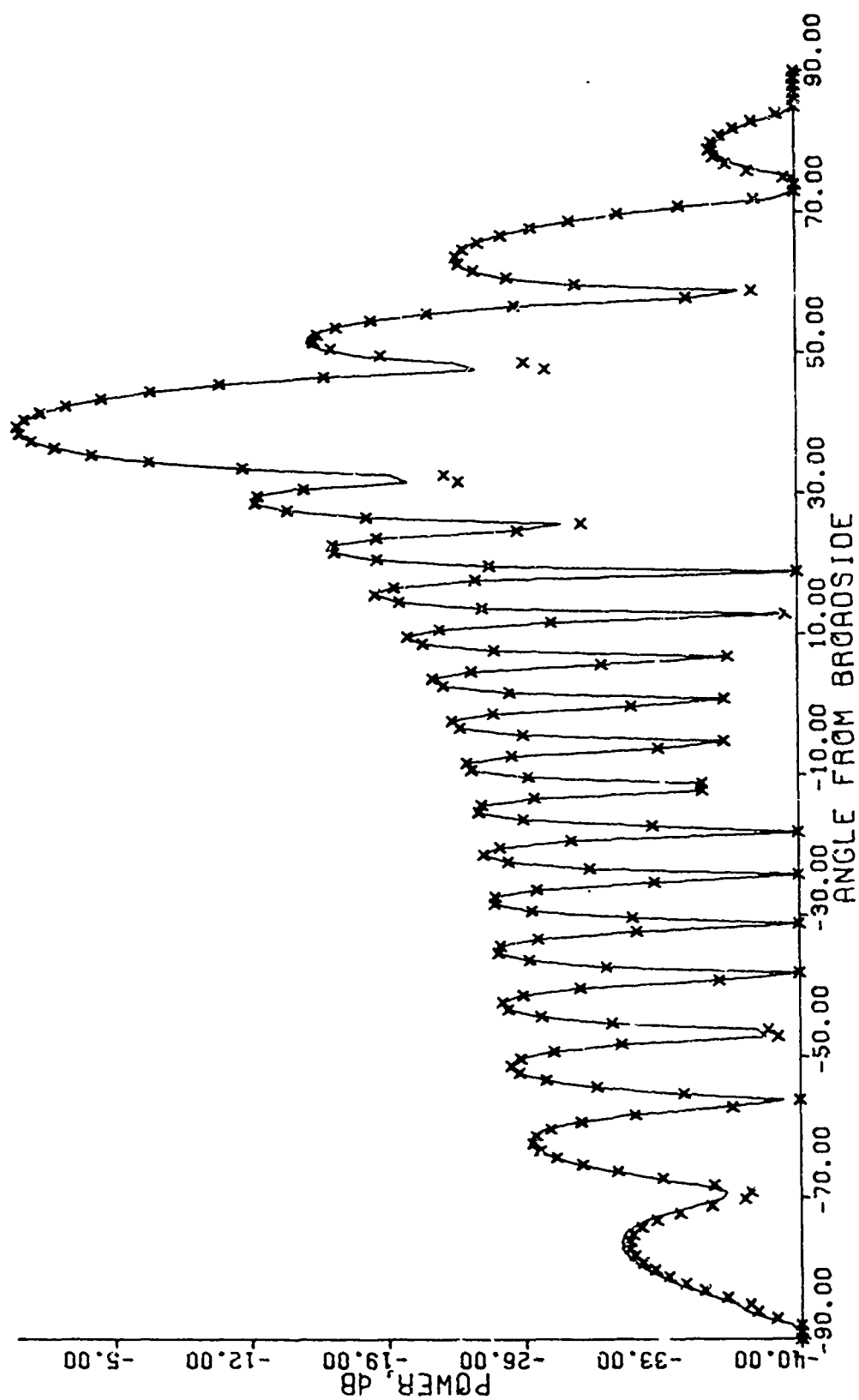
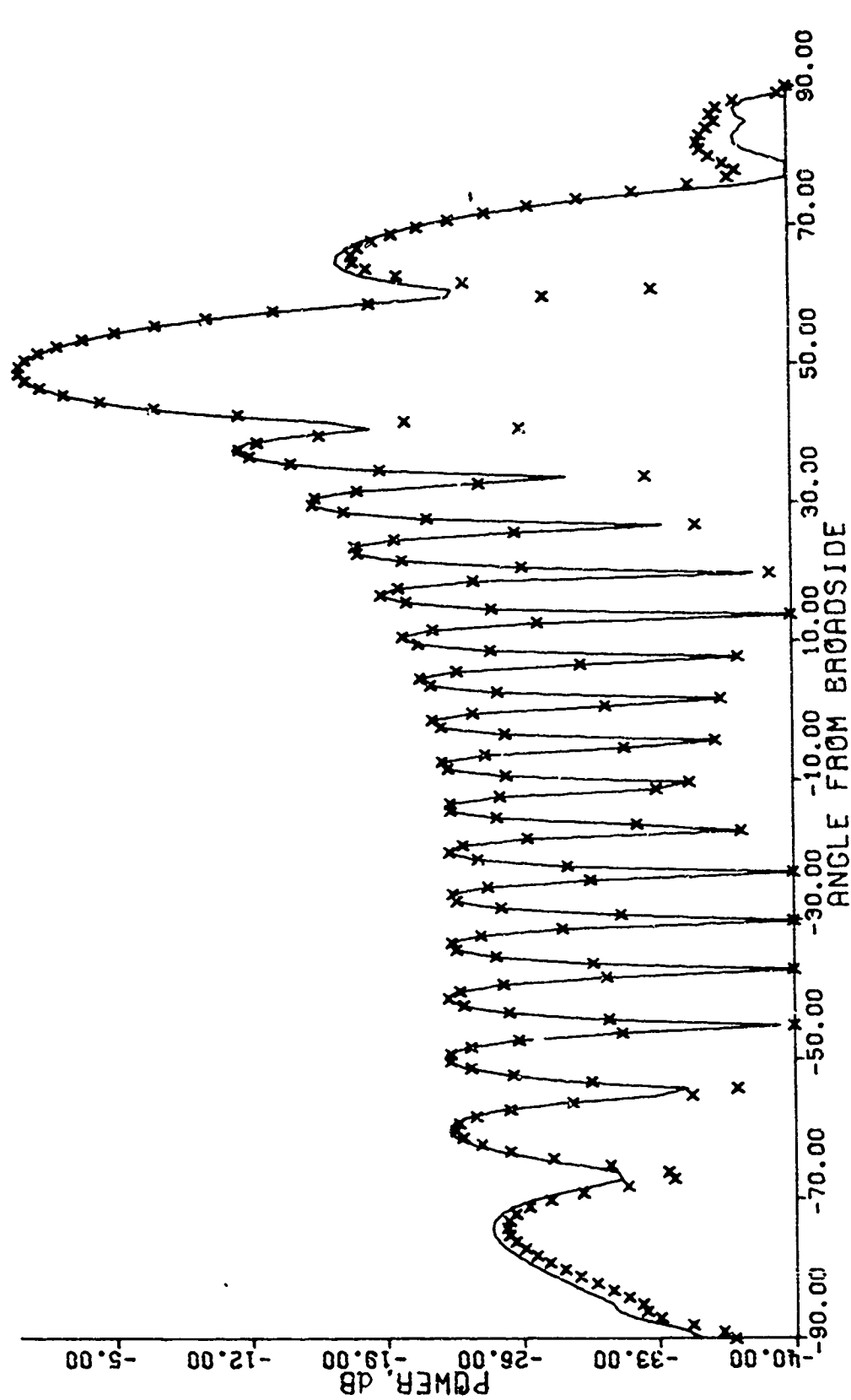


Figure 32-6 (Continued).



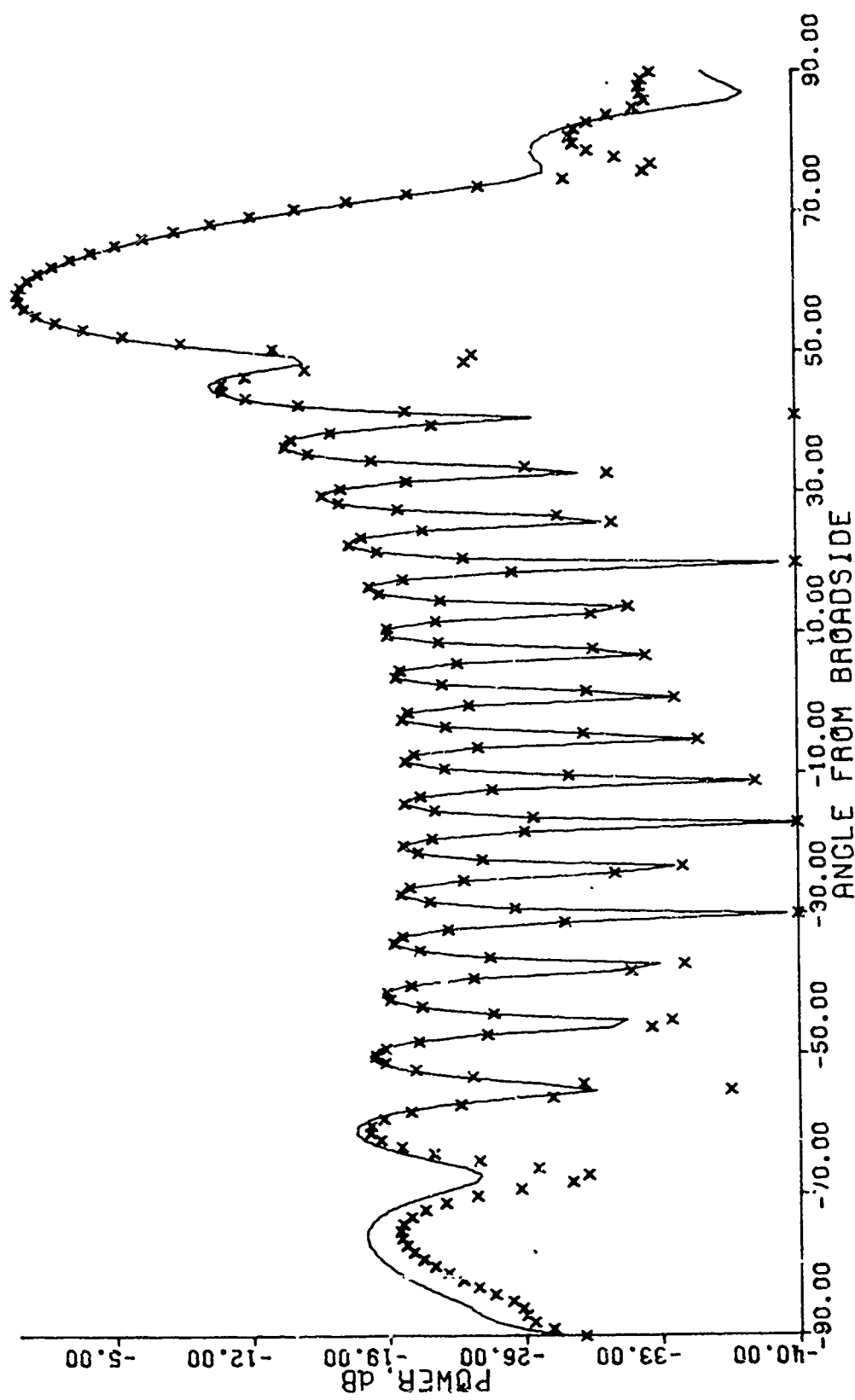
L BPD, 40°

Figure 32-6 (Continued).



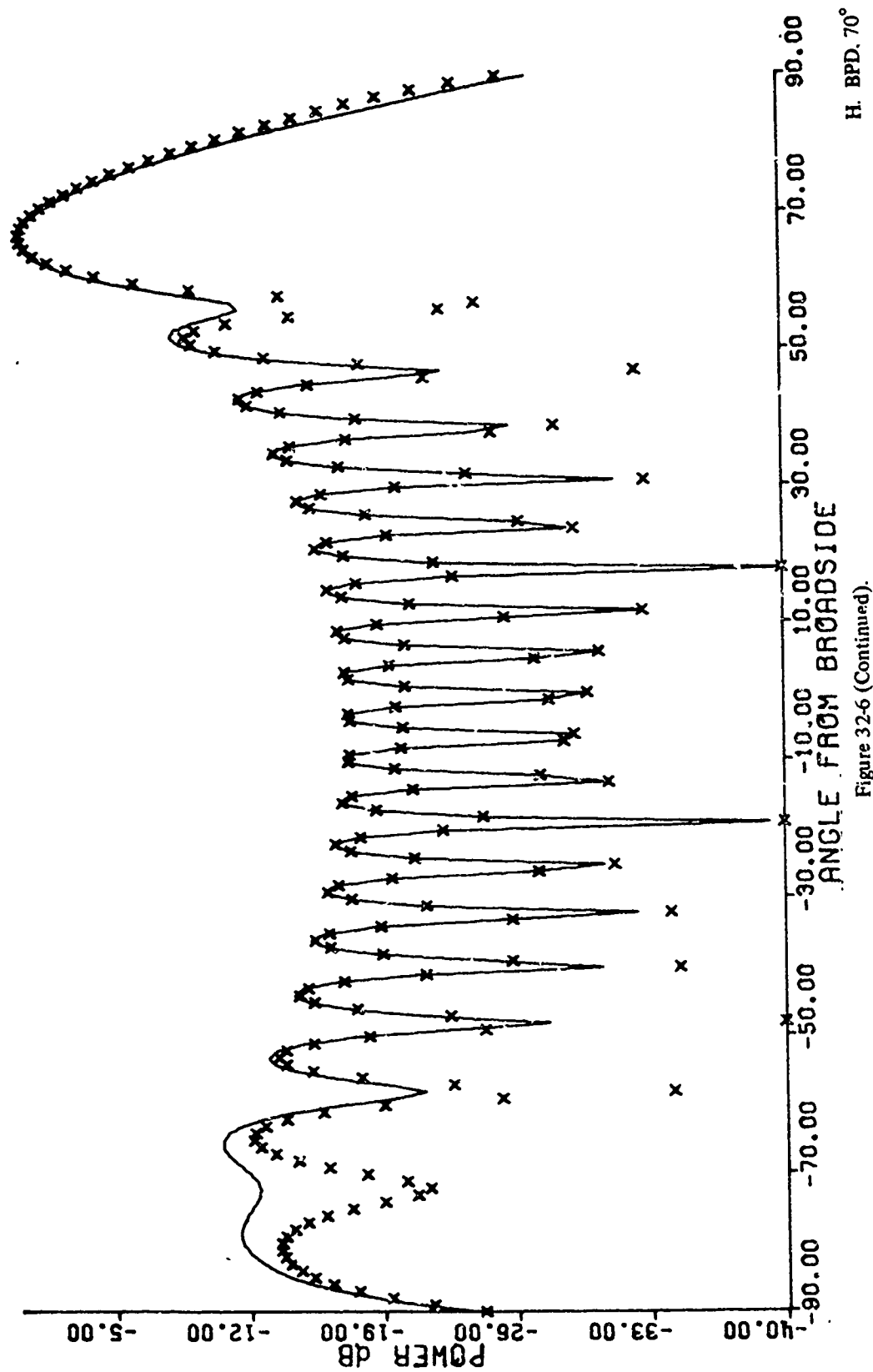
F. BPD, 50°

Figure 32-6 (Continued).



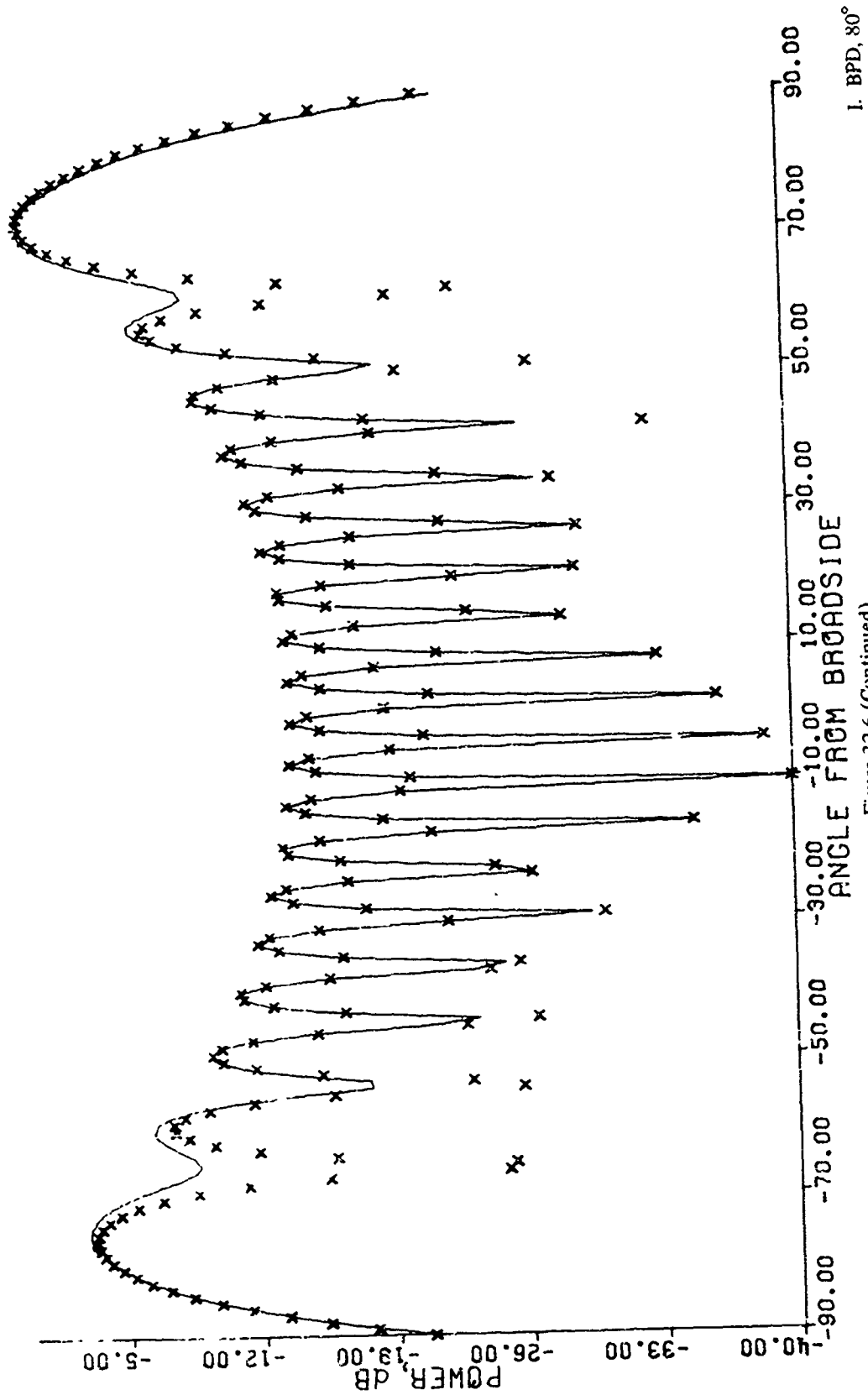
G. BPD, 60°

Figure 32-6 (Continued).



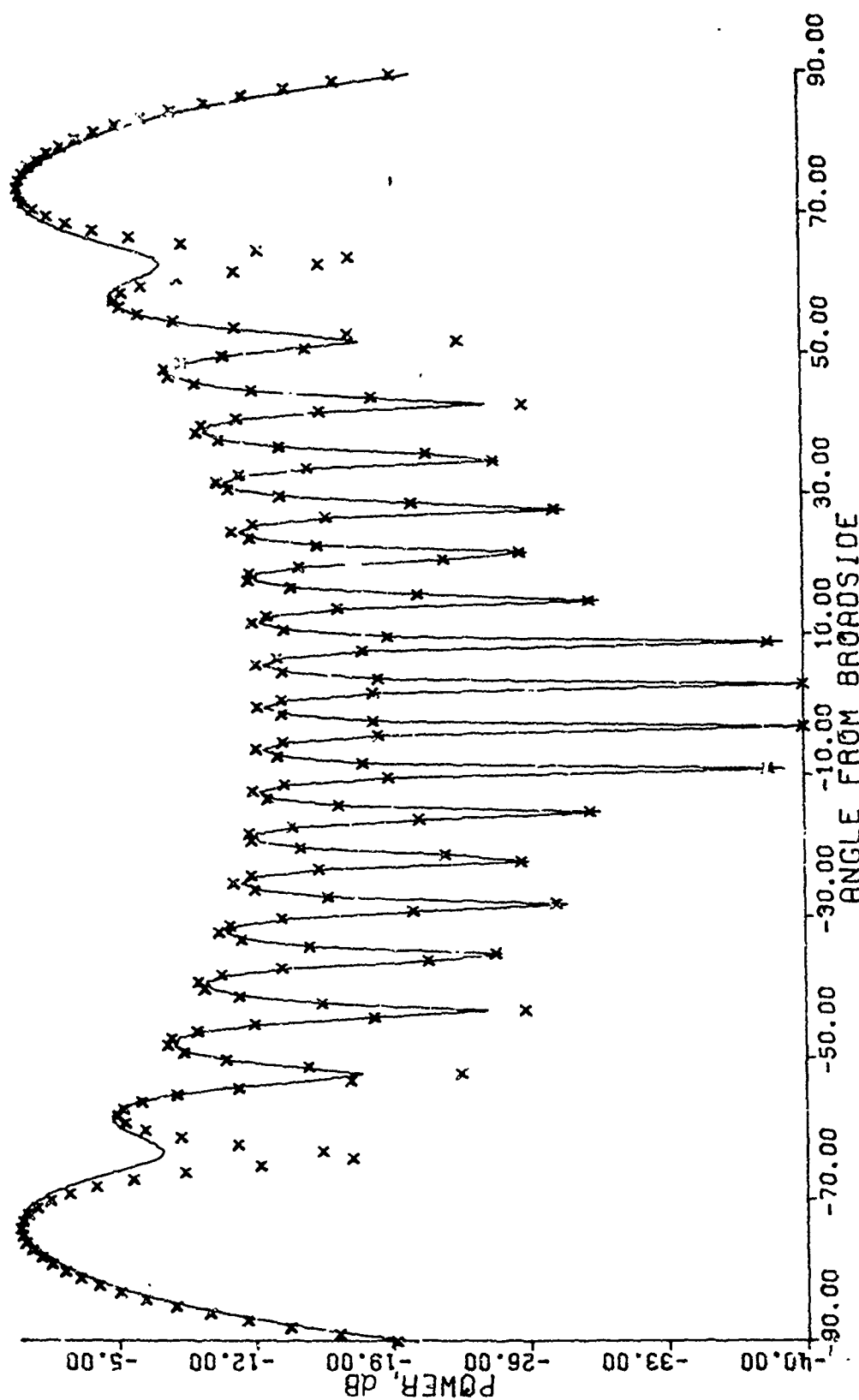
H. BPD. 70°

Figure 32-6 (Continued).



I. BPD, 80°

Figure 32-6 (Continued).



J. BPD, 90°

Figure 32-6 (Continued).

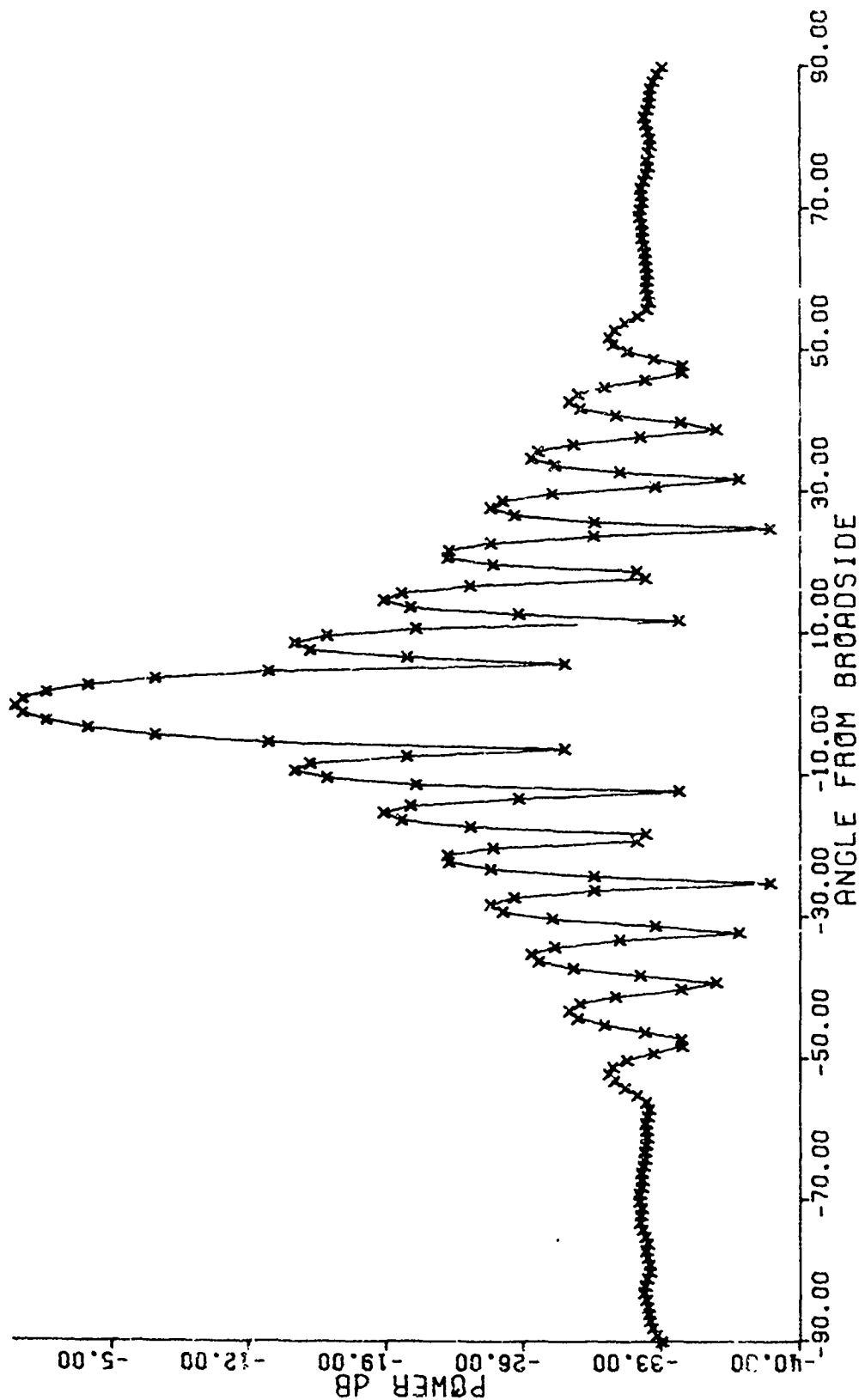
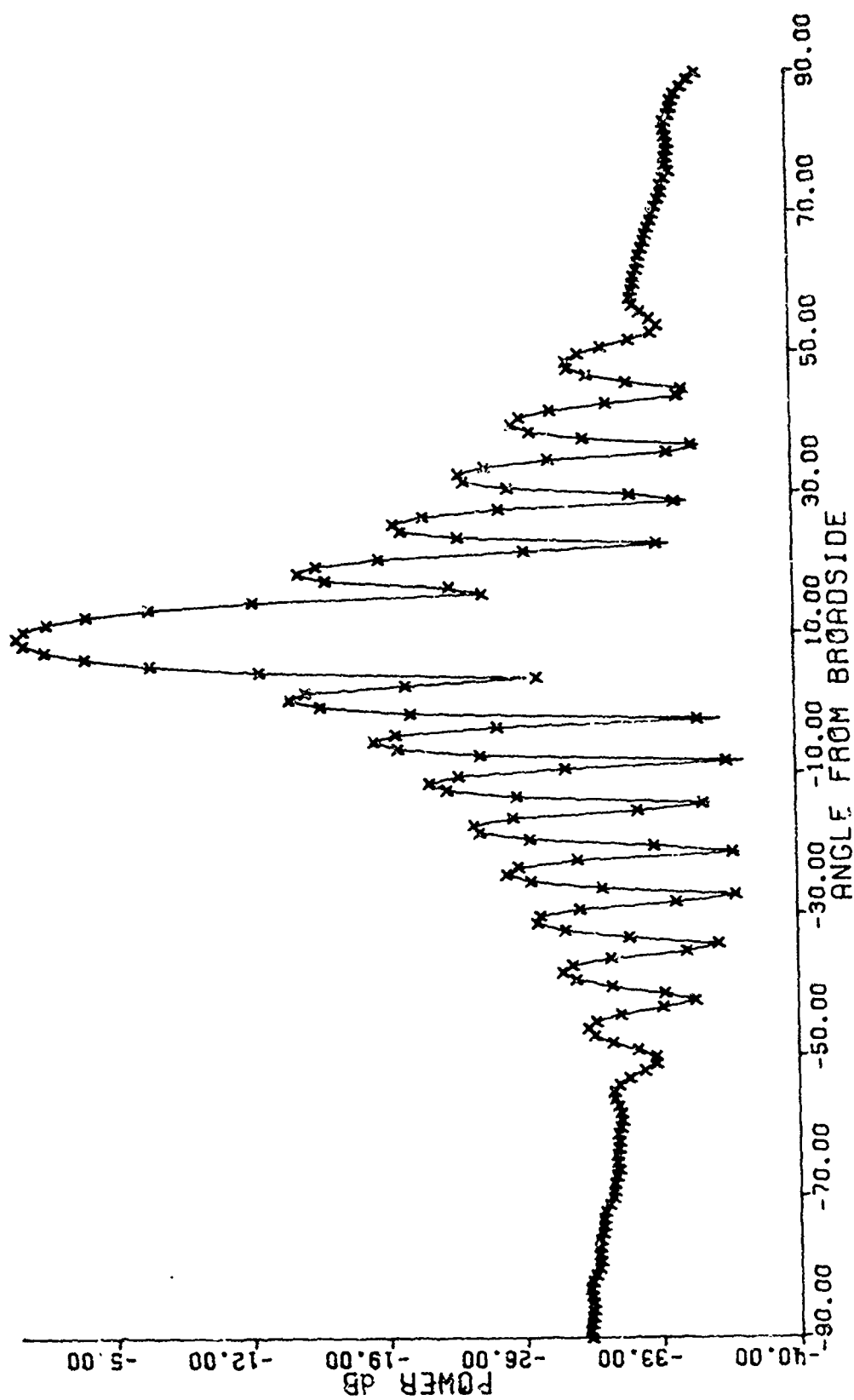


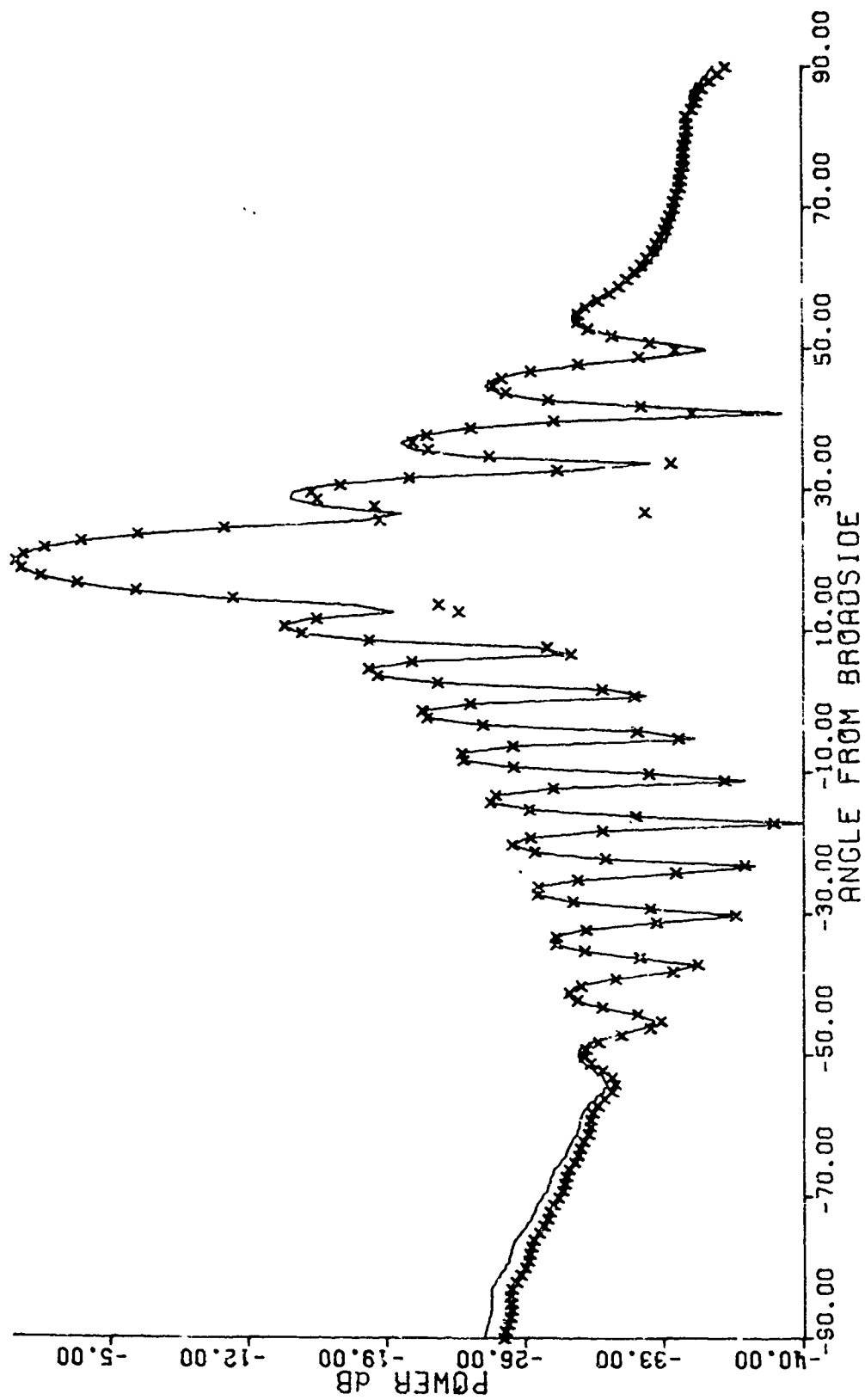
Figure 32-7. Pattern of 19 elements on a parabola. Element spacing, 0.5 wavelength projected on the X-axis. Element patterns are evenly weighted cos patterns. $P = 4.0$. Various beam pointing directions.

A. BPD, 0°



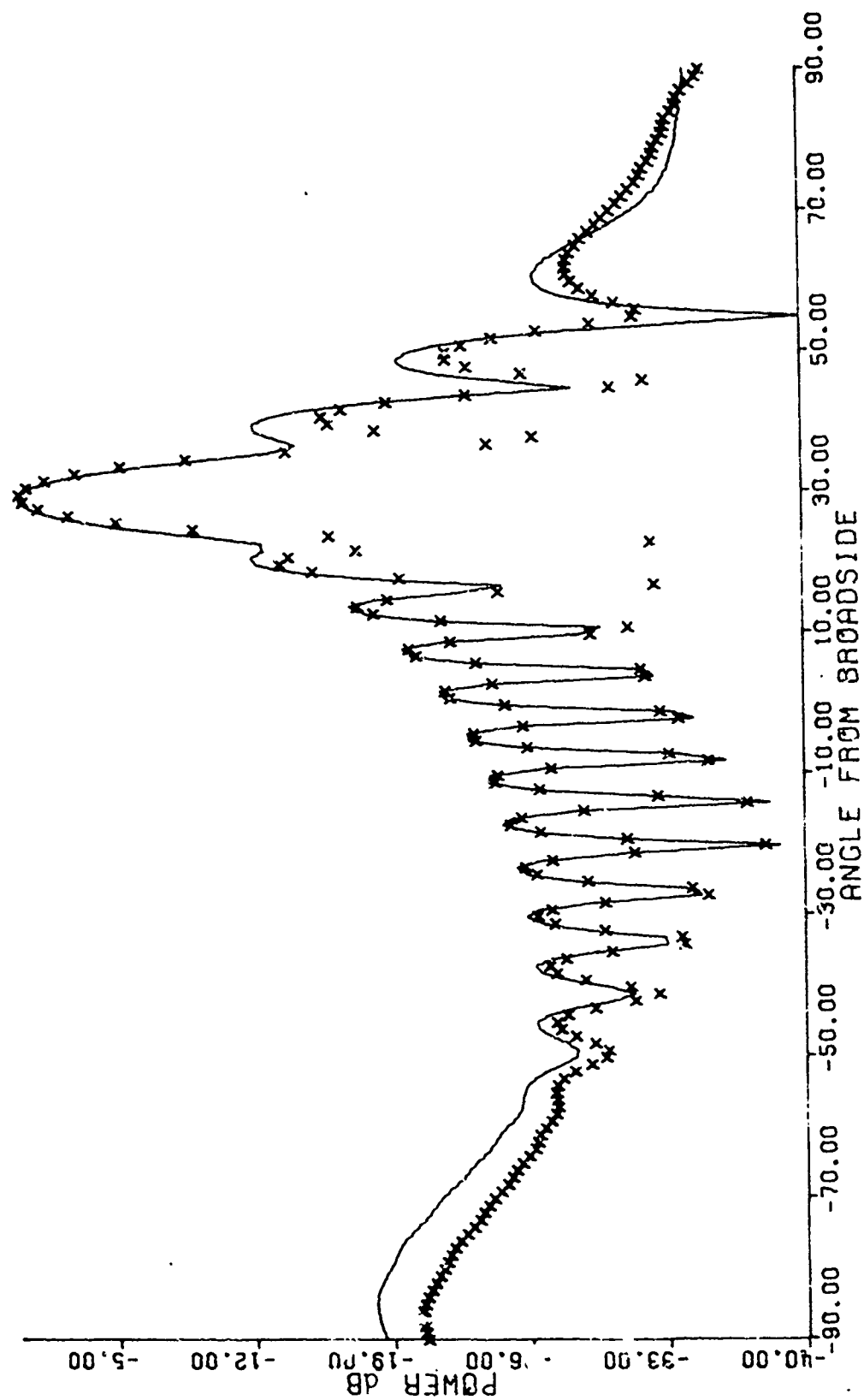
B. BPD, 10°

Figure 32-7 (Continued).



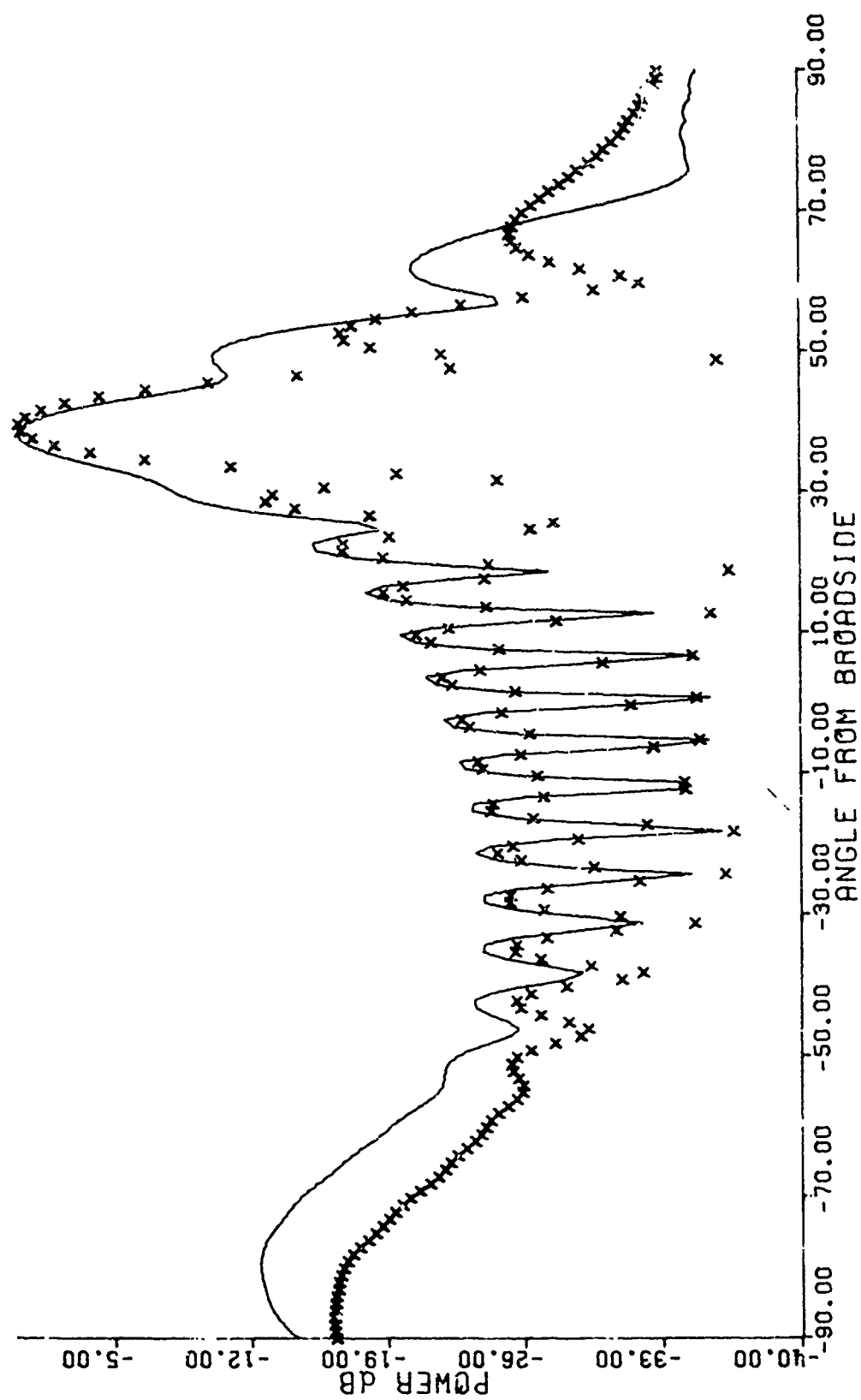
C. BPD, 20°

Figure 32-7 (Continued).



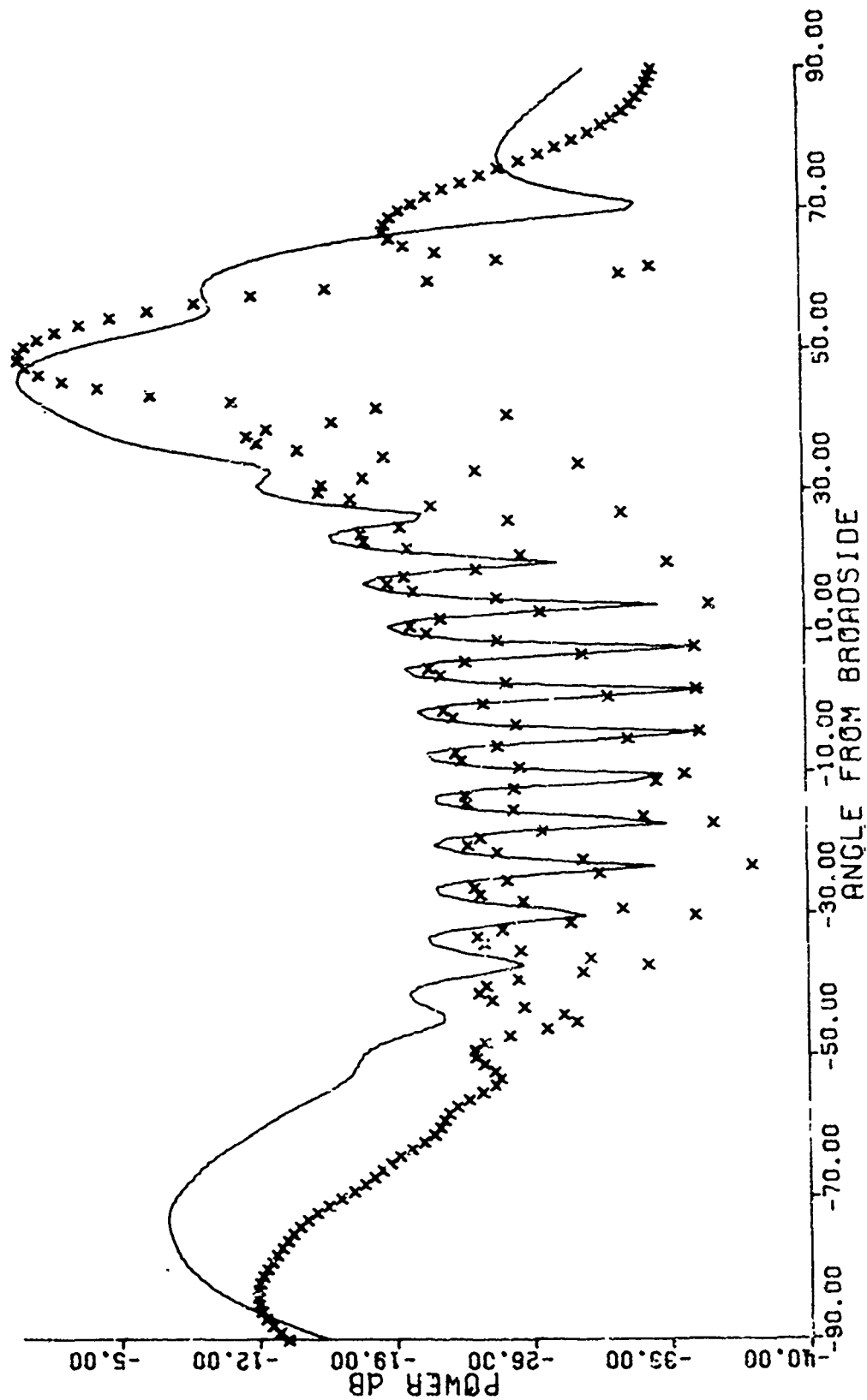
D. BPD, 30°

Figure 32-7 (Continued).



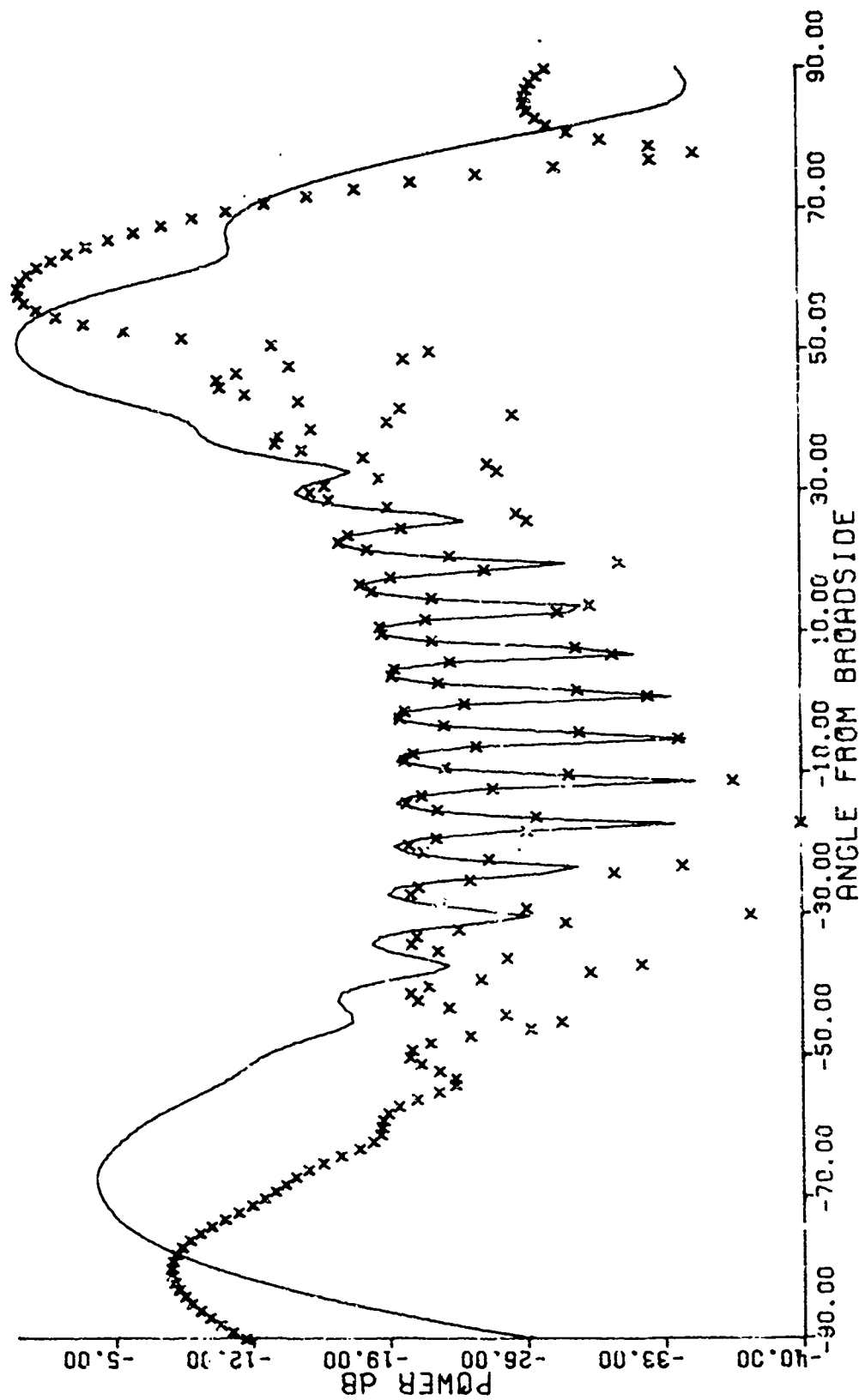
E. BPD, 40°

Figure 32-7 (Continued).

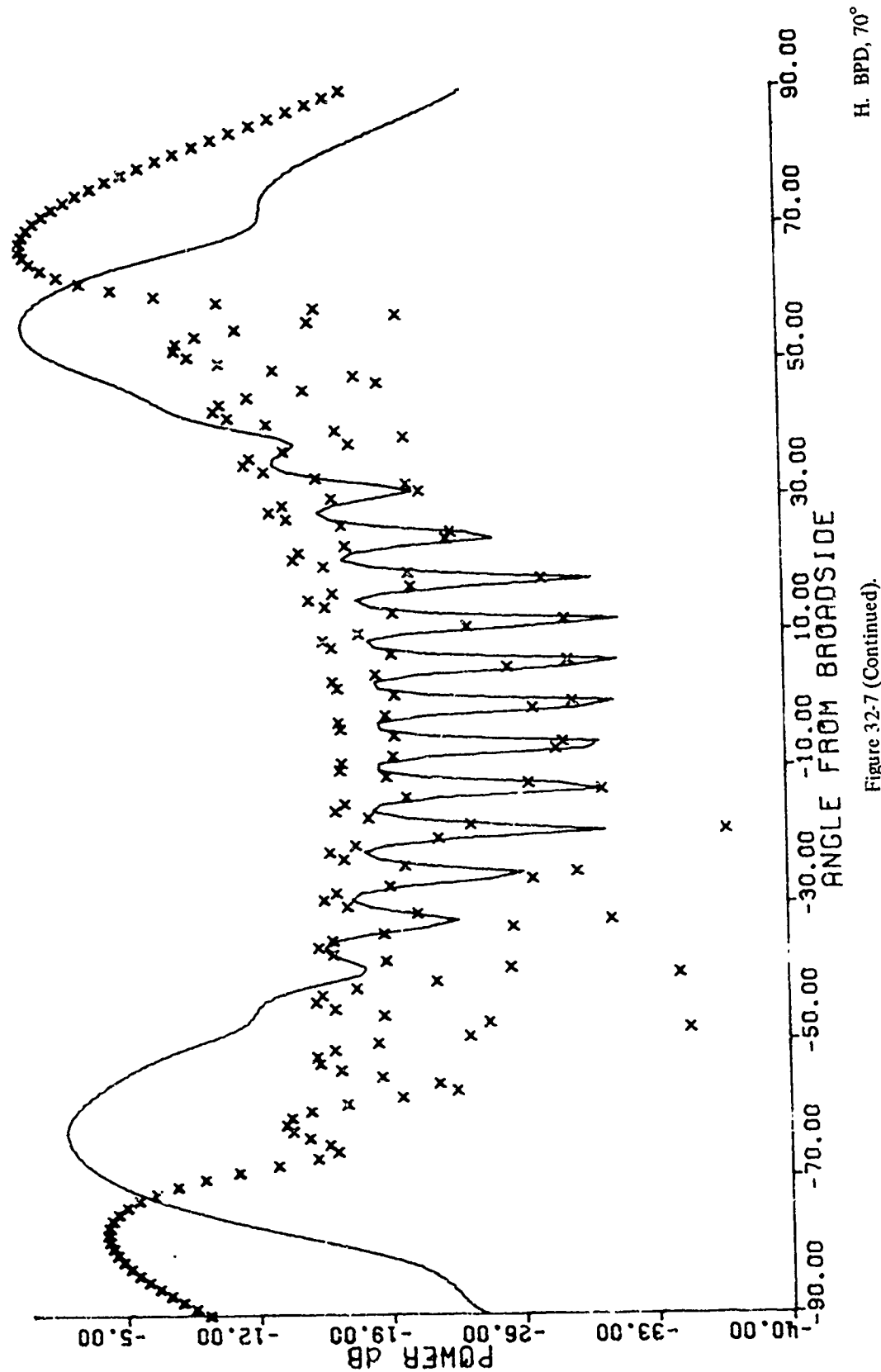


F. BPD, 50°

Figure 32-7 (Continued)



G. BPD, 60°
Figure 32-7 (Continued).



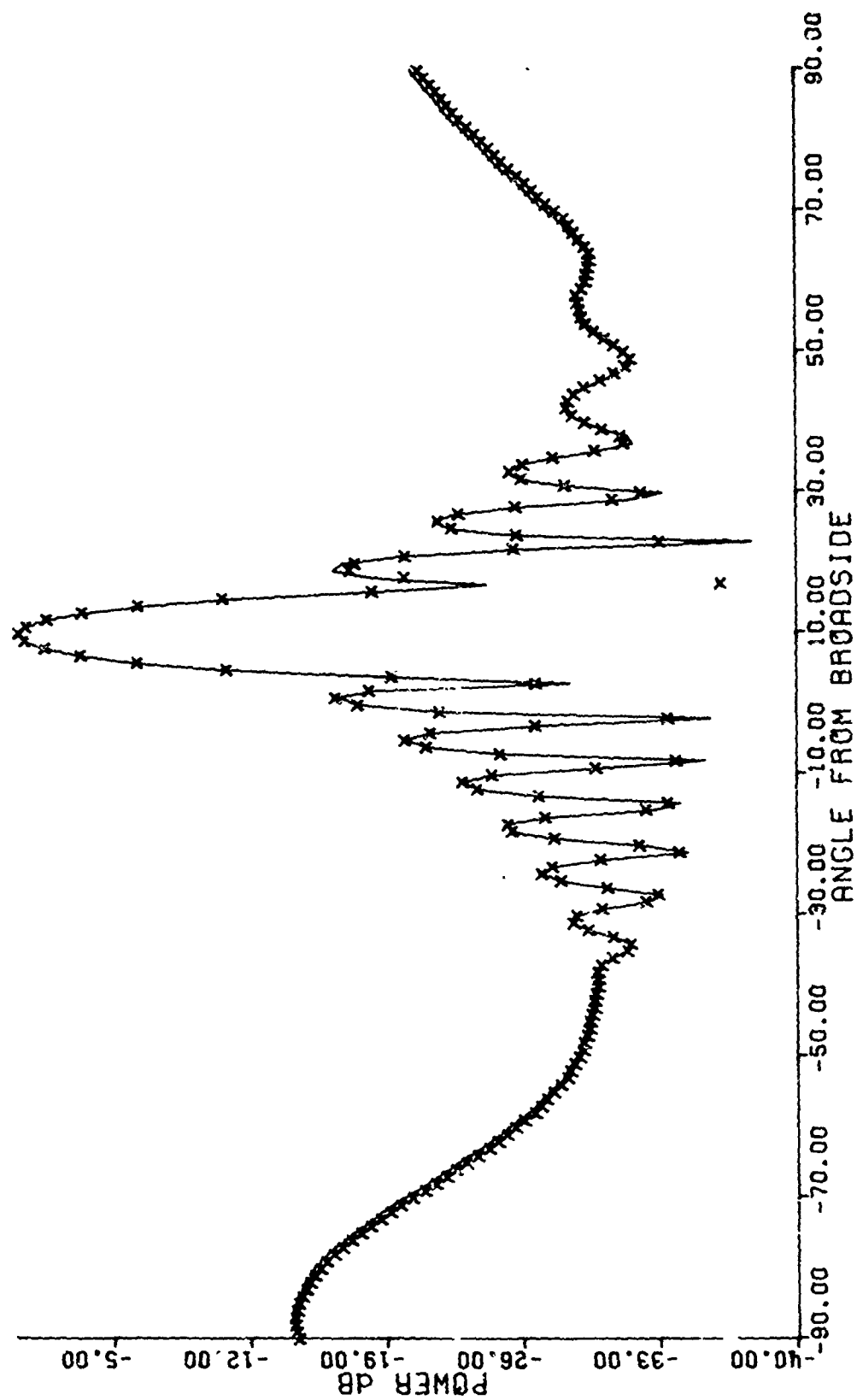
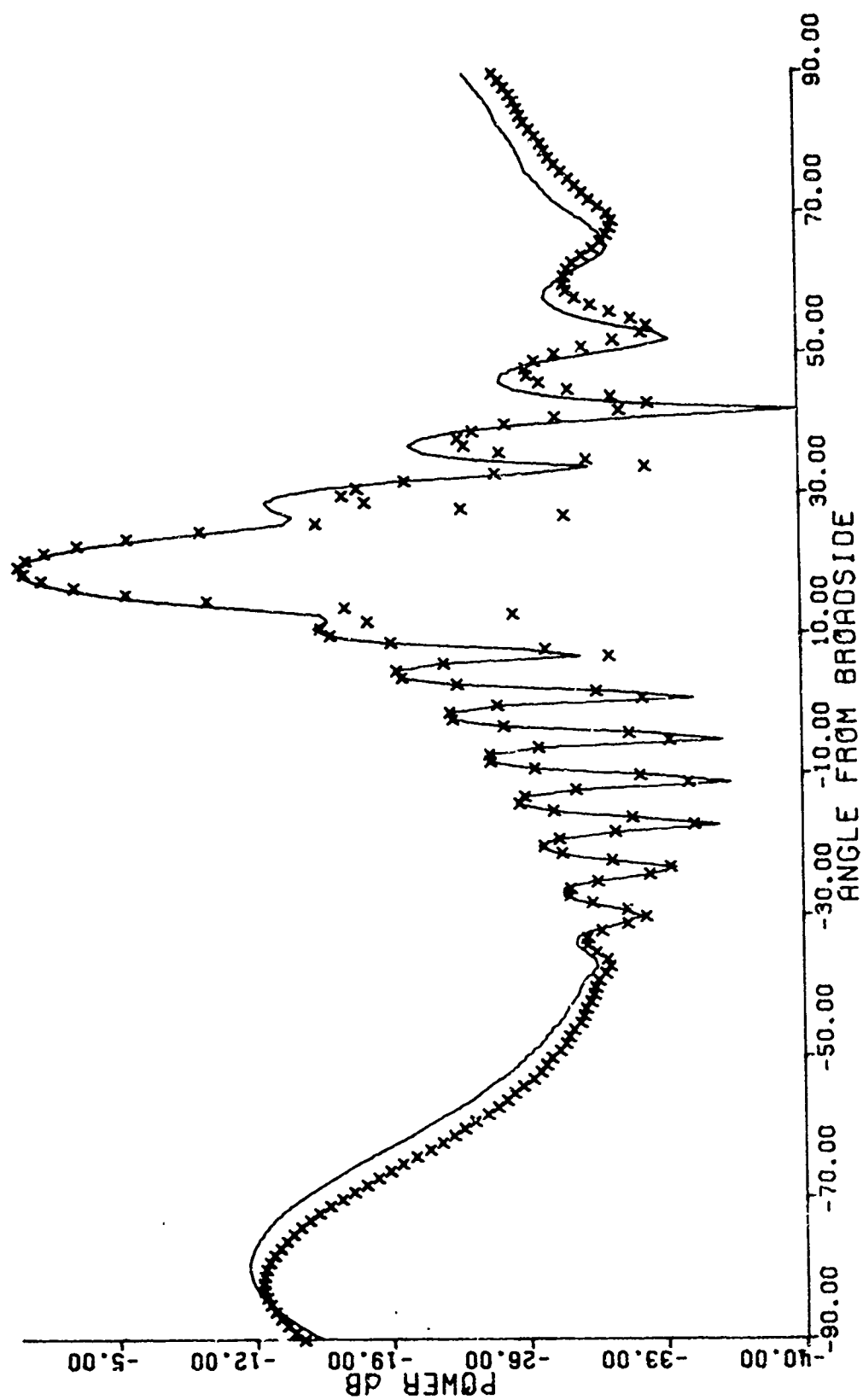


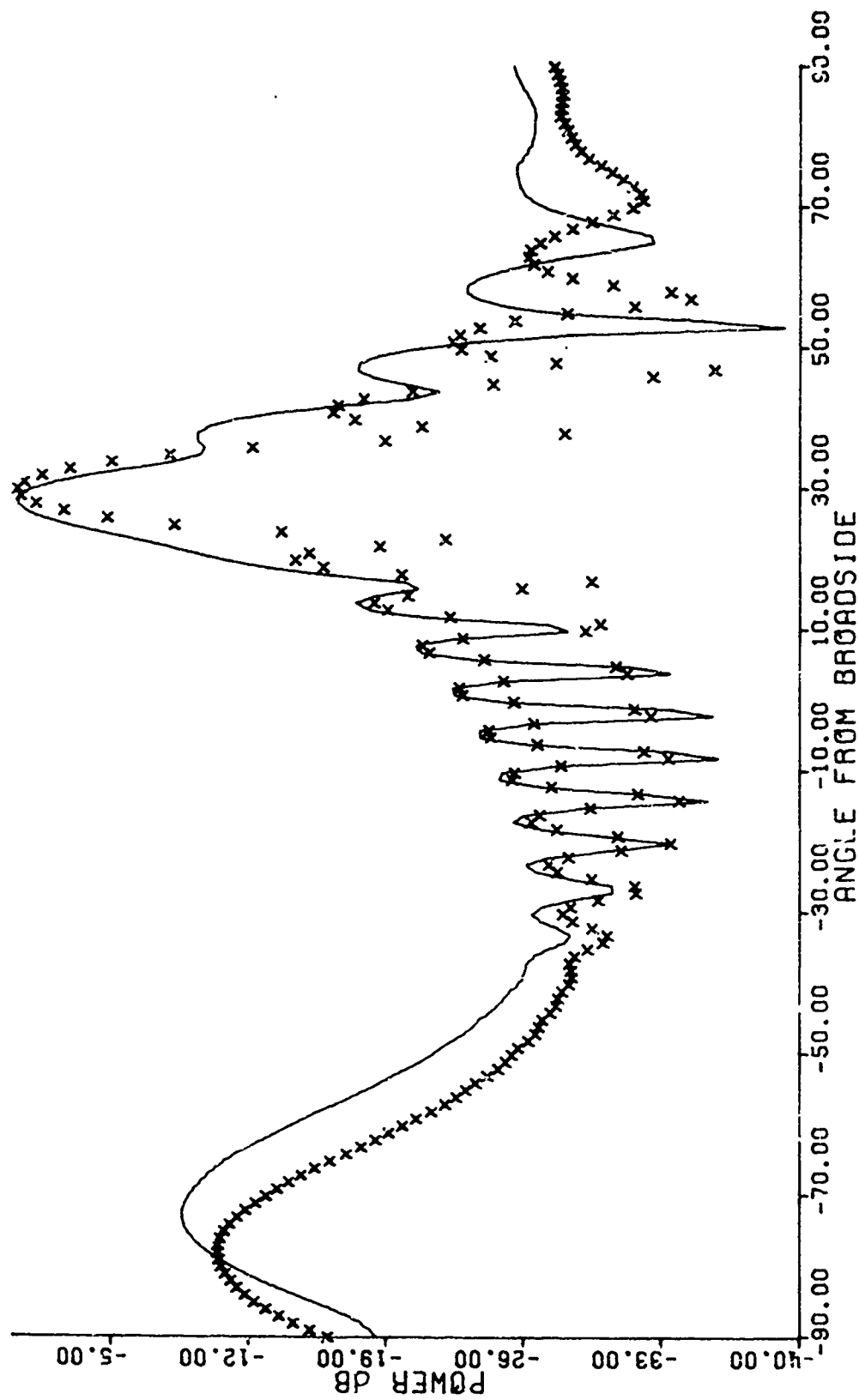
Figure 32-8. Pattern of 19 elements on a parabola. Element spacing, 0.5 wavelength projected on the X-axis. Element patterns are evenly weighted cos patterns. $P = 2.0$. Various beam pointing directions.

A. BPD, 10°



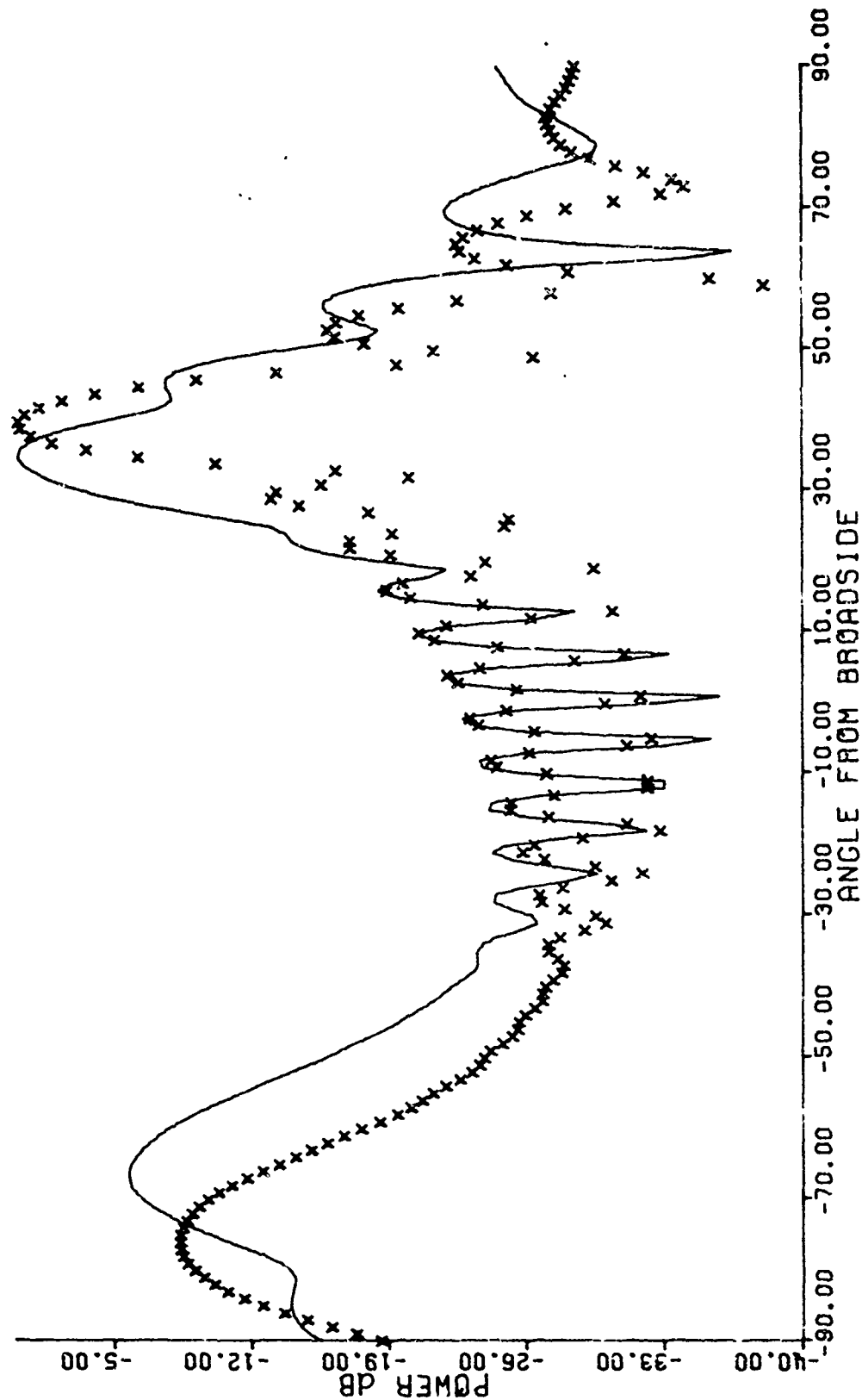
B. BPD, 20°

Figure 32-8 (Continued).



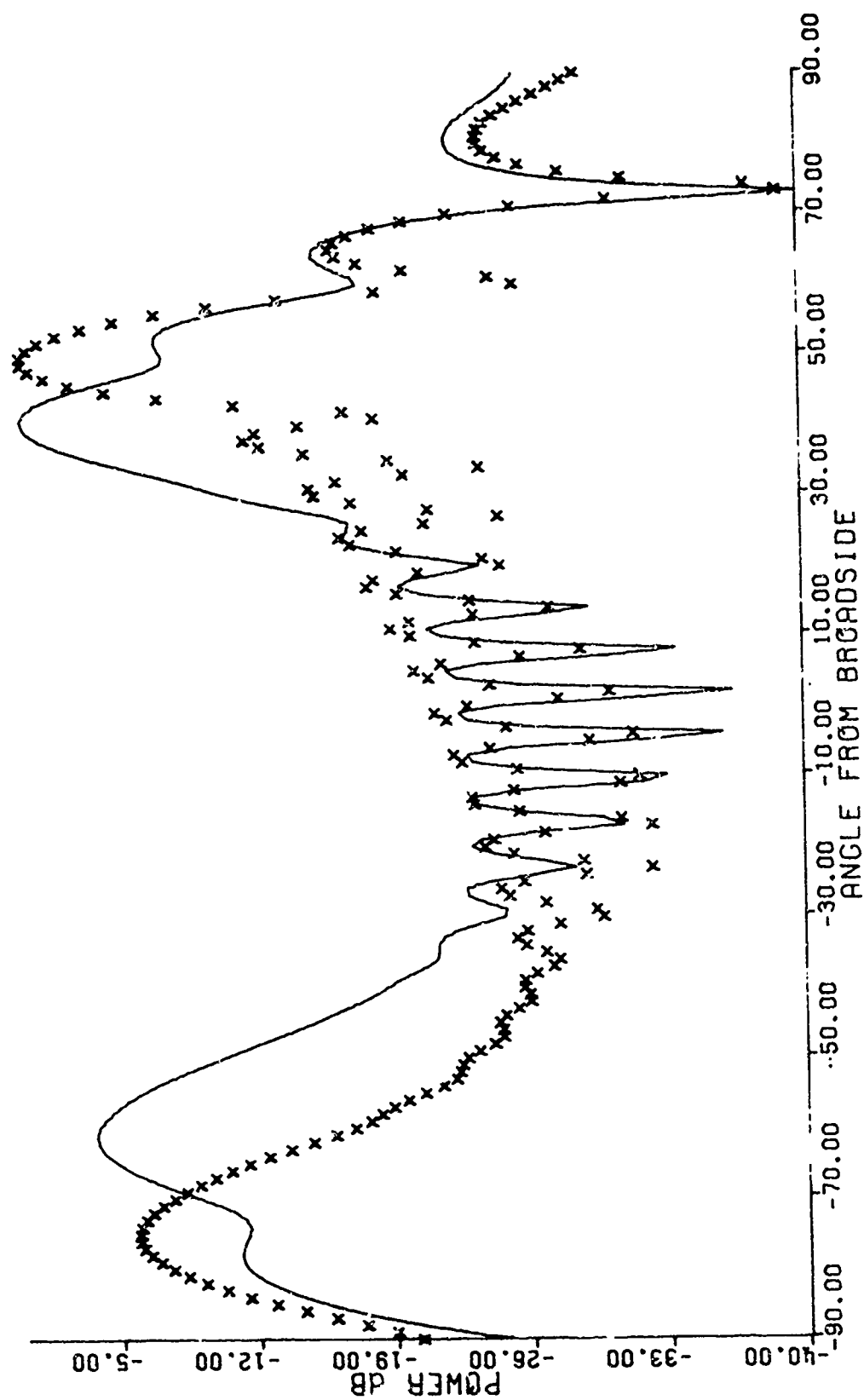
C. BPD, 30°

Figure 32-8 (Continued).



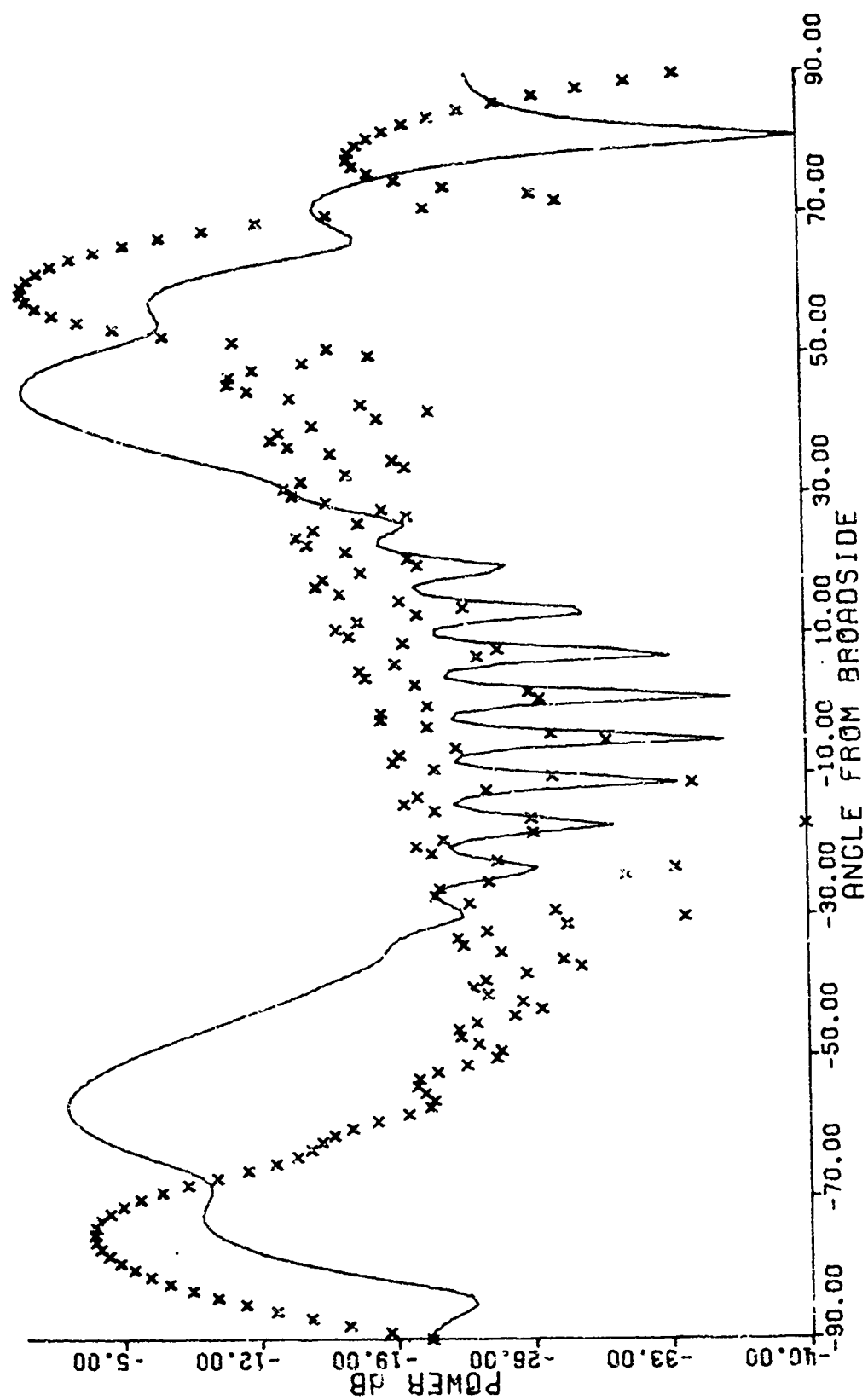
D. BPD, 40°

Figure 32-8 (Continued).



E. BPD, 50°

Figure 32-8 (Continued).



F. BPD, 60°

Figure 32-8 (Continued).

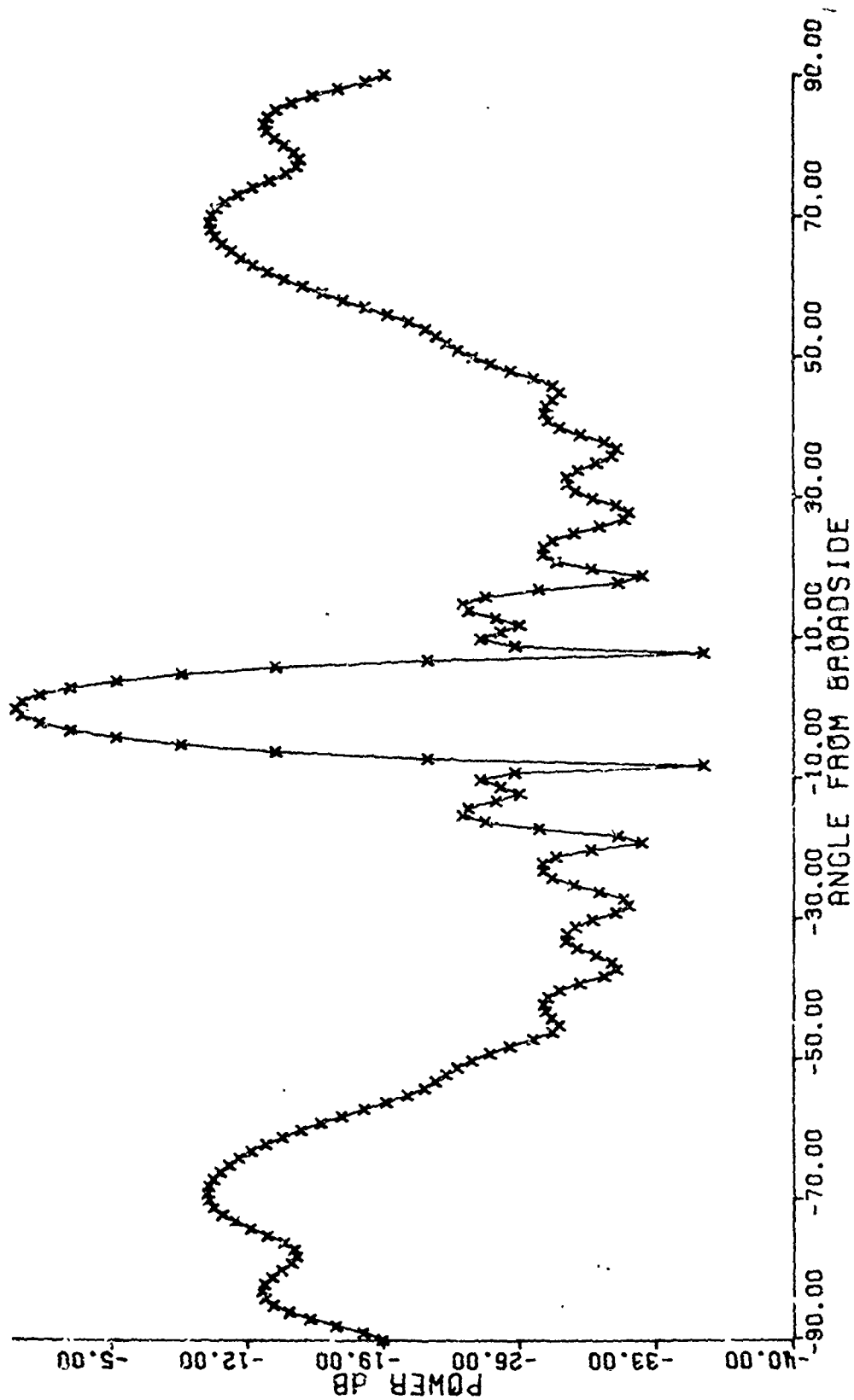
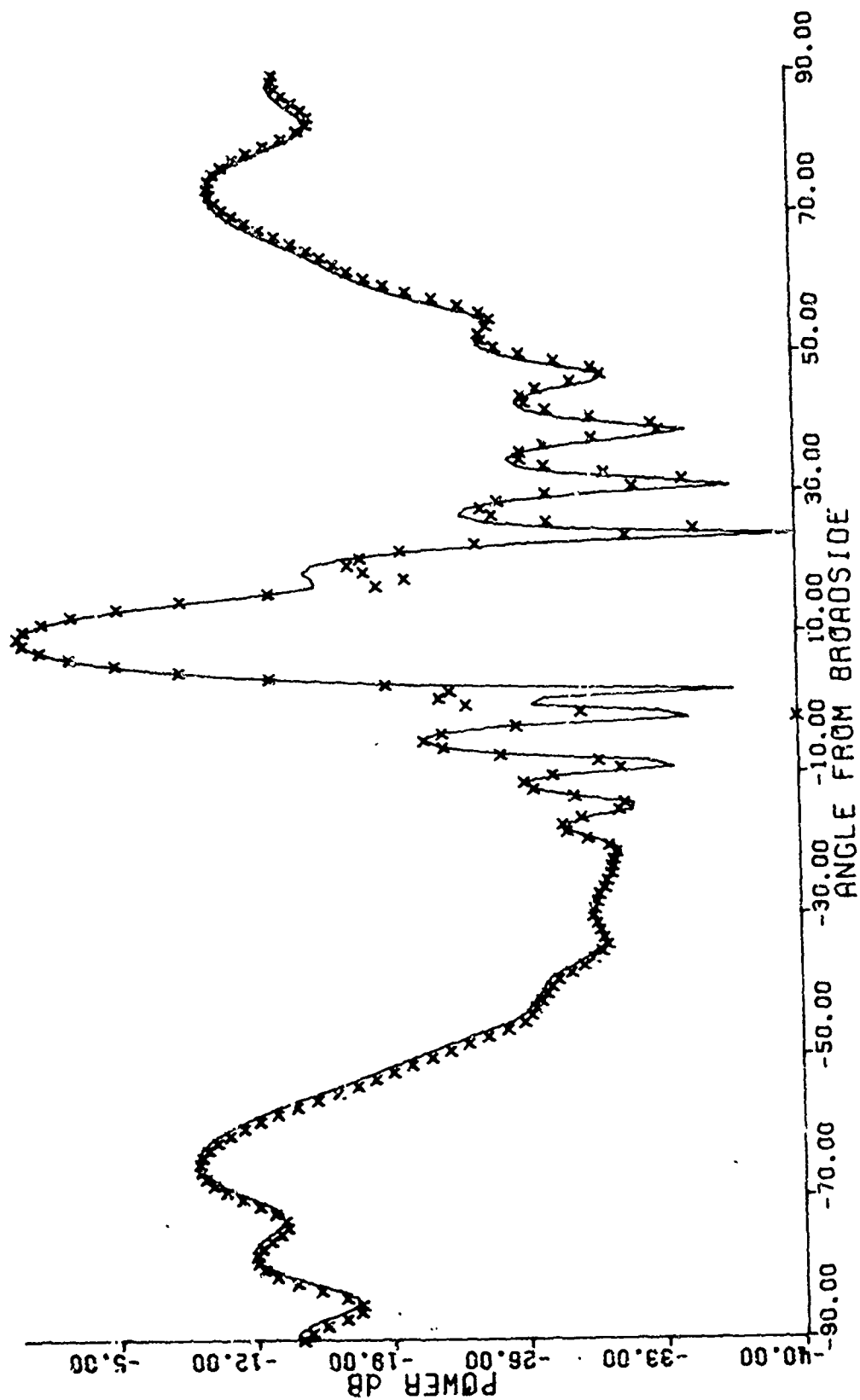


Figure 32-9. Pattern of 19 elements on a parabola. Element spacing, 0.5 wavelength projected on the X-axis. Element patterns are evenly weighted cos patterns $P = 1.0$. Various beam pointing directions.



B. BPD, 10°

Figure 32-9 (Continued)

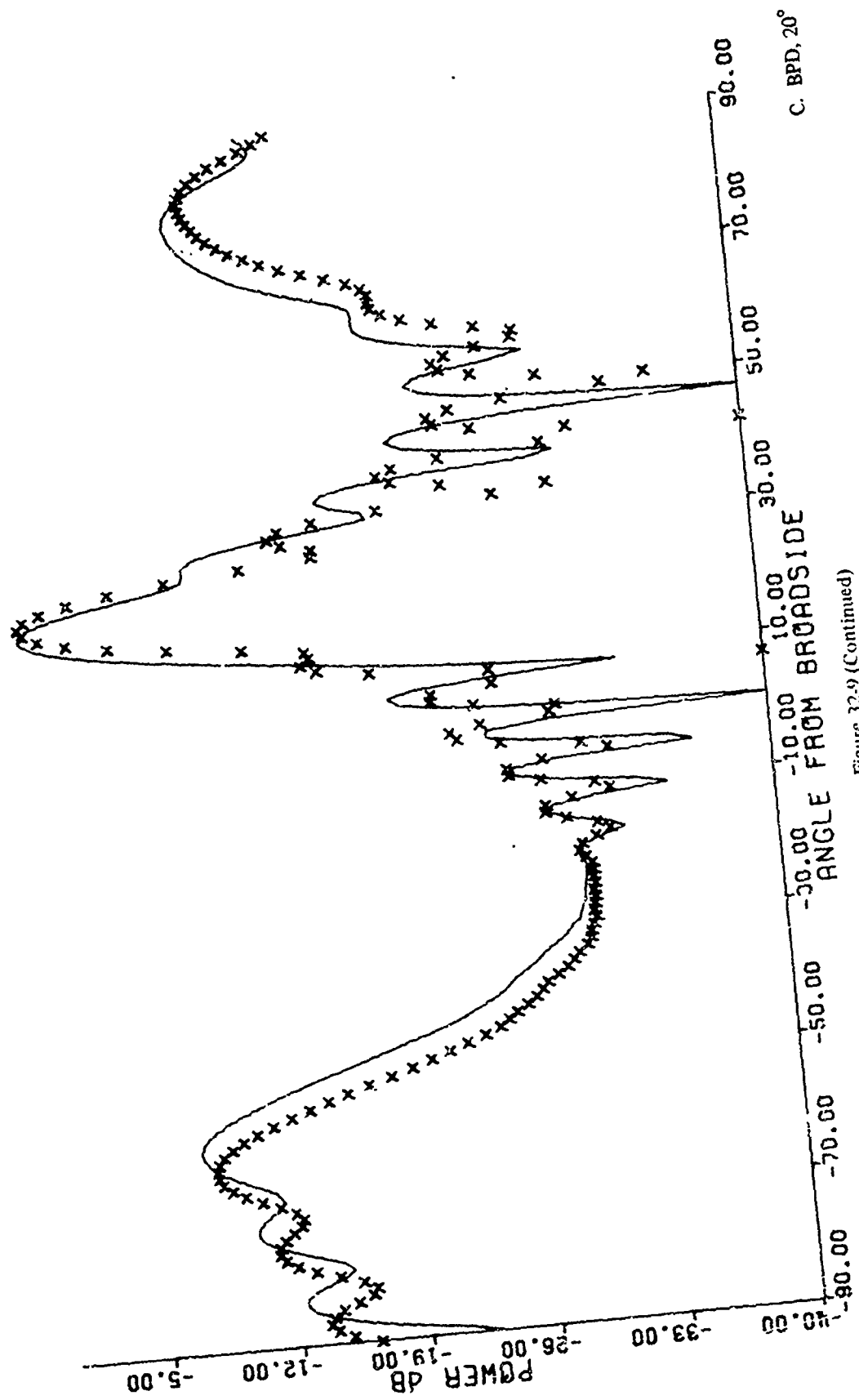
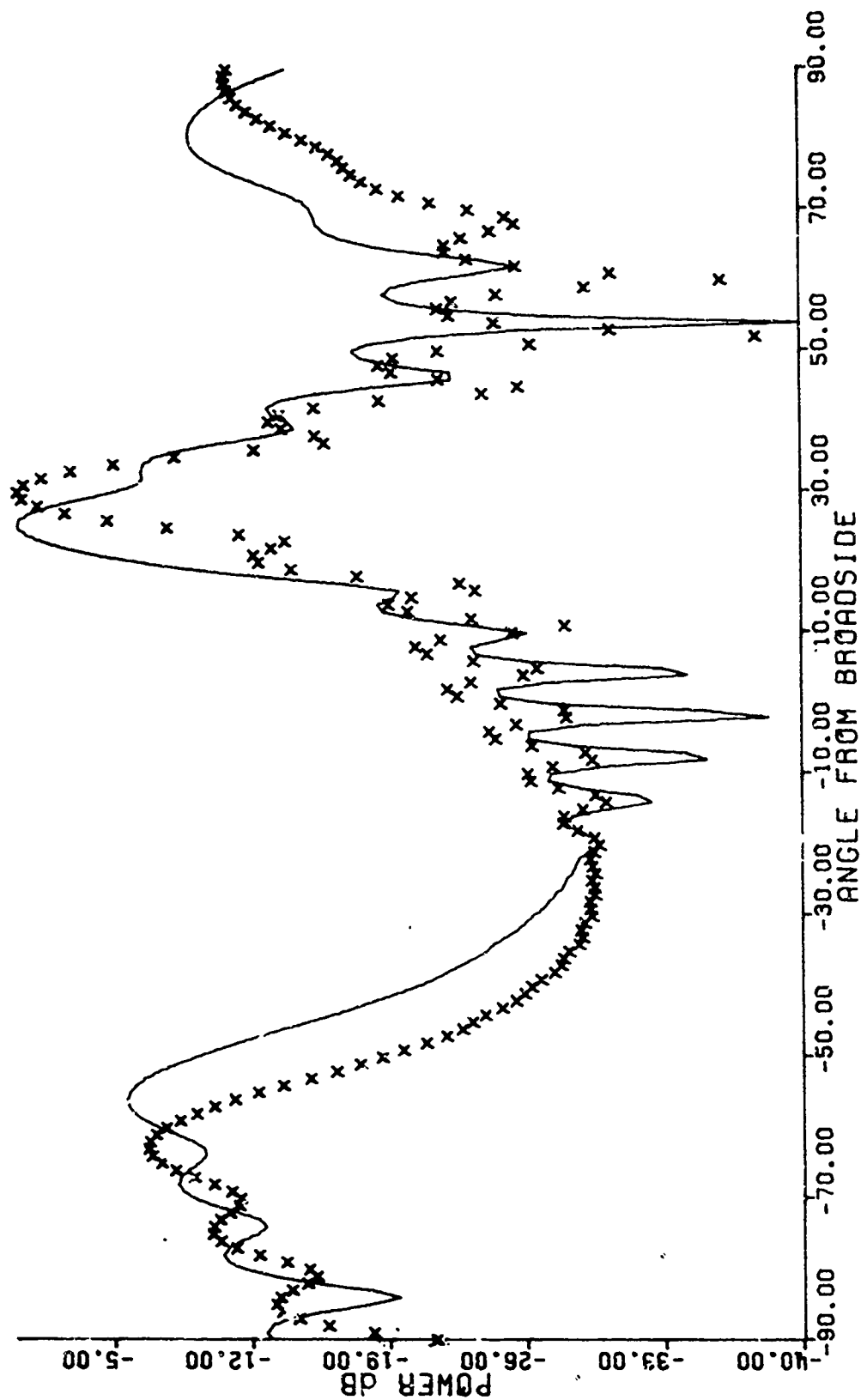
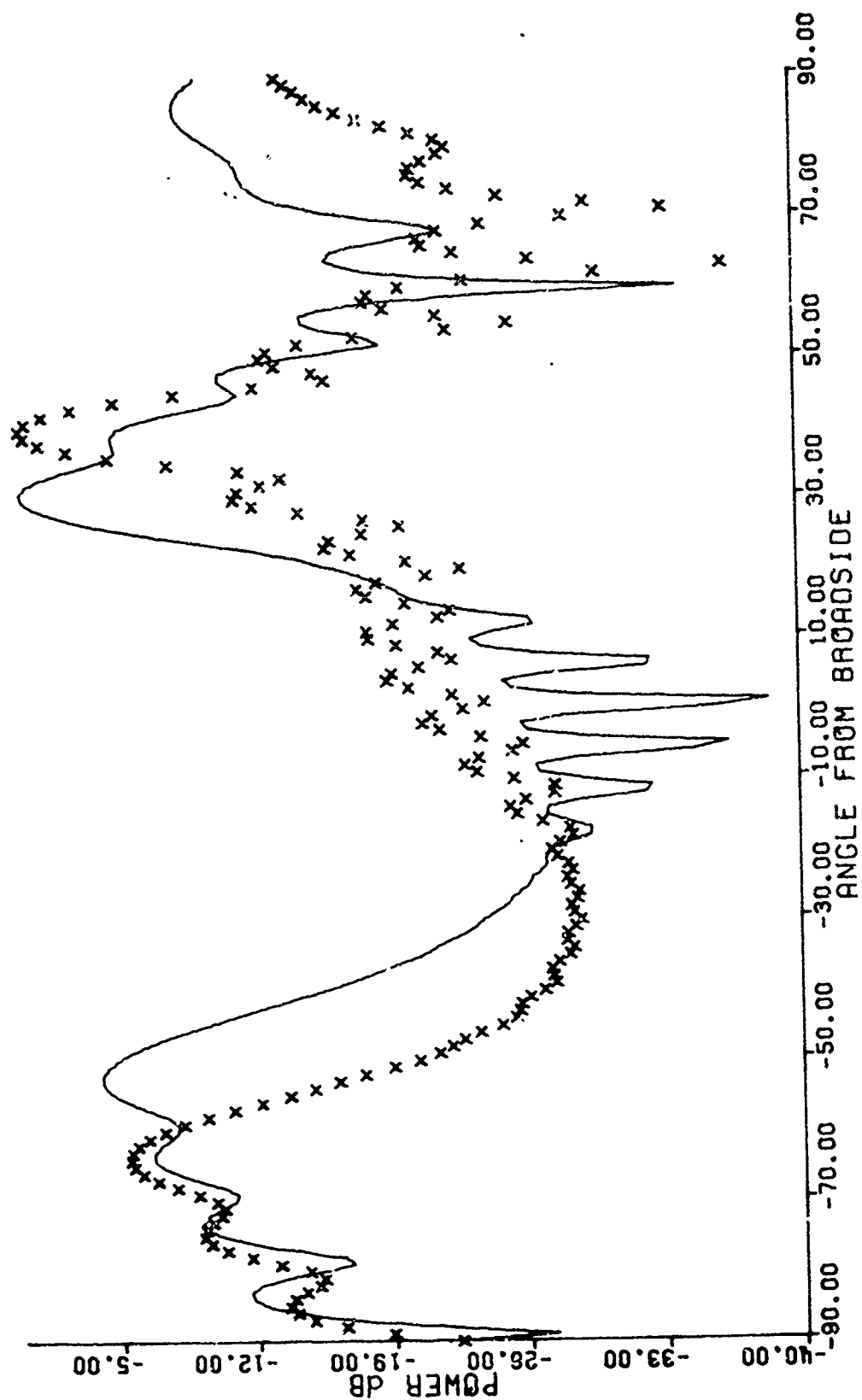


Figure 32-9 (Continued)



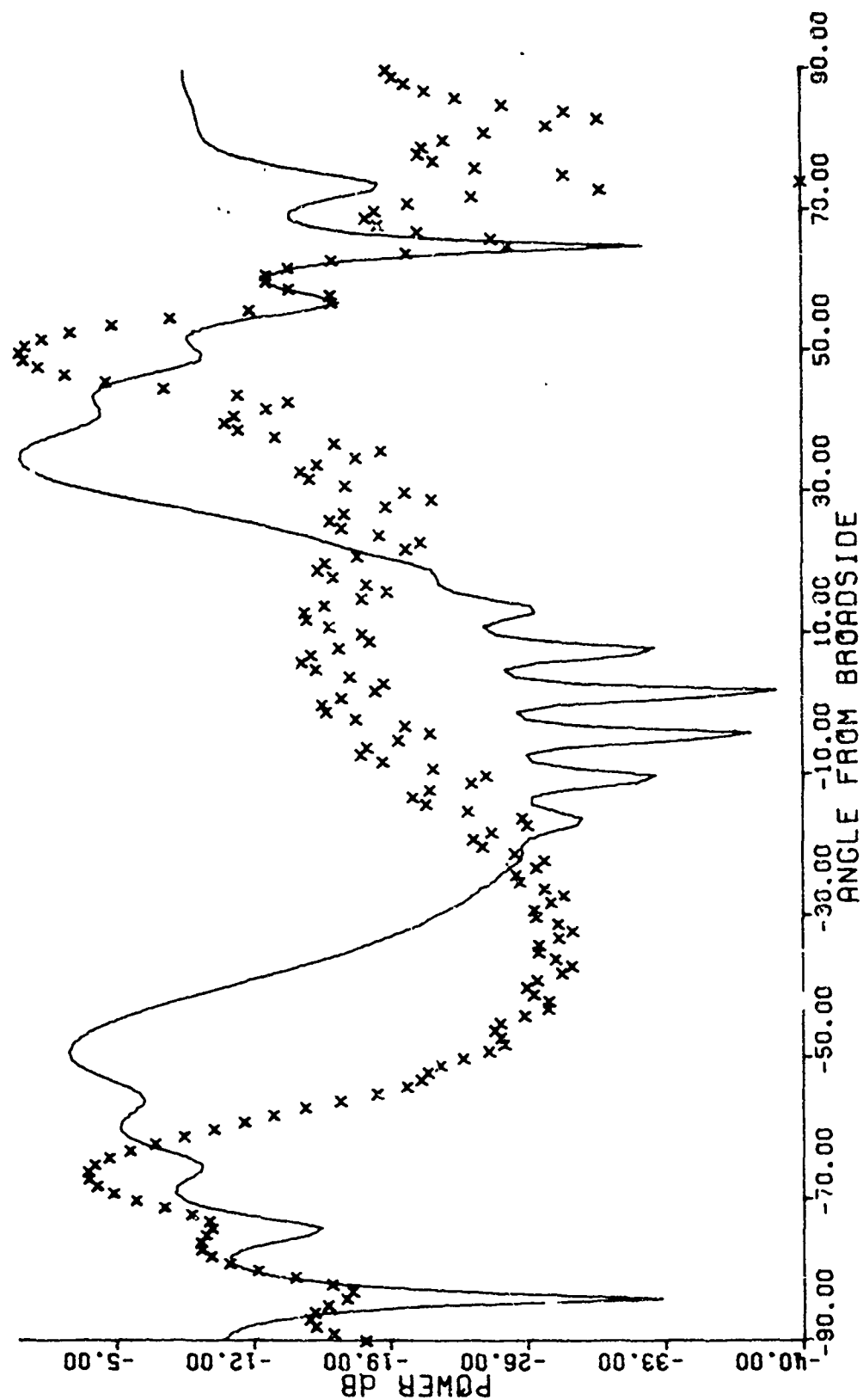
D. BPD, 30°

Figure 32-9 (Continued)



E. BPD, 40°

Figure 32-9 (Continued)



F. BPD, 50°

Figure 32-9 (Continued)

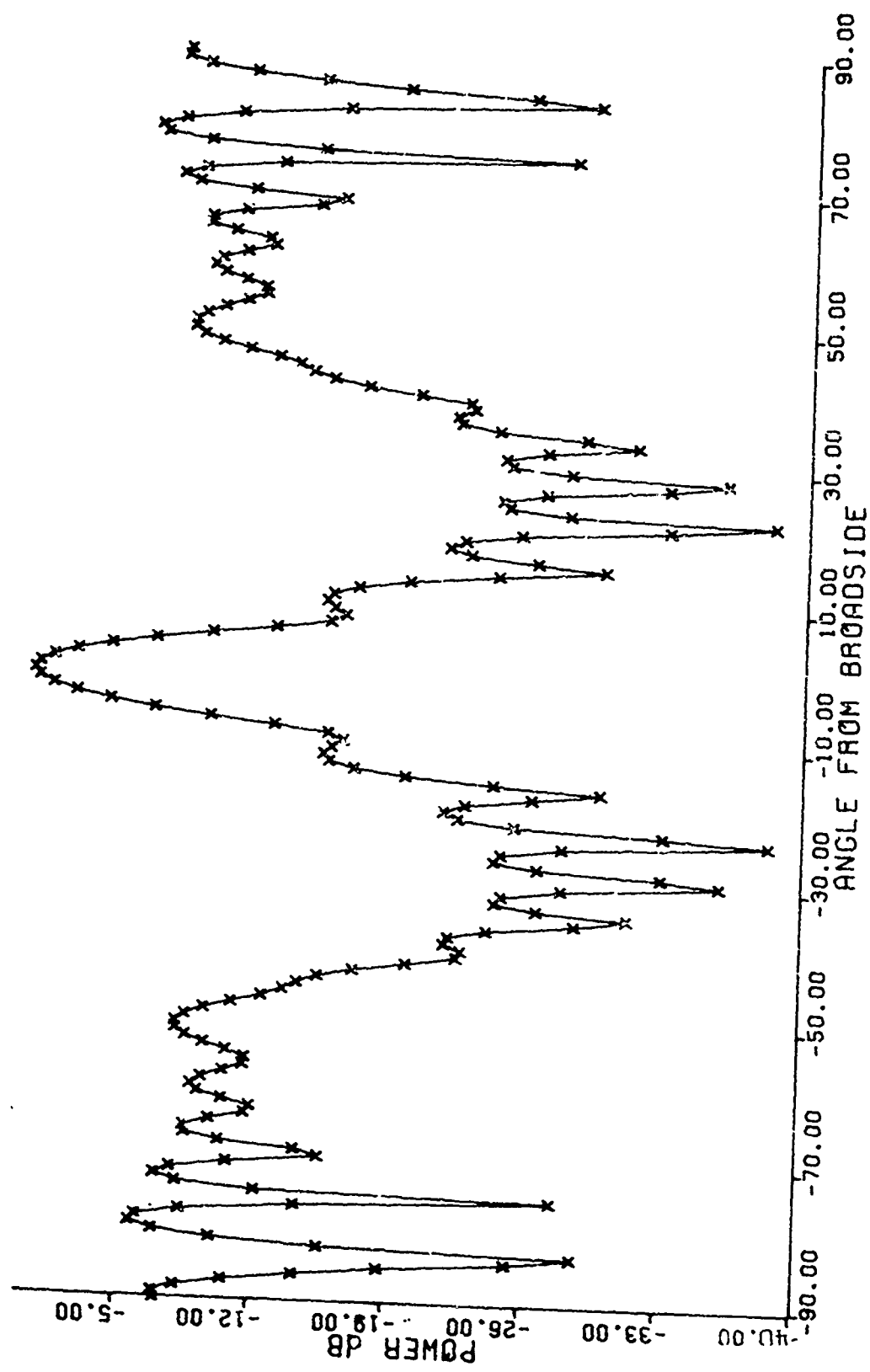
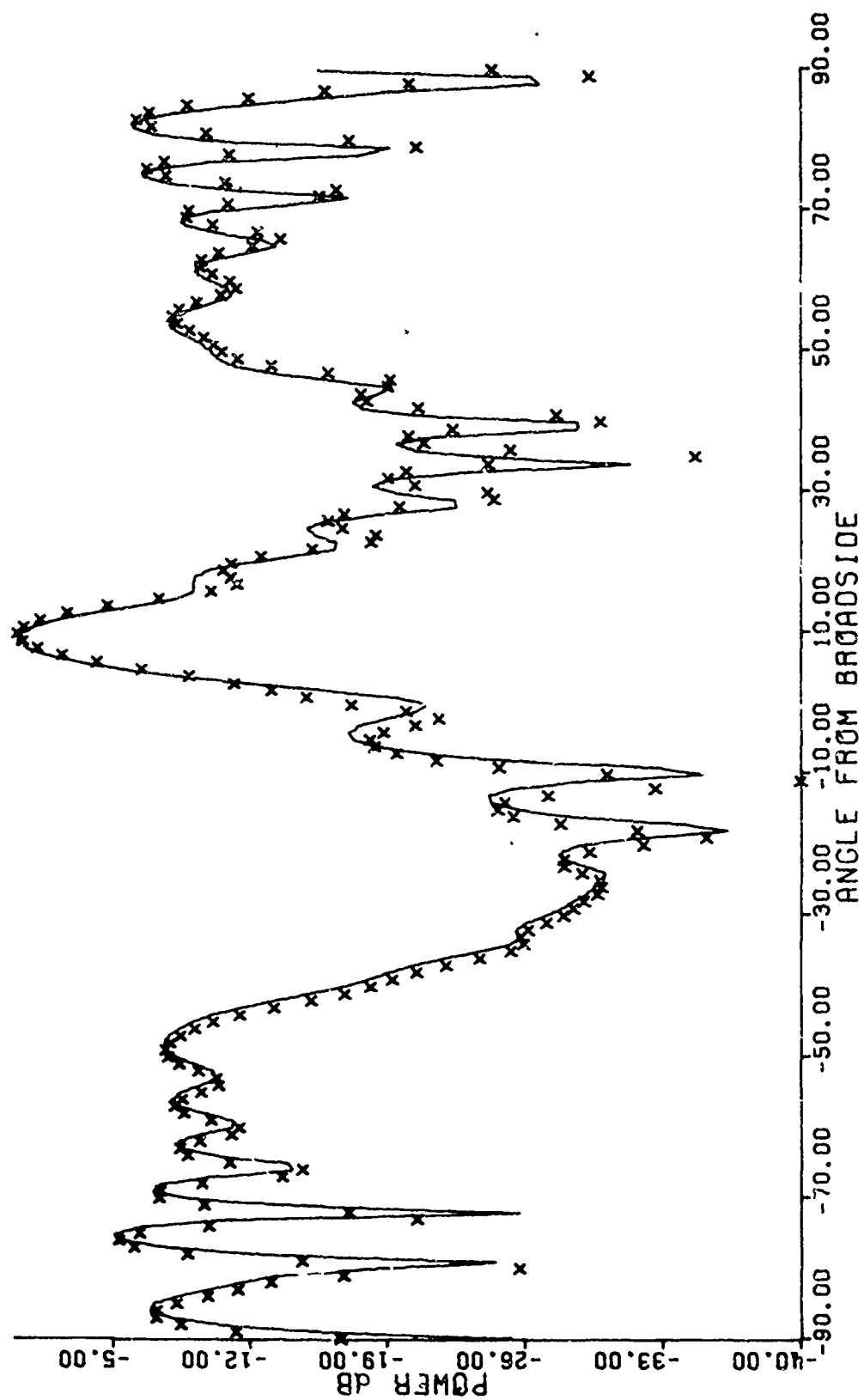
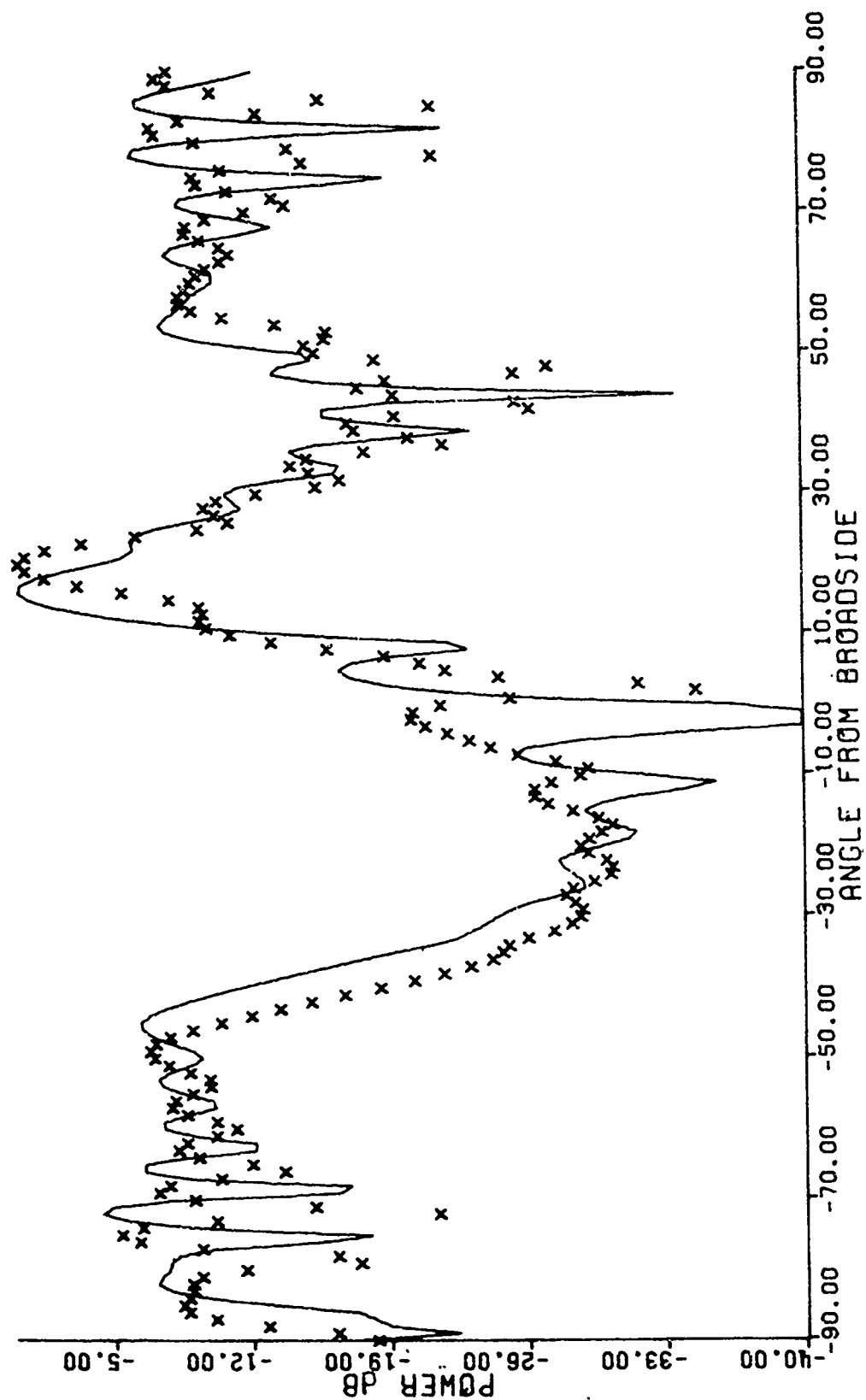


Figure 32-10. Pattern of 19 elements on a parabola. Element spacing, 0.5 wavelength projected on the X-axis. Element patterns are evenly weighted cos patterns. $P = 0.5$.
A. BPD, 0°



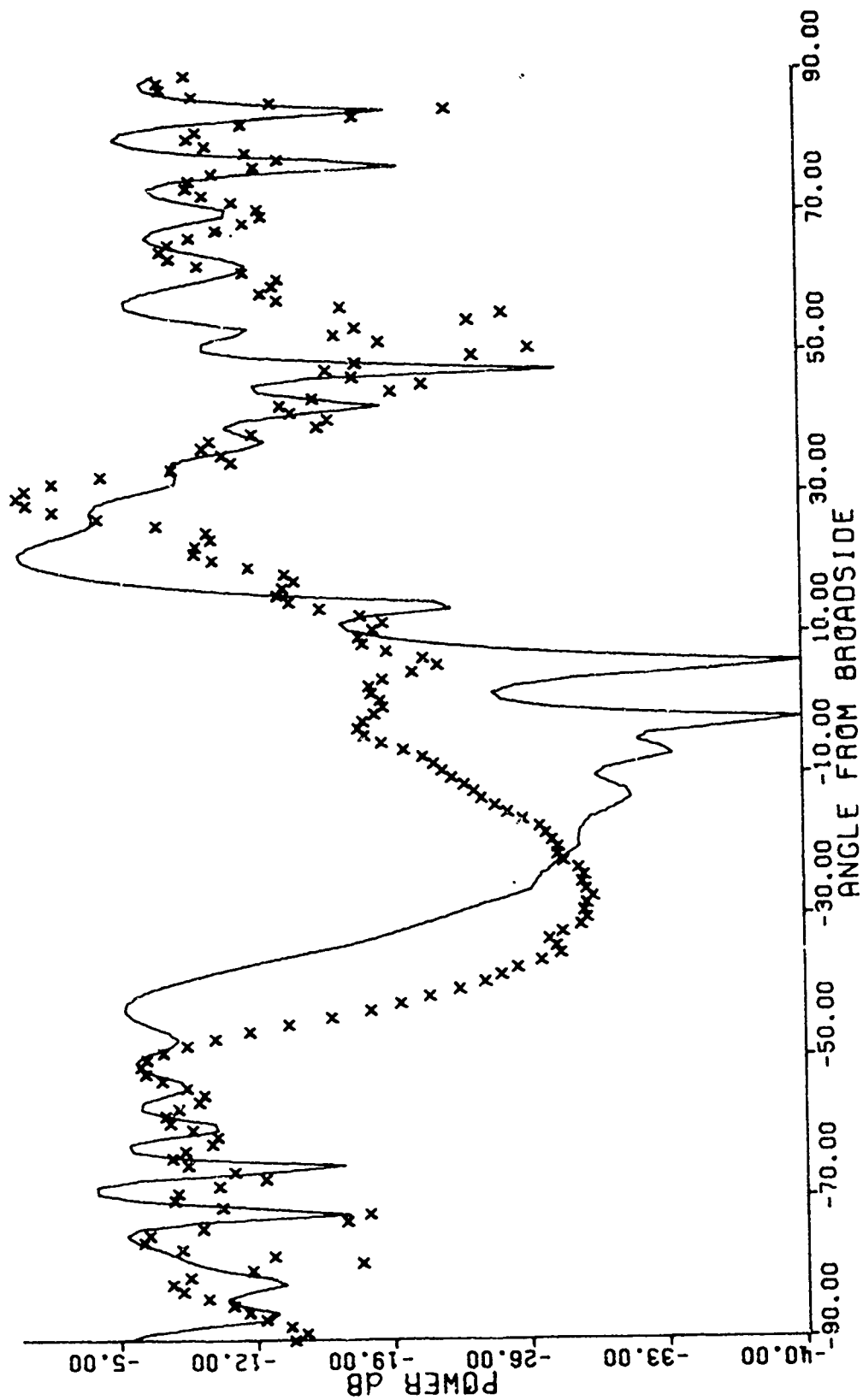
B. BPD, 10°

Figure 32-10 (Continued).



C. BPD, 20°

Figure 32-10 (Continued).



D. BPD, 30°

Figure 32-10 (Continued).

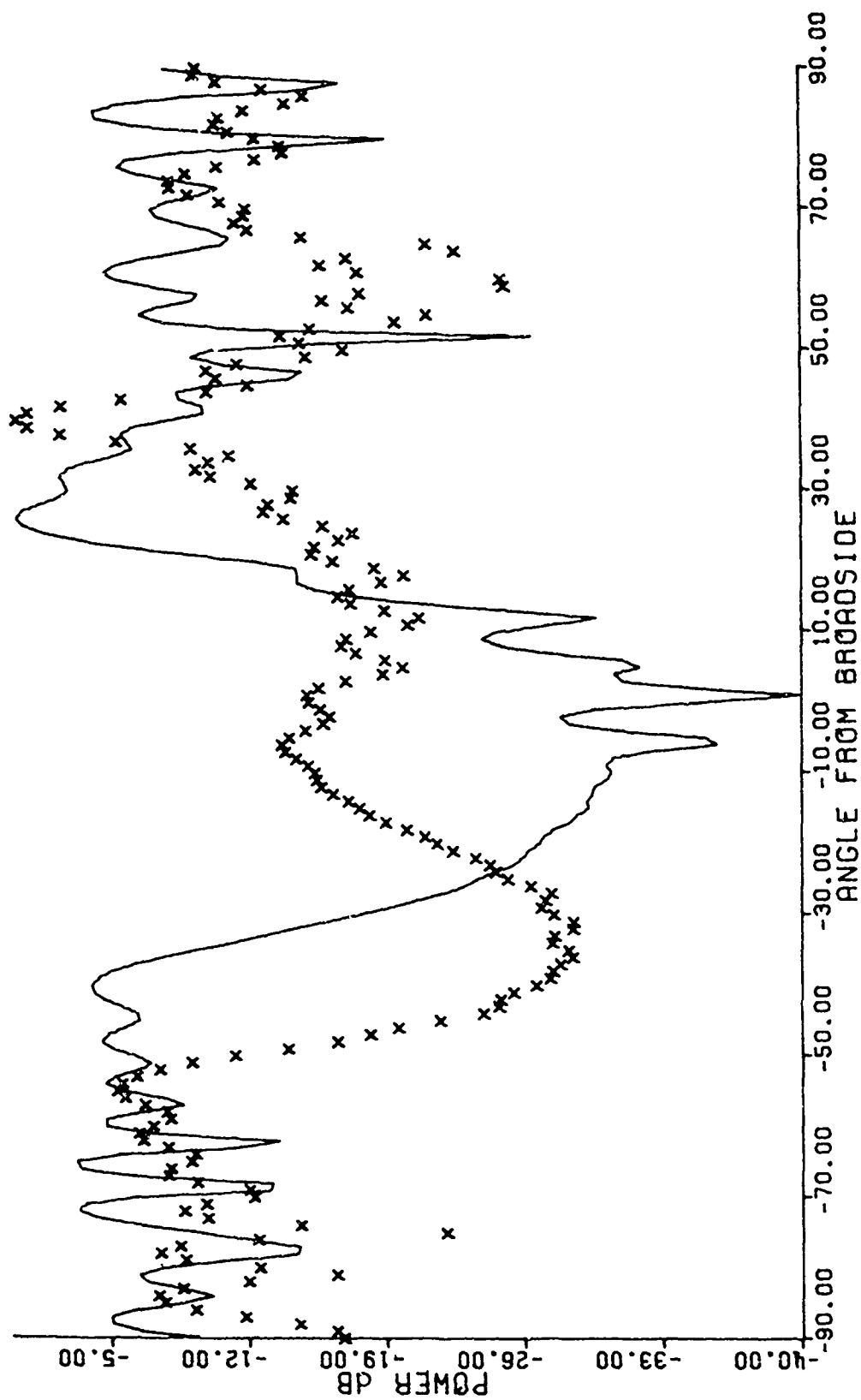


Figure 32-10 (Continued).
E. BPD, 40°

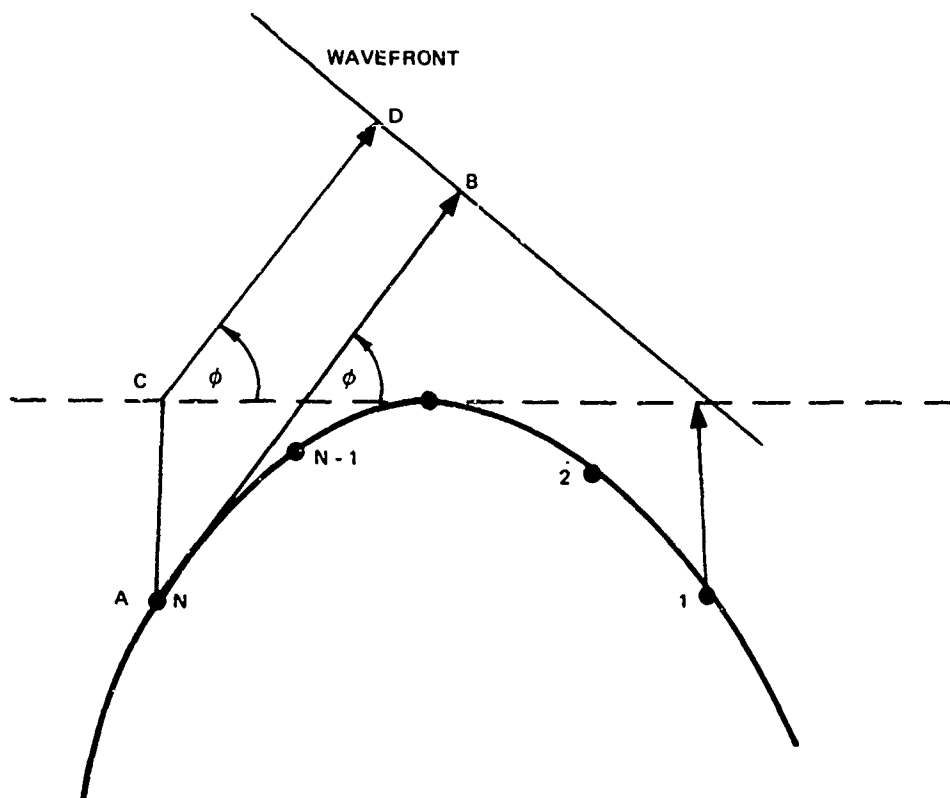


Figure 32-11. Geometry of conformal array, showing approximation used.

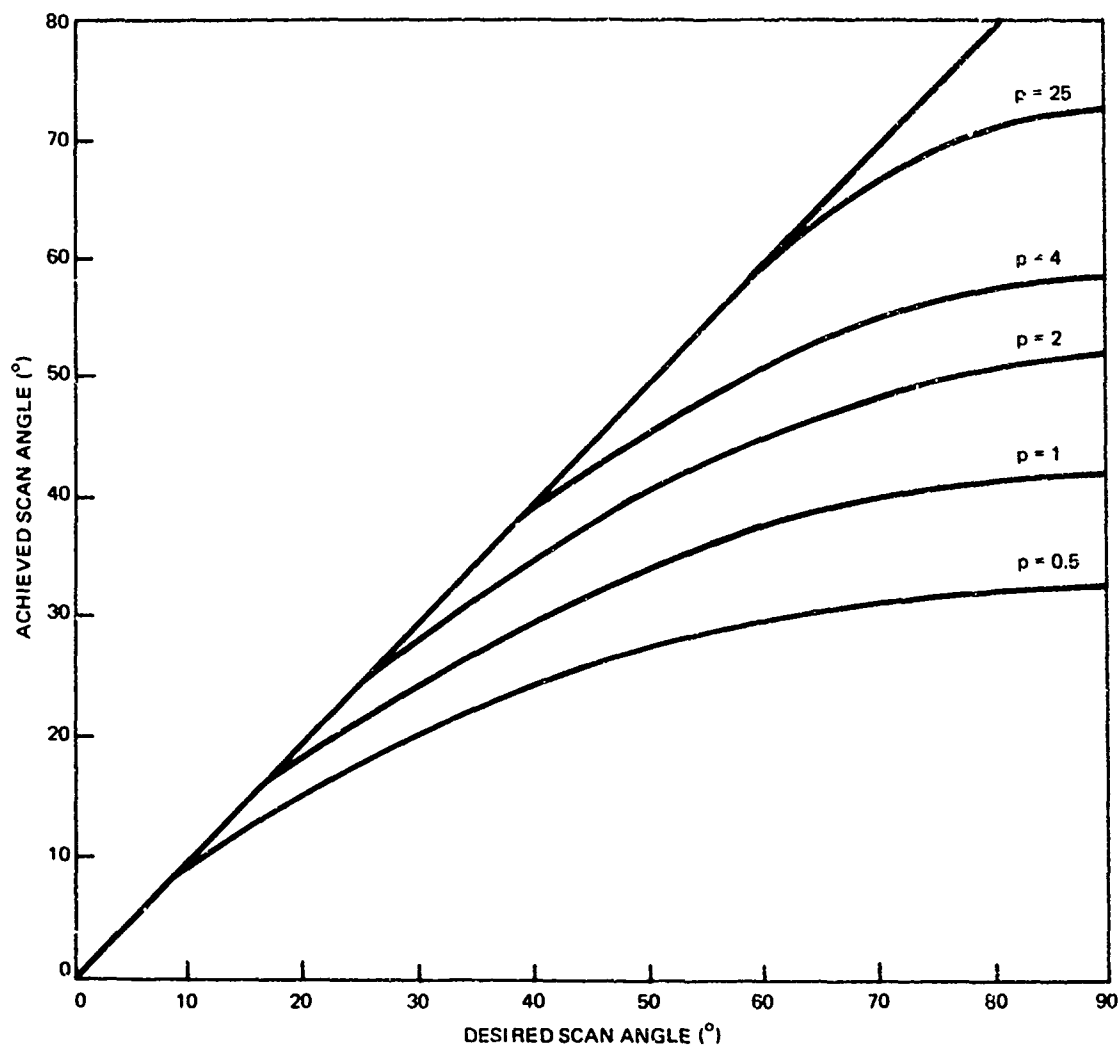


Figure 32-12. Achieved scan angle versus desired scan angle.

CONCLUSIONS

This phasing technique can be used on general conformal arrays. Beam pointing errors increase as the beam is steered off broadside and as the radius of curvature of the conformal surface decreases. This technique could be used where the curvature is slight (less than $p=2$) or where only limited steering angles are needed.

APPENDIX: DERIVATION OF EQUATIONS USED IN CONFORMAL ARRAY PROGRAMS

Figures 32-A1 and 32-A2 show the geometry of two elements on a conformal surface. The coordinates of the elements are given by X_1, Y_1 and X_n, Y_n . The element at X_1, Y_1 is the reference element and all phases are measured with respect to this element. The amount of phase shift required at the n^{th} element to point the beam in the θ direction is given by

$$\psi_n = \pm \sqrt{(X_n - XX)^2 + (Y_n - YY)^2} \cdot 2\pi/\lambda$$

where

$$XX = \frac{X_n + X_1 \tan^2 \theta + (Y_n - Y_1) \tan \theta}{1 + \tan^2 \theta}$$

$$YY = Y_1 + (XX - X_1) \tan \theta$$

θ is positive in the counterclockwise direction. In figure 32-A1 a phase delay is necessary at the n^{th} element in order to point the beam in the θ direction. In figure 32-A2 a phase advance is necessary to direct the beam in the θ direction.

In order to test for the direction of the phase shift a cross product is formed, $V_1 \times V_n > 0$ indicates a phase delay and $V_1 \times V_n < 0$ indicates a phase advance.

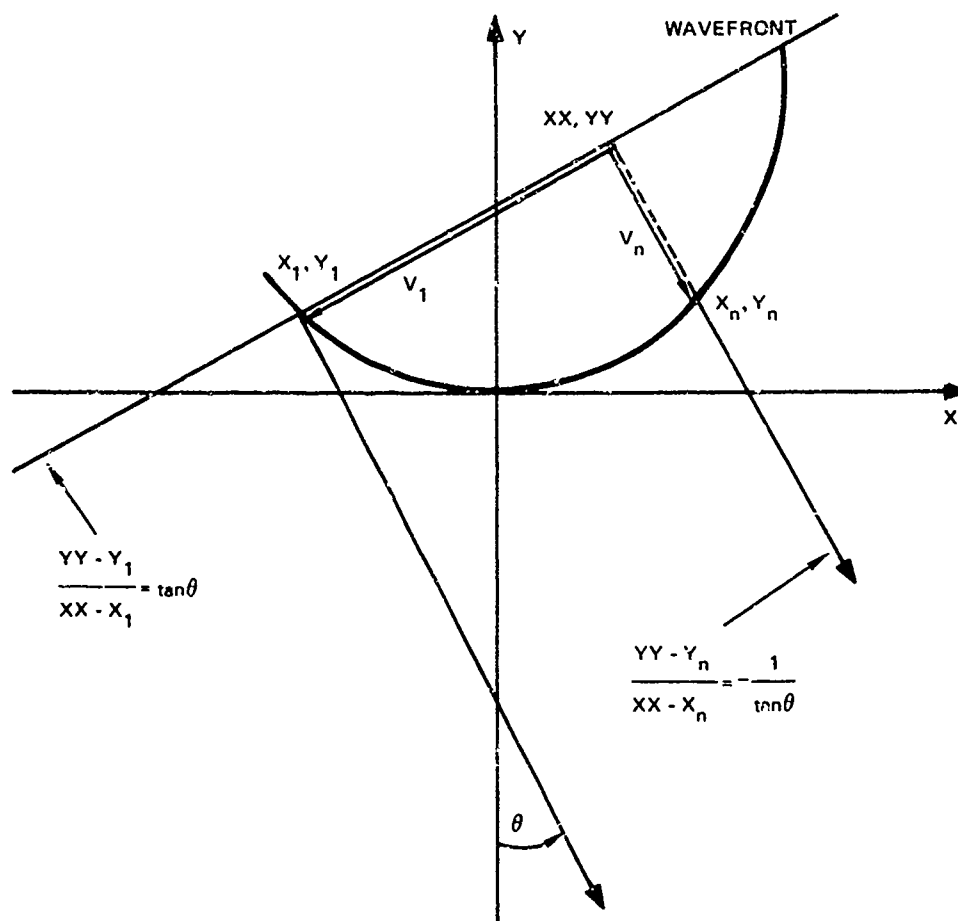


Figure 32-A1. Geometry of two elements on a conformal array steered $+\theta$ degrees.

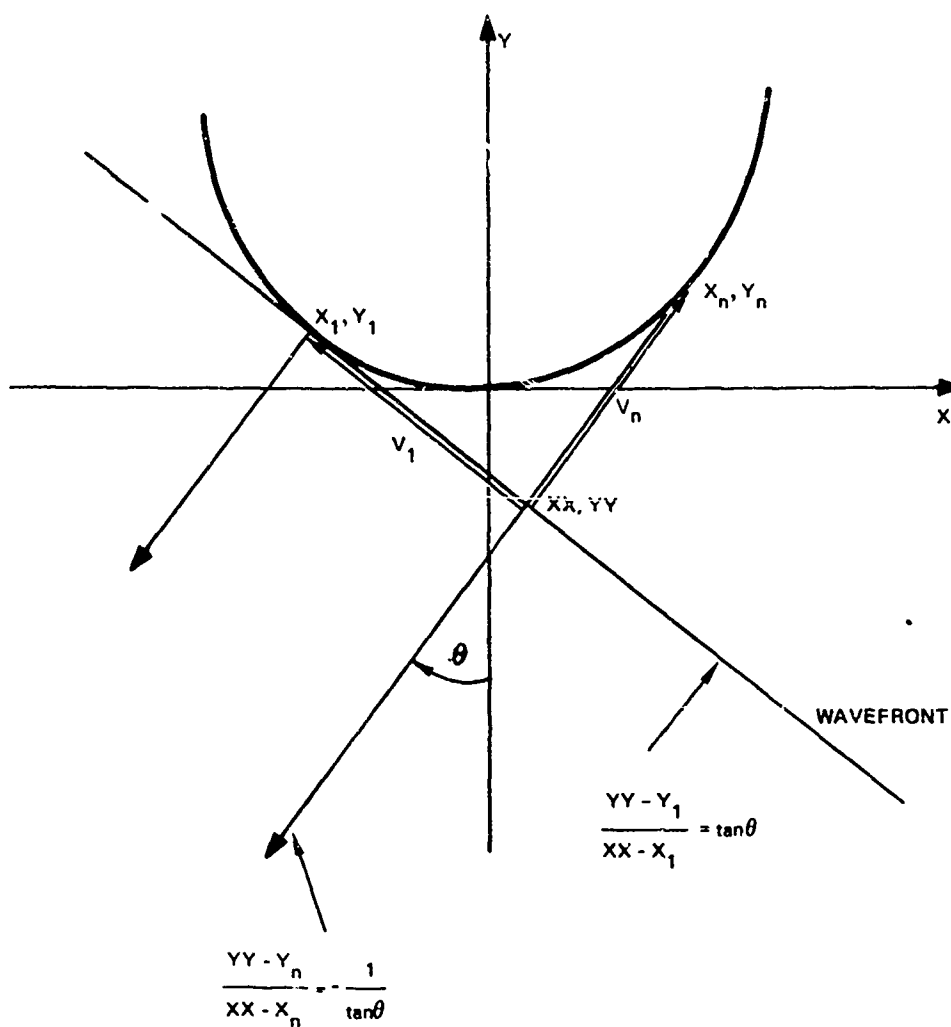


Figure 32-A2. Geometry of two elements on a conformal array steered $-\theta$ degrees.

33. BEAM SYNTHESIS TECHNIQUES FOR CONICAL ARRAYS*

by

A. T. Villeneuve and A. F. Seaton

Radar Division
Aerospace Group

Hughes Aircraft Company
Culver City, California 90230

for

ARRAY ANTENNA CONFERENCE

Naval Electronics Laboratory Center
San Diego, California

22, 23, 24 February 1972

*The work reported in this paper was sponsored by the Naval Air
Systems Command under Contract N00019-70-C-0397.

33-1a

ABSTRACT

An equivalence principle is applied to the problem of determining the distribution of sources on a cone to produce a prescribed pattern. By this method, more conventional sources such as planar or linear arrays are replaced by sources on a conformal surface such as a cone. ~~The method and patterns synthesized by it are discussed. A second,~~ largely heuristic, synthesis technique is based on trial element arrangements that are realizable. Promising arrangements are programmed for the computer and various patterns computed. Approximations and simplifications are made wherever possible.

GENERAL APPROACH TO ANTENNA PATTERN SYNTHESIS FROM SOURCES ON A CONDUCTING SURFACE

INTRODUCTION

The problem of interest is that of forming various antenna patterns by distributing sources over a conducting curved surface. No direct synthesis techniques are available when the sources are distributed over general curved surfaces. However, synthesis techniques are available for planar apertures. In this paper a technique is described that synthesizes the types of patterns obtainable from planar apertures by distributing sources over curved surfaces.

EQUIVALENCE PRINCIPLE

The initial problem is to produce the pattern of a conventional antenna, such as is illustrated in Figure 1, by sources on a curved surface. The conventional antenna is represented by a source distribution \bar{J}_i , \bar{M}_i of electric and magnetic currents that produce the desired fields \bar{E} , \bar{H} as illustrated in Figure 2.

If the actual sources are surrounded by a closed mathematical surface S , the fields \bar{E} , \bar{H} exterior to S will result if the actual sources are replaced by equivalent sources \bar{J}_s and \bar{M}_s on S where¹

$$\bar{J}_s = \bar{n} \times \bar{H} \quad (1a)$$

$$\bar{M}_s = \bar{E} \times \bar{n} \quad (1b)$$

and \bar{n} is the exterior unit normal to S as illustrated in Figure 3.

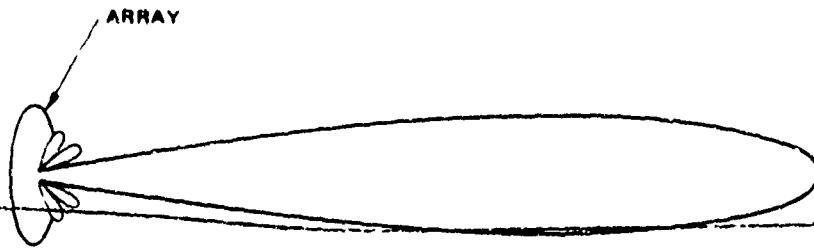


Figure 1. Array with conventional pattern



Figure 2. Sources and resulting fields

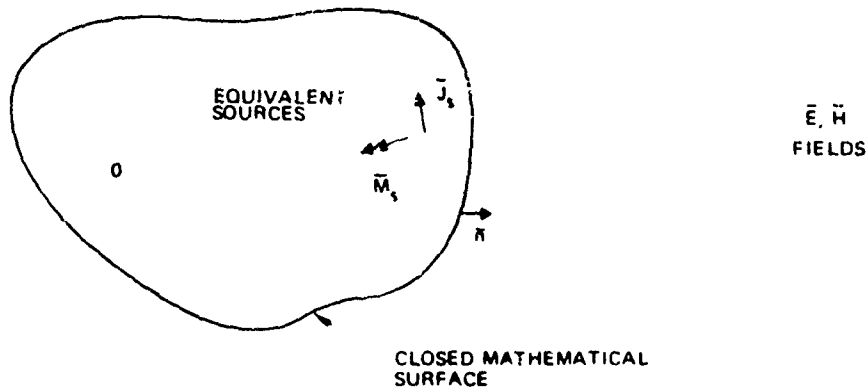


Figure 3. Equivalent sources on mathematical surface

The equivalent sources produce no fields within S . Consequently, the mathematical surface S may be replaced by a perfectly conducting surface that lies just inside the equivalent source currents \vec{J}_s and \vec{M}_s without affecting the external fields \vec{E} , \vec{H} as shown in Figure 4. The perfectly conducting surface short circuits the electric source currents. Therefore, the total field outside the surface may then be found using only the magnetic currents \vec{M}_s radiating in the presence of the conductor as shown in Figure 5.

Consequently, if the proper equivalent magnetic source currents can be synthesized on the conducting surface, the original field will

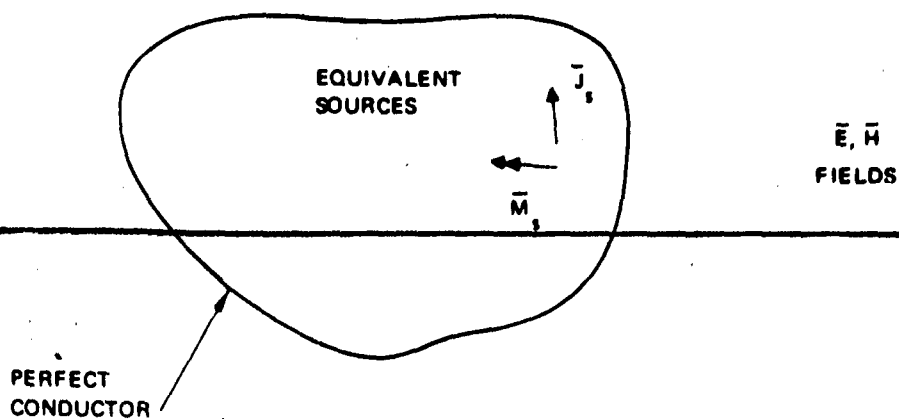


Figure 4. Equivalent sources on conducting surface

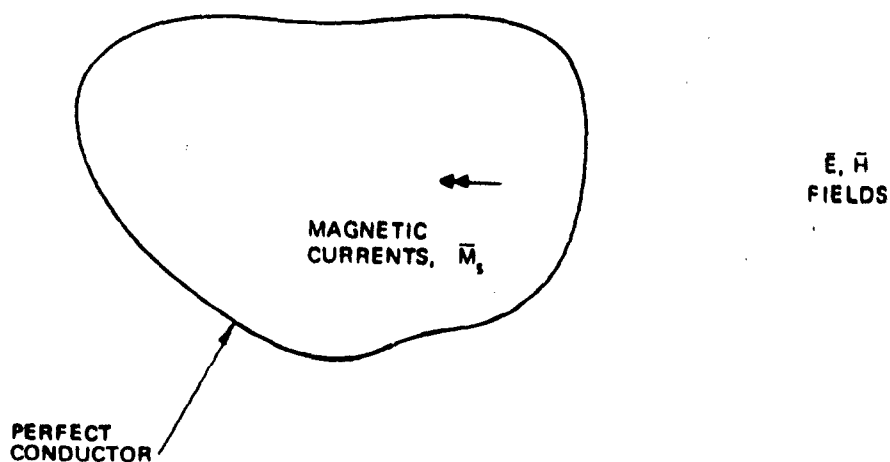


Figure 5. Equivalent magnetic sources on conducting surface

result at all points exterior to the surface. As a case of interest, the original source might be a planar array and the curved metal surface might be a conical or ogival surface. The magnetic current sheets are surface distributions of magnetic dipoles. A magnetic dipole can be approximated by a slot on a conducting surface. By proper orientation and excitation of slots on the metallic surface, the desired exterior field can then be approximated. The required source distribution is known exactly since the initial fields are known. In the following discussion this approach is applied to finding the equivalent sources on a cone to reproduce the pattern of a planar array.

DETERMINATION OF SOURCES ON A CONDUCTING CONE TO PRODUCE A PRESCRIBED PATTERN

The antenna utilized in determining the sources on a cone that are equivalent to a planar array is illustrated in Figure 6. It is a circular planar array of parallel slots that may be oriented arbitrarily within the conical surface.

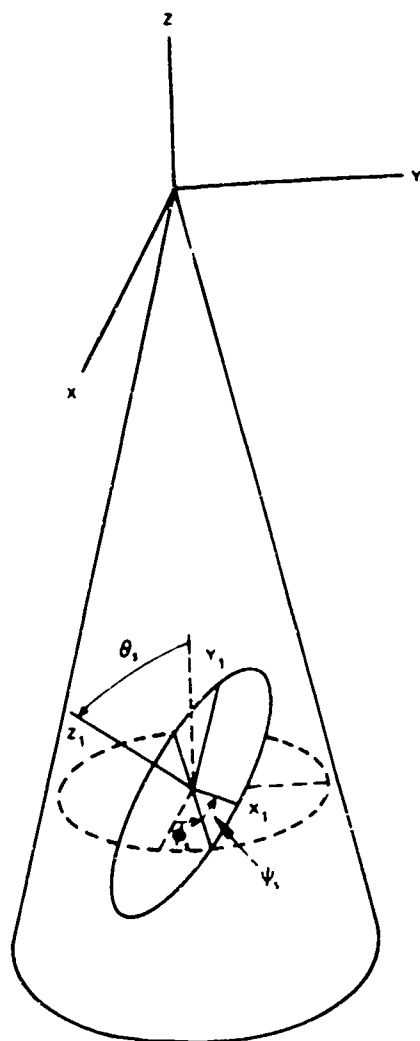


Figure 6. Planar array located within conical surface

In accordance with the field equivalence principle, the free space pattern of this array can be approximated by magnetic sources on the conducting cone that approximate the electric field strength that would be produced over the conical surface by the array. The coordinate system fixed with respect to the planar array is a rectangular system denoted by x_1, y_1, z_1 , with its origin at the array center. The slots are directed parallel to the y_1 axis.

The surface on which the calculation of electric field strength is desired is the conical surface for which the x, y, z coordinates are expressible in spherical coordinates as

$$x = r \sin \theta_0 \cos \phi \quad (2a)$$

$$y = r \sin \theta_0 \sin \phi \quad (2b)$$

$$z = r \cos \theta_0 \quad (2c)$$

where θ_0 is the cone angle measured from the positive z -axis. The equivalent magnetic source currents that must be set up on the conducting conical surface to provide the same external fields and, hence, the same pattern are given by

$$\vec{M} = \vec{E} \times \vec{n} = \vec{u}_\theta \times \vec{E} \quad (3)$$

The far-field radiation pattern from these sources will be the same as that of the original planar array. A computer program that calculates M_r and M_ϕ at selected points on a conical surface has been written.

The magnetic source currents required have been computed along rings on the surface of the cone separated along the radial direction by 0.7 wavelength. The equivalent planar array had half-wavelength slots spaced at 0.7-wavelength intervals on a square grid whose lines were parallel to the x_1 and y_1 axes. The cone had an angle, θ_0 , of 170 degrees with a base diameter of 5.08 wavelengths. Magnetic currents were then calculated for two cases:

- A uniformly illuminated planar array directed to point along the cone axis
- The same array directed to point a vertically polarized beam in the direction $\theta_p = 20$ degrees, $\phi_p = 0$ degrees.

The amplitudes and phases of the radial and circumferential components of the currents on rings about the cone are shown in Figures 7 through 10. In these figures the phases of the radial and circumferential magnetic current densities are denoted as ψ_r and ψ_ϕ , respectively. Since the magnitudes are all symmetrical about

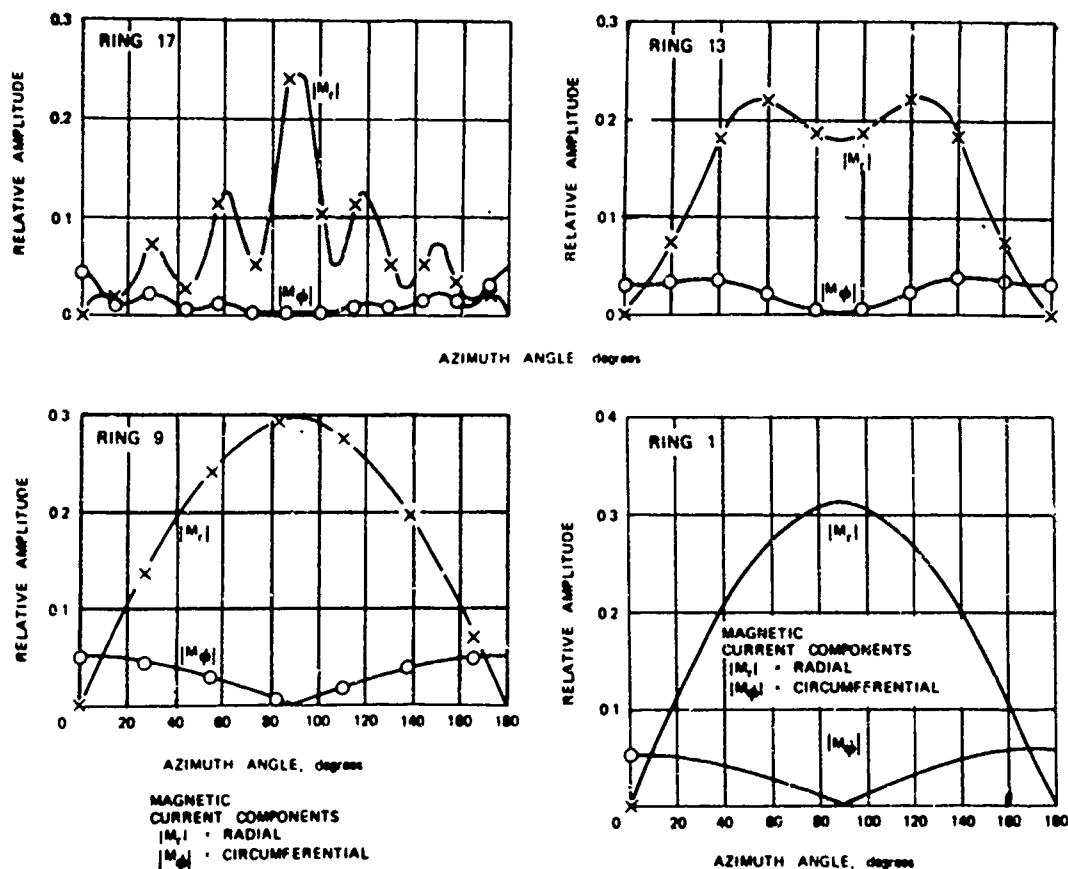


Figure 7. Magnitude of radial and circumferential components of equivalent magnetic source currents on surface of conducting cone to produce an x-polarized on-axis pencil beam

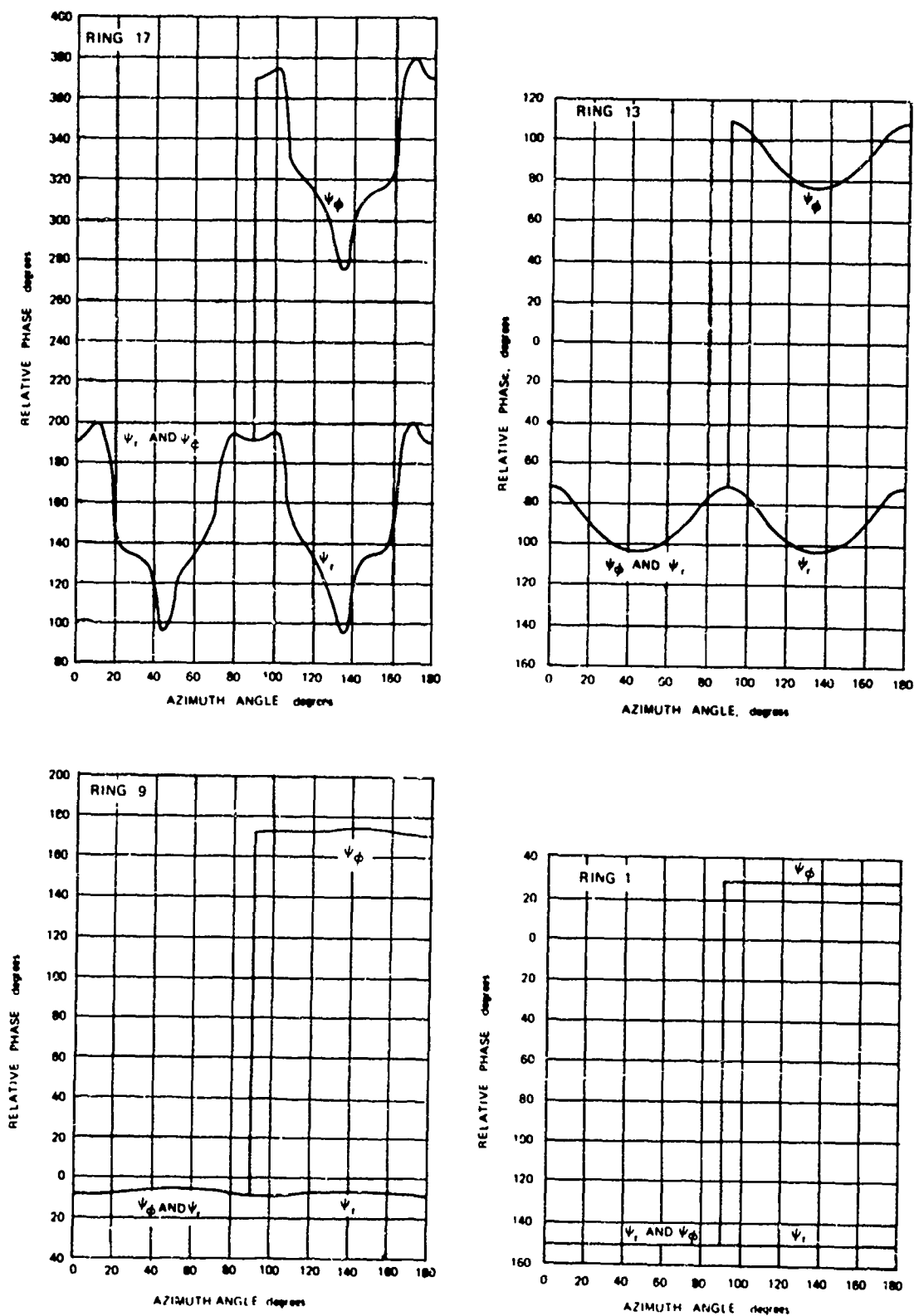


Figure 8. Phase of magnetic source currents of Figure 7

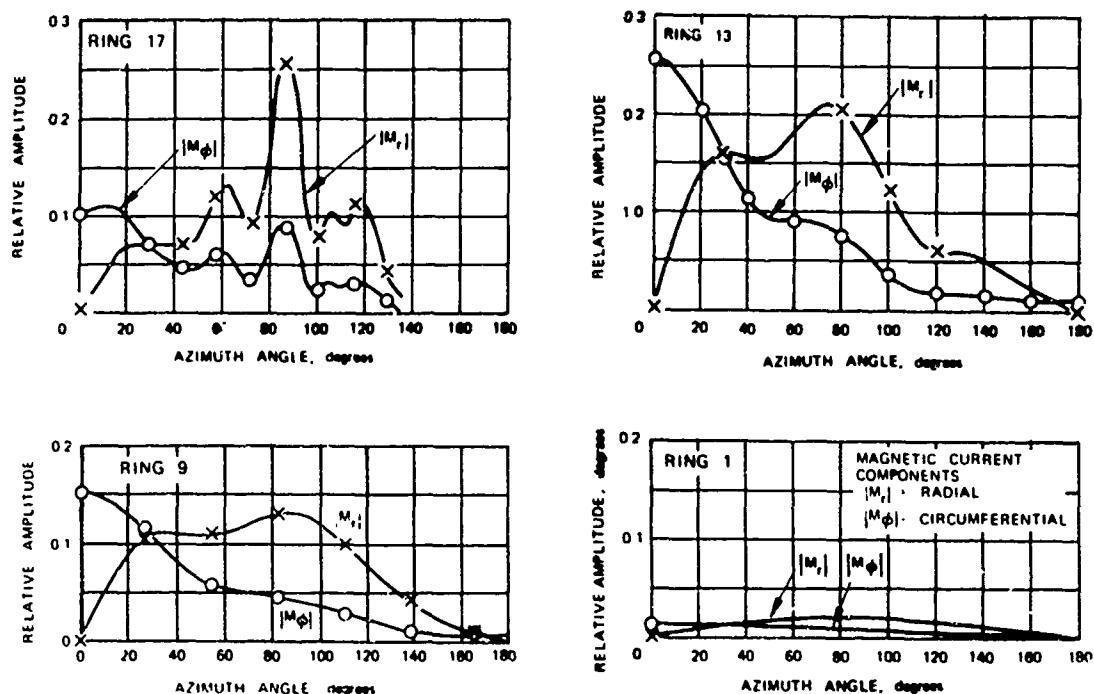


Figure 9. Magnitude of radial and circumferential components of equivalent magnetic source currents on surface of conducting cone to produce a θ -polarized beam in the direction $\theta = 20$ degrees, $\phi = 0$ degree

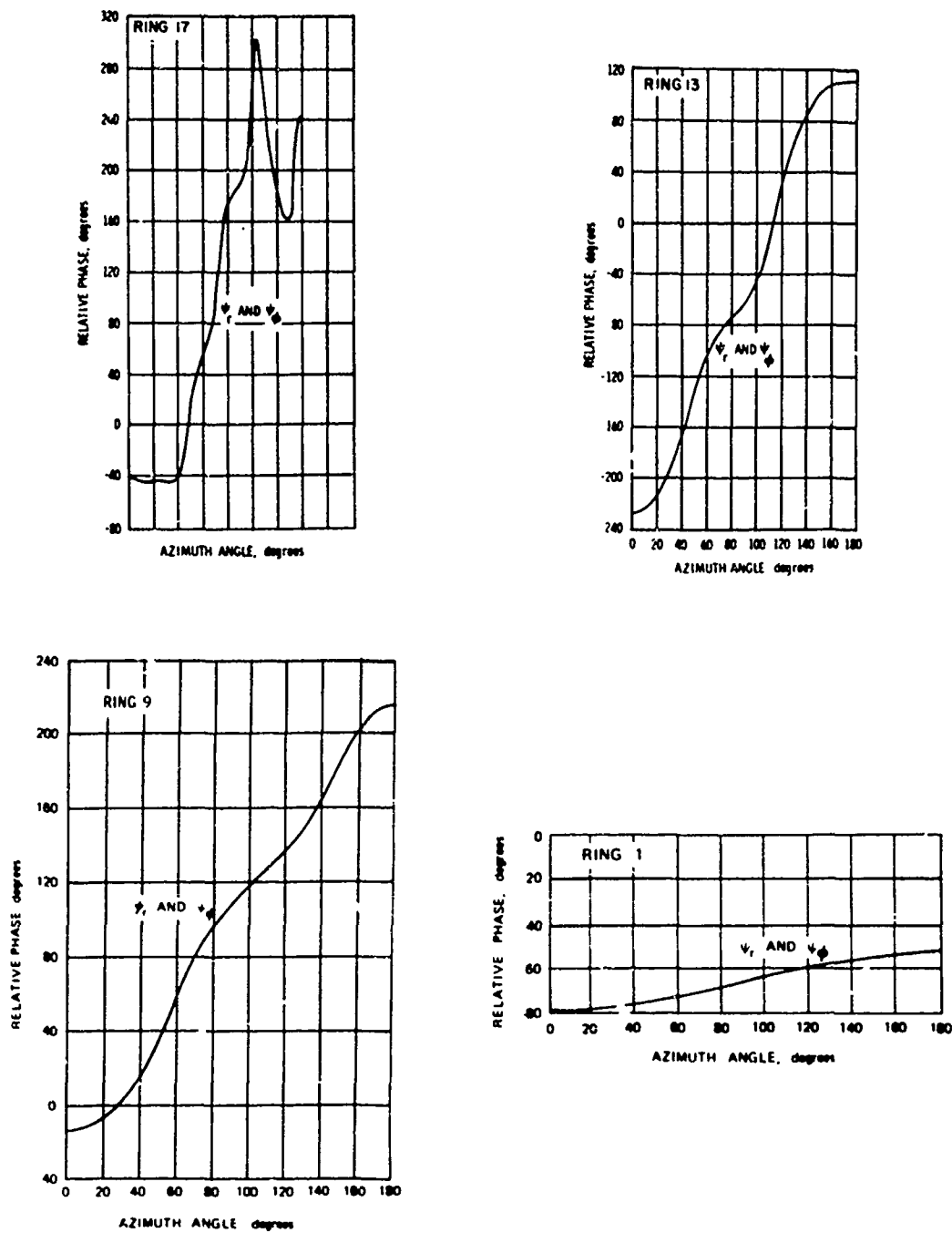


Figure 10. Phase of magnetic source currents of Figure 9

$\phi = 0$ degree, they are only shown in the range $0 \text{ degree} \leq \phi \leq 180$ degrees. The phase ψ_ϕ is also symmetrical about $\phi = 0$ degree. The phase ψ_r is shifted by 180 degrees in the range $180 \text{ degrees} \leq \phi \leq 360$ degrees as compared with its value in the range $0 \text{ degree} \leq \phi \leq 180$ degrees. The rings are numbered from the cone tip: ring 1 is 0.7-wavelength from the tip, ring 2 is 1.4 wavelengths from the tip, etc.

The symmetry of the distributions is evident for the case in which the planar array looks directly through the nose of the cone (Figures 7 and 8). It is also evident that the radial currents (slots) are most heavily excited in this case.

For the case in which the planar array looks through the side of the cone (Figures 9 and 10), at $\phi_p = 0$, the heaviest excitation of the cone lies in the region about $\phi = 0$, as would be expected. In addition, the ϕ -directed magnetic currents (slots) are more heavily excited than in the former case.

In any practical situation, the required magnetic current density can only be approximated by discrete magnetic sources distributed over the conical surface. Consequently, the pattern that will result from the placement of discrete magnetic sources will deviate from the desired pattern. The seriousness of this deviation will depend on the spacing of the sources on the conical surface. This spacing should be as large as possible to minimize the number of sources required but will be limited by the amount of allowable pattern deterioration. Approximate patterns, resulting from slots on the cone excited in the manner indicated, are being computed. The slots are crossed slots with one arm lying along the generatrices and the other directed toward the azimuth. Such an arrangement allows both radial and circumferential magnetic currents to be synthesized.

The locations of elements about the cone are shown in Figure 7 and 9 by "x" for the radial current density and by "o" for the circumferential current density. They are not shown on the phase curves but only on the curves of magnitude.

PRAGMATIC APPROACH TO BEAM SYNTHESIS

INTRODUCTION

A second approach to generating steerable beams from a conical array is largely heuristic. Trial element arrangements that are realizable are chosen on the basis of past experience with planar and cylindrical arrays. The most promising arrangements are then programmed for the digital computer and various patterns computed. Simplifications and approximations are made wherever possible to keep computer time from becoming excessive.

APPROXIMATE ONE-DIMENSIONAL SCANNING

It is very attractive to attempt to find arrangements of elements that are geometrically regular and that will not give rise to grating lobes over the scan angles of interest. In this section this problem is studied and several possible arrangements are considered for crossed-waveguide radiators.²

In the conical array advantage can be taken of the circular symmetry of the surface to reduce the steering problem essentially to that of scanning in one dimension only. Figure 11 shows an end-on view of the cone with the shaded portion representing the excited area of the surface. If the beam lies in the plane perpendicular to the cone axis, its position will be as shown in the figure — and symmetrical with respect to the active area of the array. If the beam is scanned toward endfire while ϕ_1 is held fixed, it can be seen that the projection of the beam onto the plane of the paper will still fall at ϕ_1 . Hence, the active area is still symmetrically located with respect to the beam. The beam can be thought of as being broadside to the cone in the ϕ plane and capable of being electronically scanned in the plane θ at passes through the cone axis (the θ plane).

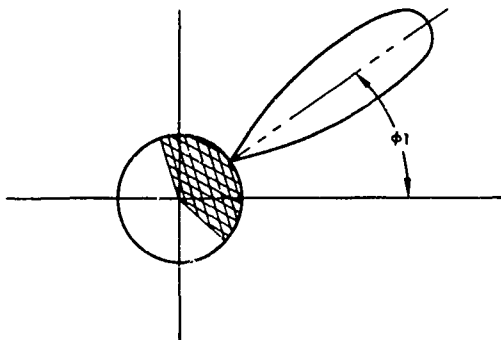


Figure 11. Excited portion of cone for beam pointing to ϕ_1

If the beam is now steered around in the ϕ plane to ϕ_2 , ideally the active portion of the array will follow it to maintain a symmetrical relationship with the new beam pointing direction as shown in Figure 12. Here also, the beam can be electronically steered toward endfire without changing the angle ϕ_2 or disturbing the symmetry conditions. Hence, it may be concluded that for any angle of ϕ , in the ideal case of a continuously illuminated aperture, the beam can be considered to be broadside to the cone in the ϕ plane and need

be electronically scanned only in the θ plane.

With a discrete number of elements on the cone, the ideal situation outlined above can only be approximated. However, if a reasonably large number of elements is used, the approximation will be quite close. For example, if 16 elements are used in the larger rings around the cone, the largest portion of the area of excitation can be switched in 22-1/2-degree steps. Thus, it is necessary to electronically scan the beam only $\pm 11-1/4$ -degrees off the perpendicular to the excited area to achieve full coverage around the axis of the cone by a sequence of switching and phasing operations. This concept has been applied to a cylindrical array at the Hughes Aircraft Company on another program and the array is called a switched-beam phased array. Since any one

active area of the cone scans only $\pm 11\frac{1}{4}$ -degrees in the ϕ plane, the interelement spacing in that plane need be only slightly less than the spacing required for an array that does not scan at all in that plane. Hence, the interelement spacing problem is reduced approximately to that associated with scanning in the θ plane only.

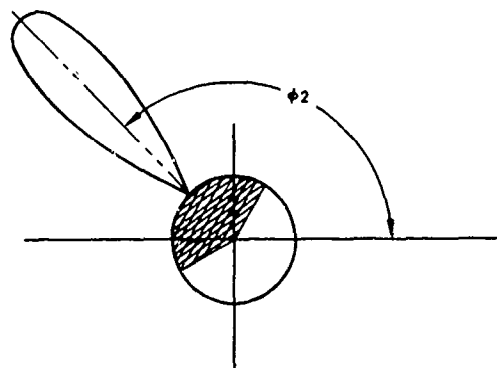


Figure 12. Excited portion of cone for beam pointing to ϕ_2

Cylindrical arrays that are phased to produce narrow beams tend to be more susceptible to grating lobe problems than do comparable planar arrays because of two factors: (1) On the sides of the active portion of the array the element patterns do not point in the direction of the beam; and (2) in this same region it is necessary to introduce a large interelement phase shift into the excitation to compensate for the curvature of the cylinder. The latter is equivalent to scanning the side portion of the array to some angle off the normal to the cylinder at that point; hence, the interelement spacing must be kept correspondingly small to prevent the formation of grating lobes.

The conical array can be thought of as a set of cylindrical arrays of different radii as a first-order approximation. Hence, it is to be expected that it, too, will have a tendency to have grating lobes in the ϕ plane. Therefore, it is anticipated that the interelement spacing in that plane will have to be kept smaller than would normally be necessary for an equivalent planar array. However, the fact that each circle of elements on the cone nearer the tip is smaller than the previous one may tend to alleviate this problem by introducing a modest amount of quasi-randomness into the element placement.

A more nearly continuous illumination in both principal axes of the cone can be achieved by staggering the elements in alternate circles as shown in Figure 13. Thus, although the actual spacing between any two elements on a circle with an 8-inch diameter is $1.2 \lambda_0$ (assuming 16 elements per circle), the effective spacing is only one-half that value. An interelement spacing of $0.6 \lambda_0$ is rather large for a circular array; however, each circle nearer the tip of the cone will bring the elements closer together until the point of physical interference is reached. The average interelement spacing in the ϕ plane for the section of the cone that has 16 elements per ring should thus be less than $0.5 \lambda_0$.

In the smaller regions of the cone, fewer elements will be needed per circle. The type of element to be used will influence the decision on just how many should be used in each circle. The crossed waveguide elements² can be fitted together quite closely on a flat surface

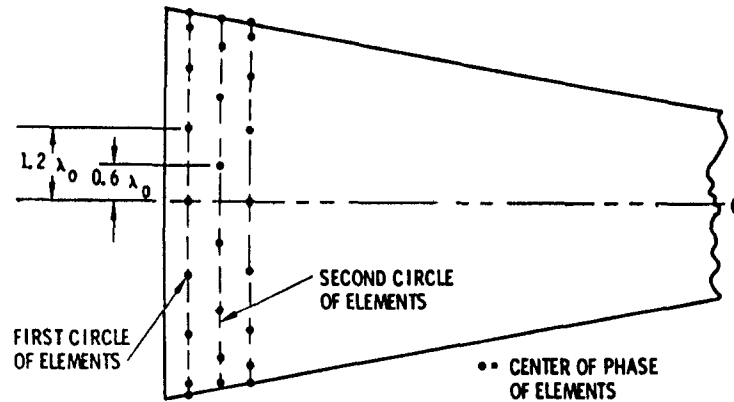


Figure 13. Effect of staggering elements in alternate circles on cone

provided that they are rotated at an angle of approximately 20 to 25 degrees, depending on wall thickness, to the principal axes of the lattice (see Figure 14). They can be brought most closely together on a curved surface if they still maintain that angle. When the elements in alternate circles are staggered in a symmetrical fashion, the lattice is rotated 45 degrees as shown in Figure 15.

PATTERN COMPUTATIONS

The unusual geometry of the cone requires special consideration of the coordinate system used to represent the patterns. It has been found that in some coordinate systems it is impossible to properly define the two principal planes of the beam when they are scanned to the nose-fire position.³ Hence, a special coordinate system was devised that follows the peak of the beam as it is scanned.⁴ The major requirement for the new coordinate system is that two fixed planes of the new system intersect the main beam of the antenna pattern at right angles. This requirement is satisfied by a variable spherical coordinate system, with angular coordinates ϕ' and θ' . The system is positioned so that $\phi' = 0$, $\theta' = 90$ degrees corresponds to the main beam pointing direction $\phi = \phi_1$, $\theta = \theta_1$. This variable coordinate system can be related to the fixed conventional coordinate system through the transformations presented in Reference 5. In this reference,

$$\cos \theta = \cos \theta' \sin \theta_1 + \sin \theta' \cos \phi' \cos \theta_1$$

$$\sin \theta = \sqrt{\sin^2 \theta' \sin^2 \phi' + (\sin \theta' \cos \phi' \sin \theta_1 + \cos \theta' \cos \theta_1)^2}$$

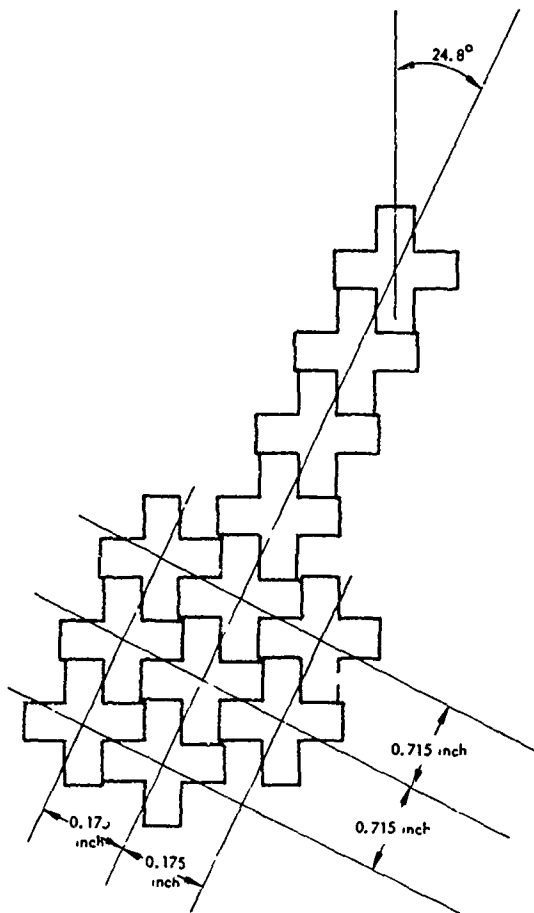


Figure 14. Tilted lattice for closest packing arrangement of crossed-waveguide elements

$$\sin \phi = \sin \theta' \sin \phi' / \sin \theta$$

$$\cos \phi = (\sin \theta' \cos \phi' \sin \theta_1 - \cos \theta' \cos \theta_1) / \sin \theta$$

The transformations have little effect on the pattern representations for broadside beam pointing directions (θ_1 near 90 degrees), but have considerable effect for end-fire beam pointing directions (θ_1 near 0 degree).

Another transformation is necessary to preserve the polarization of the test point used to perform the pattern plots. The test point polarization must be fixed in the Cartesian frame of the physical antenna cone. Again using Reference 5, the new polarizations are related to the old polarizations through

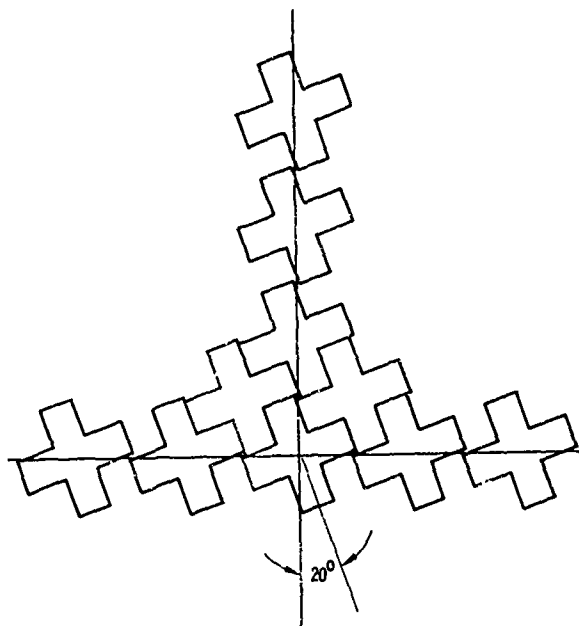


Figure 15. Crossed-waveguide elements tilted at angle of ~20 degrees in staggered arrangement to obtain closest packing

$$\begin{aligned}\frac{1}{\theta'} &= \frac{1}{\sin \theta'} \left[\frac{1}{\theta} (\cos \theta \cos \phi \cos \theta_1 + \sin \theta \sin \theta_1) - \frac{1}{\phi} \sin \phi \cos \theta_1 \right] \\ \frac{1}{\phi'} &= \frac{1}{\sin \theta'} \left[\frac{1}{\theta} \sin \phi \cos \theta_1 + \frac{1}{\phi} (\cos \theta \cos \phi \cos \theta_1 + \sin \theta \sin \theta_1) \right]\end{aligned}$$

For convenience, the new coordinates were renormalized as $\phi = \phi'$ and $\theta = \theta' - 90$ degrees, so that the main beam peak is always centered at $\phi = 0$ degree, $\theta = 0$ degree.

Using these modifications to the coordinate system, a computer program was written and a series of patterns calculated for a crossed-slot configuration that partially filled a cone. The slot arrangement consisted of six rings of crossed slots with 24 slots per ring. The two arms of each crossed slot were fed in such amplitude and phase that linear polarization of the proper orientation resulted at the peak of the beam. The large end only of the cone was filled with elements, and the ring nearest the tip was 10 wavelengths from it. Total length of the cone was $12.2 \lambda_0$ and the base had a diameter of $4.4 \lambda_0$. The elements thus extended only about 20 percent of the way from the base of the cone to its tip, and the computer patterns only present a rough indication of those of a completely covered cone.

In the calculations each element was weighted by the gain that it has in the direction of the peak of the beam. It was determined that this weighting yields the highest signal-to-noise ratio when the array is operating in the receiving mode.⁶

Figure 16 presents a series of patterns computed for a beam steered 20 degrees off the nose-fire position ($\theta_1 = 20$ degrees). These patterns represent only the desired component of polarization. There is a sizable cross-polarized component at some angles.

The asymmetry of the conical geometry impedes a straightforward presentation of the antenna patterns, as evidenced by the complexity of the set of pattern plots presented in Figure 16. A complete description of the antenna requires three-dimensional models for clarity. In an attempt to remedy the inherent confusion, the sum and difference patterns are presented in isometric views in Figure 17.⁴

PATTERN COMPUTATIONS FOR STAGGERED ELEMENT ARRANGEMENTS

The computer program used for the previous pattern computations was then modified so that it would handle elements arranged in a staggered configuration similar to that shown in Figure 13. Sixteen elements per ring were assumed for the initial computation. With that number of elements in each ring, it was estimated that 10 rings would fit on the cone. Thus, a total of 160 elements "filled" the large end of the cone. The small end of the cone was then left "empty." The diameter of the base of the cone was 6.2 inches and its total length was

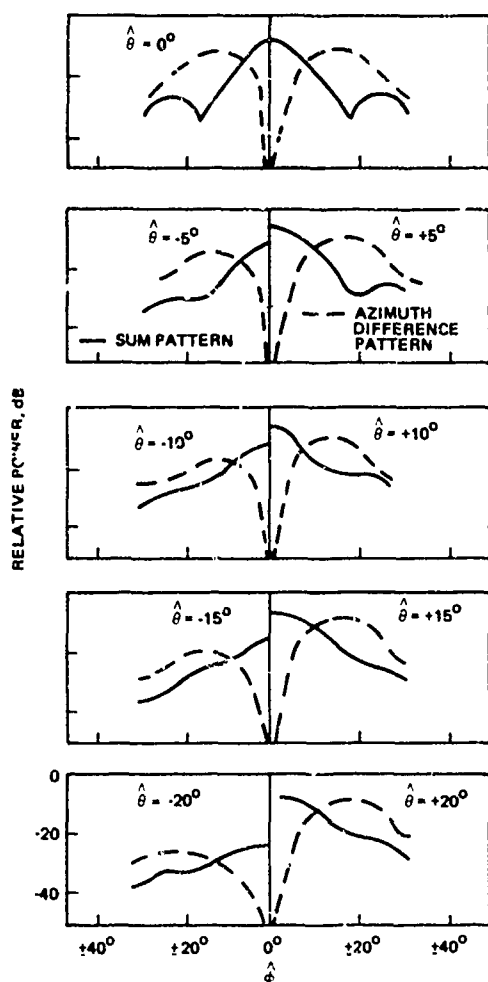


Figure 16. Two-dimensional antenna patterns for $\theta_1 = 20$ degrees for $\hat{\phi}$ -polarization optimized

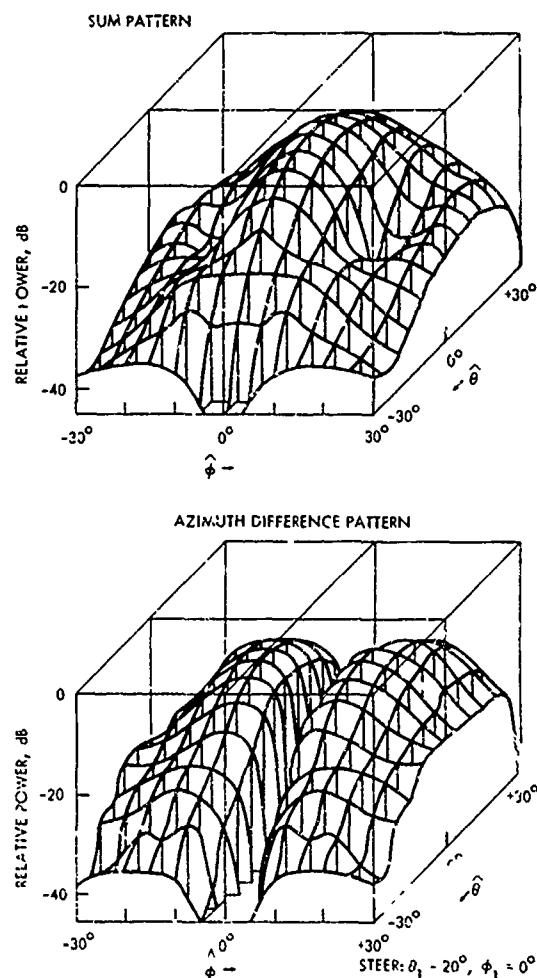


Figure 17. Three-dimensional antenna patterns for $\theta_1 = 20$ degrees for $\hat{\phi}$ -polarization optimized

17.5 inches. The frequency was assumed to be 9.0 GHz and the spacing between rings to be $0.45 \lambda_0$ to prevent grating lobes. The 10 rings of elements thus covered the lower 5.3 inches of the cone. In the nose-fire direction the projected radius of the empty area was over twice as large as the projected thickness of the annulus of the filled area.

The broadside patterns of an array of this type would be quite normal because the visible surface of the array at any one point is approximately rectangular. Further, the majority of the slots are "seen" from favorable angles in regard to polarization.

In the nose-fire direction, however, a marked difference in beamwidths for the two principal planes appears, as can be seen in Figure 18. Three reasons were determined to explain this difference:

1. The weighting applied to the elements tends to "turn off" the elements that are being viewed from an unfavorable angle. Slots in two areas of the annulus are excited normally, while those in the two areas at right angles are excited at a much reduced level. This different excitation tends to create an interferometer effect in one principal plane while the effective width of the useful aperture in the other plane is reduced to considerably less than the full diameter of the base.
2. The geometry of the cone is such that when the slots are oriented in a position to optimize the polarization of the signal in the nose-fire position, they are no longer optimum at any other angle. In the process of computing a pattern it is necessary to fix the polarizations of the slots so that there is no cross-polarized component at the peak of the beam. At other angles, more or less energy will go into this component depending on the steepness of the cone and the direction of the cut for the computed pattern. These two factors are related to the rapid change in polarization angle in the radiated pattern of a slot when viewed from a point close to either null in that pattern. This rapid change in polarization further aggravates the interferometer effect.

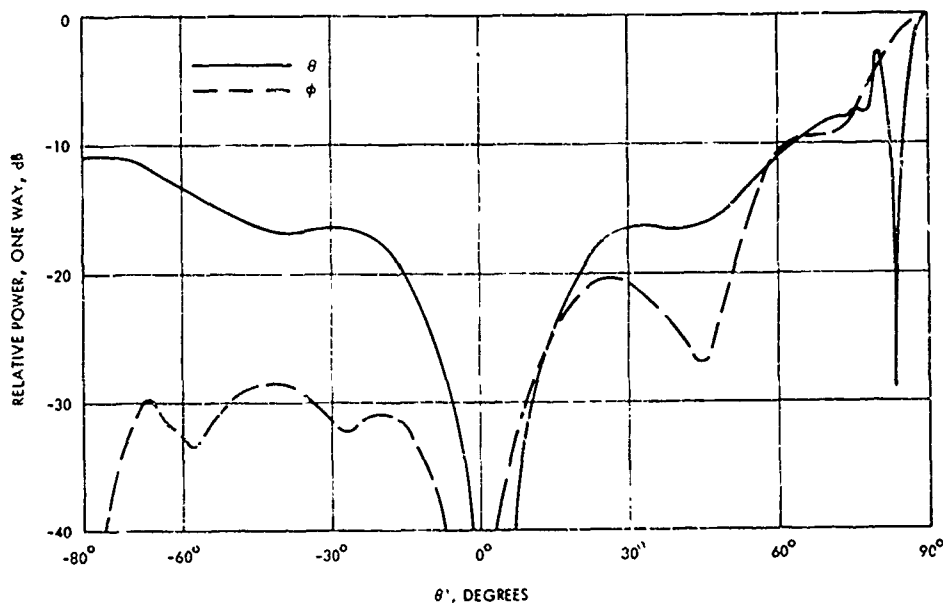


Figure 18. Computed patterns for staggered element arrangement similar to arrangement of Figure 14

5. The large empty area in the center of the "working" annulus is in essence aperture blockage which contributes also to the interferometer effect making it somewhat worse than in either of the other situations alone.

In a first step to alleviate the difference in beamwidths, the weighting applied to the elements was removed. Instead, each element was assumed driven with equal power although its element pattern was still taken into consideration when the far field patterns were computed. The differential in beamwidths between the ϕ and θ cuts was much reduced by this action (see Figure 19).

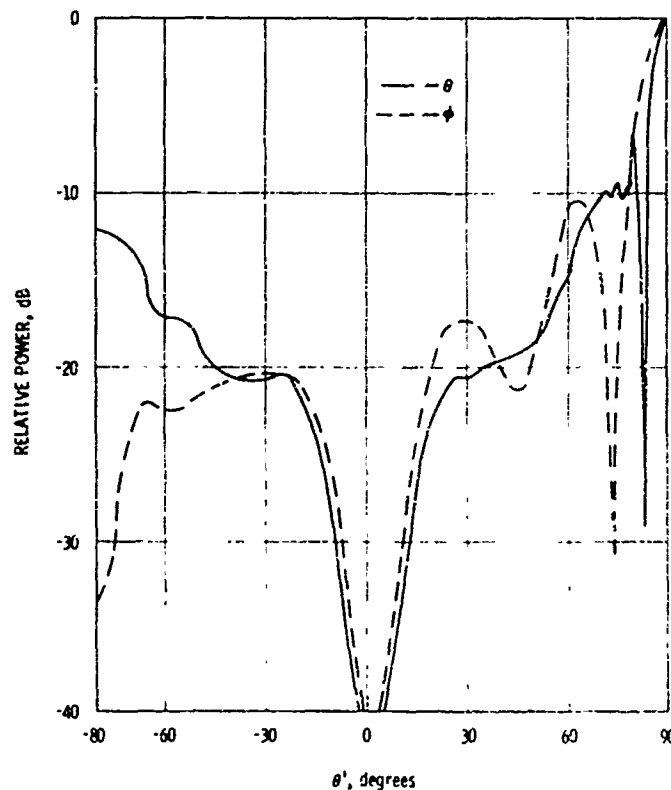


Figure 19. Patterns of same slot arrangement used for Figure 18 but with amplitude weighting suppressed

The second step was to modify the computer program so that the remaining portion of the cone was filled with elements as much as was thought practical in such a sharp cone. The cone was made larger also to correspond to a physical cone with which experimental work currently was being done. The final arrangement of elements was:

<u>Location on Cone</u>	<u>Number of Rings</u>	<u>Elements per Ring</u>	<u>Number of Elements</u>
Base of cone	9	16	144
Center portion	12	8	96
Upper portion	8	4	32
Near tip (loaded elements)	4	4	16
Total			288 elements

The center portion of the cone was assumed to contain the same crossed-waveguide elements as those near the base of the cone. The upper portion contained a crossed-waveguide element similar to the others but of a shorter length. The difference in length made matching more difficult and tolerances had to be tighter, but the short length was necessary to permit the location of as many rings as possible in the narrow region of the cone. Near the tip, the upper four rings had to use loaded elements to make packaging feasible. Even with loaded elements, the first ring was 3 inches from the tip of the cone. The projected distance between two diametrically opposite elements in this first ring was 1.04 inch or $0.79 \lambda_0$, so that a small "hole" still remained in the center of the aperture.

Computed patterns for this element arrangement with no weighting show that the ϕ and θ beamwidths are somewhat closer in value than in step two, but that the largest improvement was obtained by eliminating the element weighting. Figure 20 shows the patterns for this final and best set of results for the nose-fire case. The difference between θ and ϕ is approximately 1.5 to 1, which should not be too large to be tolerated for most applications.

It is not possible with crossed slots or crossed-waveguide elements to eliminate the rapid change in polarization that appears under certain conditions. The only solution visualized so far is the replacement of the crossed slots by crossed dipoles in certain areas of the cone. This solution is not a very attractive one because it introduces particular problems of its own.

CONCLUSION

A heuristic approach to obtaining desired patterns from a conical array has shown that at or near broadside not too many problems should be encountered. The signal-to-noise ratio of a received signal can be optimized as desired. However, attempts to scan such an array to the end-fire (or nose-fire) position present problems in obtaining equal beamwidths in the two principal planes. The root cause of this effect is the rapid change in polarization in the pattern of a slot or open-ended waveguide in the neighborhood of the null always present near each end of such elements. The rapid change in

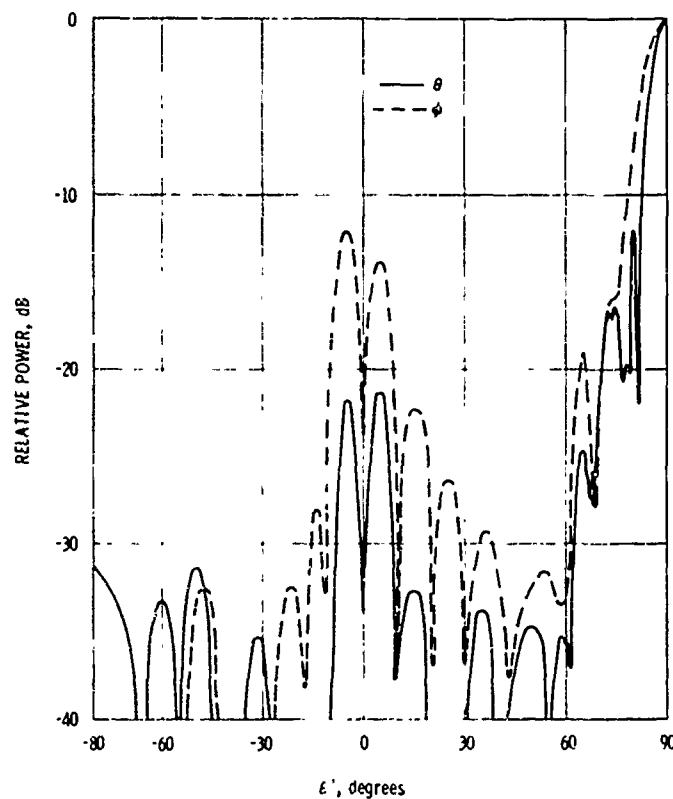


Figure 20. Patterns of cone fully covered with slots in staggered arrangement and amplitude weighting suppressed

polarization coupled with the normal drop-off in amplitude of the field at these look angles tends to produce an interferometer effect in one plane. This effect causes the beamwidth to become narrower in one plane and broader in the other. The interferometer effect can be reduced, but not eliminated, by suppressing the weighting used to optimize the signal-to-noise ratio at other beam pointing angles.

The use of the equivalence principle to synthesize patterns from curved surfaces restricts the achievable patterns to those for which synthesis techniques are known, such as linear and planar arrays. However, such patterns are quite versatile and useful, so that this restriction is not severe.

It is hoped that some of the problems associated with the heuristic synthesis and optimization techniques may be alleviated by use of the equivalence principle to synthesize patterns. It is anticipated that subsequent pattern calculations using sources obtained from the equivalence principle will bear out this belief.

REFERENCES

1. R.F. Harrington, Time Harmonic Electromagnetic Fields, pp. 106-110, McGraw-Hill Book Company, Inc., New York, 1961.
2. W.H. Kummer, "Conical Arrays," Paper No. 34, Array Antenna Conference, Naval Electronics Laboratory Center, San Diego, California, February 1972.
3. J.E. Howard, W.H. Kummer, and A.T. Villeneuve, Integrated Conformal Arrays, Final Report on Contract N00019-68-C-0214, Report No. P69-32A, Hughes Aircraft Company, 1969.
4. J.E. Howard, Integrated Conformal Arrays, Quarterly Progress Report on Contract N00019-69-C-0281, Report No. 2767.01/154, Hughes Aircraft Company, 1 January to 1 April 1969.
5. A.T. Villeneuve, Integrated Conformal Arrays, Quarterly Report No. 1 on Contract N00019-68-C-0214, Report No. P68-125, Hughes Aircraft Company, 1968.
6. W.H. Kummer, A.T. Villeneuve, J.E. Howard, and A.F. Seaton, Integrated Conformal Arrays, Final Report on Contract N00019-69-C-0281, Appendix B, Report No. 2767.01/214, Hughes Aircraft Company, January 1969 to March 1970.

ACKNOWLEDGMENTS

The authors would like to express appreciation to J.E. Howard who wrote the original computer program for calculation of the patterns of a conical array; he also contributed the three-dimensional patterns presented in the section on Pragmatic Techniques. Appreciation is expressed to Mr. J.W. Willis, Naval Air Systems Command, for his interest and many helpful suggestions. Thanks are also due Marjorie Delzell for assistance in technical editing.

34. CONICAL ARRAYS*

by

W. H. Kummer

Radar Division
Aerospace Group

Hughes Aircraft Company
Culver City, California 90230

for

ARRAY ANTENNA CONFERENCE

Naval Electronics Laboratory Center
San Diego, California

22, 23, 24 February 1972

34-1a

*The work reported in this paper was sponsored by the Naval Air Systems Command under Contract N00010-70-C-0397.

ABSTRACT

In the design of electronically scanned conformal arrays, problems arise that are different than those for arrays on planar surfaces. The purpose of this paper is to delineate these problems and to examine possible solutions. The gain of conical arrays changes as a function of the scan angle. The gain also depends on the part of the radiating structure that is visible from the far field at the beam pointing position. The polarization in the far field changes as a function of scan angle for radiating elements whose polarization is fixed with respect to the surface of the cone. Sum and difference patterns become sensitive to the incident polarization. The manner in which these quantities vary with scan angle is shown. The problem of pattern synthesis and analysis is also examined, and several techniques are discussed. In addition, the control circuitry and phase shifters required for these arrays are described.

APERTURE CONSIDERATIONS

The general configuration for conical arrays consists of a set of radiating elements placed on a conical surface. The far-field patterns to be radiated from this array are pencil beams with suitably controlled sidelobes. Difference patterns are generated to improve tracking accuracy. The pencil beam is summed from a direction perpendicular to the generatrices through the axis of the cone. For this design, a cone with a 20 degree full angle has been assumed.

ARRAY GEOMETRY

The radiating elements comprising the conical array are assumed to have symmetry in the plane perpendicular to the axis of the cone, the ϕ plane. The array placed on the conical surface is assumed to have symmetry in the θ plane. Whatever the shape of the active part of the array, the projected aperture of the active part will be a function of the position angle defining the beam pointing direction in the plane defined by the axis of the cone and a generatrix, (the θ plane). The active part is defined as that part that is turned ON to receive (or transmit) energy. The projected aperture will be constant for any ϕ scan at constant θ because of the symmetry mentioned above. Let us assume for the moment that the conical surface will be used in its entirety, that is, the active part of the array will go from the tip to a cone diameter of, say, 10 inches. To establish the theoretical upper limit of performance, let us further assume that the area is used perfectly in the electromagnetic sense. The projected area of the active part of the area will be directly proportional to the achievable gain. For purposes of comparison, we will normalize this area to that of a planar aperture of a diameter of 10 inches. Thus, we have

compared the conformal array with a mechanically scanned parabola or planar array located at the maximum diameter of the conformal array.

The graph in Figure 1 is shown for a cone angle of 20 degrees. Except for the first 12 degrees of scan (from 0 to 12 degrees) the conformal array has a larger area gain. This fact may be used as follows.

1. Let us assume that the same gain is wanted for all θ scans. The active part of the conformal array will then have a constant projected area. This could, for instance, reduce the prime power required for scan directions other than on-axis.
2. The minimum gain of the conformal array can be decreased for the on-axis direction and increased for other directions as compared with that of the mechanically scanned antenna.

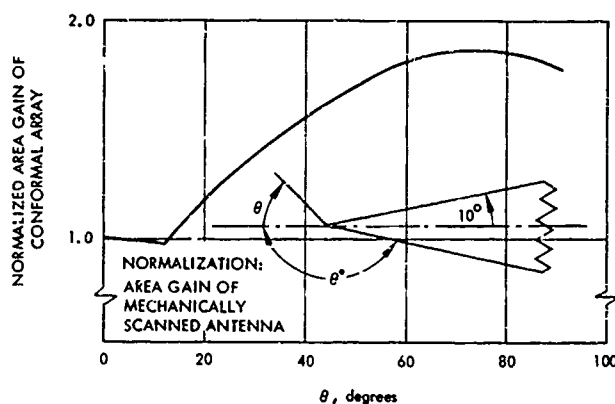


Figure 1. Normalized area gain of conformal array as a function of scan angle

BEAMWIDTH

The beamwidth of a planar array changes as a function of the beam pointing in direct proportion to the projected aperture perpendicular to the beam pointing direction. This relation is an approximation but is quite accurate for angles between broadside and 50 to 60 degrees. In a conformal array the beamwidth is not so easily related to the geometry of the array because both the shape of the active part of the array and its projected area change as a function of the beam pointing direction. An estimate of the beam and sidelobe shapes will be given below.

For the beam pointed perpendicular to the generatrix of the cone, the radiation characteristics may be approximated using an equivalent planar array whose area is the projected area of the active part of the conformal array. Thus we would expect beamwidths commensurate with the projected aperture dimensions shown in Figure 1 and near-in sidelobes below 15 dB.

At the other extreme, a beam pointed along the axis of the cone, a different condition exists. For small angles near the cone axis, the array when projected forward would look approximately like a concentric ring array. The center rings of the array are missing, since the extreme tip of the cone is probably not usable in practice. For a 6 ring by 24 element/ring array as shown in Figure 2, the pattern would be somewhat as shown

in Figure 3. For comparison, Figure 3 also shows the pattern of an array of the same size on the same cone but with the center rings filled. The latter is the usual pattern for a uniform circular array. It will be noted that the ring array has a narrower beamwidth and higher sidelobes than the filled array. This narrower beamwidth can be explained with reference to an interferometer which has a

beamwidth one-half of that of a completely filled linear array of the same length. The "sidelobes" are as high as the main beam. This particular case is an intermediate one. Thus it can be seen that there is a trade-off between array filling, beamwidth, and sidelobe level.

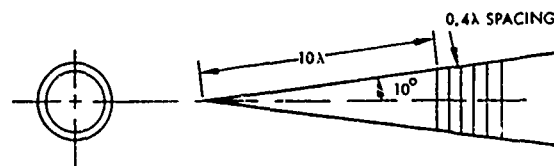


Figure 2. Layout of ring array with six rings

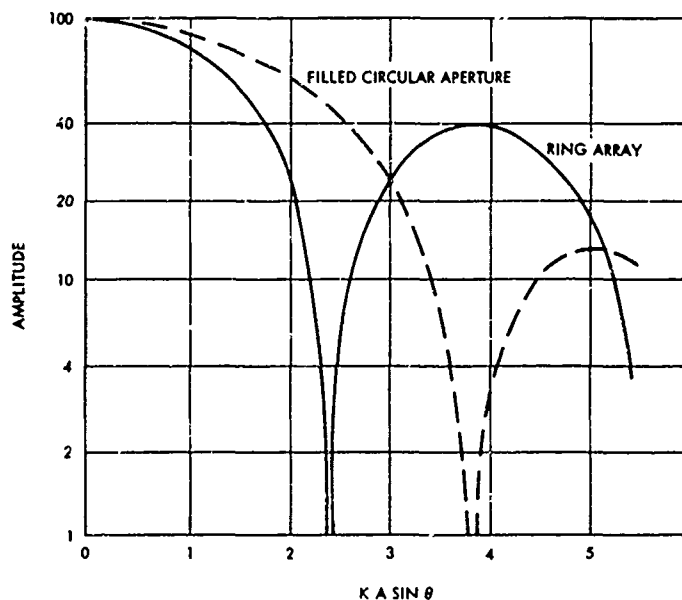


Figure 3. Patterns of circular apertures

THE PROBLEM OF PATTERN GENERATION FROM CONFORMAL ARRAYS

Pattern synthesis for the far-field patterns from current distributions on planar surfaces is well known. However, there are no proved techniques for synthesizing antenna patterns from arrays on conical surfaces. In this program three different approaches to this problem have been pursued:

1. An equivalence principle was used to determine the distribution of sources on a cone to produce a prescribed pattern. Using this approach planar arrays are replaced by sources on a conformal surface. Thus, it is possible to generate patterns using well known synthesis techniques for planar surfaces. The equivalent sources are continuous functions on the cone. The practical validity of the method depends on the accuracy with which the continuous functions can be approximated by physically realizable radiators.

2. The roots of two transcendental equations involving the associated Legendre functions and their derivatives were calculated numerically. The calculations make available the required tools for exact theoretical solutions of the radiation fields and mutual coupling effects in a region bounded by a conducting cone.

3. The computation of patterns from discrete radiators judiciously positioned on the cone was carried out. An optimization is performed to obtain the highest signal-to-noise ratio in the beam pointing direction.

The first and third synthesis techniques are covered in detail in a companion paper by A. T. Villeneuve and A. F. Seaton, entitled "Synthesis Techniques for Conical Arrays". The second technique gives an exact solution to the physical problem but appears difficult and tedious to solve numerically and thus has not been pursued at this time.

STUDIES OF RADIATING ELEMENTS

This section is concerned with the development of physical radiating elements on conical surfaces that will permit the implementation of the desired radiation characteristics. A proposed element to provide variable polarization is described that consists of crossed, independently fed waveguides.

POLARIZATION CONSIDERATIONS

The question of orienting the radiators on the cone so that optimum performance in all directions is obtained involves the geometry of the radiator. The case of a beam pointing directly ahead is considered first. Since the array is conformal, some sort of flush-mounted radiator will be required. The slot and the open-ended

waveguide are the two most commonly used flush-mounted radiators. The polarization of these radiators are nearly identical; hence the polarization of the slot radiator is considered.

The E-field in one quadrant of the far field of a slot is shown in Figure 4. In this figure the ground plane is assumed to be in the x-y plane. It can be seen that the polarization of the field is everywhere perpendicular to the ground plane in the immediate vicinity of that plane. If the slots are imagined to be placed on a ten-degree half-angle cone, then in the forward direction each slot will be viewed from an angle of ten degrees above its nominal ground plane. The polarization at that angle can be visualized by constructing a surface on Figure 4 that is ten degrees above the x-y plane. This surface is shown in the figure by dashed lines.

It is instructive to start near the x-axis and note the change in polarization angle as the ten-degree surface is followed around to the y-axis. (The scale of angles in the x-y plane is used for convenience.) At 0 degree the polarization (shown by the dark arrows) is found to be parallel to the ground plane and, hence, is termed horizontal. As the progression continues around the quadrant toward the y-axis, the polarization vector at first turns quite rapidly downward, then turns increasingly more slowly in the same direction, until at the y-axis, it is vertical. At 45 degrees, the polarization is still very nearly vertical instead of nearly 45 degrees as might be expected.

The result of this unequal rate of rotation of the polarization vector is that, when the slots are placed on a cone, they must rotate at an uneven rate with their position around the cone in order for them to all have the same polarization directly ahead.

It can be shown that, in the quadrants, the slots must be oriented so that their projections on the end-fire view are also parallel with the projections of the principal axis slots. This requirement is due to the fact that the far-field polarization of the E-field of a slot is always perpendicular to the projection of the long dimension of the slot onto a plane perpendicular to the line-of-sight.

To obtain a picture of how the slots oriented to favor end-fire operation would look from other angles in space, a paper cone was made with a number of slots drawn on it (Figure 5). When the cone is viewed from end-fire, the projections of all these slots are parallel as desired (see Figure 5a). When the slots are viewed from a broadside position nearest the axial slots, they are predominately lined up in an approximately axial fashion (Figure 5b); hence, cross-polarization would not be too much of a problem. However, when the slots are viewed from the broadside region nearest the transverse slots, they are not properly lined up at all (Figure 5c). With this slot arrangement, large amounts of the available power would go into cross-polarized lobes, and the effective aperture would be much smaller than the projected area of the cone in this direction.

There are a number of ways in which radiators providing variable polarization might be mounted on a cone, but complete symmetry

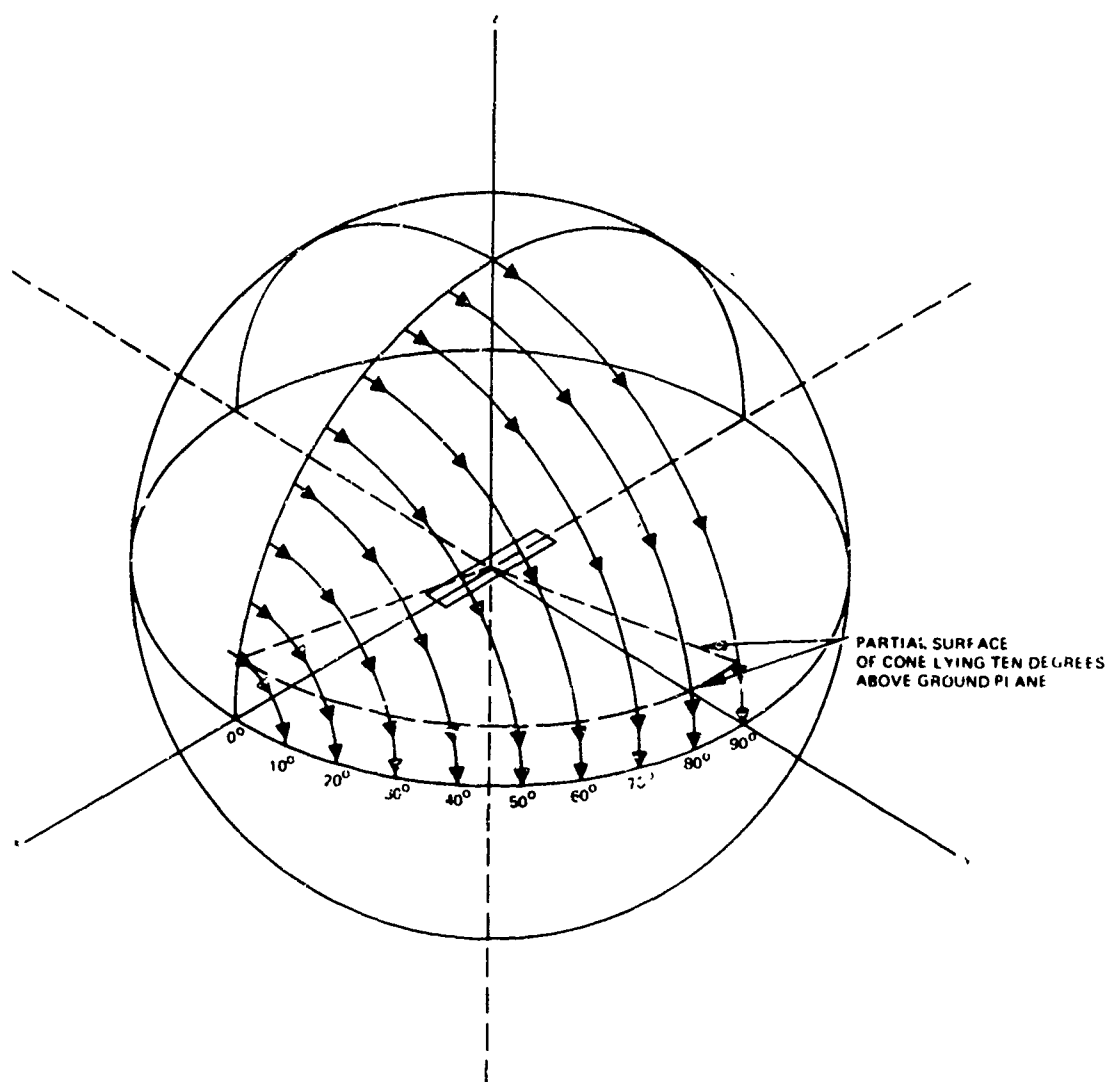


Figure 4. Polarization of field radiated by slot at locus of points ten degrees above ground plane

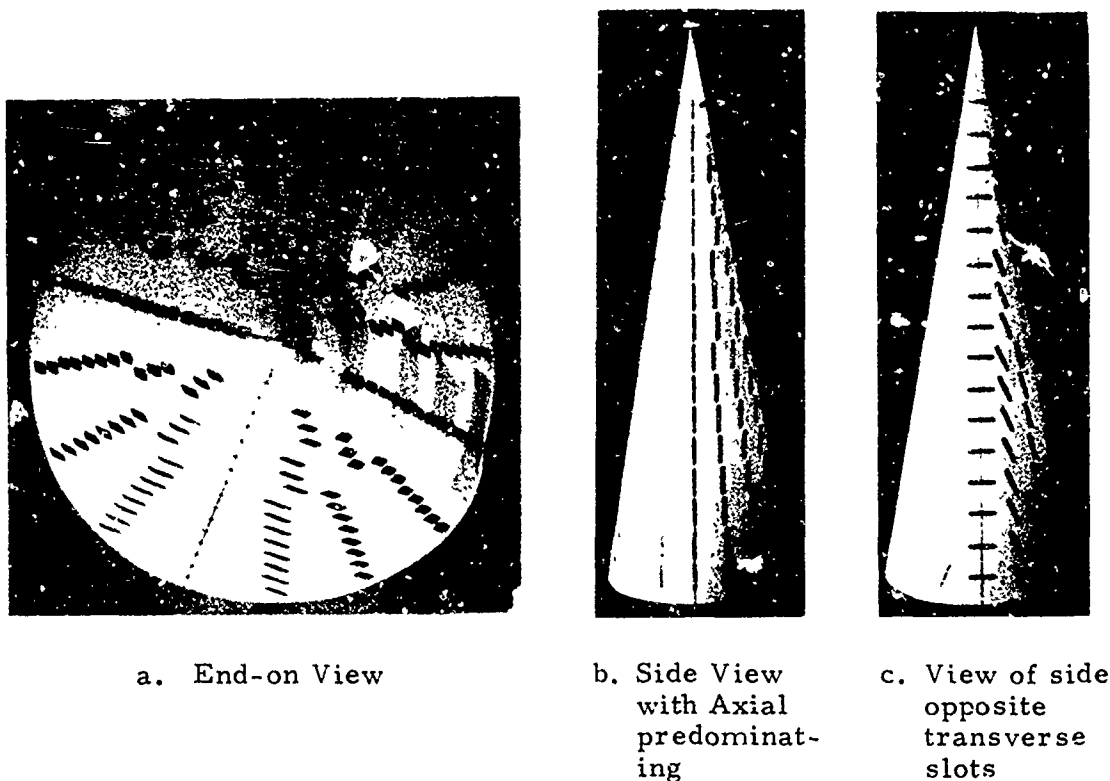
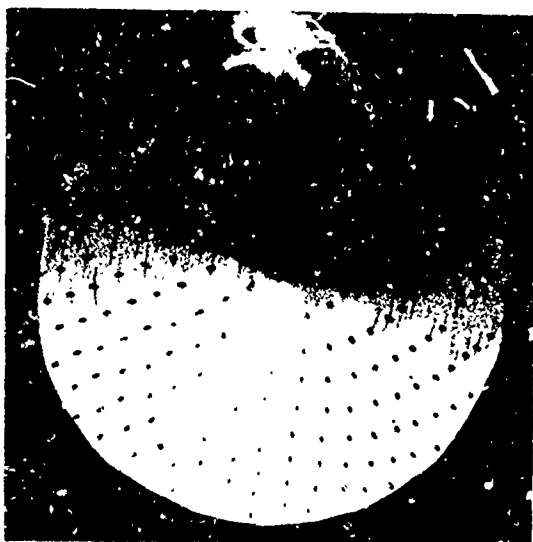


Figure 5. Cone on which slots have been placed to favor end-fire radiation

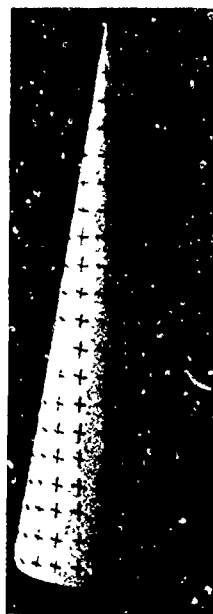
cannot be maintained with a minimum number of elements or with simple control functions for beam formation and steering. To illustrate some of the configurations that might be used, several crossed-slot configurations were sketched on additional cone models. Three views of each configuration are illustrated, a nose-view and views from two opposite sides (Figures 6, 7, and 8).

In Figure 6, the elements are placed on the vertices of a square grid laid out on the developed cone. The slots are oriented circumferentially and along the cone generatrices. With this arrangement, only the radial and circumferential excitations required at any position must be determined.

A third arrangement that further simplifies the control problem has the slots located on rings at fixed interelement spacings about each ring and oriented along generatrices and circumferentially (Figure 7). In this arrangement, only the radial and circumferential components of the excitation must be computed as in the second arrangement, but in addition, the computation of the phase function is also simplified.



a. Nose View

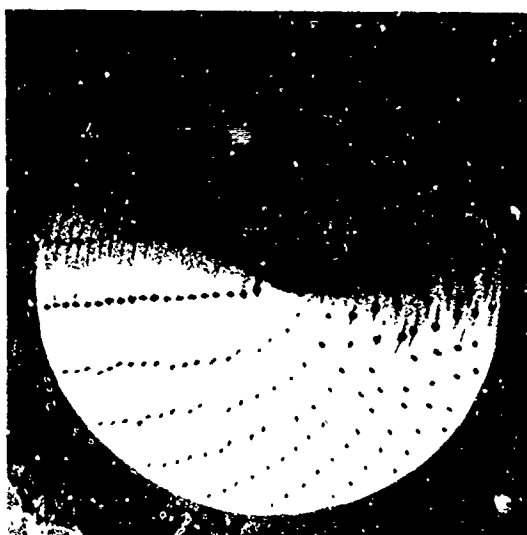


b. Side view



c. Opposite side view

Figure 6. Cone with elements on square grid and slots oriented radially and circumferentially



a. Nose view



b. Side view



c. Opposite side view

Figure 7. Cone with elements on rings

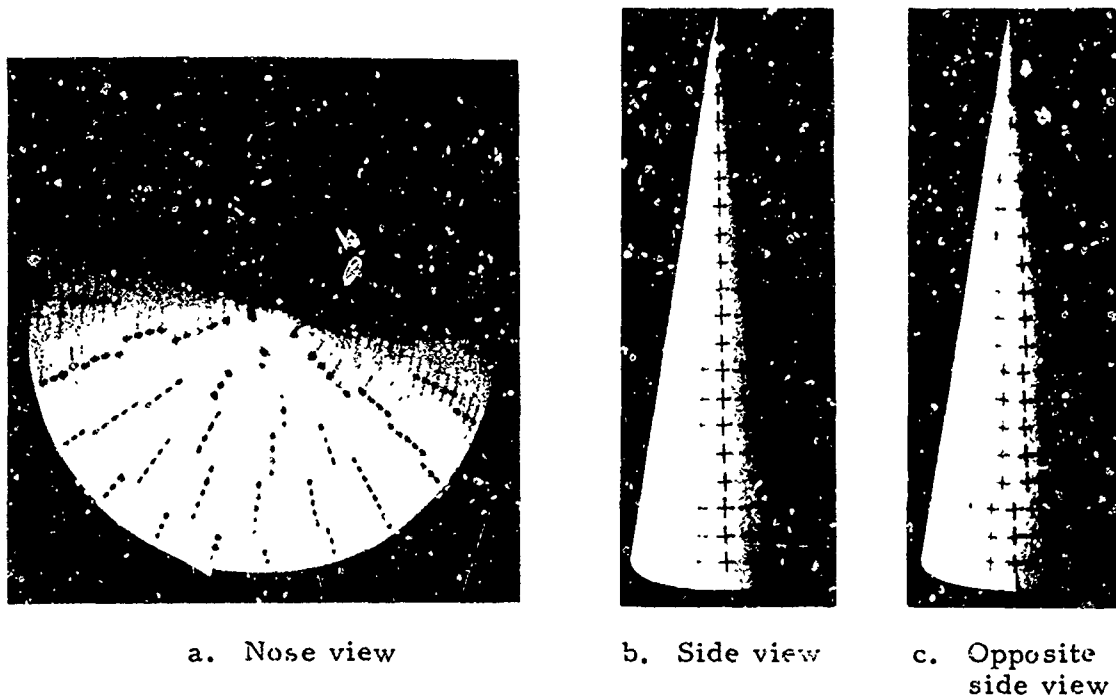


Figure 8. Cone with elements on rings and generatrices

Figure 8 shows a fourth arrangement in which elements are located on rings and, in addition, groups of rings are placed along the cone generatrices. Each ring of a group contains the same number of elements. When the spacing of elements in a ring exceeds a prescribed maximum value, an extra element is added to that ring. This new number of elements is used in succeeding rings until the element spacing again exceeds the prescribed maximum value. At that point, again another element is added. This arrangement results in a simpler control problem than in the other configurations because the phase control function for elements in any one group is simplified from that of the elements in the other configurations.

Other factors also influence the placement and orientation of elements on the cone. Physical feeding arrangements, ease of fabrication, and physical size, as well as requirements dictated by pattern specifications, must be considered before a final arrangement can be selected.

RADIATING ELEMENT CONSIDERATIONS

Several types of radiators were considered that would radiate both components of polarization. The one selected for experimental evaluation consists of an open-ended crossed waveguide as the radiator. Open-ended waveguide is not difficult to match to free space and by the use of half-height guide, the size of the element can be kept to a

reasonably small volume. Loops were used to feed the waveguides. Symmetry was maintained by placing the loops on the center lines of each of the two principal modes that can be excited in the crossed waveguide (see Figure 9). With this arrangement, only two loops

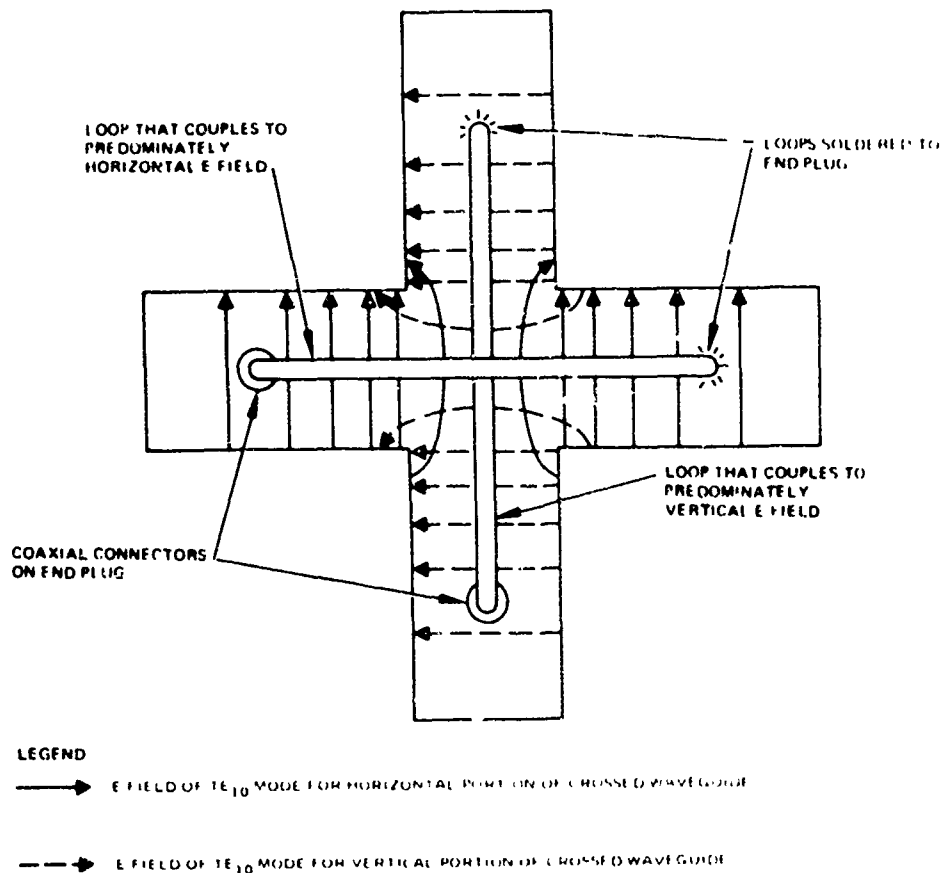


Figure 9. Field configuration and loop coupling arrangement in cross-waveguide element

and two coaxial connectors were required. A further advantage is that the connectors would not interfere with neighboring elements since they extend from the end plug of the waveguide. An experimental crossed slot radiator was designed and fabricated. The VSWR was less than 1.5 over a 5 percent bandwidth, and the cross polarization was better than 20 dB at broadside.

METHODS OF SCANNING

The radiating elements on a planar array tend to reject cross-polarized energy returned from a target because the orientation of all the radiators is the same; the truly conical array has a problem because there is no common orientation of the radiators. The approach

taken in this study has been to orient the radiators electronically so that there is no cross-polarization. There are many trade-offs to be considered. For instance, a conformal array could be made up of a number of triangular surfaces as shown in Figure 10. Electronic

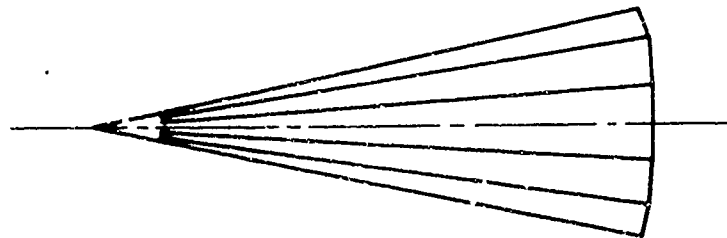


Figure 10. Conical array with planar array surfaces

orientation would still be needed in such an array, but all radiators on any one planar surface would need only one orientation and the number of controls would be substantially reduced.

For the purposes of the discussion, a true conical array is assumed. Of the several methods of changing the phase and amplitude of the energy received by the array, two are discussed: amplitude scanning and phase-and-amplitude scanning. The general case is assumed for each method: (1) each antenna element receives radiation of any polarization; (2) control is performed in every chain behind each antenna element to reject cross-polarization, (3) ON-OFF control, amplitude control, or a combination of both is used; and (4) phase control is used.

PHASE AND AMPLITUDE SCANNING

Phase and amplitude scanning is the one method normally used in phase-scanned arrays. Phase shifters are used in the RF or IF portion of the system. Because of the additional requirements of the conformal arrays, amplitude control must also be provided. An attenuator or a variable gain control in an amplifier will satisfy that requirement.

AMPLITUDE SCANNING

In the amplitude scanning concept, the RF phase and amplitude are controlled by appropriate changes in the amplitude of the signal in the IF processing system. The concept can also be used in the transmitting mode.

As can be seen with the aid of Figure 11, each radiating element has two terminals, one each for sense of orthogonal linear polarization. Phase coherent mixing is performed at every terminal, and the signal is translated to an appropriate intermediate frequency.

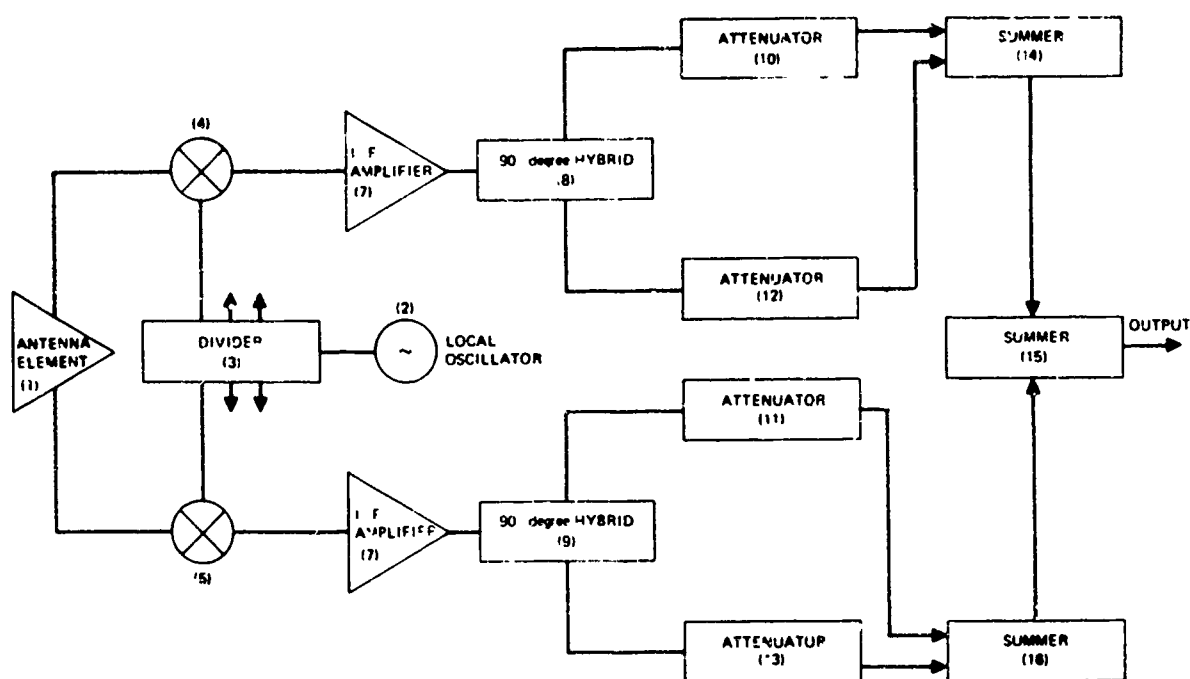


Figure 11. RF/IF system for amplitude scanning

The signal received by the n^{th} radiating element will be of the following form:

$$E_n = A_n \sin(\omega_c t + \phi_n)$$

where

A_n = the peak amplitude

ω_c = the carrier angular frequency

ϕ_n = the phase referred to a common point on the array

For simplicity the analysis is confined to one incoming frequency, and any modulation frequencies are omitted. Only the one chain for one polarization will be analyzed; the other chain behaves similarly.

After the signal is translated to an intermediate frequency ω_I (mixers, Box 4 of Figure 11) and filtered (Box 7), the voltage has the following form,

$$e_n = a_n \sin(\omega_I t + \phi_n)$$

The phase angle is preserved in the mixing process, and the signal-to-noise ratio is established in the mixer and IF amplifier.

The signal is now split into two channels using a 90-degree hybrid (Box 8). Boxes 10 and 12 control the amplitudes of these two signals. Their outputs will then be proportional to the following quantities:

$$E_{nI} = K_{nI} a_n \sin(\omega_I t + \phi_n)$$

$$E_{nII} = K_{nII} a_n \cos(\omega_I t + \phi_n)$$

The K's vary from zero to one and are generated by variable attenuators; to obtain complete control, the signs of the two K's must also be changeable; thus,

$$K_{nI, II} = |K_{nI, II}| \exp(j\psi) \quad \psi = 0 \text{ or } \pi$$

The resulting sum signal from the n^{th} element for one polarization is given by

$$E_n = E_{nI} + E_{nII} = c_n \sin(\omega_I t + \phi_n + \theta_n)$$

where

$$c_n = a_n \sqrt{K_{nI}^2 + K_{nII}^2}$$

$$\theta_n = \tan^{-1} \frac{K_{nII}}{K_{nI}}$$

The signals from the various elements can be put in phase with each other by adjusting the ratio K_{nII}/K_{nI} so that $\theta_n = -\phi_n$. The amplitudes are adjusted by adjusting the sums of the squares of K_{nI} and K_{nII} .

It will be noted that the frequencies are not specified. In practice some of the operations can be performed at DC; however, the more general case is shown.

The output of each of the arrays is achieved by the summation of the voltages from all the channels. All signals will be in phase to produce an appropriate beam in the direction chosen. At the final point of summation, the gain of the array will be realized. Strictly speaking, the signal-to-noise ratio is proportional to the array gain because of the coherent summation of the signals from the array elements and the incoherent summation of the noise generated at the first mixers. Actually, arbitrary beam shaping can be achieved: cosecant-squared beams, multiple beams, etc., can be formed. The tracking beams (i. e., monopulse, conical scan, or a combination of the two) have been omitted for simplicity of presentation.

ELECTRONIC CONTROL STUDIES

The conformal array presents a significantly more difficult scan-control problem than does the conventional planar array because the designs of the latter take advantage of the symmetry of the array and the separability of the phase function to reduce computation time and simplify hardware.

For a rectangular planar array of M-by-N elements, for example, a total of MN phase values must be generated, one for each element. The phase function is separated into x - y (row column) components so that the scan controller must generate only M + N values with a final summation on the array; this procedure greatly decreases the total computation time. In some cases, the separation of the phase function may be effected exactly; in other cases, approximations must be made. If the planar array is symmetrically illuminated, the equation for phase settings required to collimate the beam is an even function of x and y; in addition, the linear phase slope for pencil beam steering is an odd function. In this case, the phase data for only one array quadrant need be explicitly computed; data for the other quadrants are formed from the first quadrant data, either directly or by a simple change of sign.

SYMMETRY AND FUNCTION SEPARABILITY

The application of techniques of symmetry and function separability to the conformal array is not so straightforward as with the planar array. In general, the control function is more complicated because of the three-dimensional surface and must include amplitude and polarization control in addition to the phase control. Amplitude control is usually required because the elements present different aspect angles in the desired scan direction; in some cases, certain elements cannot be seen in the far field. Thus, at least an on-off type of control is desired, with variable amplitude weighting being the optimum for flexible beam-shape control and enhancement of signal-to-noise ratio. The control function is further complicated since the elements cannot generally be aligned on the array surface to present collinear polarizations for all scan angles without individual polarization

control. Another problem arises from mutual coupling between elements that give rise to a variation in element input impedance with scan angle. Because of the mutual coupling, the control function may require an additional correction term that further complicates the scan control computations.

SOME CONSIDERATIONS FOR BROADSIDE SCAN

Some basic problems related to the steering and control of conical conformal antenna arrays have been considered. A conical array was assumed in which the individual elements lay in circles about the surface of the cone and along generatrices of the cone. The individual elements were assumed to be crossed slots whose axes were normal to and along the cone generatrices. Variation of the polarization of the energy radiated from each individual element was also assumed possible with the proper control of element excitation.

As an aid to the understanding of the control problems, the generation of an antenna beam, pointed near the broadside direction and in the plane define by the y - z axes, is shown in Figure 12. It can be seen that elements of the array ± 90 degrees away circumferentially from the y - z plane can contribute little or nothing to the beam considered but can result in undesirable sidelobes. The first level of control, therefore, should consider "shutting off" those elements. This action involves establishment of angular reference within the control

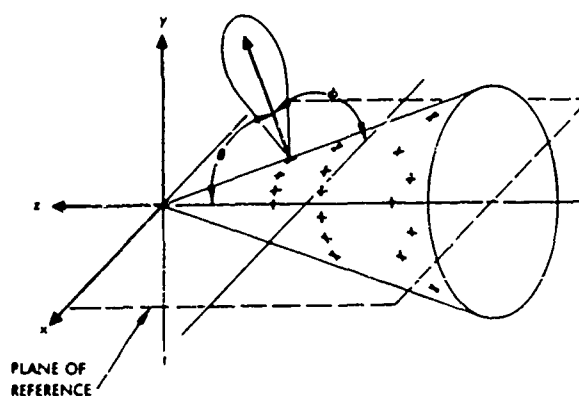


Figure 12. Coordinates associated with conical array

system from which pointing angles in the x - y plane may be measured. A slice through the cone in the x - z plane is shown as the reference, with the pointing angle in the x - y plane being denoted by ϕ .

Shown in Figure 13, in block diagram form, are the elements in one ring of the array postulated in Figure 12. Element No. 1 lies on the first generatrix in the clockwise direction from the x - z plane, and

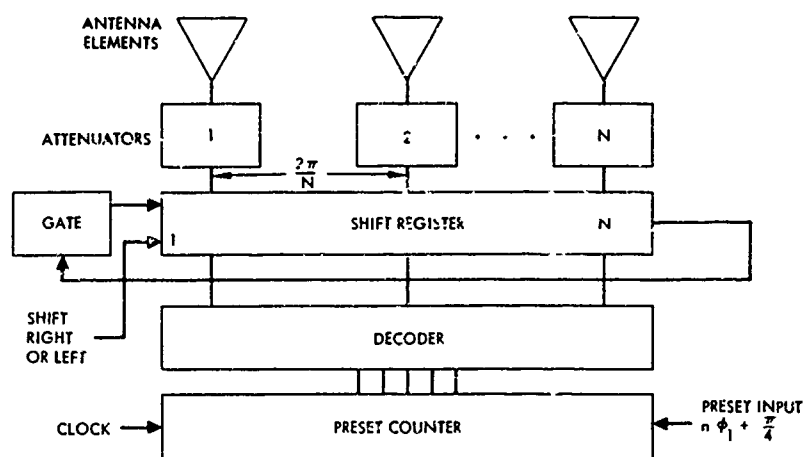


Figure 13. Element blanking for near-broadside scan

the N^{th} element lies on the first generatrix counter-clockwise from this plane. The pointing angle ϕ_1 may then be expressed as

$$\phi_1 = \left[\frac{2\pi}{N} \times \frac{\text{Element Number}}{\left(n\phi_1 \right)} \right]$$

and the elements to be blanked, approximately $N/2$ in number for scan near broadside, are located $N/4$ elements from the element number, $n\phi_1$.

A possible implementation for blanking these elements is shown in Figure 13 and may be used in conjunction with a variable attenuator. The preset counter is set to a value determined by the desired ϕ ; then $N/2$ counts are entered. The output of the decoder sets the shift register to provide maximum attenuation in the proper element feeds. As the pointing angle in the y-z plane, θ , decreases towards the nose-fire direction, a value is reached at which elements that are greater than 90 degrees away circumferentially from the main beam now contribute to its generation. In the block diagram of Figure 13, the preset input and the number of counts entered into the preset counter may now be varied as a function of θ . This implementation has obvious utility in connection with rotating scan and roll correction programs.

Another consideration in the generation of the broadside beam is the variable amplitude weighting of the various element signals. Shown in Figure 14 is one complete ring of elements that lies on a section of the cone parallel to the plane of the x-y axes of Figure 12. For optimum control of beam shape and directivity, the gain of the elements

should be varied as a function of ϕ . The implementation of Figure 13 would lend itself to such weighting if the attenuation in each element feed were variable.

Examination of Figure 14 also points up the need for control of the phase signal at each element as a function of the angle ϕ . For generation of a beam in the ϕ_1 direction, this phase control must compensate for the varying physical separation of elements from the normal to the pointing direction ϕ_1 . This separation is depicted by d_4 of Figure 14

for the fourth element from ϕ_1 , and a phase correction term $2\pi d_4/\lambda$ must be supplied at the element to provide an equiphase wavefront in the ϕ_1 direction. As the value of θ shown in Figure 12 is varied from broadside towards endfire, a phase bias that varies as a function of θ must also be added to the existing phase of each element.

In addition to the phase and amplitude control, polarization control must be added. For scan near broadside, the elements present the most nearly collinear polarizations for single-slot excitation. For scan near nose-fire, however, the polarization are clearly not collinear unless variable amplitude control between the two orthogonal slots is provided.

CONCLUSION

Several facets of conformal arrays have been taken up. Both problems and some solutions to the scanning of a pencil beam from discrete elements located on a cone have been outlined. More parts of the overall problems are being attacked. These include the scanning from broadside to endfire of linear arrays located along generatrices of a conical surface. Experiments and theoretical analyses of the behavior of patterns, gain, and impedance are being carried out. A solution of the many interrelated problems touched on in this paper will lead to an overall understanding of the scanning of controlled radiation from conical surfaces.

ACKNOWLEDGMENTS

The results summarized are the efforts of several members of the Radar Division: M. C. Behnke, T. S. Fong, A. T. Villeneuve, A. F. Seaton, J. E. Howard, T. O. Mutton, and M. Rosen. The author would also like to acknowledge the continuing encouragement of J. W. Willis of the Naval Air Systems Command during the course of these programs.

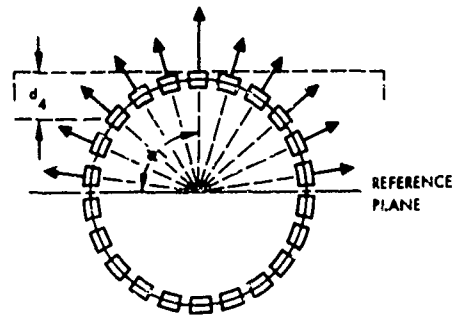


Figure 14. Typical ring from conical array

35. SOME ASPECTS OF TEM SLOT DESIGN IN STRIPLINE

by

David Proctor

Code 2330

Naval Electronics Laboratory Center
San Diego, California 92152

for

ARRAY ANTENNA CONFERENCE

22, 23, 24 February 1972

35-1a

Naval Electronics Laboratory Center
San Diego, California 92152

INTRODUCTION

The concept of using the same area or aperture space to perform several antenna functions has received limited attention.¹ Recently, as the crowding of antennas on operational vehicles becomes more critical, especially on spacecraft, interest has risen for practical solutions involving the development of an integrated antenna system. Benefits resulting from an integrated antenna are: (1) improvement in system performance due to reduction of mutual interactions between many separated antennas; and (2) more antennas can have a clear look into space.

The feasibility of integrating several functions at different frequencies into one antenna must be investigated in order to outline areas requiring a concentrated study effort. This problem involves considerably more than one antenna configuration since the integrated-array antenna design will be more complicated than the conventional array.

This report covers the preliminary investigation of the design of an L-band TEM radiating slot, as one aspect of a multifrequency array operating in L-, S-, and X-bands. The basic antenna is a 12-by-12-ft S-band array, in which sections of L and X frequency bands are interlaced. The L-band section of the antenna is to be interlaced into the lower 12 inches of the main array. At this time we are not concerning ourselves with such problems as mutual coupling, etc. Initially, we are concerned with the design of a "stripline" slot which substantially radiates all the power available.

STRIPLINE CONSTRUCTION

Strip transmission lines, commonly called striplines, consist of a flat conducting strip between and parallel to conducting ground planes (fig. 35-1). The area between the ground planes and the center strip is filled with a dielectric. Some of the common dielectrics used are Rexolite 2200 and PTFE fluorocarbon glass.

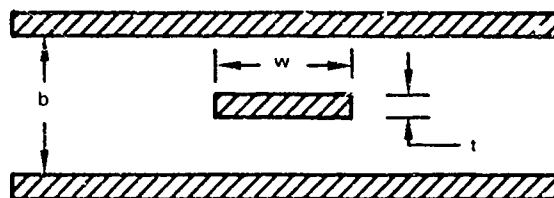


Figure 35-1. Stripline cross section.

Electrically, stripline is almost equivalent to coaxial line. Theoretical analysis has shown that if the center strip is small compared to the ground planes, the electric field does not extend outside the dielectric and the propagation is in the TEM mode.² Higher-order modes can exist, but are easily suppressed by proper physical arrangement of the circuits.

The TM mode is no problem at L-band. The cutoff wavelength for the first TM mode is equal to twice the ground-plane spacing. For example, a ground-plane spacing of $\frac{1}{4}$ inch would give a TM mode cutoff in the K_u band region (18 GHz). The TE mode is not so conveniently dealt with. The cutoff wavelength for the first TE mode is equal to the average circumferential path between the ground planes. When the stripline width is such that this mode could exist, it is suppressed by placing screws shorting the ground planes together at a distance less than $\frac{1}{4}$ wavelength from the center strip.

The phase velocity in stripline is $1/\sqrt{\epsilon}$ times the free-space value, giving a stripline wavelength of $\lambda/\sqrt{\epsilon}$. The characteristic impedance for the perfectly conducting strip of zero thickness is given by³:

$$Z_0 = 30\pi K'(k)/K(k')$$

where $K(k)$ and $K(k')$ are complete elliptical integrals of the first kind

$$k' = \tanh \pi w/2b$$

$$k = \operatorname{sech} \pi w/2b$$

where w is the width of the center conducting strip and b is the ground-plane spacing.

In the practical case, the strip has a finite thickness. A valid formula for this case has been shown to be⁴, for w/b equal to or less than 0.35:

$$Z_0 = 60/\sqrt{\epsilon} \ln 4b/\pi d_0$$

where d_0 is a function of the strip dimensions and is equal to $w/2$, giving us finally

$$Z_0 = 60/\sqrt{\epsilon} \ln 8b/\pi w$$

And, like coax, the impedance is fixed by the dimensional ratio of the inner and outer conductors, and is essentially independent of frequency.

DESIGN REQUIREMENTS

Initial design goals for the L-band array are:

± 90 degrees scan

18 degrees half-power beamwidth

Vertical linear polarization

1.03 - 1.09 GHz frequency range

The array will be approximately 1 by 12 feet and will contain approximately 32 elements in two rows of 16 each.

It is necessary to fit the L-band elements between the S-band elements. A section of the basic array is shown in figure 35-2. The spacings between the S-band elements are 0.553 inch and 0.440 inch. It is obvious that the choice of elements is then restricted to dipoles or slots. Previously an interlaced array was constructed using printed-circuit dipoles in L- and S-bands, but the L-band elements seriously shadowed the S-band elements. Accordingly, we decided to try slots. Since very little space is available, inclined and shunt slots were ruled out, and it was decided to construct the array using series slots.

The waveguide approach is a straightforward method of designing the slots; it involves cutting a resonant slot, generally a half-wavelength (guide), adjusting the short position for maximum radiation, and then adjusting the slot position to improve the VSWR. A similar procedure should suffice for stripline.

A slot antenna consisting of a half-wave slot cut in a flat metal sheet is a very efficient radiator.⁴ Such a slot antenna may be conveniently energized with a coaxial line,

with the outer conductor bonded to one side of the sheet and the center conductor connected to the far end of the slot as shown in figure 35-3. We then transfer this concept to stripline. The slot is cut in one ground plane and the center strip is shorted to the ground plane at the far end and the center of the slot. It is often difficult to get a good short in stripline at a precise point, so one should extend the center strip a quarter-wavelength beyond the specified short position and terminate it in an open circuit.

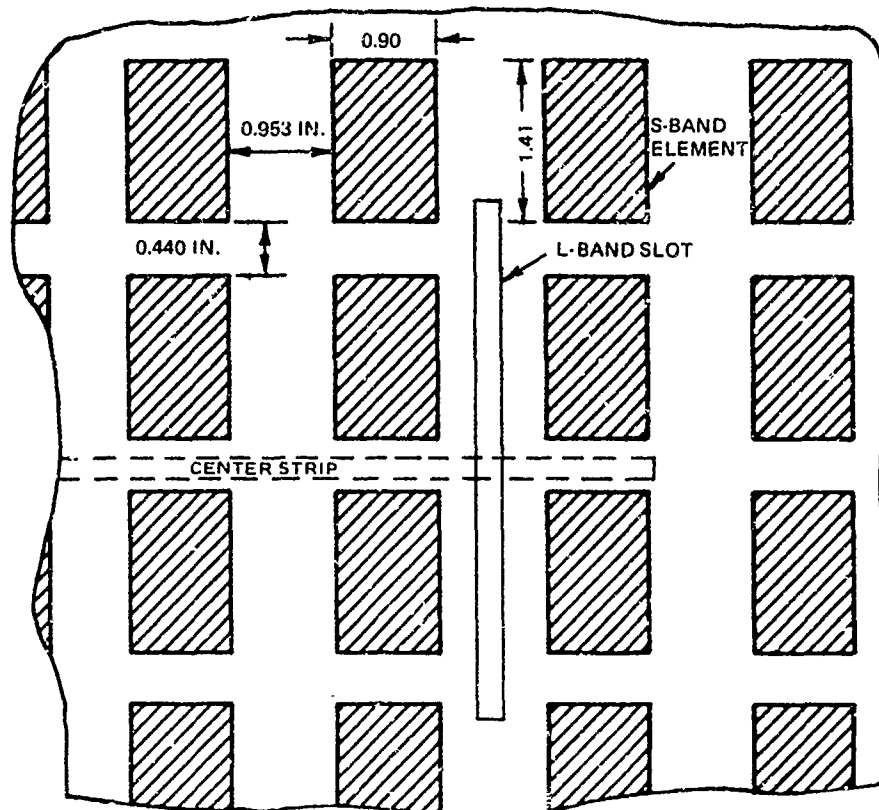


Figure 35-2. Section of multifrequency array, showing S- and L-band elements interlaced.

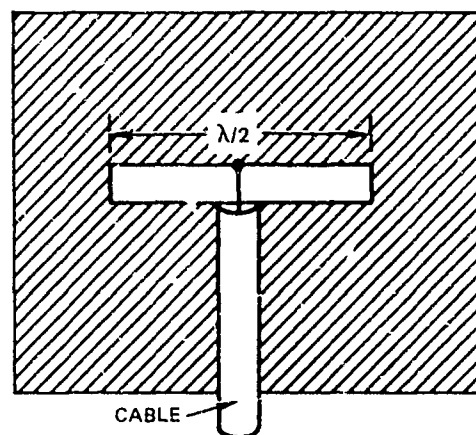


Figure 35-3. Slot antenna fed by coaxial line (ref. 4).

The slot conductance can be calculated from Oliner⁵ as follows:

$$G/Y_0 = 16/3\pi K(k')/K(k) (a'/\lambda)^2 [1 - 0.374(a'/\lambda)^2 + 0.130(a'/\lambda)^4]$$

where K is the complete elliptic integral of the first kind,

$$k = \tanh(\pi w/2b) \text{ and } k'^2 = 1 - k^2$$

This expression was evaluated for values of (a'/λ) from 0.44 to 1.00 using values of $w/2b = 0.33$, which corresponds to $Z_0 = 50$ ohms for $\epsilon = 2.56$ (PTFE glass) and the results are given in table 35-1.

By applying Babinet's principle, it is observed that lengthening a half-wave slot makes it more capacitive and shortening it would make it more inductive. Hence a slot which is cut to resonate at a given frequency will be inductive below resonance. If the slot is modified, either by dumb-belling or by introducing an obstacle which partially fills it, the effect is to make it more capacitive, and the condition of resonance is restored. Accordingly, then, by reducing the length of the slot, the slot resonances can be shifted to higher frequencies and a shunt capacitance can be used to tune the slot. The fundamental resonances will be unchanged, but all higher frequencies will be shifted to new frequencies, some higher and some lower than before. The net result is that the resonant conductance of the slot is reduced.⁶

A slot was constructed using 1/8 copper-clad boards with a dielectric constant of 2.56, w of 0.167, and b of 0.250, giving an impedance of 50 ohms. The slot was first constructed with a' (the slot length) of $\lambda/2$ at the center frequency of 1060 MHz using the guide wavelength. This turned out to be wrong, and it was determined that the slot should be $\lambda/2$ using the space wavelength. After this correction was made, the slot radiated and patterns in elevation and azimuth were taken (figs. 35-4 through 35-9).

In view of the narrow space between the S-band elements, it was decided to try to make the slot using a smaller ground-plane spacing, which would then allow the use of a narrower strip if the same impedance were retained. Accordingly, a slot section was constructed using a 1/16-inch board, allowing the strip width w to be reduced to 0.083 inch and b , the ground-plane spacing, 0.125 inch. Absolutely nothing worked with this slot; no adjustment in its parameters -- length, width, or offset -- made any but the slightest change. It was finally determined that the effective impedance of the slot was much lower than expected because of the very small ground-plane spacing.⁷ For a stripline cavity shown by the following expression

TABLE 35-1. SLOT CONDUCTANCE AS A FUNCTION OF SLOT LENGTH.

A/LAMDA	C/YO
.3999999	.2288409
.4099999	.2397420
.4199999	.2508487
.4299999	.2621569
.4399999	.2736627
.4499999	.2853622
.4599999	.2972513
.4699998	.3093261
.4799999	.3215827
.4899999	.3340172
.4999999	.3466254
.5099999	.3594037
.5199999	.3723433
.5299999	.3854555
.5399998	.3987211
.5499998	.4121419
.5599999	.4257143
.5699999	.4394346
.5799999	.4532994
.5899999	.4673055
.5999998	.4814495
.6099998	.4957285
.6199998	.5101395
.6299998	.5246797
.6399999	.5393456
.6499999	.5541355
.6599998	.5690463
.6699998	.5840768
.6799998	.5992236
.6899998	.6144860
.6999998	.6298617
.7099998	.6453485
.7199998	.6609465
.7299998	.6766539
.7399998	.6924692
.7499998	.7083930
.7599998	.7244238
.7699998	.7405626
.7799998	.7568091
.7899998	.7731633
.7999998	.7896268
.8099998	.8061997
.8199998	.8228838
.8299998	.8396820
.8399998	.8565943
.8499998	.8736246
.8599998	.8907746
.8699998	.9080496
.8799998	.9254531
.8899998	.9429817
.8999998	.9606494
.9099998	.9784570
.9199998	.9964082
.9299998	1.014512
.9399998	1.032771
.9499997	1.051196
.9599998	1.069791
.9699998	1.088564
.9799998	1.107524
.9899993	1.126678

EDIT

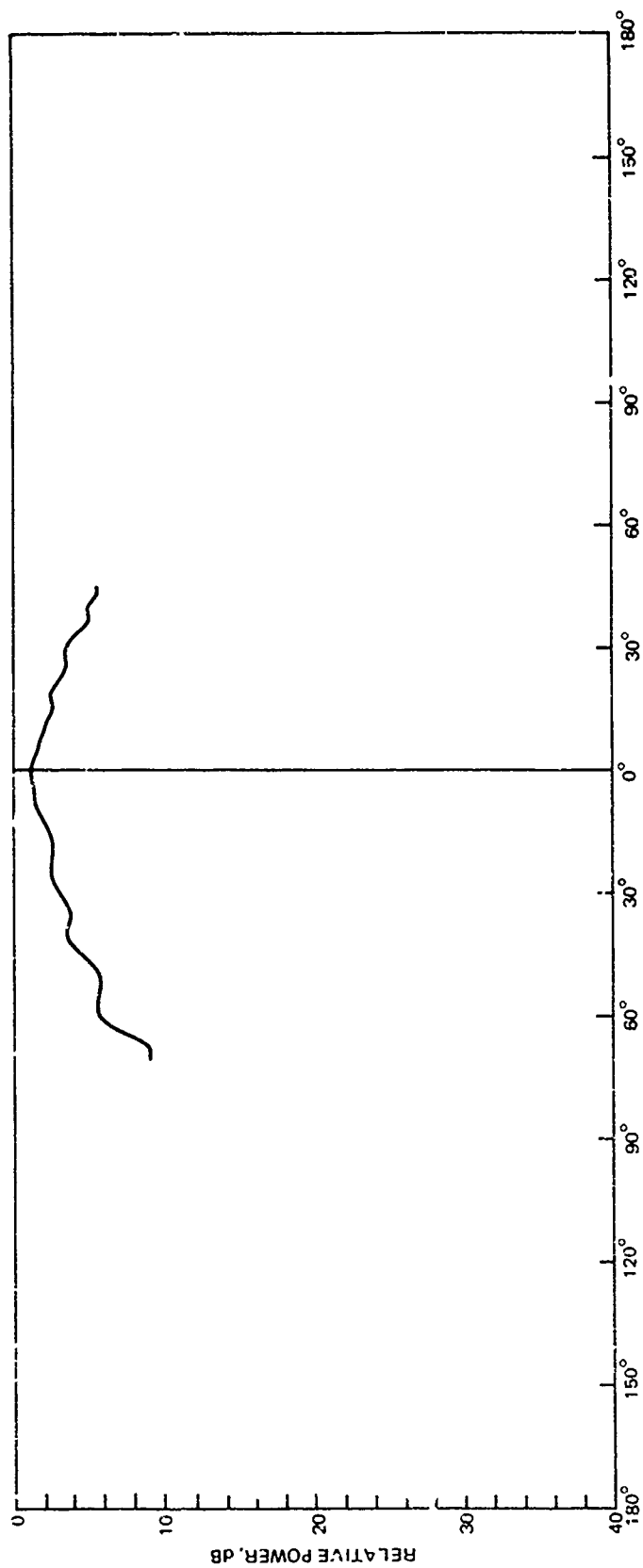


Figure 35-4. Elevation pattern, vertical polarization, 1.03 GHz.

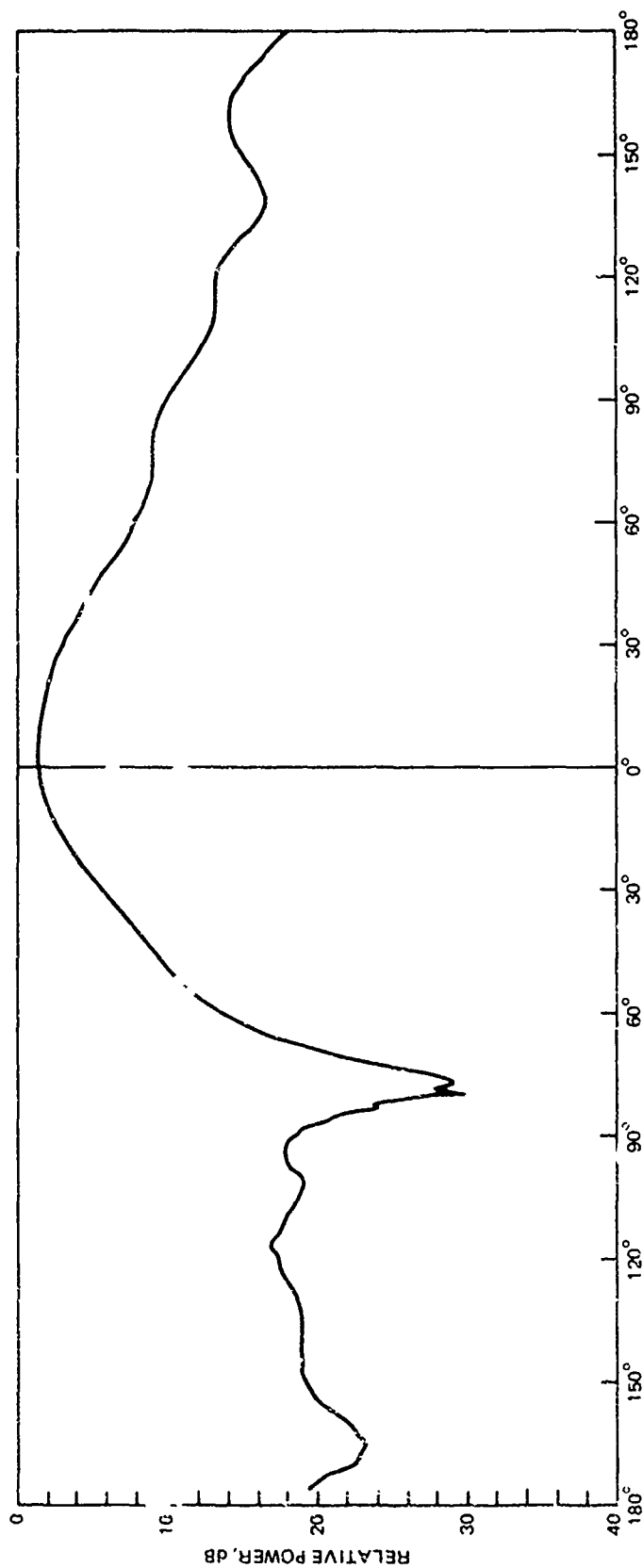


Figure 35-5. Azimuth pattern, vertical polarization, 1.03 GHz.

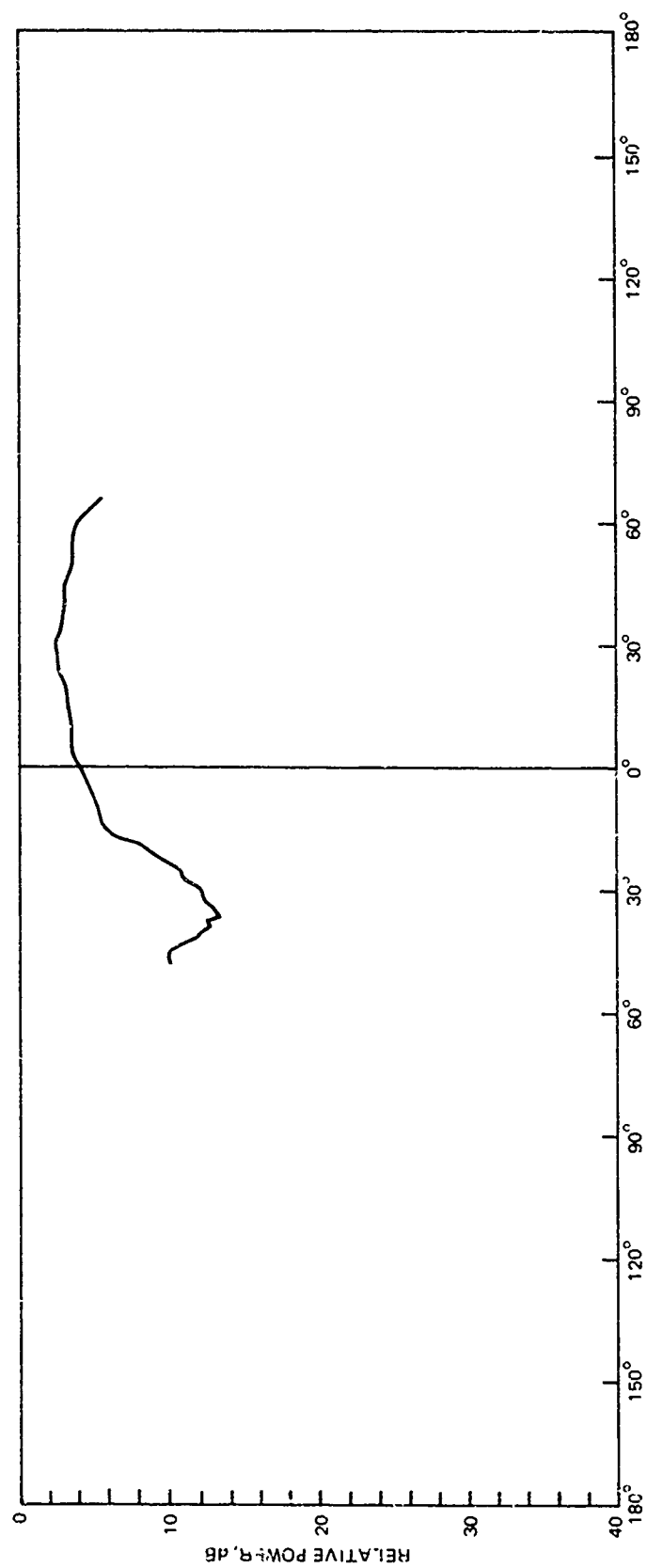


Figure 35-6. Elevation pattern, vertical polarization, 1.06 GHz.

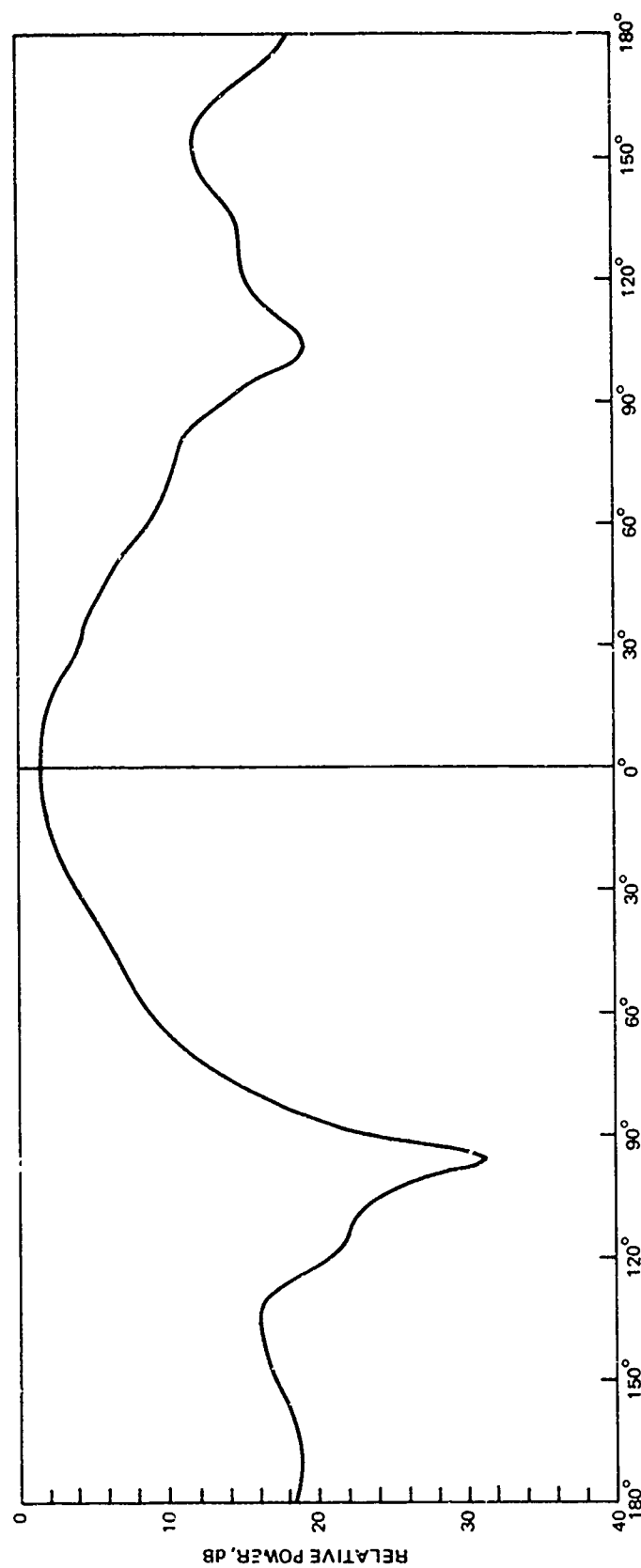


Figure 35-7. Azimuth pattern, vertical polarization, 1.06 GHz.

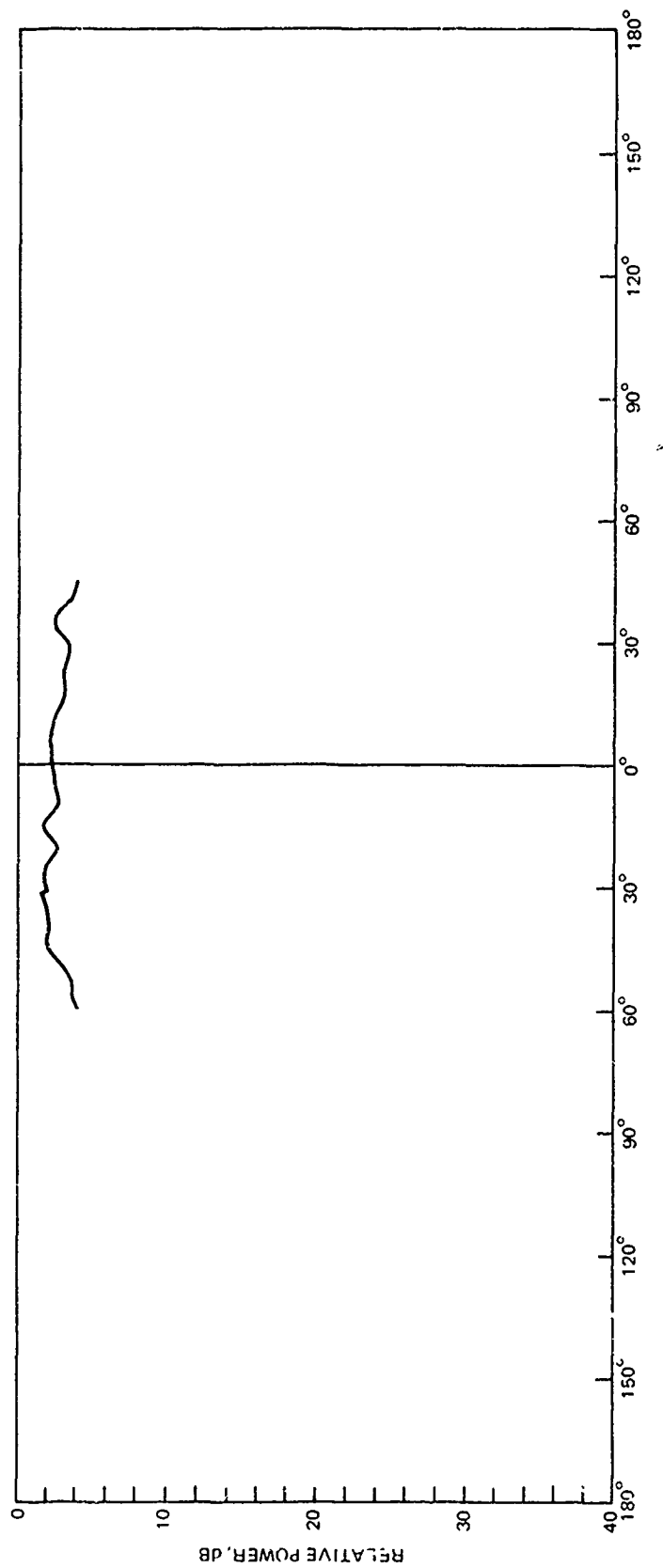


Figure 35-8. Elevation pattern, vertical polarization, 1.09 GHz.

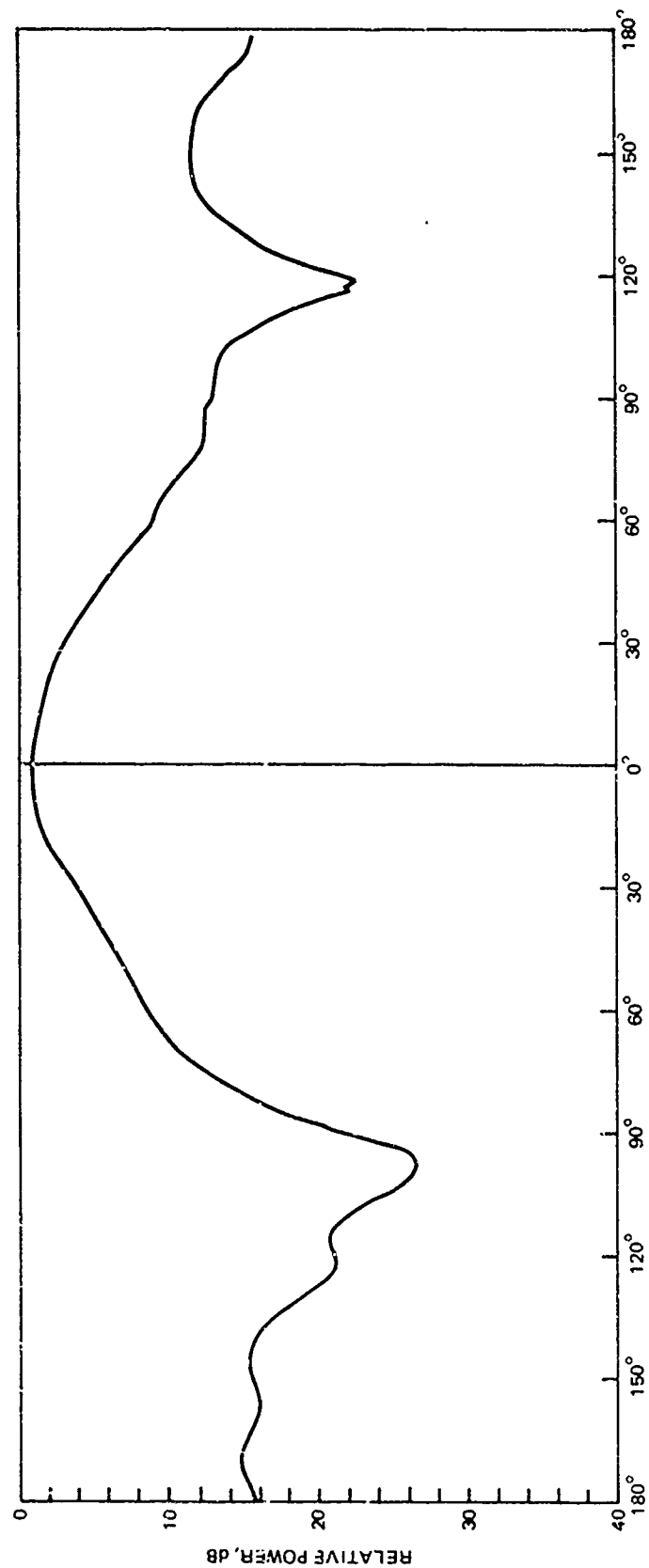


Figure 35-9. Azimuth pattern, vertical polarization, 1.09 GHz.

$$Z_{\text{eff}} = Z[1 - \exp(j4\pi b/\lambda)]$$

A new section is being made using 3/16-inch board to yield a ground-plane spacing of 0.375 inch.

One other effect should be mentioned here. It was found that variations in ground-plane spacing caused effects greatly exceeding those obtained by varying the slot parameters. Closely spaced screws would reduce this effect but not eliminate it entirely. A method suggested to us by Henry and Waterman of New Mexico State University⁸ eliminates the problem. This uses HX-1000 fluorocarbon bonding film to bond the two dielectric boards together.

CONCLUSIONS

Stripline slot radiators are practical and are easily constructed at microwave frequencies. The simplicity of their design, with no protuberances, makes them ideal elements for an integrated array. However, there are design problems. The narrow spacings between the S-band frequency elements severely restricts design freedom. For instance, it does not allow a full $\lambda/2$ cavity size about the slot. This may necessitate going to a $\lambda/4$ cavity backed slot. In addition the scan angles for all frequency bands must necessarily be compromised by the physical sizes of the integrated elements.

This work will be continued at NELC along the lines suggested here. A four-element L-band array has been built and tested. An integrated array consisting of the four-element L-band array interlaced into a section of the S-band array is under construction and will be tested shortly.

REFERENCES

1. Provencher, J. H. and Boyns, J. E., "Multi-frequency Multi-function Array Antennas," International Symposium on Antennas and Propagation, Sendai, Japan, 1-3 September 1971, Proceedings, p. 49-50
2. Begovitch, N. A., "Capacity and Characteristic Impedance of Strip Transmission Line with Rectangular Inner Conductors," Institute of Radio Engineers, Transactions, PGMTT-3, No. 2, p. 127-133, 1955
3. Cohn, S. B., "Problems in Strip Transmission Lines," Institute of Radio Engineers, Transactions, PGMTT, No. 2, p. 127-133, 1955
4. Kraus, J. D., Antennas, McGraw-Hill, 1950
5. Oliner, A. A., "The Radiation Conductance of a Series Slot in Strip Transmission Line," Institute of Radio Engineers, 1954 Convention Record, v. 2, Pt. 8, p. 88-90
6. Pedinoff, M. E., "The Negative-Conductance Slot Amplifier," Institute of Radio Engineers, Transactions, PGMTT-9, no. 6, p. 557-566, November 1961
7. Hemmi, C., Texas Instruments Co., private communication
8. Waterman, J. and Henry, D., "Stripline Strap-On Antenna Array," 21st Annual Symposium, USAF Antenna Research and Development Program, University of Illinois, Urbana, Illinois, 12-14 October 1971

36. WIDEBAND PHASE LOCKING AND PHASE SHIFTING

USING FEEDBACK CONTROL OF OSCILLATORS

by

D. Rubin

Code 2330

Naval Electronics Laboratory Center
San Diego, California 92152

for

ARRAY ANTENNA CONFERENCE

22, 23, 24 February 1972

Naval Electronics Laboratory Center
San Diego, California 92152

36-1a

INTRODUCTION

Solid-state, phased-array antenna systems invariably use amplifiers as power sources instead of locked oscillators whenever large bandwidths are required. The primary reason for this choice is the difficulty in phase-locking high-Q, low-noise oscillators over large frequency ranges.

This paper describes a method of phase-locking both current-tuned and voltage-tuned oscillators over very wide bandwidths and, in addition, provides a method of phase-shifting outputs with respect to one another without external phase-shifters.

Experiments performed with two YIG-tuned Gunn oscillators (Watkins-Johnson Mod. 5008-2) have yielded 3-GHz locking range in X-band using injected power 10 dB below oscillator output power. Output phase remained within $\pm 1^\circ$ over a 1.2-GHz band and controlled phase shifting was achieved using applied voltages within a dc feedback loop.

FREQUENCY TRACKING METHOD

For oscillators to phase-track one another over large frequency ranges, it is first necessary that their free-running frequencies be brought to within the appropriate range¹

$$\Delta f \leq \frac{f_o}{2Q_o} \sqrt{P_i/P_o} \quad (1)$$

where $\Delta f = |f_i - f_o|$ is the frequency difference between the master and slave oscillators without signal injection, P_i is the power injected into the slave oscillator cavity, P_o is the slave oscillator output power, and Q_o is the loaded Q of the slave cavity. The above formula holds for $P_i \ll P_o$. Even with oscillators and magnetic structures built to extremely close mechanical tolerances, with the same current through the two coils, their free-running frequencies may differ as much as 200 MHz and have linearity variations of ± 15 MHz throughout the X-band region. Frequency-locking measurements at 10 GHz, wherein the locking range of the slave oscillator is measured as a function of the P_i/P_o ratio, gave a Q_o of 450, indicating that the slave frequency must be held to within 3.5 MHz of the master frequency for locking to occur with $P_i/P_o = 0.1$.

In addition to the main frequency-controlling current, which was series-connected to both YIG coils, a small additional current was added to one of the coils. Without injection locking, the latter current was varied until the two oscillator frequencies were approximately the same, as noted on a spectrum analyzer. This additional current was noted at incremental frequencies throughout X-band, first with frequency increasing, then with frequency decreasing. The currents were different for the two cases due to hysteresis of the magnetic circuit. Figure 36-1 shows the additional currents needed for frequency tracking and also shows a current synthesized by the circuit of figure 36-2.

For the frequency tracking circuit, one connection serves as both input and output. The input voltage is taken from the slave oscillator YIG coil and rises linearly with frequency. Operational amplifiers 1 and 2 serve as voltage follower and inverter, respectively, and do not load the YIG coils. At frequencies below 7.5 GHz, all diodes are held below breakdown, and a constant current enters op-amp #3 through a resistor connected to $-V_s$. As the frequency is raised, each diode in turn breaks down, first removing, then

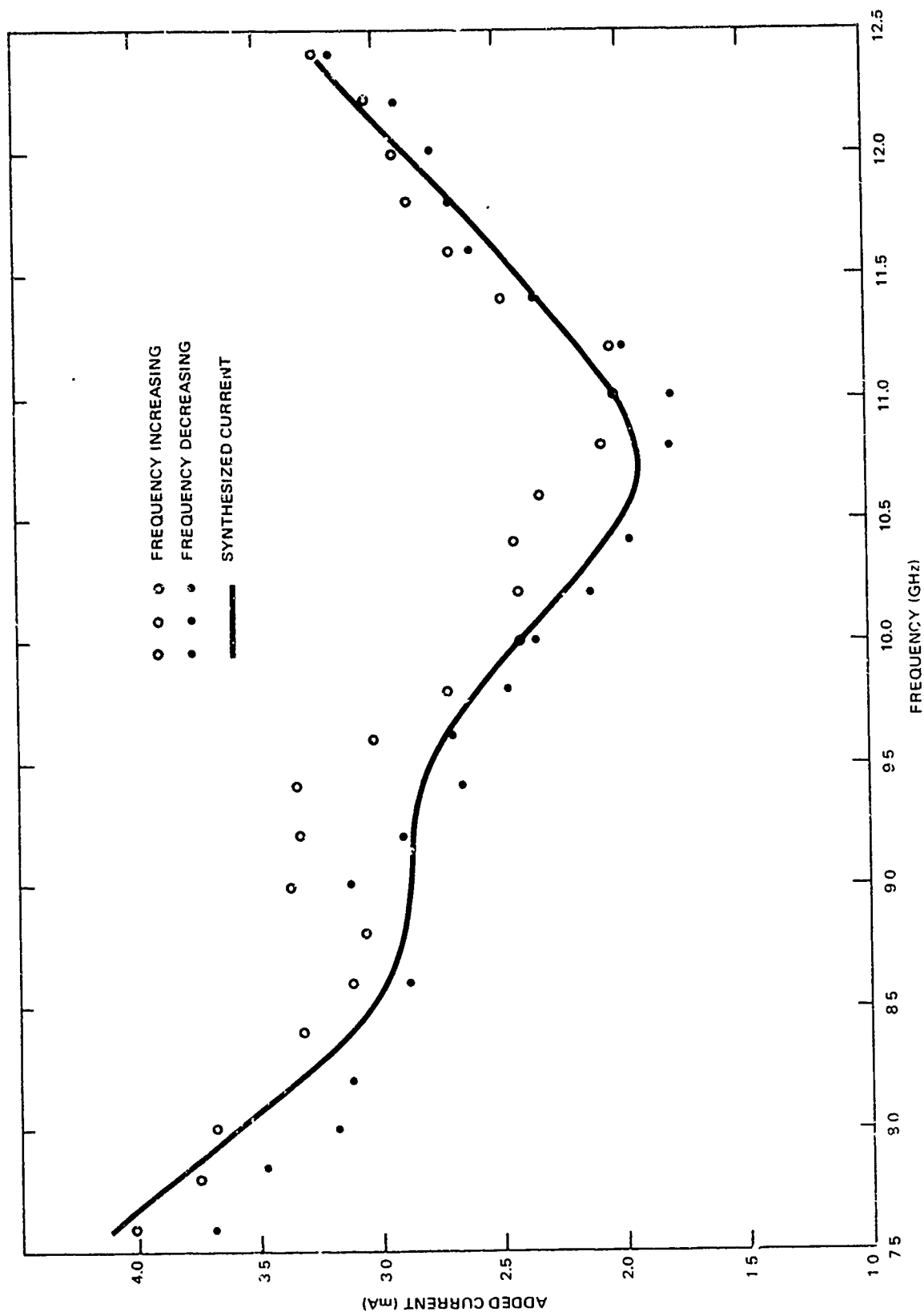


Figure 36-1. Current excess required by slave YIG coil in order to frequency-track master oscillator.

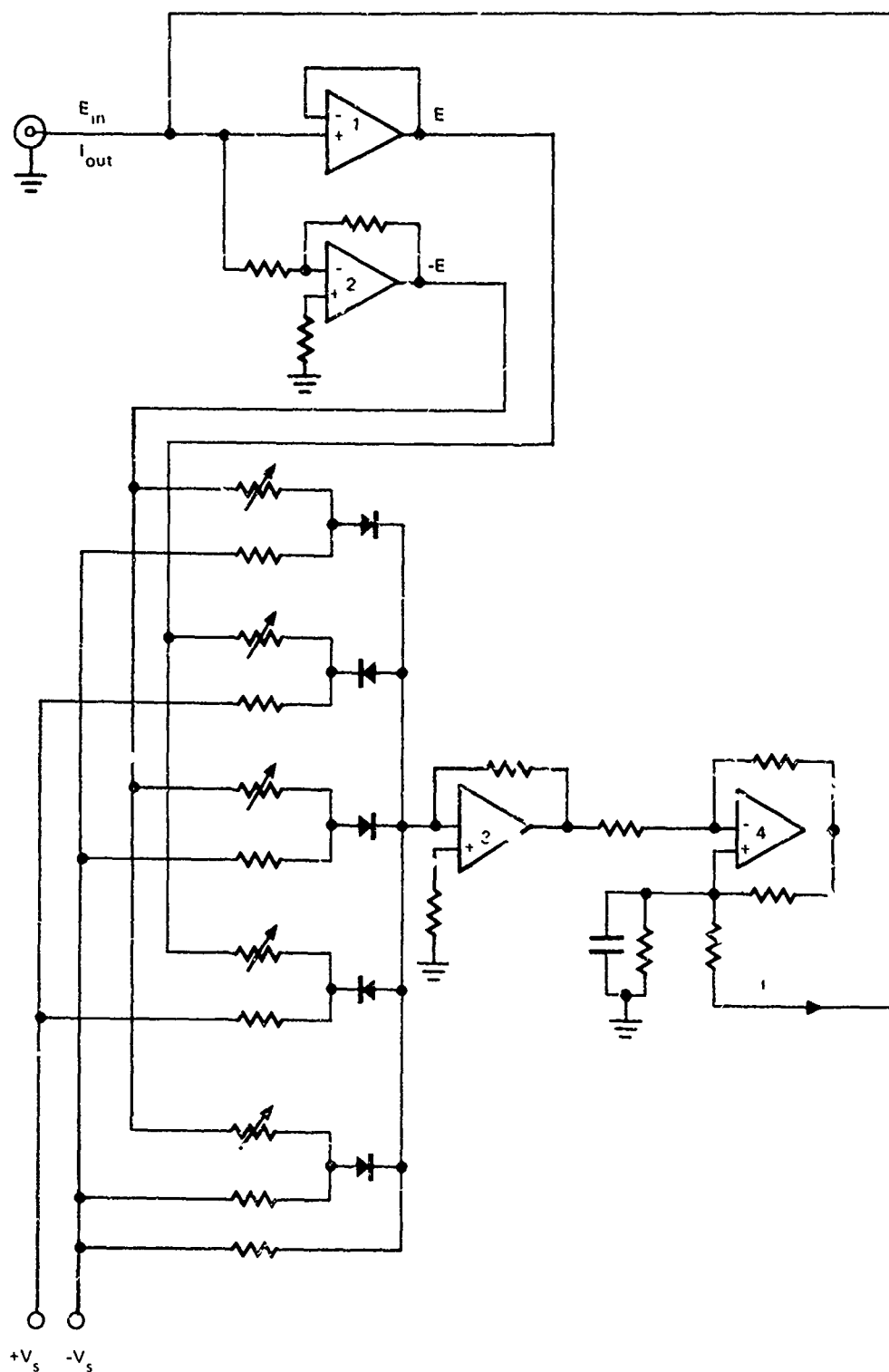


Figure 36-2. Current syntheses circuit used for frequency-tracking of YIG-tuned oscillators.

adding, current to the input of op-amp #3. The input voltage at which a diode breaks down, and the amount of current conducted through a diode, is dependent on the two resistors connected to it. The current entering op-amp #3, and hence its output voltage, is thereby made nonlinear with respect to the input frequency.

Op-amp #4 is called a Howland pump.² It delivers an output current proportional to the voltage input, i.e., even though the load itself is a resistance in series with a voltage source. The delivered current is shown as the solid line in figure 37-1. With this circuit the YIG oscillators could track to 2 GHz. Also note that a similar method could be used for tracking varactor-tuned oscillators, wherein the input would be a voltage proportional to frequency, and the nonlinear output voltage would go to a varactor diode instead of being returned to the input. In the latter case the Howland current pump would be unnecessary.

PHASE LOCKING AND PHASE SHIFTING

Figure 36-3 is a block diagram showing the feedback method used. The phase comparator used is a 3-dB quadrature coupler with input and normally isolated terminals connected to the input rf sources and with output terminals connected to diode detectors. The detected voltage difference is proportional to the sine of the input phase difference. This provides the input for a dc amplifier and pump circuit. This in turn feeds current to the slave oscillator YIG coil which tends to adjust its free-running frequency until the inputs to the phase comparator are in phase. If a dc reference voltage E_{ϕ} is connected to one of the terminals of the latter differential amplifier, the feedback circuitry will adjust the current until the output voltage of the phase comparator provides approximately the same voltage to the other terminal of the difference amplifier.

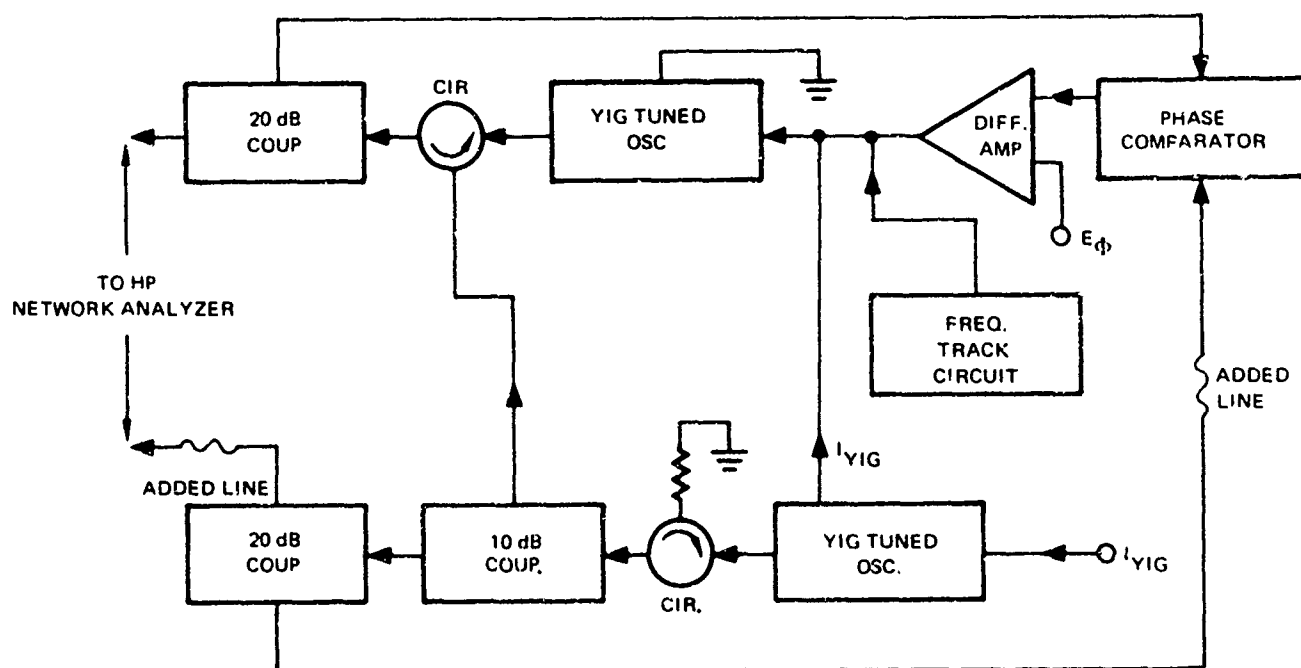


Figure 36-3. Phase-locked loop for YIG-tuned oscillators. Wideband power amplifiers could be used in front of the 20-dB couplers.

Hence, one could adjust the gain of the pump circuit so that if 1 volt at reference terminal E_Φ represented $+90^\circ$ phase shift, one could set a reference voltage E'_Φ so that $\sin\Phi = E'_\Phi$ and get a phase range which in practice will be less than $\pm 90^\circ$. For accuracy over wide bandwidths, power levelers should be used, so that $P_i/P_o = \text{constant}$. For the experiments to be described, the power output of both YIG oscillators varied similarly over the band so that $P_i/P_o = 0.1$ over most of the frequency range.

With feedback, the locking range at any given frequency is increased.³ Likewise, a given phase change due to the differences in the free-running frequencies is reduced. This can be seen from the following argument:

Let $\Delta\phi$ and $\Delta\phi'$ be the phase differences between YIG oscillator outputs with and without feedback as seen at the input terminals of the phase comparator. Corresponding to $\Delta\phi$ and $\Delta\phi'$ are the free-running slave oscillator frequencies f_o and f'_o . These frequencies are linearly dependent on the YIG coil current, so that

$$f_o = c_1 I_o + c_2$$

$$\text{and } f'_o = c_1(I_o + I_f) + c_2$$

where I_f is the current fed back from the phase comparator circuit. The latter is proportional to the sine of the phase difference, i.e., $I_f = c_3 \sin \Delta\phi' \approx c_3 \Delta\phi'$ for small phase differences. The Adler formula (1) becomes, for small angles

$$\Delta\phi \approx c_4(f_o - f_i) \quad (2)$$

$$\Delta\phi' \approx c_4(f'_o - f_i) \quad (3)$$

$$\text{where } c_4 = \frac{2Q_o}{f_i} \sqrt{\frac{P_o}{P_i}} \quad (4)$$

$$\text{hence, } I_f \approx c_3 c_4 (f'_o - f_i)$$

$$\text{and } f'_o \approx f_o + c_1 c_3 c_4 (f'_o - f_o)$$

Solving for f'_o we have from (2) and (3)

$$\frac{\Delta\phi'}{\Delta\phi} \approx \frac{f'_o - f_i}{f_o - f_i} \approx \frac{1}{1 - c_1 c_3 c_4} \quad (5)$$

For the YIG oscillators used, $c_1 = 17 \text{ MHz/mA}$. For the feedback system used, $c_3 = -(360/2\pi) \times 8 \times 10^{-3} \text{ mA/radian}$

Inserting values previously given into (4) we find $c_4 = 0.3 \text{ radian/MHz}$.

$$\text{Hence, } \frac{\Delta\phi'}{\Delta\phi} \approx \frac{1}{3}.$$

This reduction in phase shift with feedback was observed at fixed frequencies.

It is extremely important to adjust the lengths of lines to the phase comparator so that, over the frequency range to be used, there will be near-zero phase difference at the terminals at the center of the locking range. This is best done with a network analyzer taking the place of the phase comparator. By manually adding a small current to the slave oscillator coil, one can find a particular phase difference θ_1 at the center of the locking range at some frequency f_1 . The phase difference θ_2 is then found at the center of the locking range at another frequency f_2 . For a path-length difference L between the locked and unlocked sources,

$$\theta_1 = \frac{360}{c} f_1 L$$

$$\theta_2 = \frac{360}{c} f_2 L$$

where c = velocity of propagation of the lines used, and θ_1 and θ_2 are in degrees. Then

$$L = \frac{c}{360} \frac{\theta_2 - \theta_1}{f_2 - f_1}$$

With the correct cable length, the output of the comparator should always change polarity in the same direction when the free-running frequency of the slave oscillator becomes higher than that of the master oscillator. A similar method is also used to equalize the lengths of signal paths to the final output.

Figure 36-4 shows the degree of locking obtained using the above methods. The signal paths to the network analyzer were made slightly unequal, to decrease the change in phase angle at the low end of the band. For this reason the phase difference at the output is greater than $+90^\circ$ over part of the phase-locked frequency range.

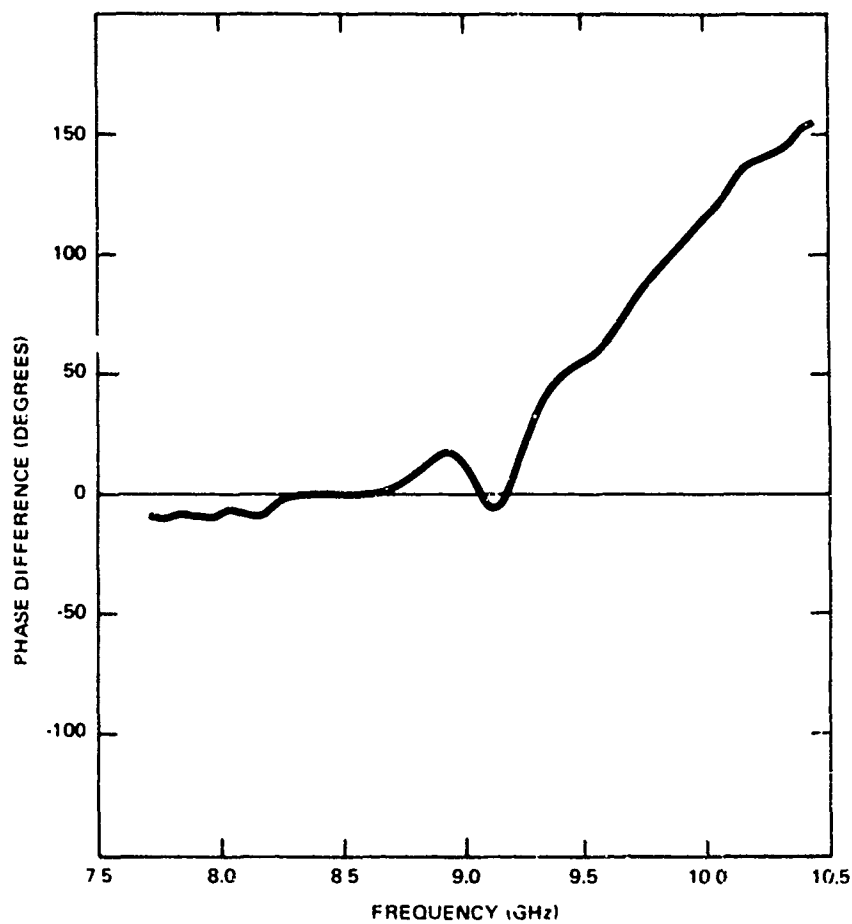


Figure 36-4. Phase difference vs. frequency of phase-locked oscillators.

Under the above conditions, the voltage E_{Φ} was set to incremental values and a slowly changing ramp current was applied to the series YIG coils. A plot of output phase with frequency (fig 36-5) is shown as a function of the applied voltage E_{Φ} . As expected, the output phase differences varied linearly with the applied voltage for small phase angles.

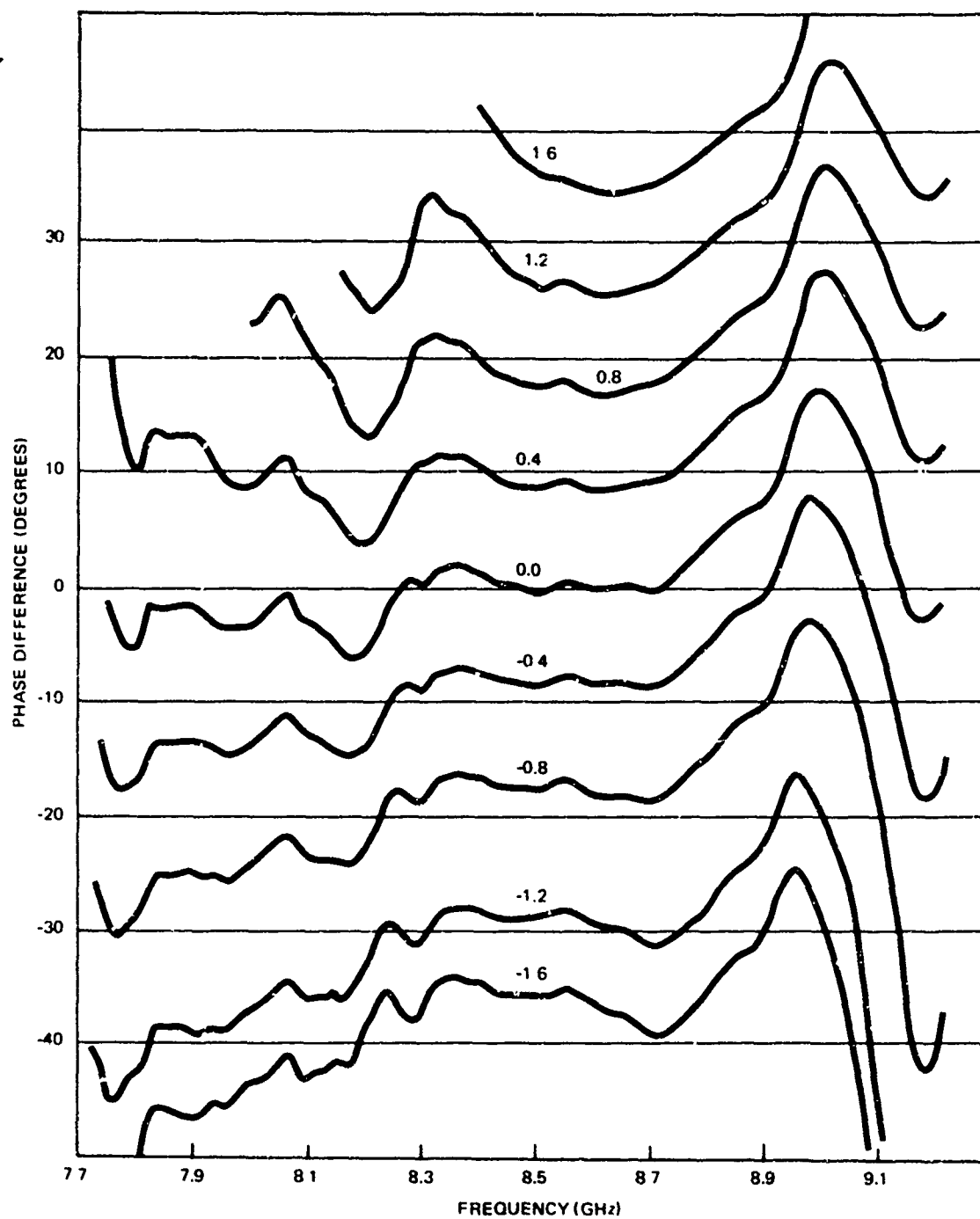


Figure 36-5. Phase difference as a function of E_ϕ .

CONCLUSIONS

Large frequency-locking ranges for injection-locked oscillators have been demonstrated using a combination of analog frequency control and dc feedback. In addition, controlled phase shifting has been demonstrated using applied dc voltages within a feedback loop.

It appears that the degree of success in using this method of phase shifting depends very much on the accuracy of frequency tracking. It is expected that varactor-tuned oscillators, in which hysteresis has no effect, would be preferable to the YIG-tuned oscillators used in this experiment.

Oscillators capable of tuning large frequency ranges generally have low output power capability, because of coupling of power into the lossy elements which cause the frequency changes. It is therefore expected that a practical system, based on the methods described, would also utilize wideband power amplifiers. The feedback method has the additional capability of correcting for differences in phase tracking between similar amplifiers used before the final couplers.

REFERENCES

1. Adler, R., "A Study of Locking Phenomena in Oscillators," Institute of Radio Engineers. Proceedings, vol. 34, p. 351-357, 1946
2. See for example, Application Manual for Computing Amplifiers, George A. Philbrick Researches, Inc., 1966
3. Stickler, J., "Injection-locking of Gunn Oscillators with Feedback Stabilization," Institute of Electrical and Electronic Engineers. Proceedings (letters), v. 57, p. 1772-1773, 1969

37. COMPUTER-AIDED DESIGN OF MICROWAVE COMPONENTS
FOR A LINEAR PHASED ARRAY

by

J. Reindel

Code 2330

Naval Electronics Laboratory Center
San Diego, California 92152

for

ARRAY ANTENNA CONFERENCE

22, 23, 24 February 1972

Naval Electronics Laboratory Center
San Diego, California 92152

37-1a

INTRODUCTION

Antenna array analysis generally assumes a certain current distribution available at the input to various antenna structures. The beam shape is determined by the array configuration, mutual coupling, etc. The assumed power and phase distribution are quite satisfactory for most design aspects but are not very helpful in error analysis because there is no connection between, say, a diode failure and the corresponding phase error.

This paper describes a program that calculates the beam patterns of a linear 32-port, phase-switched array (fig. 37-1) in which the phase and power distribution is determined by the microwave components.

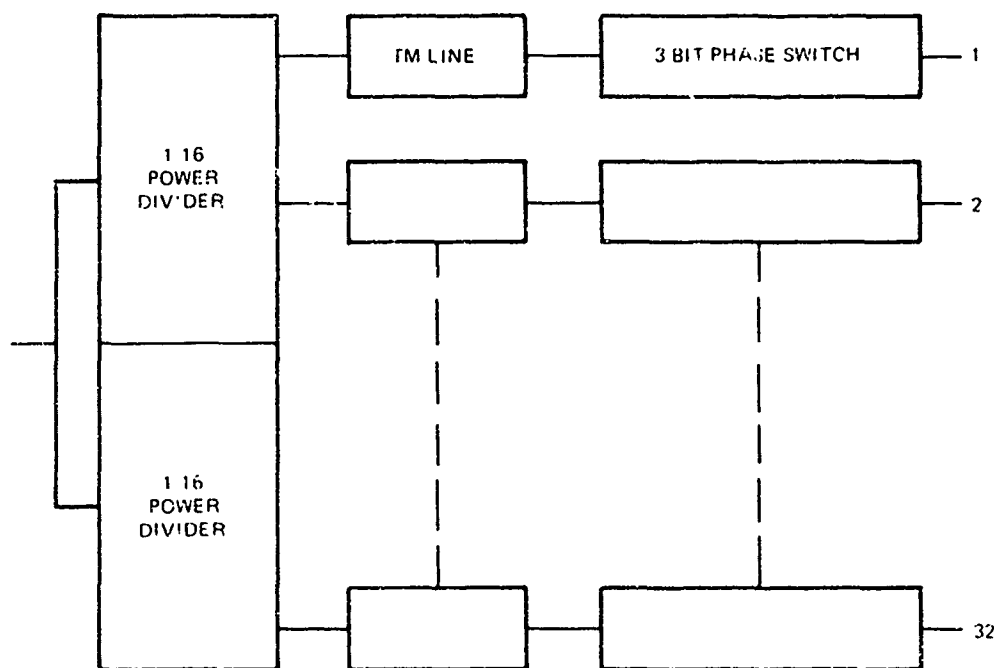


Figure 37-1 Linear 32-port, phased array

The components consist of transmission lines and diode circuits entirely specified by impedances, line lengths, and measurable diode parameters. Thus there is a direct relationship between the component and the array performance in terms of beam patterns and side-lobe levels. The program can show the effect of specified component errors and frequency limitations.

Separate programs design, analyze, and optimize the microwave components used for the array analysis. The divider-circuit impedances can be designed for a number of preselected current distributions or for any desired specified distribution.

These separate programs analyze and optimize three different PIN diode phase switches, a switched-line phasor, a side-coupled hybrid phasor, and a branch-coupled hybrid phasor. Each phasor has three bits or eight programmable 45° steps of phase increments.

The array system is analyzed by cascading the divider, an array of transmission lines, and an array of phase switches. The array patterns are calculated and plotted for various combinations of phase switches, at specified frequencies and with specified circuit errors.

The paper will first discuss the component routines, the divider, and the three phase-switch circuits.

CAD OF 16-PORT DIVIDER WITH SPECIFIED POWER DISTRIBUTION

The corporate binary transmission line divider consists of 31 quarter-wave transmission lines connected as shown in figure 37-2. The program designs the 31 impedance values and optimizes the values to provide a specified current or power distribution. The following current distributions can be selected by code numbers.¹

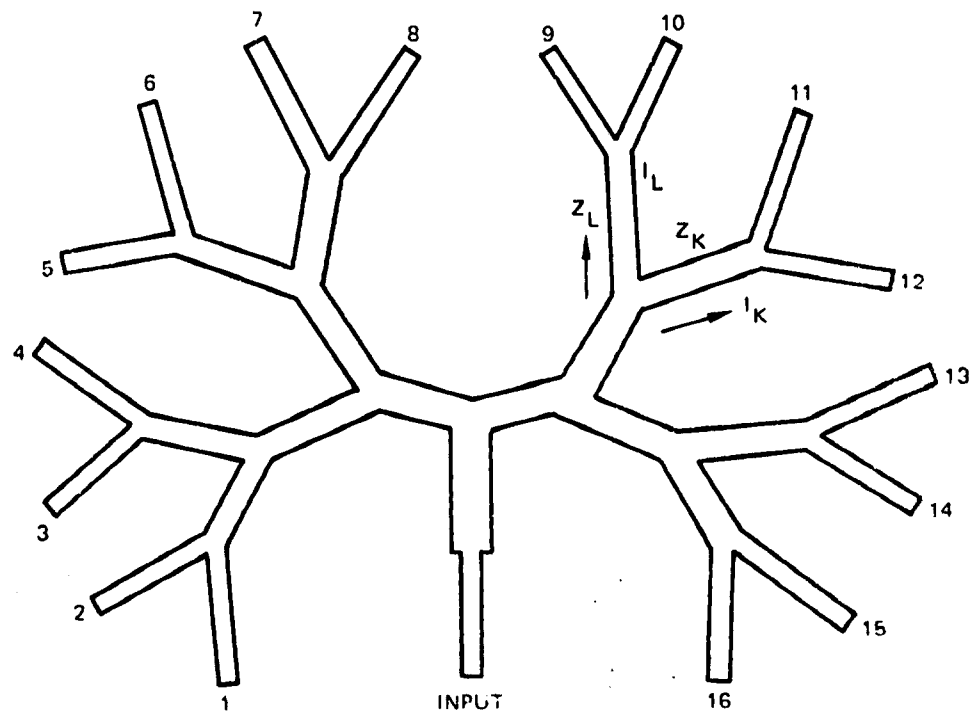


Figure 37-2. Stripline 16-port power divider.

1. uniform
2. cosine
3. cosine squared
4. $1-\text{Mod}(x)$
5. constant plus cosine squared

The corresponding power distributions are calculated.

The design of the transmission-line impedances take the following steps:

1. Approximate circuit design
2. Analysis of circuit
3. Calculation of circuit power division and error, i.e., difference between desired and calculated circuit power
4. Optimization of impedance values

The approximate design is derived from the known current distribution at each circuit node and from the assumption that each junction is independently matched in a 50-ohm system. Thus, given a current ratio $n = I_K/I_L$ (where $n < 1$) at a junction within the tree structure, where I_K and I_L are the currents at the respective nodes, the impedances of lines K and L are

$$Z_K = 25\sqrt{1 + \frac{1}{n}}$$

and $Z_L = 25\sqrt{1 + n}$

At the extremities of the branches the impedances are

$$Z_{KX} = 35.4\sqrt{1 + \frac{1}{n}}$$

$$Z_{LX} = 35.4\sqrt{1 + n}$$

An ABCD matrix is calculated for each transmission line given by

$$A = \begin{vmatrix} \cosh \gamma \ell & Z_0 \sinh \gamma \ell \\ \frac{\sinh \gamma \ell}{Z_0} & \cosh \gamma \ell \end{vmatrix}$$

where $\gamma = \alpha + j\beta$ is the complex propagation

ℓ = line length

Z_0 = characteristic impedance

The entire circuit is analyzed by transfer matrix multiplication and the output power at each port is calculated. The error in power at each port and the sum of errors are then reduced by an optimization routine through a search for the best values of the 31 impedances.

The optimization routine increases one impedance value at a time, recalculates the power distribution and error, and compares the new error to that previously calculated. If it is smaller, the impedance is increased exponentially; if it is greater, the impedance is reduced. The new distribution error is compared to the old and again the impedance value is changed, and so on until the first parameter has been optimized. The rest of the parameters are likewise optimized. The search then repeats the optimization from the first to the last of the parameters for a given number of iterations. Other more sophisticated optimization routines were used but were not found more effective.

Figures 37-3 and 37-4 show power distributions of the divider before and after optimization relative to an ideal cosine-squared distribution. Figure 37-5 shows the calculated beam pattern with the power distribution from the optimized circuit.

Figures 37-6 and 37-7 show the cosine square on pedestal distributions before and after circuit optimization. Figure 37-8 has the beam patterns.

The figures show that the power distribution error was reduced considerably. Beam patterns of the optimized circuit have side-lobe levels approximately equal to those of the ideal power distributions.

A modification of the program used for analysis of the 32-port phased array excludes the circuit design and optimization. The subroutines analyze the circuit and generate a set of 16 transfer matrices – one for each port – to be cascaded with the phase switches.

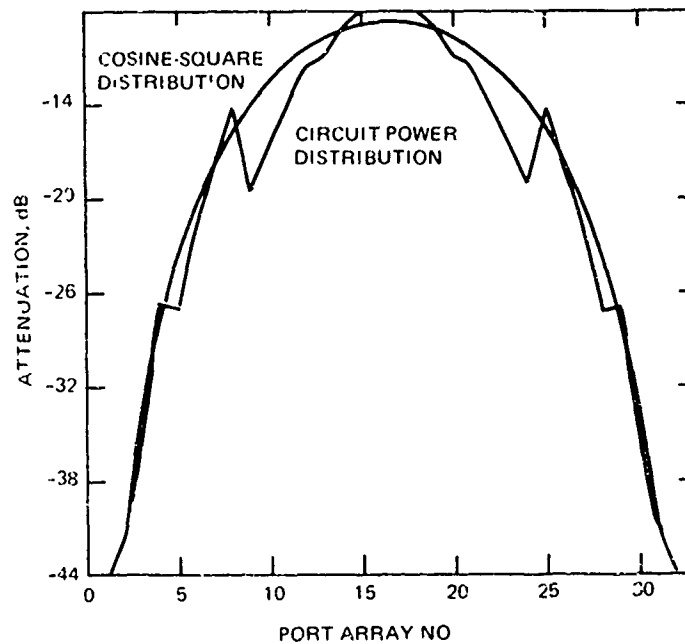


Figure 37-3. Power distribution of two 16-port reactive transmission line dividers before circuit optimization

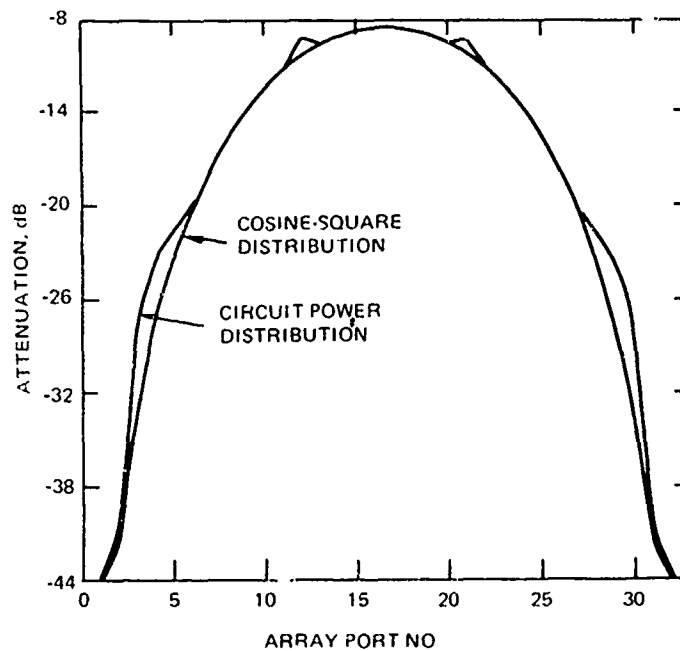


Figure 37-4. Power distribution of two 16-port reactive transmission line dividers after circuit optimization

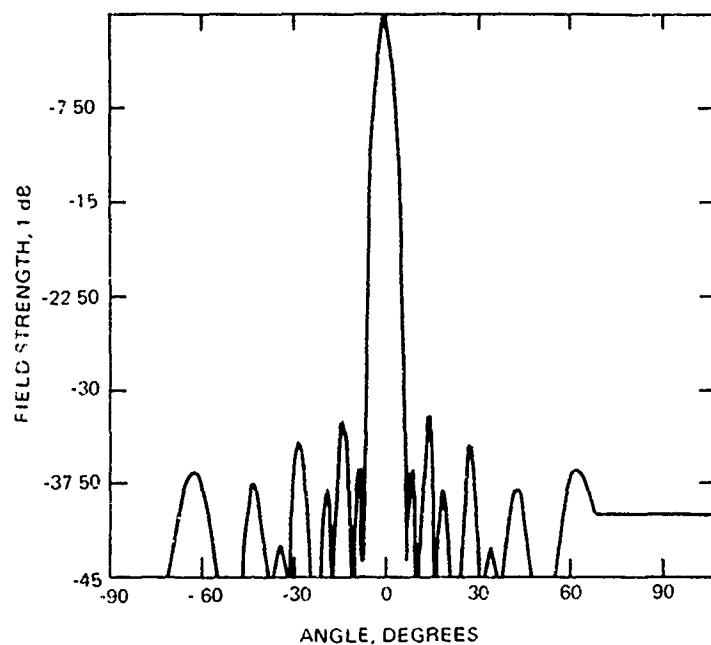


Figure 37-5. Broadside beam pattern by 32-port array fed with optimized divider circuit designed for cosine-square distribution.

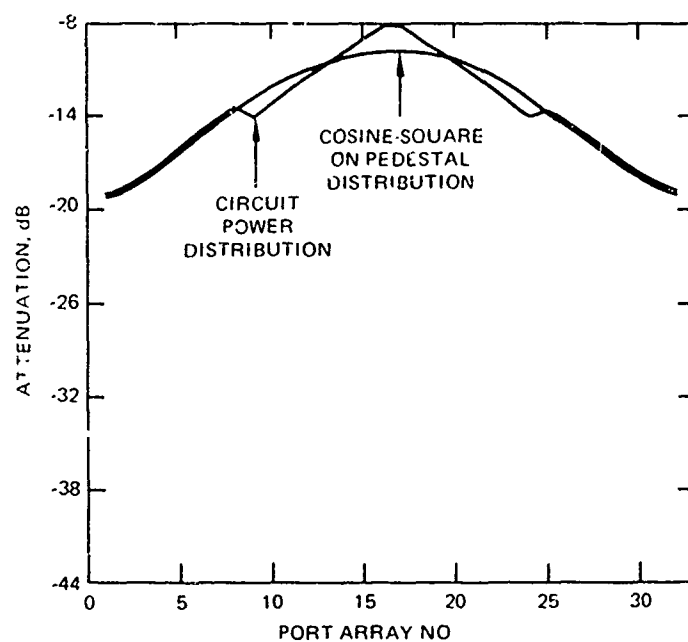


Figure 37-6. Power distribution of two 16-port reactive transmission line dividers before circuit optimization.

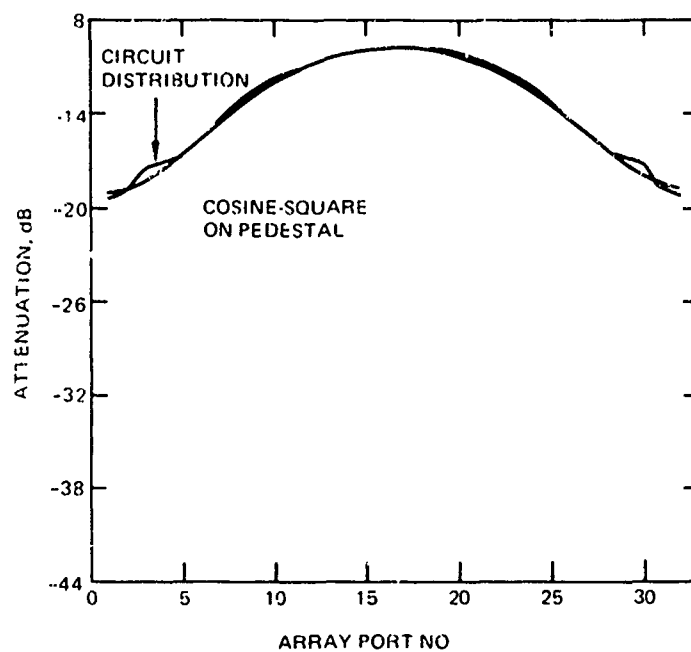


Figure 37-7. Power distribution of two 16-port reactive transmission line dividers after circuit optimization.

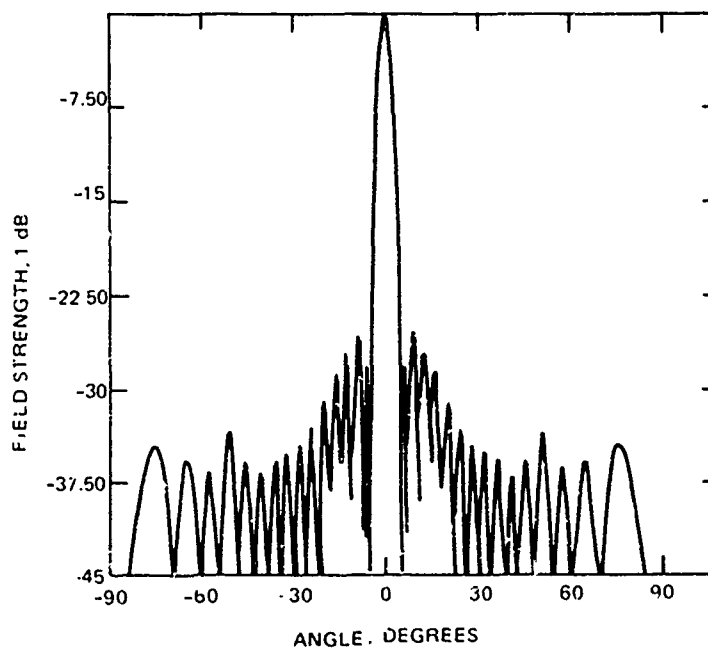


Figure 37-8. Broadside beam patterns of 32-port array fed by optimized divider circuit designed for cosine square on pedestal distribution.

DIODE PHASE SHIFTERS

SWITCHED-LINE DIODE PHASE SWITCH

The program was modeled after an MIC circuit already built² and extensively tested as shown in figure 37-9. The 3-bit phasor circuit has 8 shunt diodes; each is connected between a 50-ohm line and a capacitive plate. In forward bias the diode inductance and the capacitance resonate and short the line. The diode transfer matrix is derived from the equivalent circuit shown in figure 37-10.

The 180° and 90° phase bits consist of switched loop lines. The three diodes in each loop are switched complementary so that the circuit path lengths are varied by 180 and 90 degrees. The top phase bit increases the phase delay by 45° when the reactances reflected from the two open lines are changed from inductive (short line lengths terminated in forward-biased diodes) to capacitive (open lines greater than 3/4 wavelength). The circuit is analyzed by transfer matrix multiplication. The circuit loops of the 180° and 90° bits, which consist of two and three line segments separated by diode circuits, are first cascaded by multiplication, then transformed to Y matrices, added, and reconverted to ABCD's.

The 8 plate capacitors, and the 11 line lengths and impedances are optimized by a feedback approach similar to the one described for the divider. The optimization routine seeks a minimum of a variable which is a sum of the circuit response characteristics, VSWR, insertion loss, and phase error. The routine makes a search by the Hooke and Jeeves method. Figures 37-11, 37-12, and 37-13 show the computed VSWR, insertion loss, and phase increments respectively.

The program was modified as a subroutine for the array analysis by excluding the optimization. The subroutine analyzes the optimized circuit and provides a set of 8 ABCD matrices – one for each phase state.

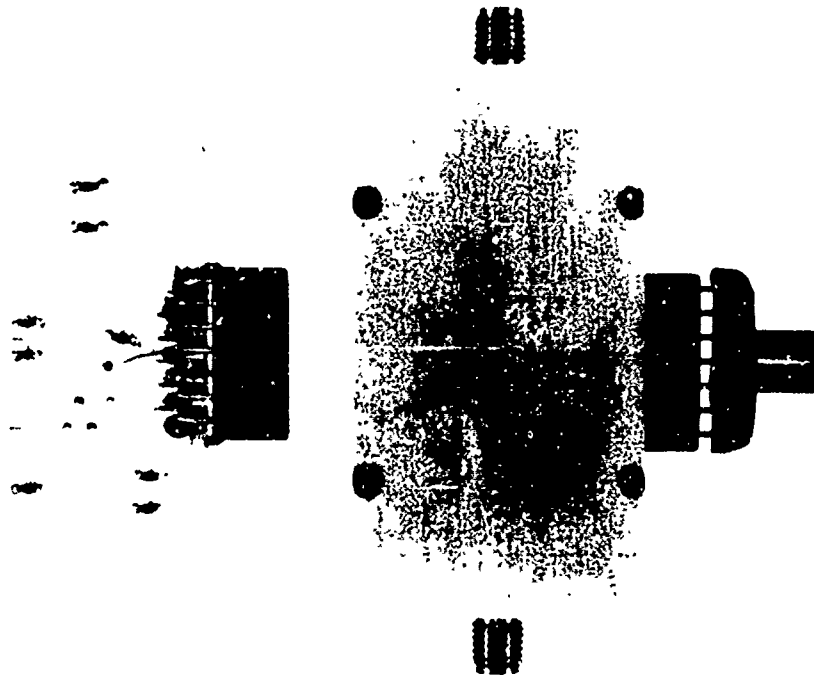


Figure 37-9. Switched line diode phase shifter. (NELC photograph 27-1-70)

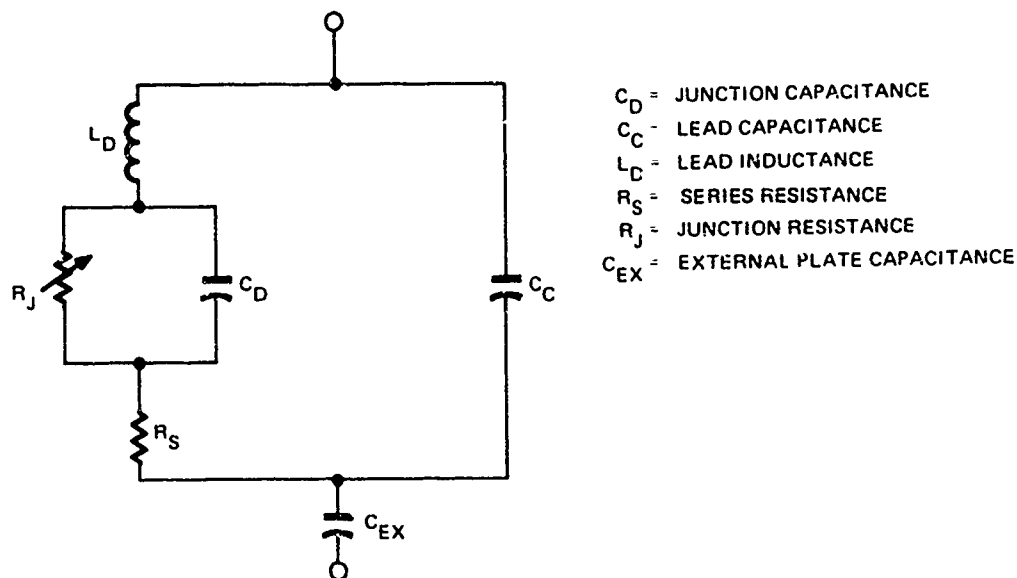


Figure 37-10. Equivalent diode circuit.

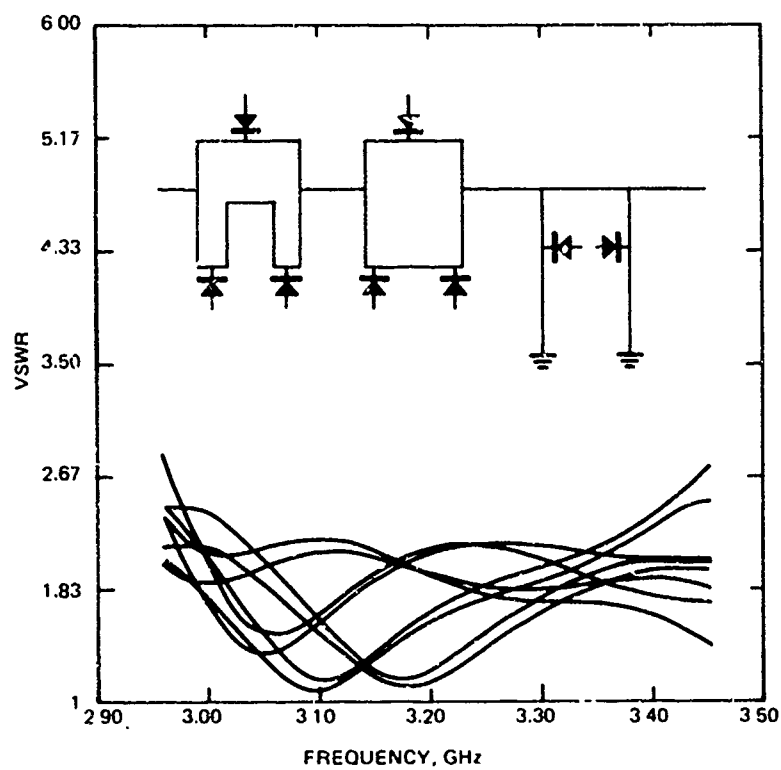


Figure 37-11. VSWR of 3-bit switched-line diode phase switch.

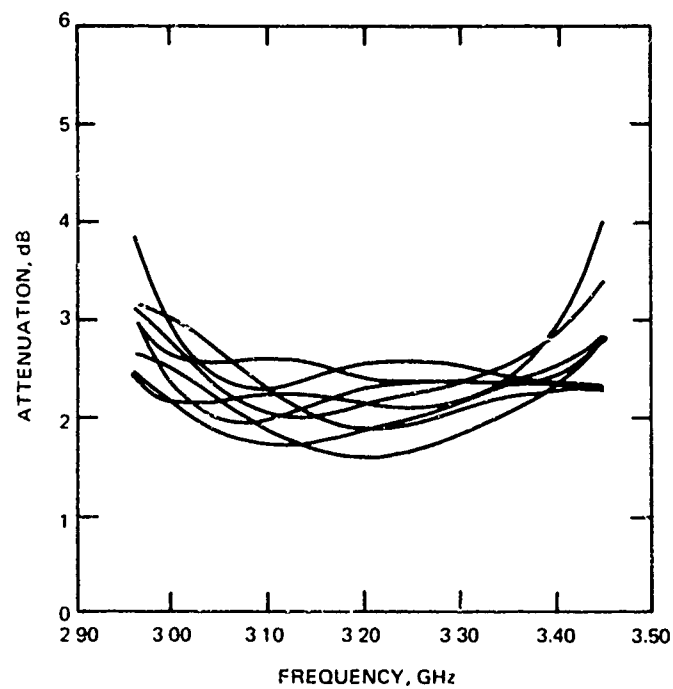


Figure 37-12. Insertion loss of 3-bit switched-line diode phase switch.

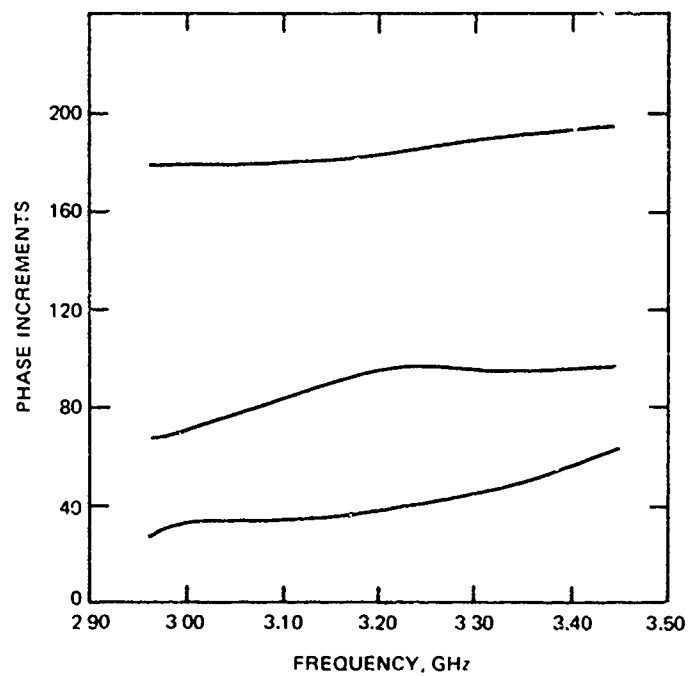


Figure 37-13. Phase increments of 3-bit switched-line diode phase switch.

HYBRID COUPLED 3-BIT PHASE SWITCH

The transmission line and diode circuit are shown in figure 37-14. The circuit consists of three cascaded, side-coupled, 3-dB, directional couplers that are terminated in three pairs of diodes and shorted transmission lines. The length of the short-circuited stubs behind the diode pair determines the phase shift of the respective phase bit. The couplers are characterized by the even and odd coupling admittances and by the length of the coupling lines.

The 4-port hybrids are analyzed by admittance matrix inversion as described by P. Green.² The circuits are cascaded by transfer matrix multiplication. The six external capacitors, the six shorted line stubs, and the two interconnecting line lengths are optimized as described in the preceding section. VSWR, insertion loss, and phase increments are plotted in figures 37-14, -15, and -16 respectively. The circuit has been built both on stripline (fig. 37-17) and with microstrip (fig. 37-18). The circuit requires closer tolerances than that of the switched-line phasor.

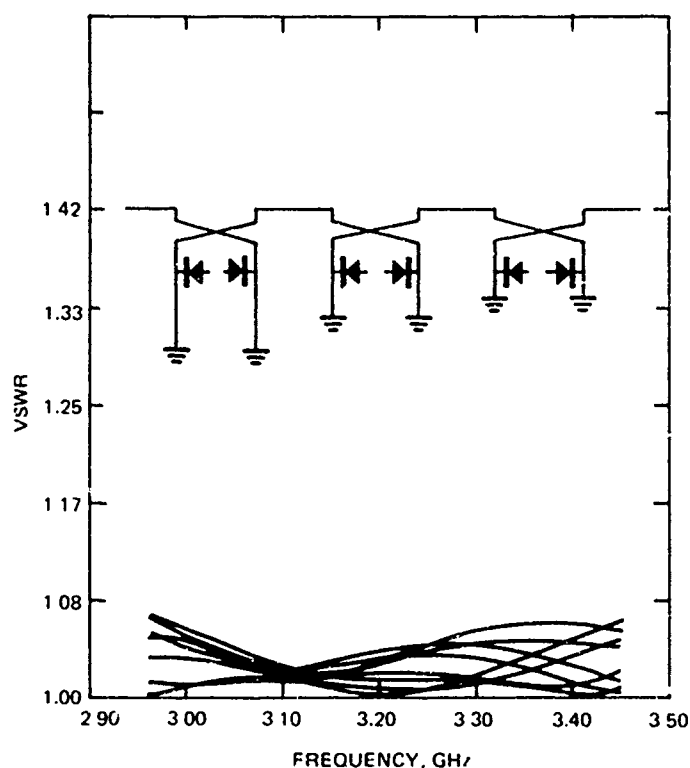


Figure 37-14. VSWR of 3-bit hybrid-coupled diode phase switch.

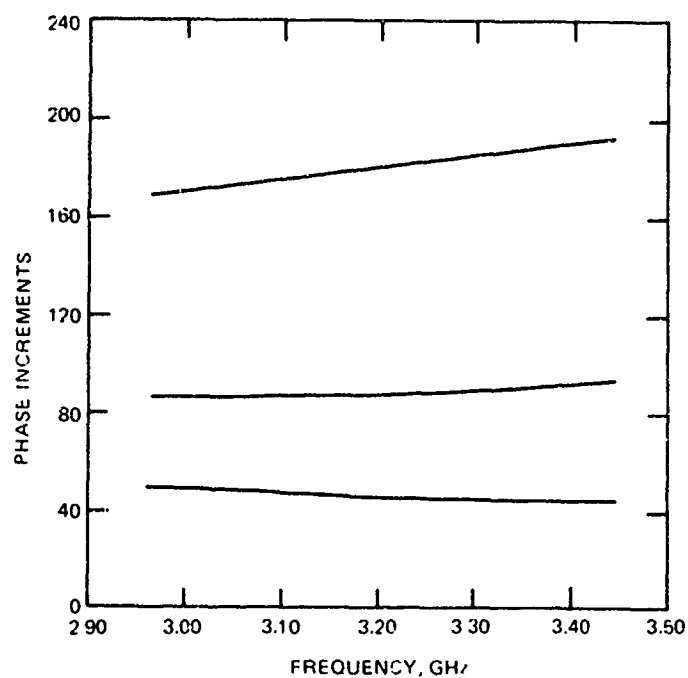


Figure 37-15. Phase increments of 3-bit hybrid-coupled diode phase switch.

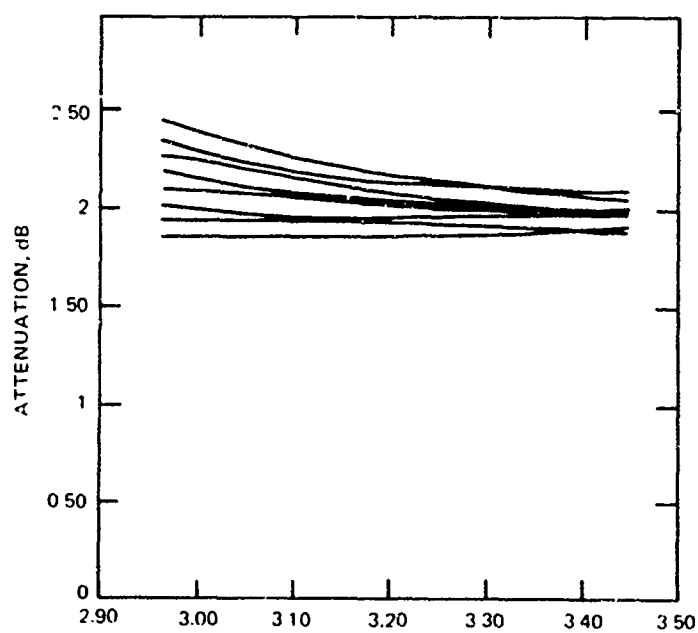


Figure 37-16. Insertion loss of 3-bit hybrid-coupled diode phase switch.

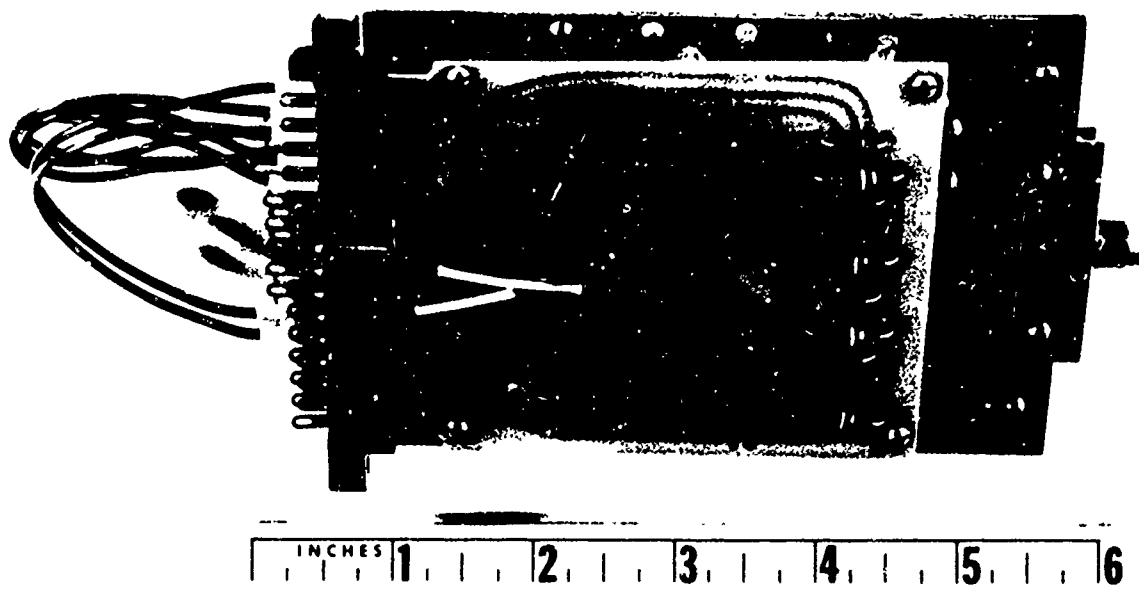


Figure 37-17. Stripline hybrid phasor with drive circuit. (NELC photograph LSF 91-1-69)

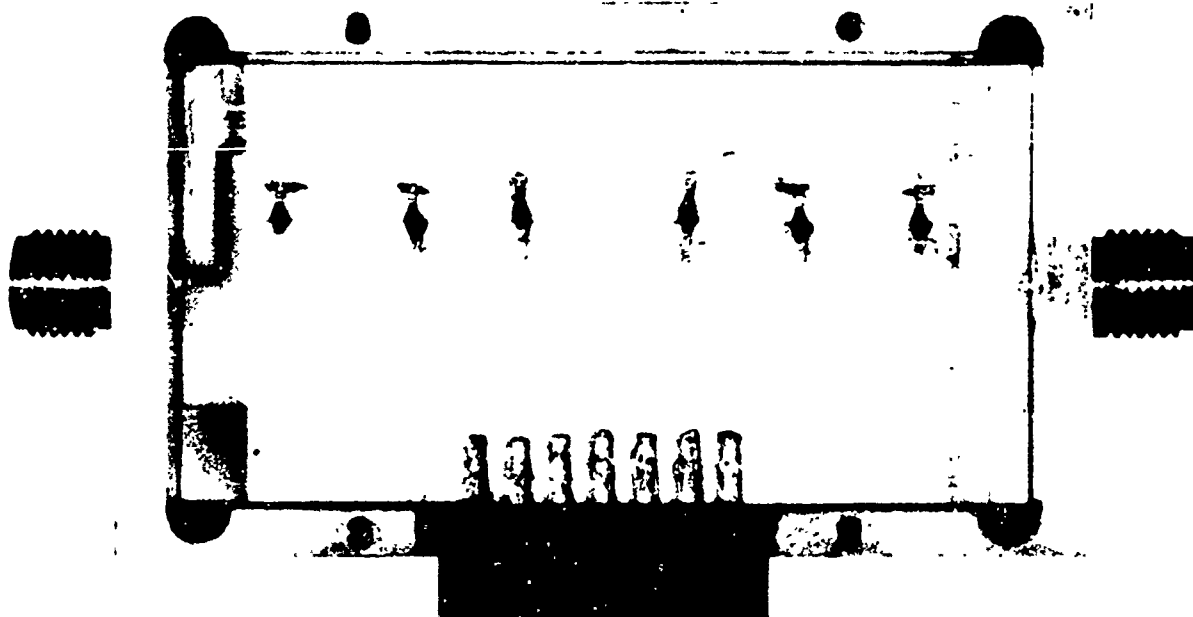


Figure 37-18. Microstrip hybrid phasor. (NELC photograph LSF 2201-6-70)

BRANCH-COUPLED PHASE SWITCH

The circuit consists of a 3-dB branch-type coupler with three arms, as shown in figure 37-19. The two output ports are terminated in shorted transmission lines and tuned diode circuits. The program analyzes the circuit using both admittance and transfer matrix techniques. Three different lengths of shorted stubs are analyzed and cascaded. The computed loss and phase increments are shown in figures 37-19 and 37-20 respectively.

The program was modified as a subroutine for the linear array analysis. The subroutine returns a set of eight ABCD matrices, one for each phase state.

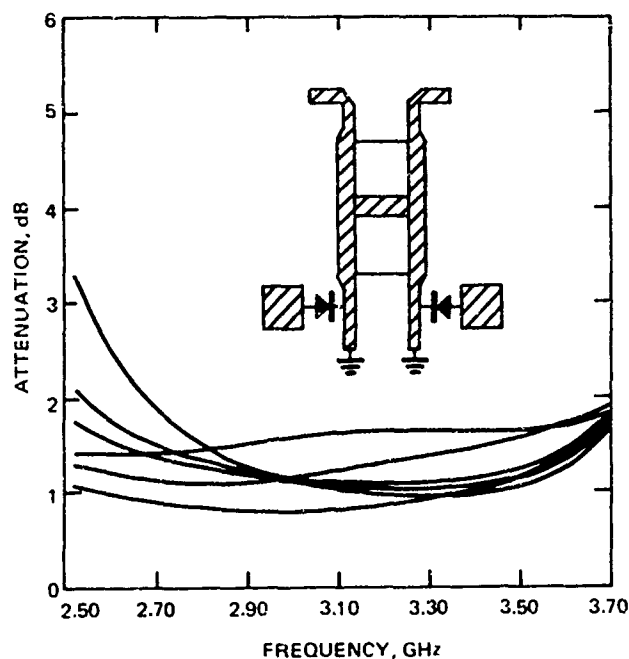


Figure 37-19. Branch-coupled diode phase switch.

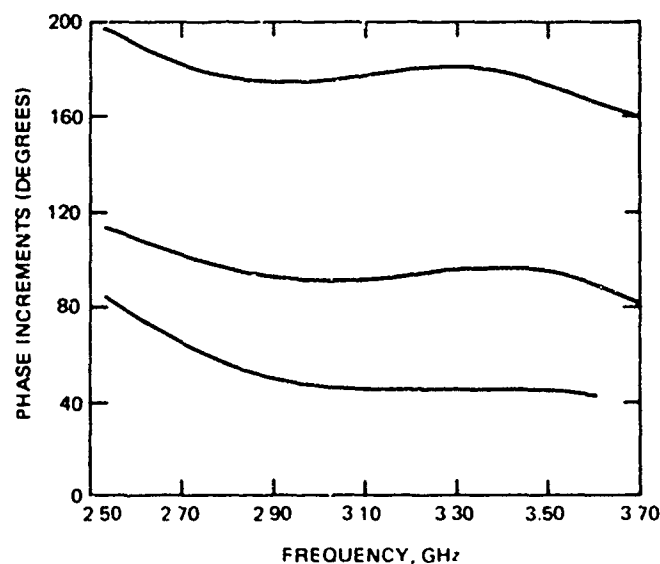


Figure 37-20. Branch-coupled diode phase switch.

32-PORT LINEAR PHASED ARRAY

The phased array system, as shown in figure 37-1, consists of two 16-port power dividers, a set of phase shifters, and connecting transmission lines. The optimized circuit values are entered through a Block Data subroutine. Three different phase-shifter circuits are programmed, the switched-line phasor, the hybrid-coupled phasor, and the branch-coupled phasor. The diode parameters and the optimized circuit dimensions for each circuit are entered by the Block Data. The spacing of the array radiators are specified as $\frac{1}{2}$ wavelength at the design center frequency.

The circuit components are analyzed in the respective circuit subroutines. The 16-port divider subroutine returns a set of 16 ABCD matrices (one for each output port) to the main program. Likewise each phase switcher subroutine returns a set of 8 ABCD matrices (one for each phase setting). The transmission lines (32) used for connecting the divider output ports and the phase shifters are analyzed in a LINE subroutine. A set of four matrices is made, one for each of four slightly different lengths of line. The differences between the lines can be varied as needed to simulate various degrees of errors. The four different lines are entered, or connected to the array, in a random way stipulated by a Block Data array IERROR. The 16 ABCD matrices of the divider, the four matrices of the lines and the eight matrices of a selected phase switch are cascaded by matrix multiplication. The complex-array currents are calculated from the resulting matrices, one for each of the 32 transmission paths, and a beam pattern is calculated from the 32-order array of currents. Beam positions are selected by arranging the order of the phase matrices in the multiplication process.

The program first calculates the power distribution across the 32-port array and plots power versus distance. The distributions vary with frequency as the performance of the phasor drops off and with the selection of phase switches. Figure 37-21 shows a typical power distribution.

The beam patterns are plotted from -90° to $+90^\circ$, as shown in figures 37-22 through 37-26. The plots show that the side-lobe level is mostly set by the phase error of the phase switch and the simulated random line-length error. With a 15° error the side-lobe level is at about -20 dB regardless of type of phasor and power distribution.

The switched-line phasor has the poorest bandwidth, as judged by the side-lobe level. The program can be used to evaluate the effect of various faults such as open-circuited diodes or shorted transmission lines. It can be used to estimate the usable bandwidth as specified by a side-lobe level or a beam shape and to estimate the effects on the beam by changing the design of any part of the system. For example a modified copy of the program was tested with simulated open diodes in each of the three phase bits. The array beam patterns, figure 37-26, show a small increase in the side-lobe level with ten circuit errors.

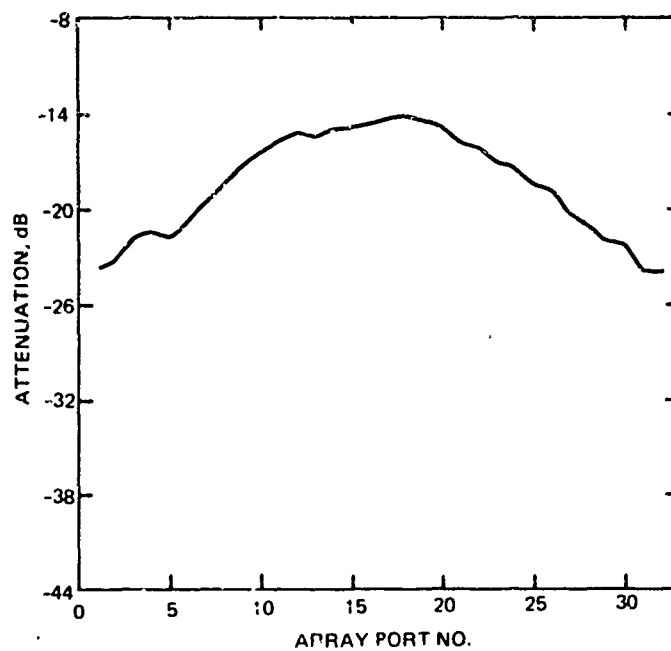


Figure 37-21. Array power distribution with cosine square-on-pedestal power divider and switched line phasor (3.0 GHz, at 20° off broadside).

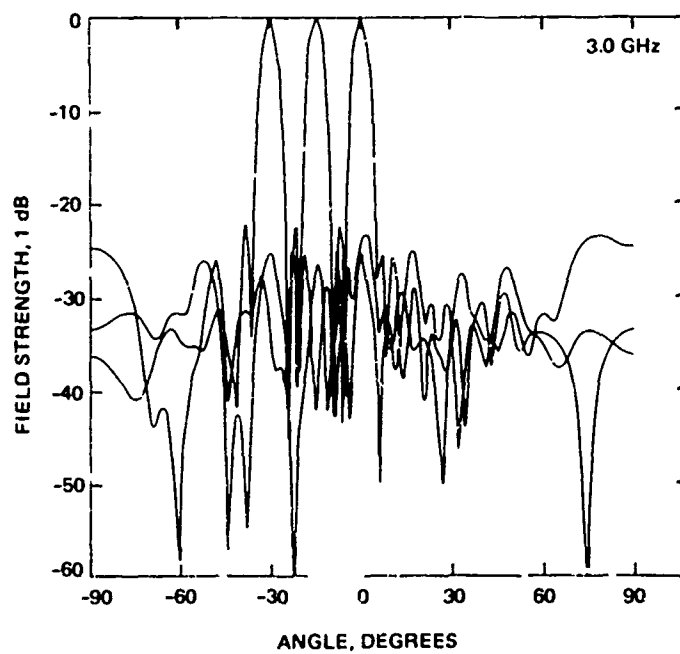


Figure 37-22. Beam patterns of 32-port phased array controlled by 3-bit hybrid-coupled diode phase switches.

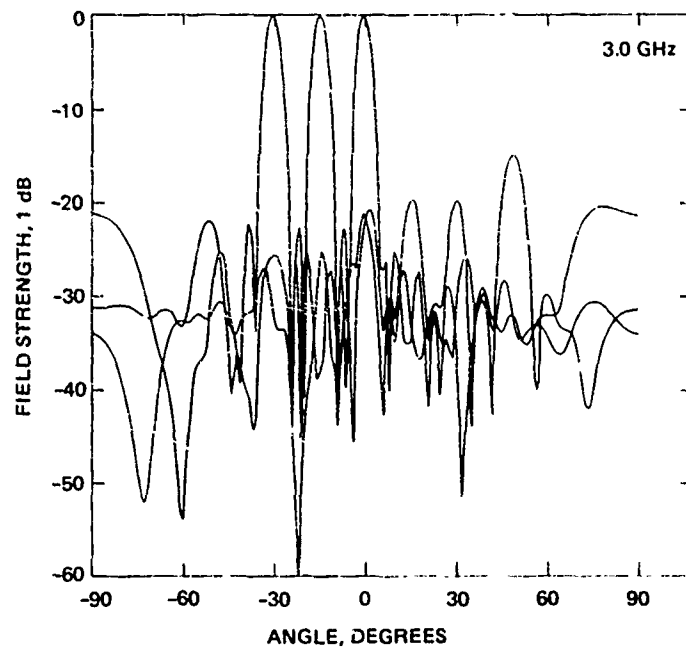


Figure 37-23. Beam patterns of 32-port phased array controlled by 3-bit switched-line diode phase switches.

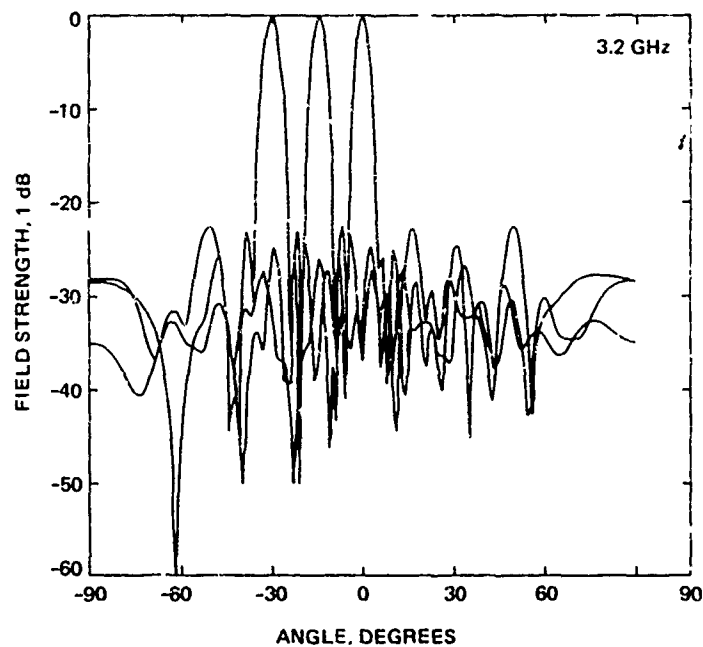


Figure 37-24. Beam patterns of 32-port phased array controlled by 3-bit switched-line diode phase switches.

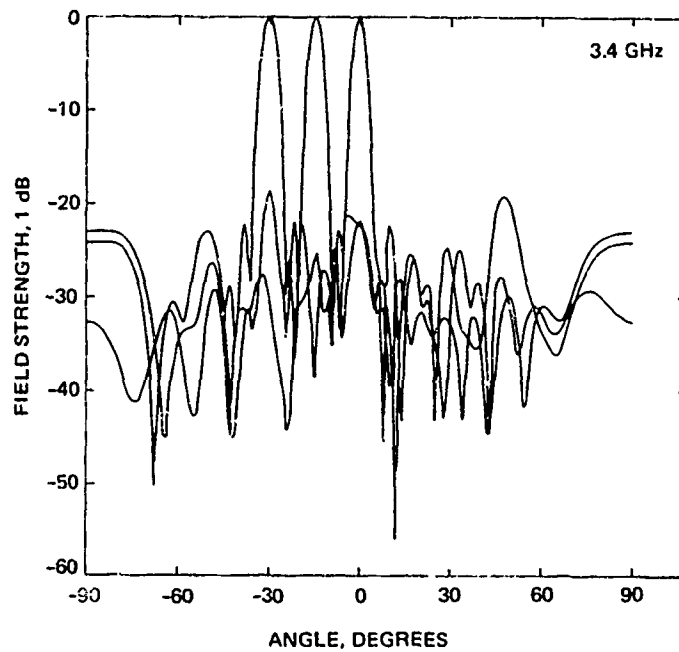


Figure 37-25. Beam patterns of 32-port phased array controlled by 3-bit switched-line diode phase switches.

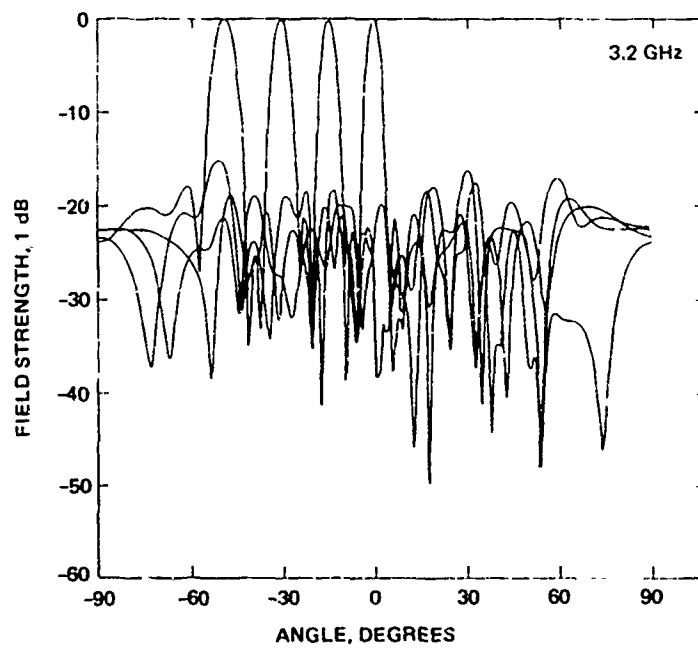


Figure 37-26. Beam patterns of 32-port phased array with circuit errors in 10 phase switches.

SUMMARY

The computer programs described in this paper optimize the design parameters for microwave power dividers and diode phase switches. The program calculates the beam patterns of a 32-port linear phased array fed by the programmed microwave components. It plots the beam patterns for selected angular positions and graphically displays the effect on the side-lobe level of simulated circuit malfunctions.

REFERENCES

1. "Computer Calculation of the Radiation Pattern of a Planar Array," Working Paper No. 18, W. R. E. Aerials and Microwaves Group, 5 May 1971
2. Reindel, J., Microwave Integrated Circuits for Phased Arrays, Naval Electronics Laboratory Center Technical Report 1739, 30 October 1970
3. Green, P. E., "General Purpose Programs for the Frequency Domain Analysis of Microwave Circuits," IEEE, Transactions, MTT-17, No. 8, p. 506-14, August 1969